A Study of K^+d interactions between 2 and 3 GeV/c

by

Sunanda Banerjee

A thesis submitted for the degree of Doctor of Philosophy of the University of London.

Department of Physics
IMPERIAL COLLEGE
London SW7

July, 1975.

ABSTRACT

A study of a K^+d experiment at 2.18, 2.43 and 2.70 GeV/c is presented here. The extraction of information about the nucleon interaction from the scattering of the deuteron has been discussed. The mechanism responsible for the excess of large momentum spectator nucleons has been investigated.

The cross-section of the K^+n elastic charge exchange process has been compared with the cross-section for the line reversed reaction and also with an SU(3) sum rule. The invariant four momentum transfer distribution of the process has been studied in the light of several Regge pole models.

The cross-sections and resonance production in the processes involving one pion production have been studied. They are dominated by the $K^*(890)$ resonance and in one case $\Delta(1236)$, the production mechanisms in terms of t-channel exchange have been studied. The decay distribution of the $K^*(890)$ suggests a possible S-P wave interference effect in the K-π system. The reaction $K^+n \rightarrow K^+\pi^-p$ is partially due to some diffractive dissociation of the target neutron.

A partial wave analysis of the reaction $K^+N \rightarrow K^*(890)N$ has been attempted. The different isospin contributions were separated out and the angular distributions were then independently fitted by partial wave amplitudes. No positive evidence of any strong Z^* production in the KN system has been found.

The final states involving a deuteron together with one or two pions have been studied. These reactions are dominated by $K^*(890)$ production. The t channel isospin filter is used to study the w-f trajectories in the reaction $K^+d \rightarrow K^{*+}(890)d$. Some structure in the $d\pi$ mass spectrum has been observed in both the reactions. However this structure cannot be identified with a resonance. A Deck type model

is used to explain the structure in the reaction $K^+d \rightarrow K^{*o}(890)\pi^+d$.

The cross-sections of the 3-pion production reactions have been presented. The final state with neutral '3π' system is dominated by η^o and ω^o production whereas the final states with a nonneutral '3π' system are dominated by $K^*(890)$ production.

TABLE OF CONTENTS

CHAPTER I

1.1 INTRODUCTION

The divisibility of matter has led so far to the discoveries of the so called elementary particles which can be broadly divided into two categories, the hadrons and the nonhadrons, according to the types of interactions in which they are involved. Each of these groups are subdivided into two according to their spin-statistics. The hadrons are divided into mesons and baryons. One useful way of getting information about the structure of an object is to have a systematic classification of the objects, e.g. Mendeleev's table for chemical elements led to the ideas about the structure of atoms. Similarly a symmetric scheme has been developed for the hadrons - this is the SU(3) group with an SU(2) subgroup of isotopic spin and a U(1) subgroup of hypercharge. One usually predicts singlet, octet, decuplet, 27-plets and so on in an SU(3) group. The members of a particular multiplet should have the same J^P value and also the same mass. But equal mass objects are very seldom found: so one introduces a breaking in the SU(3) symmetry and this led to the mass relations. However, one surprising feature is that all the baryonic states so far established can be associated in singlets, octets or decuplets atmost and nothing beyond that. This led to the idea of Gellmann-Zweig quarks that all the hadrons are built up of 3 basic quarks and their antiquarks and a particular baryon state has got only 3 quarks. All other states are regarded as exotic states. The spin of the quarks has also been incorporated and this led to a larger group SU(6). This scheme is successful in studying the nonstrange baryonic resonances and also strange baryonic resonances with $S < 0$.

One of these so called exotic states is a baryon state with strangeness + 1. This can be incorporated in an SU(3) [10] or [27] multiplet.

This would require at least four quark and one antiquark combination. Evidence of such a state was first reported by Cooletal(1966) and Abrams et al. (1967) from some structure in the K^+p and the K^+d total cross-sections. If such a baryonic state (called Z^*) exists, it would also indicate the existence of a large number of otherwise unpredicted states in the SU(3) group.

In the I=1 state, bumps were observed at total centre of mass energies 1.9 GeV, 2.2 GeV and 2.5 GeV with widths around 150 MeV. All these enhancements were found to be largely inelastic. In the I=0 state, two enhancements were observed at 1.7 GeV and 1.9 GeV with strong coupling to the elastic channel. These led to a number of partial wave analyses of the K^+N system. None of the analyses so far seems to be very conclusive. The strongest candidates for resonance behaviour in the past have been a PP3 wave in the I=1 state and a PP1 wave in the I=0 state (BGRT Collaboration). Though the PP3 wave shows the correct behaviour on the speed plot, the PP1 wave does not. Further there could be other solutions for the existing data which do not involve a resonating partial wave.

Explanations without the resonances were attempted for the bumps in the total cross-section by means of the rapid opening of the single pion and double pion production channels near the K^* thresholds. However, according to Aaron et al. (1971), this could be a dynamical mechanism to drive an inelastic K^+N resonance.

With all these facts in mind, an experiment was proposed in 1967 (I. Butterworth, 1967) to study the K^+N interaction in isospin 0 and 1 states. The experiment described in the thesis is a joint Imperial College - Westfield College K^+d experiment at beam momenta 2.18, 2.43 and 2.70 GeV/c. The experiment intended to use a high statistics (927000 pictures) study for a continuous coverage of centre of mass energy from 2.15 GeV to 2.55 GeV. Just before this experiment a control K^+p experiment was undertaken in the same centre of mass energy range to provide checks on the techniques to be used in the K^+d film. The analysis of this K^+p experiment at nominal values of beam momenta 2.1, 2.3, 2.5 and 2.7 GeV/c has been finished and published in Nuclear Physics. This K^+p experiment also increases the isospin 1 data of the K^+N system to provide more data for a complete phase shift analysis.

The primary purpose of the present experiment is to study the relatively unexplored intermediate energy region with particular emphasis on the s-channel structure. One can however study as well the structure of the mesonic systems $K\pi$ or $K\pi\pi$ in the corresponding reactions. The structure of the deuteron can also be studied by its interaction as a coherent neutron-proton state with the K^+ meson.

When the author joined the Imperial College Bubble Chamber Group in October 1972, the film taking had already been completed and the main parts of scanning and predigitising the film had also been done. However, the bulk of first and second measurements have been carried out since and the author took part in the day to day processing. The processing of the data has been shifted from the CDC 6600 to the IBM 360/195 during May 1973, and the author took part in changing some parts of the data analysis chain. The analysis described in the following chapters has been entirely done by the author himself.

The thesis is organized as follows. The following sections in Chapter 1 describe the experiment and its measurement chain with various corrections necessary and the problem of absolute cross-section normalization. Chapter 2 describes a study of the deuteron as a neutron or proton target. Chapter 3 describes an analysis of the elastic charge exchange process $K^+n \rightarrow K^op$. Chapter 4 describes the production and decay mechanisms of the resonances in the channel $K^+N \rightarrow K\pi N$. Chapter 5 gives a study of the s-channel behaviour of the K^+N system. Chapter 6 describes a study of the final states with a deuteron, and Chapter 7 lists the cross-sections for other possible final states measured in this experiment.

1.2 EXPERIMENT

Pictures were taken at the Rutherford Laboratory 1.5 metre British National Bubble Chamber between November 1969 and April 1970, using the electrostatically separated K^+ beam from the Nimrod K9 beam line. The Bubble Chamber was filled with deuterium at a density of 0.135 gm/cc. The Bubble Chamber magnetic field was 12.3 K.Gauss and on average there were 12/14 beam tracks per picture. A total of 927,000 pictures were taken which were divided into 3 beam momenta of 2.18, 2.43 and 2.70 GeV/c, each with a mean spread of 0.03 GeV/c.

400,000 pictures	2.18 GeV/c
200,000 pictures	2.43 GeV/c
327,000 pictures	2.70 GeV/c

To ensure good stereoscopic conditions for the event reconstruction three views were taken for each frame using 3 cameras with their optical axes parallel and situated at the vertices of an isosceles triangle. There was an average of one event of interest in every five frames.

The film was scanned twice for three and four prong events and for one, two, three and four prong events with an associated V_o decay. Only those four prong events were retained in which a positively charged track was stopping in the chamber. A flow chart of the measurement chain for these events has been supplied in diagram 1.1.

The events were rough digitised using an online program. The rough digitised data were edited and then used to make roads for the

HPD, which is on line to a PDP computer. The HPD using a flying spot digitiser scanned through the film in two possible orthogonal modes and digitised an event one view at a time by constructing some masterpoints. If the HPD failed to produce these master points on a track by confusion with an overlapping track or due to a badly defined road, the track could be recovered by a program called RESCUE which was on line to a CRT device and there was an operator with a light pen to redefine the road points of the track in question. Then the measurements of the three views were merged together and this was used as the input to the geometry programme.

The geometric reconstruction of the charged tracks in the three dimensional space was done by the CERN programme mass dependent THRESH. The programme takes into account the optical distortion in the chamber lenses.the variation of the magnetic field inside the chamber and the energy losses of the tracks due to ionisation inside the liquid. The programme thus calculates and writes on an output tape the position of all the vertices and the end points of the stopping tracks in the three dimensional space and the curvature, the dip angle, the azimuth of the tracks at the respective vertex with the corresponding errors. The track parameters calculated depend on the mass assigned to the corresponding particle and the output tape has a record of all such successful assignments.

This output tape was used as the input to the kinematic fitting programme called GRIND. In cases of events with an odd number of prongs, one proton (or deuteron) track in the final state is probably unobserved. This happens rather frequently in a deuteron target experiment when the proton in the deuteron does not take part in the interaction. The so called spectators are often with momenta too small to make a visible impression on the film. A proton (deuteron) track with a momentum of 75 MeV/c (120 MeV/c) leaves a track of 1 mm in space, i.e. 80 μ on the film plane in liquid deuterium. If one tries to fit such events with a proton (deuteron) track as unmeasured, the number of constraints in the fit is reduced by 3 and thus it becomes unfeasible to fit that event with one neutral particle in the final state. So the program was modified for these odd prong events to assign an additional proton (deuteron) track with momentum components $P_x = P_y = P_z = 0$ MeV/c and errors $P_x = P_y = P_z/1.37 = \pm 30$ MeV/c for protons and $\pm$ 40 MeV/c for deuterons. The 3 prong events can also be due to the tau decays of the incident beam particles. If the measurement errors were large, the program preferably picks up the event as an interaction rather than the decay. Thus one can obtain pseudo four constraint fits for final states with no neutral particles or pseudo one constraint fits for final states with one neutral particle.

For failing beam tracks, the track parameters were taken up from the beam title block. The output of the program was written on a tape and this was then subjected to an automatic choicing programme called the AUTOGRIND. GRIND usually has more than one successful fit to any event, the major problem being the distinction of a fast π from a fast K. This programme utilises the bubble density information of the charged tracks (measurement of the bubble densities on the HPD) and also imposes cuts in the missing mass calculated by GRIND. This produces as its output a printout giving details of the geometry of the event and the successful kinematic fits applicable to it. It also produces a tape which gives a list of successful fits for each event.

Then the events with resolvable ambiguities were looked on the scanning table and a final selection of the hypothesis was made. The information was fed into an edit programme through a list of edit cards. This programme edits the AUTOGRIND output tape and produces a similar edited tape. This tape was then used along with the GRIND output tape to run the CERN programme SLICE which in its turn produced the data summary tape (DST).

Approximately 30% of all events contained at least one failing track (excluding the beam track). These events are either sent for remeasurement on a manual measuring machine or marked as an unmeasurable event if it has poor track visibility or short straight tracks due to secondary scatters. The bookkeeping system consists of a tape which contains a record of each event, its roll-frame-event-measurement number, topology, measurement status and also the hypotheses numbers if it is a successfully measured event. The edited AUTOGRIND tape updates this masterlist tape every time after a measurement and also produces the remeasure list.

1.3 VARIOUS SOURCES OF LOSS OF EVENTS

Since the films were scanned twice and then passed through a checkscan one can estimate the possible scanning losses under each topology. If the numbers of events for a given topology seen on each scan are n_1 and n_2 and the number seen in both the scans is n_{12} then assuming the two scans to be independent, one gets the scanning efficiency η to a good approximation as

$$\eta = \frac{n_{12}(n_1+n_2-n_{12})}{n_1 n_2} \qquad 1.1$$

The scanning efficiencies for the different topologies have been listed in table 1.1. There is no significant variation among the different topologies. This makes the maximum uncertainty in any cross section due to scanning losses to be 1%.

However, there are certain classes of events within a particular topology which are intrinsically more difficult to scan. In particular, events with a short proton track travelling along the camera axis are unlikely to be detected during scanning. If such events are missed, it would result in depopulation of a particular region of the angular distribution. So one looks at the distribution of the azimuthal angle of the plane of the outgoing particles about the beam direction at the point of interaction. This is shown for processes $K^+d \rightarrow K^o pp$, $K^+d \rightarrow K^{*o}pp$ and $K^+d \rightarrow K^{*+}pn$ on the diagram 1.2. One essentially gets a flat distribution within statistical fluctuation and hence no correction has been introduced.

The biases in the measurement procedure can be examined by introducing a term called the measuring efficiency. This essentially gives the ratio of the numbers of events of any particular topology which have been identified successfully to the total number of measurable events under the topology. These values have been listed in table 1.1. Here however the topological variation is not insignificant. However one cannot separate the measuring efficiency for tau decays from that of other 300 topology reactions. So no correction has been made on this account. It was found that in the batch of events measured on the HPD, the number of tau decays of the beam tracks was significantly less than what one finds in a sample measured on the conventional measuring machine. This is probably due to the fact that the tau decay fits are very susceptible to the measurement of the beam track and the HPD often confuses between the overlapping beam tracks. So for absolute normalisation of the data sample one uses only a part of the data corresponding to the rolls which had been measured at least twice, once on the HPD and once on a conventional measuring machine.

By including only events in which a K^o is seen to decay in the chamber, the data only includes a definite fraction of all the events producing a K^o. Events are lost in three possible ways. Firstly the K^o decays into a system of neutral particles and hence remains undetected in this bubble chamber technique. Secondly they decay in a charged mode but so close to the vertex that it cannot be distinguished as a strange V_o decay. Rather a normal 2 prong event would pass on as a 4 prong event; a 4 prong event as a 6 prong event and so on. The third possibility is that the K^o decays outside the bubble chamber and thus prevented from being detected.

It is possible to take into account all these losses from a knowledge of the decay mechanism of the K_o. K_o is an even mixture of the two states K_S^o and K_L^o. One of the decay modes of K_S^o gives $\pi^+\pi^-$ in the final state and the corresponding branching ratio is 0.688. For K_L^o such a decay mode is forbidden by CP invariance. This leads to the fact that only one in every 2.91 K^o's would be seen to decay to $\pi^+\pi^-$. The CP violation effect affects this number by at most 0.2%. Due to the fact that not all the K^o decay to $\pi^+\pi^-$ final state can be observed one makes a further investigation in the decay distribution of K_o. Assuming an exponential decay rate one can calculate the probability of a K_o decaying to $\pi^+\pi^-$ within a distance l from the K_o production vertex and it is found to be

$$\text{PROBABILITY} = 1 - \exp(-l/L) \qquad 1.2$$

where L is the theoretical mean decay length (for that particular final state). So the probability that the K_o will not decay into $\pi^+\pi^-$ inside the inlite volume of the bubble chamber will be

$$\exp(-P/L) \qquad 1.3$$

where P is the potential length, defined to be the distance along the K^o direction from the primary vertex to the boundary of the inlite volume. To allow for the loss of K^o's decaying at an unobservedly small distance from the production vertex, a cut was chosen as the minimum projection length. For a particular K^o, this cut corresponds to a length l' along the line of flight. Then the probability of the K^o decaying at an observable length from the production vertex will be

$$\exp(-l'/L) \qquad 1.4$$

Thus the probability that the K^0 will decay in an observable distance from the production vertex and also inside the inlite volume is

$$\exp(-l'/L) - \exp(-P/L) \qquad 1.5$$

To allow for unseen decays, each event was given a weight of

$$\frac{1}{\exp(-l'/L) - \exp(-P/L)} \qquad 1.6$$

Double counting of events was avoided by neglecting the events with the V_0 vertex closer than a distance l' from the production vertex. The total number of weighted events were calculated using various values of minimum observable projection length and these have been plotted on figure 1.3. The cut on the projected length was selected to be 4 mm where the distribution on the figure 1.3 was getting flat. This gave a mean weight for a K_o decay decaying inside the chamber and being detected to be 1.056 ± 0.008.

1.4 ABSOLUTE NORMALISATION

The absolute normalisation of the cross-sections was done on the basis of the calculation of the total path length of the incident K^+ meson. If the mean free path for a particular final state is λ, the corresponding cross-section will be given by

$$\sigma = \frac{1}{n\lambda} \qquad 1.7$$

where n the total number of deuteron nuclei per unit volume of the target can be expressed as a function of the deuteron density ρ as

$$n = N_A \rho / A \qquad 1.8$$

where N_A = Avogadro's number = 6.022×10^{23} per mole

A = gramatomic weight of the target = 2.014 gram

λ is given by

$$\lambda = L / N_i \qquad 1.9$$

where N_i = total number of interactions with that particular final state

L = total path length of the incident K^+ meson

The total path length was measured on the basis of the number of tau decays of the K^+ beam tracks observed in the chamber. This gives a correct value of L independent of π^+ or μ^+ contamination in the beam. If N_τ be the observed number of tau decays.

$$L = \frac{P_b \, c\tau_K N_\tau}{B \, m_K} \qquad 1.10$$

where P_b = laboratory momentum of the beam particles

c = speed of light

τ_K = lifetime of the K^+ meson ($c\tau_K$ = 370.8 cm)

B = branching ratio of K^+ to the $\pi^+\pi^+\pi^-$ (tau) decay mode

= 0.0559

m_K = mass of the K^+ meson = 0.4937 GeV

Thus one obtains

$$\sigma = \frac{N_i}{N_\tau} \frac{A B m_K}{c\tau_K N_A \rho} \frac{1}{P_b} = \frac{N_i}{N_\tau} \frac{1.843}{P_b(\text{in GeV/c})} \text{mb} \qquad 1.11$$

As has been mentioned earlier, the tau decays are difficult to fit unambiguously. To help to overcome this problem at the GRIND fitting stage the rare one constraint hypothesis $K^+ \rightarrow \pi^+\pi^0 \rightarrow \pi^+e^+e^-\gamma$ was fed into the program. One can test if events giving a fit to this hypothesis were really taus by changing the e^+e^- to $\pi^+\pi^-$ and plotting the effective '3π' mass distribution (figure 1.4). There is a clear enhancement at the K-mass whereas the '$e^+e^-\gamma$' effective mass plot (figure 1.5) show only a small peak around π^o mass with a large accumulation of events at a higher mass. These events which cause the large mass enhancement are responsible for the peak at K^+ mass in '3π' effective mass plot. This indicates that they are mostly misfitted tau decays. Further one can select out other 3 prong events where GRIND gives an interaction type fit e.g. $K^+d \rightarrow K^+\pi^+\pi^-(d)$ or $K^+d \longrightarrow K^+\pi^+\pi^-(p\ n)$ and change the K^+ (final state) mass to a π-mass and then plot the effective '3π' mass distribution (figure 1.6). This again shows a clear enhancement at the K^+ mass. So a cut in the effective '3π' mass-squared was made between 0.2 GeV^2 and 0.28 GeV^2. This gave a 1.3% increase in the overall number of taus.

TABLE 1.1

	SCANNING EFFICIENCY			MEASURING EFFICIENCY		
	1 or 2 prong events with a V_o	3 or 4 prong events without a V_o	3 or 4 events with a V_o	1 or 2 prong events with a V_o	3 or 4 events without a V_o	3 or 4 prong events with a V_o
2.18 GeV/c	97.2±0.6%	96.5±0.4%	95.4±2.1%	78.1±0.7%	76.2±0.8%	64.9±6.5%
2.43 GeV/c	97.1±0.7%	96.6±0.6%	96.6±1.8%	84.1±1.3%	89.0±0.9%	81.3±3.7%
2.70 GeV/c	93.9±0.5%	95.4±0.3%	94.9±1.1%	81.6±0.9%	83.1±0.6%	72.1±2.2%
Combined	96.0±0.2%	95.2±0.4%	95.2±0.9%	79.4±0.5%	82.4±0.4%	70.7±1.5%

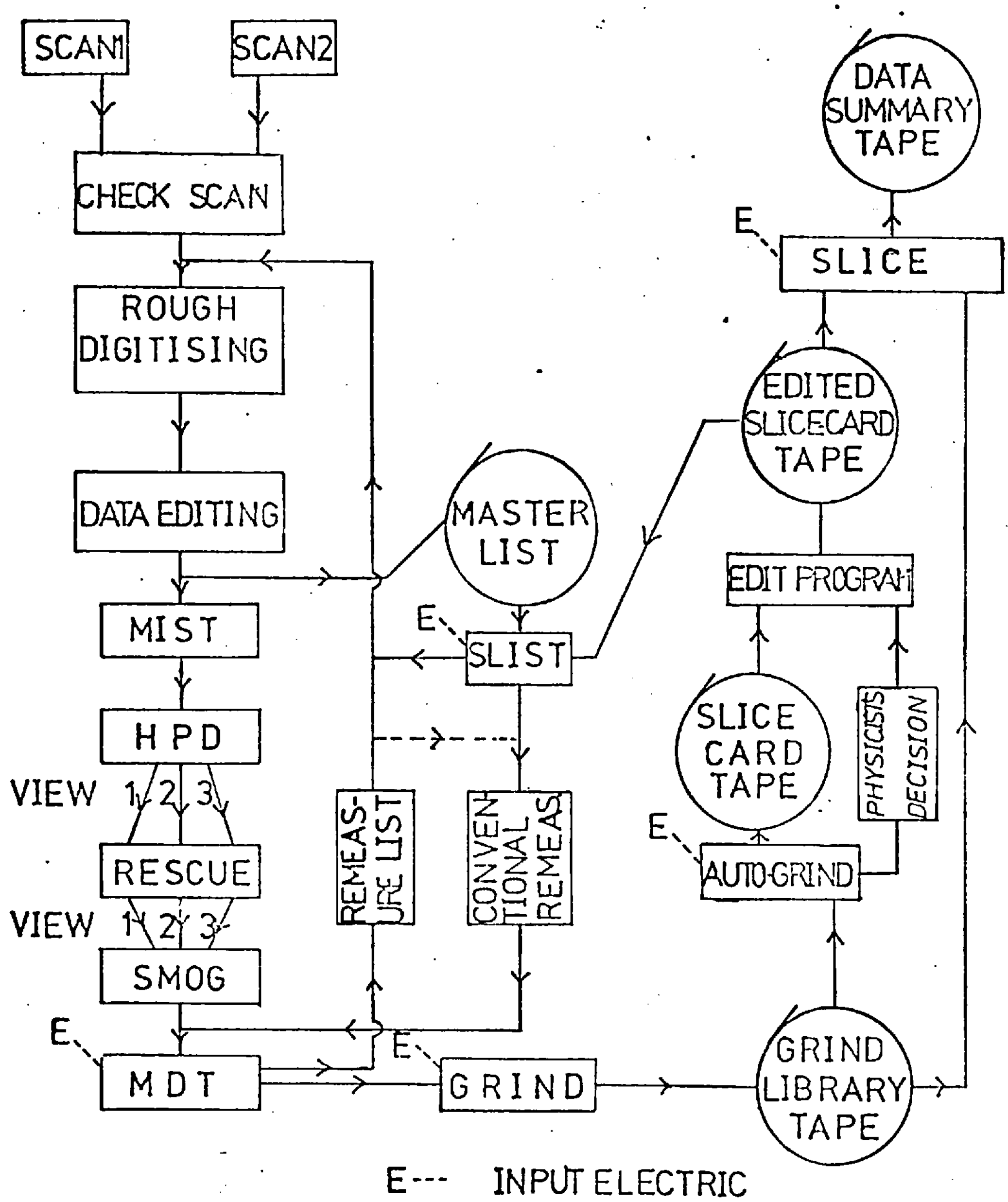

1.1 THE DATA PROCESSING SYSTEM

1.2 SCAN-BIAS ANGLE

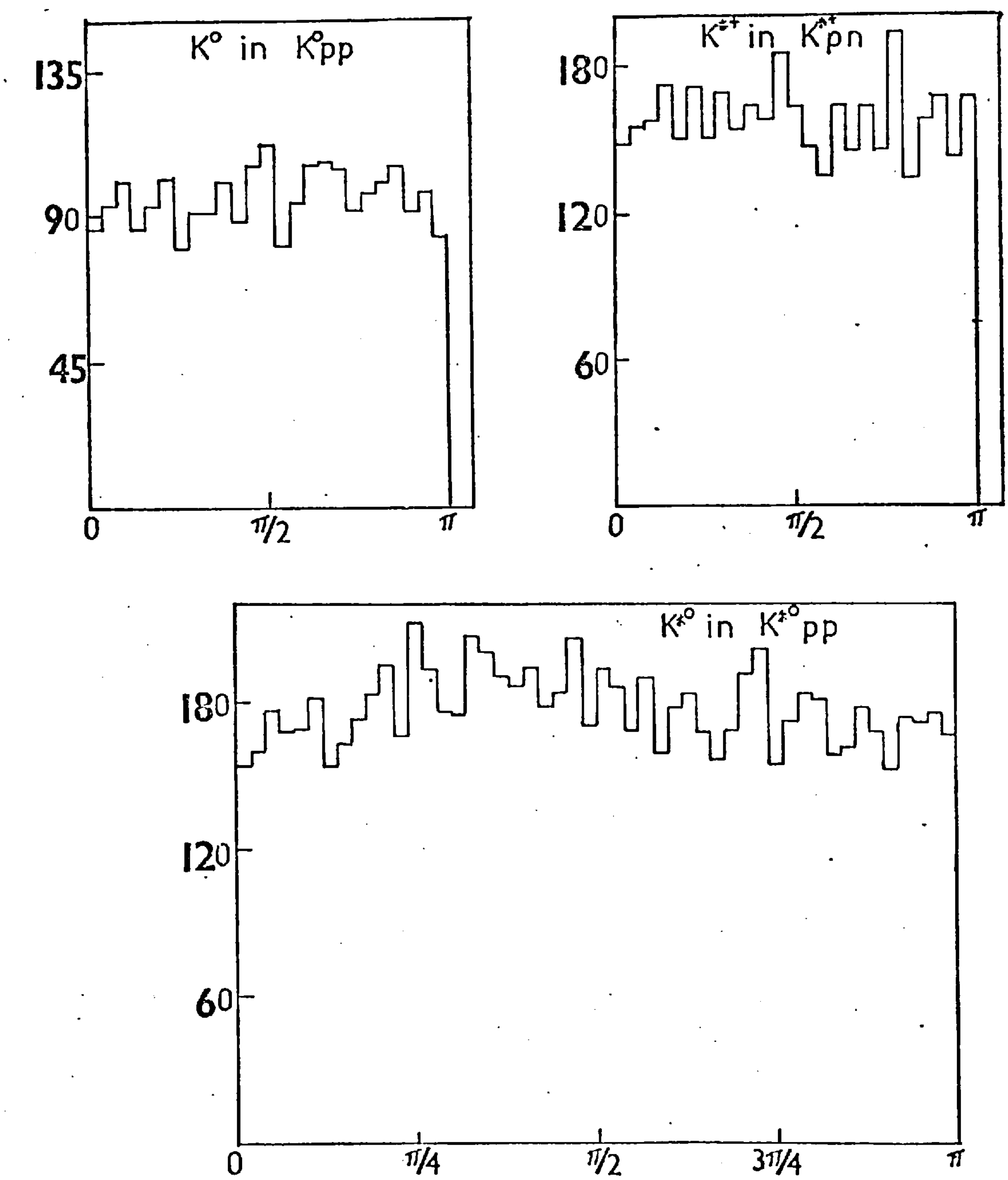

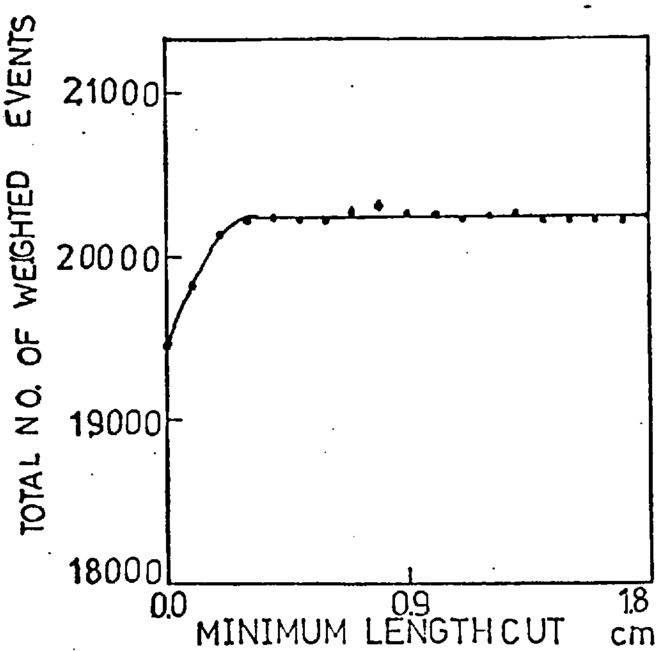

1.3

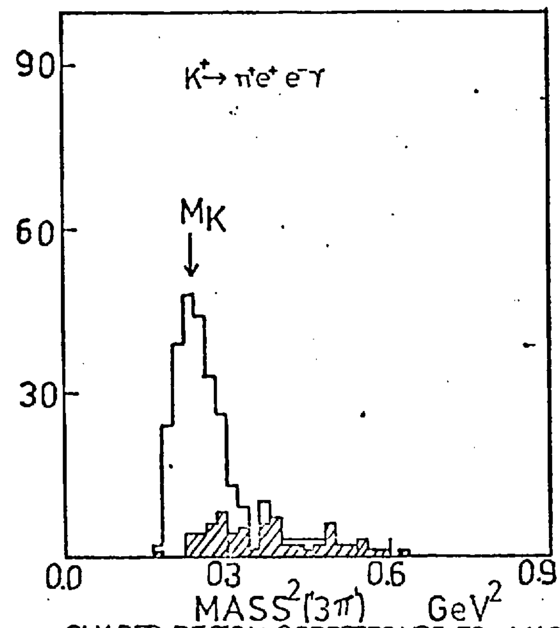

SHADED REGION CORRESPONDS TO MASS($e^+e^-\gamma$) < 0.16 GeV

1.4

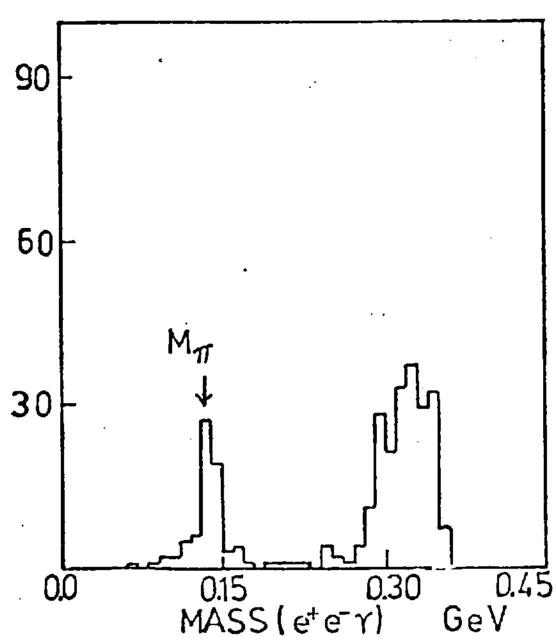

1.5

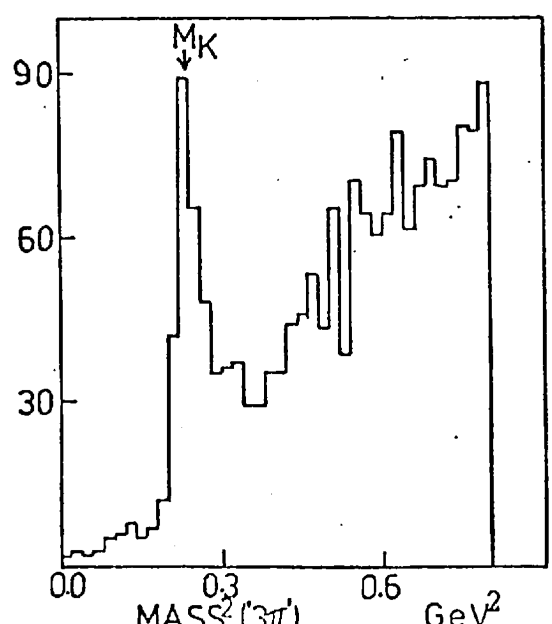

IN $K^+(d) \to K^+\pi^+\pi^-(d,pn)$

1.6

CHAPTER 2

The nonavailability of free neutron targets makes the deuteron an obvious choice as a target for extracting neutron cross-sections. But then comes the problem of relating the deuteron cross-section to the free nucleon cross-section. To understand the assumptions involved in the process of extraction it is better to go through the main properties of a deuteron nucleus. The nucleus consists of a proton and a neutron bound with an energy of 2.225 MeV. The nucleus is in a total angular momentum J=1 state and isospin I=0 state, the mean separation between the nucleons being 4.3 Fermi. The nonzero electric quadrupole moment suggests that the deuteron wave function is not purely spherically symmetric but possesses a D-wave admixture. The admixture is however small, the probability of the target being found in the D-state is about 7%. However, there may be sometimes an interference between the S- and D-wave effects in the cross-section so that the relative parameter for D-wave contamination may well be as high as 25% which is no longer insignificant. For a pure S-wave, the deuteron wave function takes the form (Hülthen 1957)

$$\psi(r) = N\frac{(\exp(-\alpha r) - \exp(-\beta r))}{r} \qquad 2.1$$

where r is the inter nucleon distance, N is a normalization constant and $1/\alpha$ measures the radius of the deuteron nucleus. The values of β vary slightly in the different texts. Here β is chosen to be equal to 7α and α = .0456 GeV/c. When expressed in terms of α and β

$$N = \frac{1}{\beta-\alpha}\sqrt{\frac{\alpha\beta(\alpha+\beta)}{2\pi}} \qquad 2.2$$

The fourier transform of $\psi(r)$ gives the momentum space wave function

ϕ(p) from which one can find the momentum distribution function of one of the nucleons in the deuteron nucleus.

$$P(p)dp = 4\pi|\phi(p)|^2 p^2 dp$$
$$= \frac{4\alpha\beta(\alpha+\beta)}{\pi(\beta-\alpha)^2}\left[\frac{1}{p^2+\alpha^2} - \frac{1}{p^2+\beta^2}\right]^2 p^2 dp \quad 2.3$$

2.1 IMPULSE APPROXIMATION

One of the important effects of the second nucleon lies in the target particle binding. These are usually reflected in things no more complicated than various form factors associated with the deuteron wave function. Applying Watson's multiple scattering series in the case of deuteron one gets the total amplitude as the sum of a series of terms for multiple scatterings with the bound nucleon as shown in figure 2.5.

With the bombarding energy large compared to the deuteron binding energy, it would be eminently reasonable to neglect the effect of the nucleons being off mass shell. This is the impulse approximation. Now the probability of the multistep process which involves an intermediatemeson state is related to the internucleon separation and also the meson momentum. The Hulthen wave function predicts that the mean nucleon separation corresponds to 50 MeV/c whereas when the momentum transfer to one of the nucleons is small, the momentum of the intermediate meson state is approximately 2 GeV/c. Then the probability of such processes is small and one can thus truncate the expansion within this closure approximation.

With the above assumptions one thus relates the deuteron cross-section to the corresponding free nucleon cross sections where the second nucleon remains a spectator to the reactions. Then one expects the momentum distribution of the spectator nucleon should be given by the deuteron wave function and the spectator nucleons should be isotropically distributed in the deuteron rest frame which is the laboratory frame in this experiment. The deuteron wave function predicts the momentum to be peaked near 50 MeV/c and approximately 98% of the spectators should have their momenta less than 300 MeV/c. This obviously suggests that the nucleon with smaller momentum is more likely to be the spectator. So throughout the experiment one chooses the spectator on the above criterion. The spectator momentum distribution has been studied separately for the various channels.

<u>a) 4 constraint kinematic fits:</u> The spectator momentum for the process $K^+n(p) \rightarrow K^0p(p)$ has been shown in the diagram 2.1. The fitted curve is a calculation from the equation 2.3 normalised to the total number of events. At low momentum values, the experimental distribution closely follows the shape of the theoretical prediction. However, it has a much larger high momentum tail than the theoretically predicted value. 15.3% events have spectator momentum greater than 300 MeV/c whereas the theory expects only 1 - 2%. For the other highly constrained channel $K^+n(p) \rightarrow K^+\pi^-p(p)$ (Figure 2.3A), one sees a similar effect. The only difference is that the tail contains 2.1% of the total events. The discrepancy between these two channels results from the scanning criterion that only those 400 topology events which have got a proton track stopping inside the chamber should be measured. One other observation can be made for this channel, namely there is slight depletion of events at low spectator momenta.

The angular distribution of the spectator nucleon with respect to the beam particle are shown in figure 2.2. (for the process $K^+n(p) \rightarrow K^0p(p)$) and figure 2.4A (for the process $K^+n(p) \rightarrow K^+\pi^-p(p)$). The shaded regions correspond to the events with a seen spectator. The distributions show slight angular dependence in both the processes. This has been explained in Section 2.3.

b) One constraint kinematic fits with a neutron spectator: The neutron momentum distribution for the process $K^+p(n) \to K^o\pi^+p(n)$ is shown in figure 2.3D. When it is compared with the theoretical prediction, the distribution looks much broader than is expected. This is due to the large error involved in the less constraint fits. Also when the proton is unseen, the event is essentially a zero constraint fit and this severely distorts the distribution. The tail of the distribution beyond 300 MeV/c contains 12.3% of the total events.

The angular distribution shown in figure 2.4D for these events has an anomalous peak near $\cos\theta \sim 0$, where θ is the laboratory angle between the spectator neutron and the beam. This distribution together with the spectator momentum distribution may suggest a possible contamination with the channel $K^+d \to K^o\pi^+\pi^o pn$ with a slow π^o. However the missing mass squared distribution (figure 2.7) shows no asymmetry, suggesting that such a contamination is unlikely.

c) One constraint kinematic fits with a proton spectator: The spectator proton momentum distributions for the processes $K^+n(p) \to K^o\pi^o p(p)$ and $K^+n(p) \to K^o\pi^+n(p)$ have been plotted on the figures 2.3B and 2.3C respectively. They show an obvious distortion at the low spectator momentum range. This results from the pseudo 1C fits. One encouraging feature is that above 100 MeV/c, the experimental distribution closely follows the theoretical prediction (except the high momentum tail). This suggests that the real 1C fits fit with the impulse model nicely. Furthermore the fraction of events with an unseen proton track is 66.2%, comparable to the same quantity in the higher constrained fits. The tails correspond to 12.0% and 15.4% of the total events respectively. The angular distribution for all the events in the reaction $K^+n(p) \to K^o\pi^+n(p)$ (figure 2.4C) shows a dip at $\cos\theta \sim 0$. However the events with a seen spectator do not show this anomalous dip.

The large high momentum tail of the spectator nucleon has been studied in some more detail for the process $K^+d \to K^o pp$. Figure 2.9A shows the Chew-Low plot for the process, namely a scatter plot of $t(K^+ - K^o)$ against the effective mass-squared of the two proton system. The main feature of the plot is a straight narrow band of events in the centre of the plot. If one assumes that (a) the closure approximation is true and (b) the spectator nucleon is stationary in the deuteron rest frame, one gets a linear relation between t and M^2_{pp}, namely

$$-t = M_{pp}^2 - 4m_p^2 \qquad 2.4$$

m_p being the proton mass. This linear relation between t and M^2_{pp} together with the motion of the spectator nucleon explains this band of events reasonably well. There is also some accumulation of events near the Chew-Low boundary. The events where the spectator momentum is greater than 300 MeV/c have been separately plotted on a similar scale on figure 2.9B and the events near the boundary as a matter of fact correspond to these large spectator momentum events. So these events were selected out and examined separately. The cuts used were at $M^2_{pp} = 3.85$ GeV^2 and $-t = 0.04$ GeV^2.

These events may correspond to exchange diagrams like figure 2.6. Thus the data would essentially give the scattering of a virtual ρ or A_2 with the deuteron to give two protons in the final state. The only existing angular distribution data for some similar process are those for the reaction $pp \to \rho^+ d$ at 18 GeV/c (Allaby et al. 1969) which show a very sharp forward peak. This does not explain the fast spectator proton angular distribution in the pp rest frame from this low energy $K^+d \to K^o pp$ data. However the angular distribution of that process is expected to be very much different as one comes down in the centre of mass energy. Anderson et al. (1971) studied the two processes $pp \to \pi^+ d$ and $pp \to \rho^+ d$

at similar energies and observed a remarkable similarity in the two processes at very high energies. If one assumes this similarity is present also at low energies ($E^* \sim 2.8$ GeV) one can compare the polar angular distribution of the fast proton in the proton-proton rest frame with the existing data for the process $pp \rightarrow \pi^+ d$ (Heinz 1968). This comparison has been shown on the figure 2.8 and the present data are consistent with the pp scattering data in very good detail. This might suggest that a mechanism like ρ or A_2 exchange with the deuteron as a whole may be responsible for the large spectator momentum events.

On the other hand, the fast spectator momentum events may arise due to the scattering of the spectator nucleon with the other nucleon or the meson. Since nucleon-nucleon cross section is much larger than meson nucleon cross section, the scattering between the two nucleons is more likely. Thus one would expect the momentum transfer between the two protons to be relatively small. One finds that the two proton system in this $K^+ d \rightarrow K^o pp$ data has a highly forward peaked angular distribution in the pp rest frame (figure 2.14). A simple minded model calculation was done where the spectator proton scatters off the other proton in the final state. The experimental angular distribution of the process $K^+ n \rightarrow K^o p$ and the $pp \rightarrow pp$ scattering data were fed into the calculation. The forward dip for the reaction $K^+ n \rightarrow K^o p$ has not been taken into account, this might improve the fit. An attempt has been made to explain the proton angular distribution in the pp rest frame (in this experiment), see figure no. 2.14. The fit is reasonable within uncertainties of this experiment. However in contrast to the fit described in the previous paragraph this fit is rather poor. So the first mechanism more likely seems to be responsible for the large spectator momentum events.

For a pure S-wave deuteron, the nucleons are oscillating in a radial direction, having a maximum momentum when coincident at the centre of the deuteron. At this point the probability of screening and hence of multiple scattering is a maximum and as a result of the double interaction, the spectator should have a tendency to go forward. The angular distribution of spectators in events with spectator momentum greater than 300 MeV/c is shown in figure 2.10 which shows a sharp forward peak. Furthermore the forward backward asymmetry (as shown in figure 2.11) increases with multiplicity of the channel. These facts support the explanation by multiple scattering of the spectator nucleon, but with the existing data set, it is not possible to say conclusively which mechanism is responsible for the large spectator momentum events. Kisslinger (1970) and others suggested that the deuteron consists of baryon resonances as well as nucleons. This helped to explain the n-p backward scattering data. Following this idea C.P. Horne et al. (1974) established the existence of two Δ's in the double pion production channel of K^+d and π^+d scattering. The relevant channel in this experiment is $K^+d \rightarrow K^+\pi^+\pi^-pn$. A true signal of such processes is a backward going Δ^{++} which decays in a P wave to $p\pi^+$ system. Though there is some accumulation of events near the Δ-mass in the spectator proton-π^+ system, very few of them go in the backward direction and also the mass distribution does not correspond a Breit Wigner. However kinematics suggest that at the energy of this experiment such a reaction is very unlikely. So in this experiment one can assume that the data (with spectator momentum $<$ 300 MeV/c) come from single nucleon interaction with K^+ beam. Since the impulse and closure approximations are not valid at large spectator momentum, a truncation of events is made at spectator momentum 300 MeV/c. The impulse and closure approximations are assumed to be valid for the rest of the data sample. This has been supported by the fact that the cross-section and angular distribution of the process $K^+p(n) \rightarrow K^0\pi^+p(n)$

determined in this experiment (based on the spectator momentum cut) tally reasonably well with those measured in hydrogen target experiments (see Chapter 4)

2.2 GLAUBER SCREENING:

The existence of the second nucleon may cause a reduction of the total cross-section especially at higher energies. Since the incident wavelengths in these cases are much smaller than the ranges of interaction, the nucleons may be thought of casting fairly well defined shadows. The absorption or scattering by either nucleon is then reduced when it enters the shadow of the others. If one assumes that the interaction ranges are small compared to the average separation r of the nucleon, then the probability density of the second nucleon is isotropic about the first. Using an optical analogy one relates the deuteron cross-section to the free proton and neutron cross-sections by

$$\sigma_d = \sigma_n + \sigma_p - \frac{\sigma_n \sigma_p}{4\pi}\left\langle\frac{1}{r^2}\right\rangle_d \qquad 2.5$$

This was first studied by Glauber (1955) and later developed in much more detail by Wilkins (1966) and others. At the energies of this experiment, the Glauber correction to the total K^+N cross-section is about 3%, so the refinements of 2.5 have been ignored in this case.

2.3 FERMI MOTION OF THE NUCLEONS:

The Fermi motion of the nucleons inside the nucleus has two effects on the observed cross-section. (a) Depending on the direction and magnitude of the velocity of the target nucleon, the total centre of mass energy of the system is increased or decreased. This results a smearing of the centre of mass energy E^* at any fixed beam momentum. This makes it possible to measure the parameters of any reaction as a function of E^*. The beam momenta were so chosen that the different E^* bands overlap on one another and one gets a continuous E^* spectrum. This property has been utilised in Chapter 5 to study the s-channel behaviour of the process $KN \rightarrow K^*N$. The low constraint fits have a narrower E^* band as has been expected since the neutrals in pseudo 1c fits are preferably fitted with very small momenta. (b) The incident flux depends on the relative velocity between the two interacting particles and so when the target particle is moving, its velocity will change the flux and hence the total cross-section. This flux factor is a maximum when the two particles collide head on and it is a minimum when the two velocities are in the same direction.

These two effects can jointly explain the spectator angular distribution since the total cross-section is a function of the centre of mass energy, the probability of having head on collisions (where centre of mass energy is a maximum) will be different from the probability of having the target moving transversely. Furthermore the interaction probability is proportional to the flux factor. This effect is analogous to the Doppler effect. Neglecting the dependence on centre of mass energy. One gets a spectator angular distribution of the form

$$W(\text{Cos}\theta) = \text{const} \times (1 + \beta_s \text{Cos}\theta / \beta_k) \qquad 2.6$$

where β_s and β_k are the spectator and the beam velocities. So this can take into account a maximum of 20% variation from forward to backward direction.

2.4 EFFECT OF PAULI EXCLUSION PRINCIPLE:

Due to Fermi statistics, certain angular momentum states of the two nucleons system are restricted and this is reflected on the observed deuteron differential cross-section. When one has two protons or two neutrons in the final state, then at t = 0, the two nucleons are very close together and in the S-wave deuteron they form a spin 1 state. The isospin flip of the nucleons should then be compensated by a spin flip to have a total antisymmetric wave function. This results in the non spin flip component being suppressed in the forward direction.

The deuteron cross-section can thus be expressed in terms of the spin flip and spin non flip components of the free nucleon cross-section as

$$\left.\frac{d\sigma}{dt}\right|_d = (1-D(t))\left.\frac{d\sigma}{dt}\right|_N^{NF} + \left(1-\frac{1}{3}D(t)\right)\left.\frac{d\sigma}{dt}\right|_N^{SF} \qquad 2.7$$

where D(t) is the deuteron form factor. In terms of α and β

$$D(t) = \frac{2\alpha\beta(\alpha+\beta)}{(\beta-\alpha)^2\sqrt{-t}}\left[\tan^{-1}\left(\frac{\sqrt{-t}}{2\alpha}\right)+\tan^{-1}\left(\frac{\sqrt{-t}}{2\beta}\right)-2\tan^{-1}\left(\frac{\sqrt{-t}}{\alpha+\beta}\right)\right] \quad \text{for } t<0$$

$$= 1 \qquad \text{for } t=0 \qquad 2.8$$

Thus

$$\left.\frac{d\sigma}{dt}\right|_N = \left.\frac{d\sigma}{dt}\right|_d \frac{1}{1-D(t)\left[\frac{1-R(t)/3}{1-R(t)}\right]} \qquad 2.9$$

where R(t) is the ratio of the spin non flip and spin flip cross-sections with a free nucleon tartet. Since R(t) cannot be determined in a model independent way, there is no such way of extracting free nucleon cross-sections. However D(t) is very sharply peaked and it is negligibly small above $-t = .1$ GeV^2. Thus the correction is only meaningful at small t values (i.e. $-t < .1$ GeV^2). Unless specified, the cross-sections listed in the following chapters do not include these corrections. All these corrections in effect can increase the uncertainties in the quoted values.

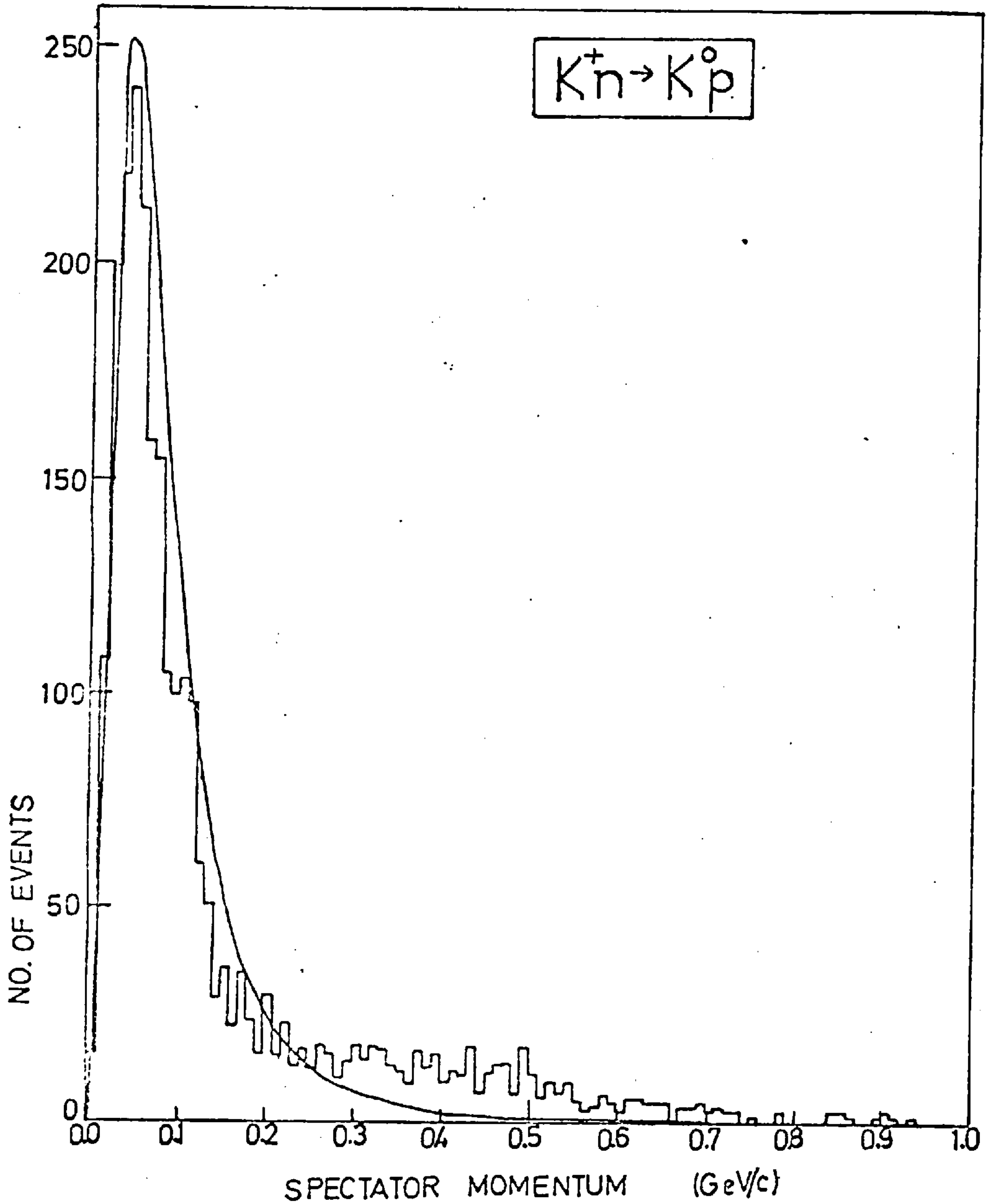
$K^+n \to K^0p$
NO. OF EVENTS
SPECTATOR MOMENTUM (GeV/c)
0
50
100
150
200
250
0.0
0.1
0.2
0.3
0.4
0.5
0.6
0.7
0.8
0.9
1.0

2.1

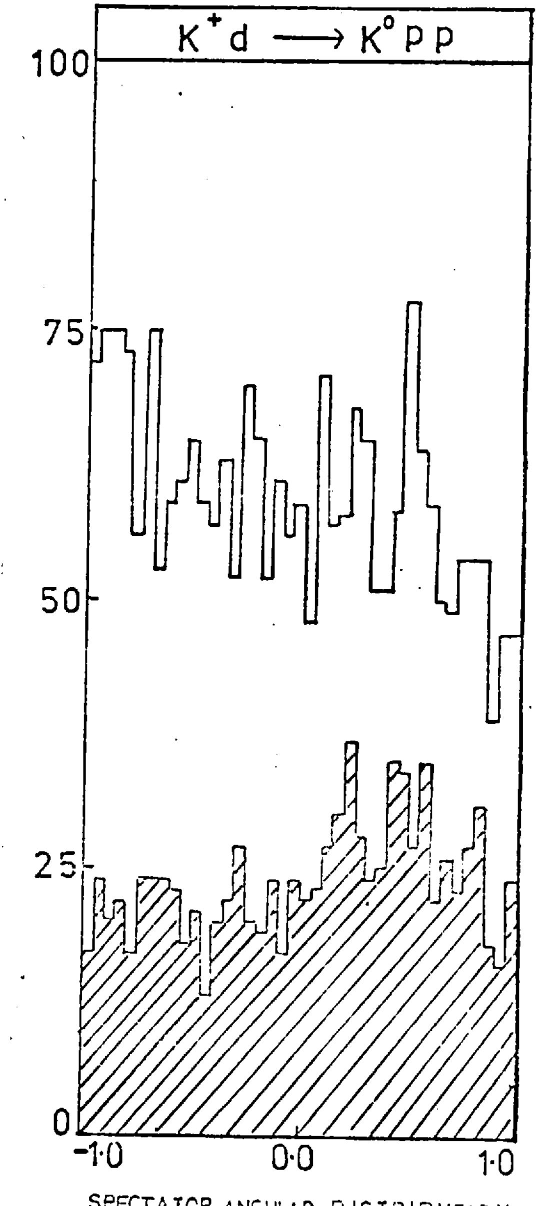
$K^+d \longrightarrow K^0pp$
0
25
50
75
100
-1·0
0·0
1·0
SPECTATOR ANGULAR DISTRIBUTION

2.2

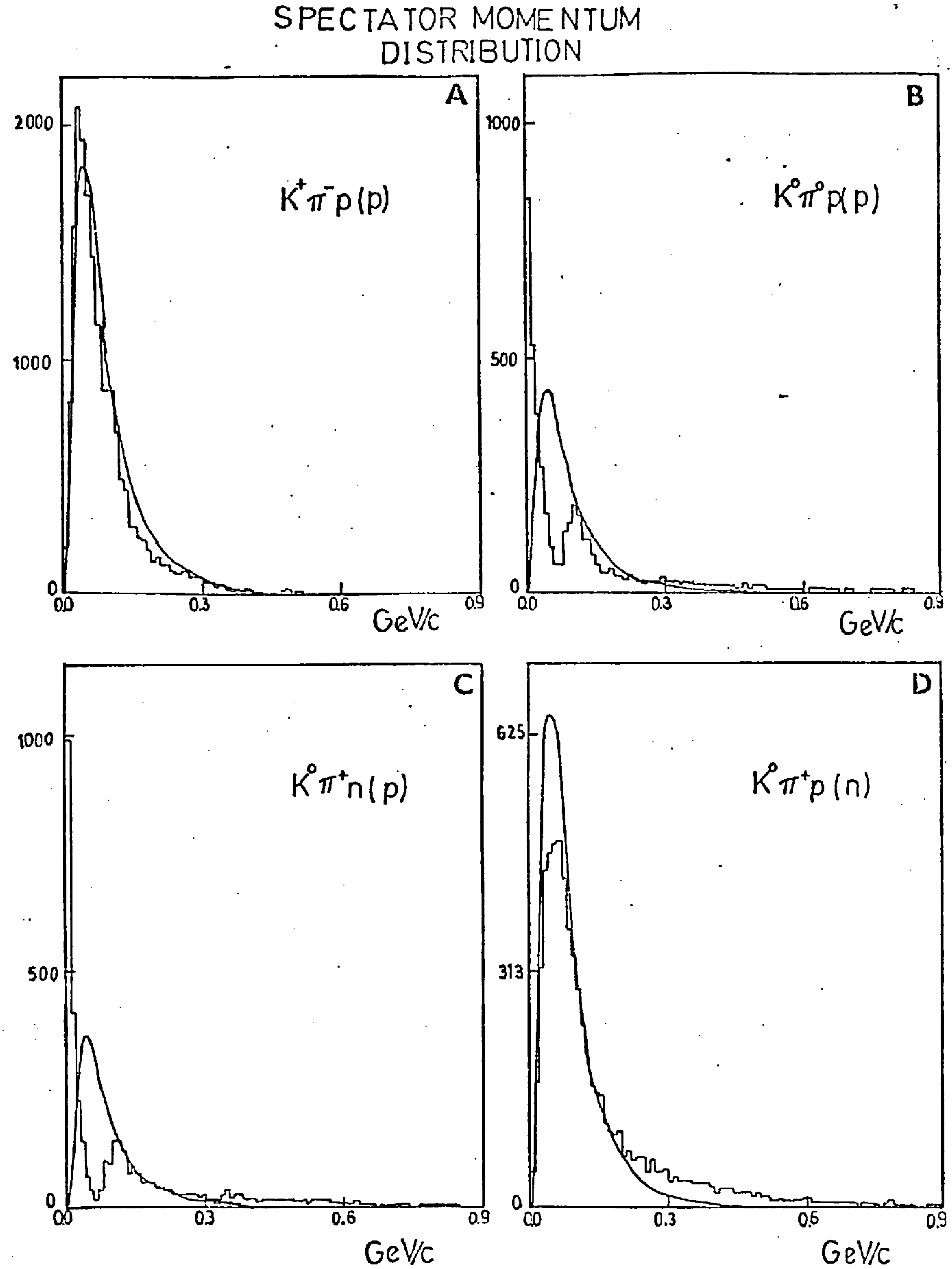
SPECTATOR MOMENTUM DISTRIBUTION
A
2000
1000
0
$K^+\pi^- p(p)$
0.0
0.3
0.6
0.9
GeV/c
B
1000
500
0
$K^0\pi^0 p(p)$
0.0
0.3
0.6
0.9
GeV/c
C
1000
500
0
$K^0\pi^+ n(p)$
0.0
0.3
0.6
0.9
GeV/c
D
625
313
0
$K^0\pi^+ p(n)$
0.0
0.3
0.6
0.9
GeV/c

2.3

SPECTATOR ANGULAR DISTRIBUTION

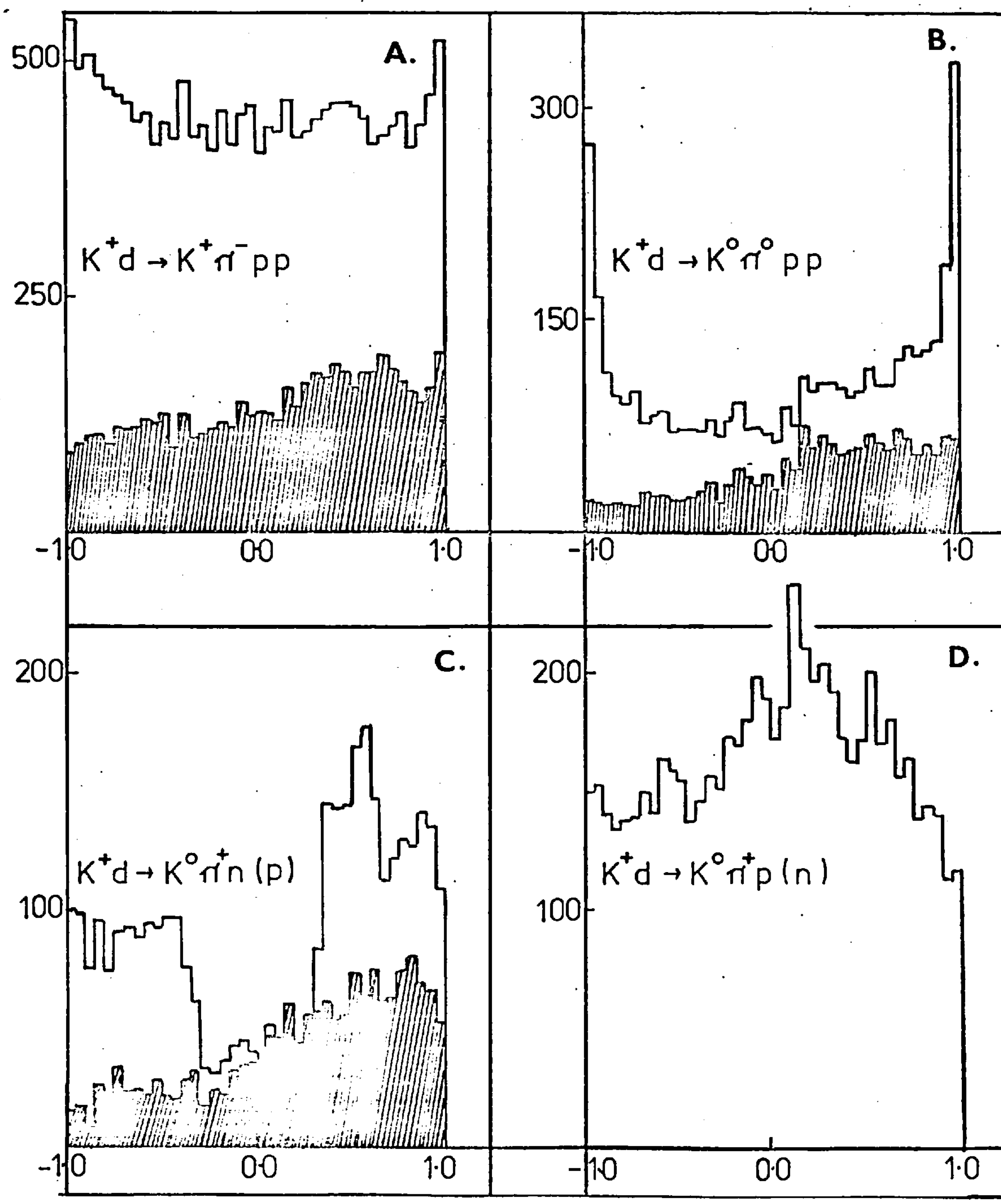

2.4

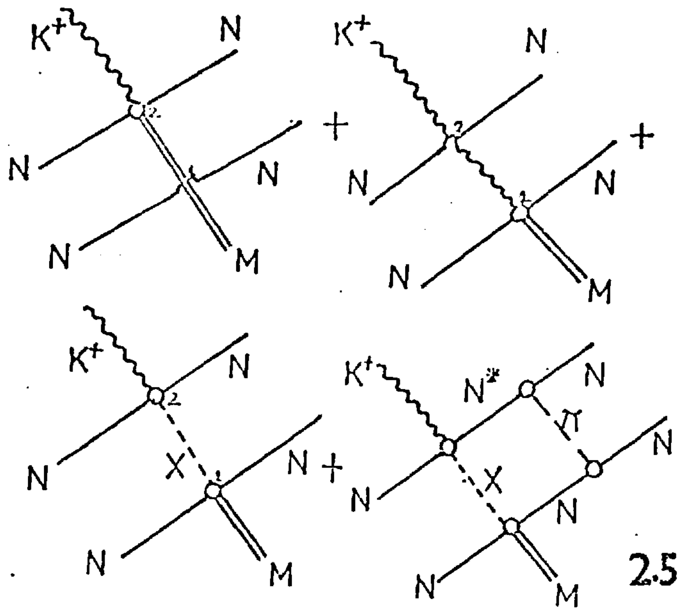
K+
N
M
X
N*
π

2.5

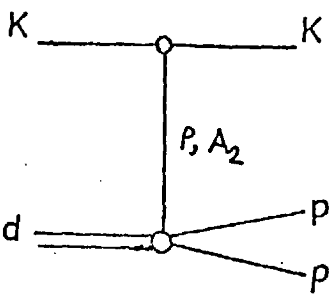
K
K
ρ, A2
d
p
p

2.6

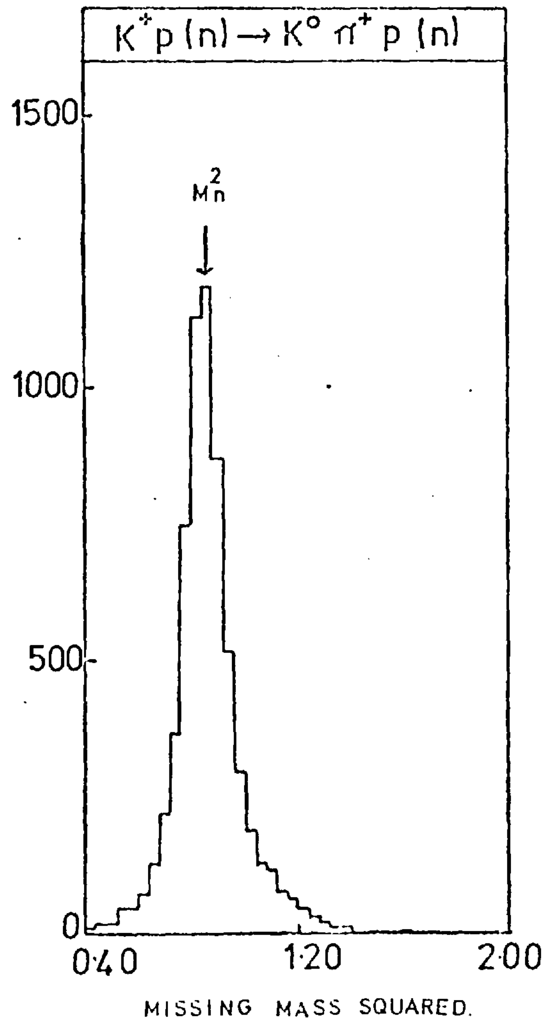
K+p (n) → K° π+ p (n)
1500
1000
500
0
Mn2
0·40
1·20
2·00
MISSING MASS SQUARED.

2.7

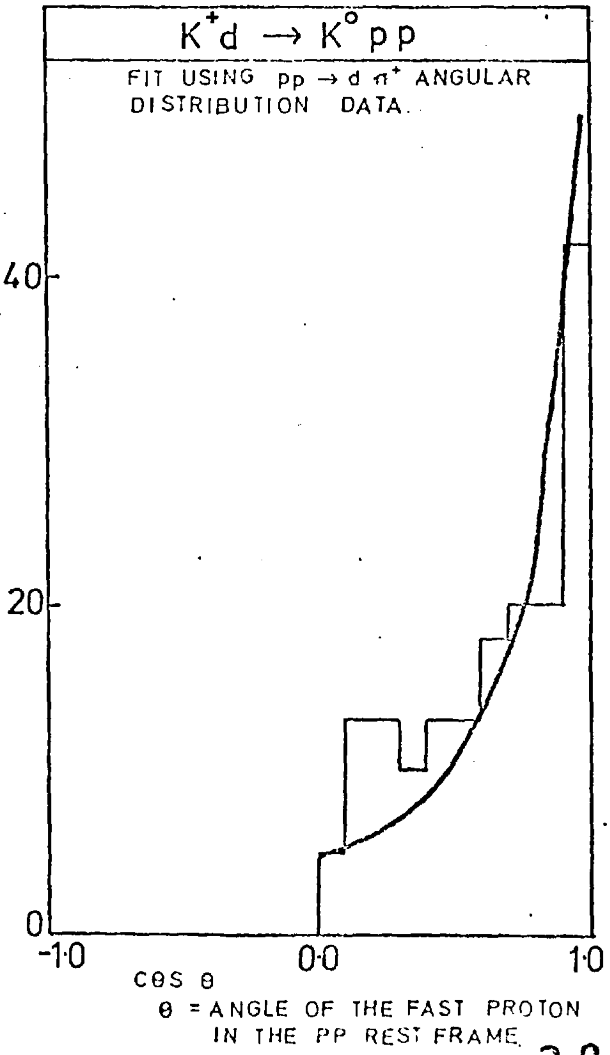
K+d → K° p p
FIT USING pp → d π+ ANGULAR DISTRIBUTION DATA.
40
20
0
-1·0
0·0
1·0
cos θ
θ = ANGLE OF THE FAST PROTON IN THE PP REST FRAME.

2.8

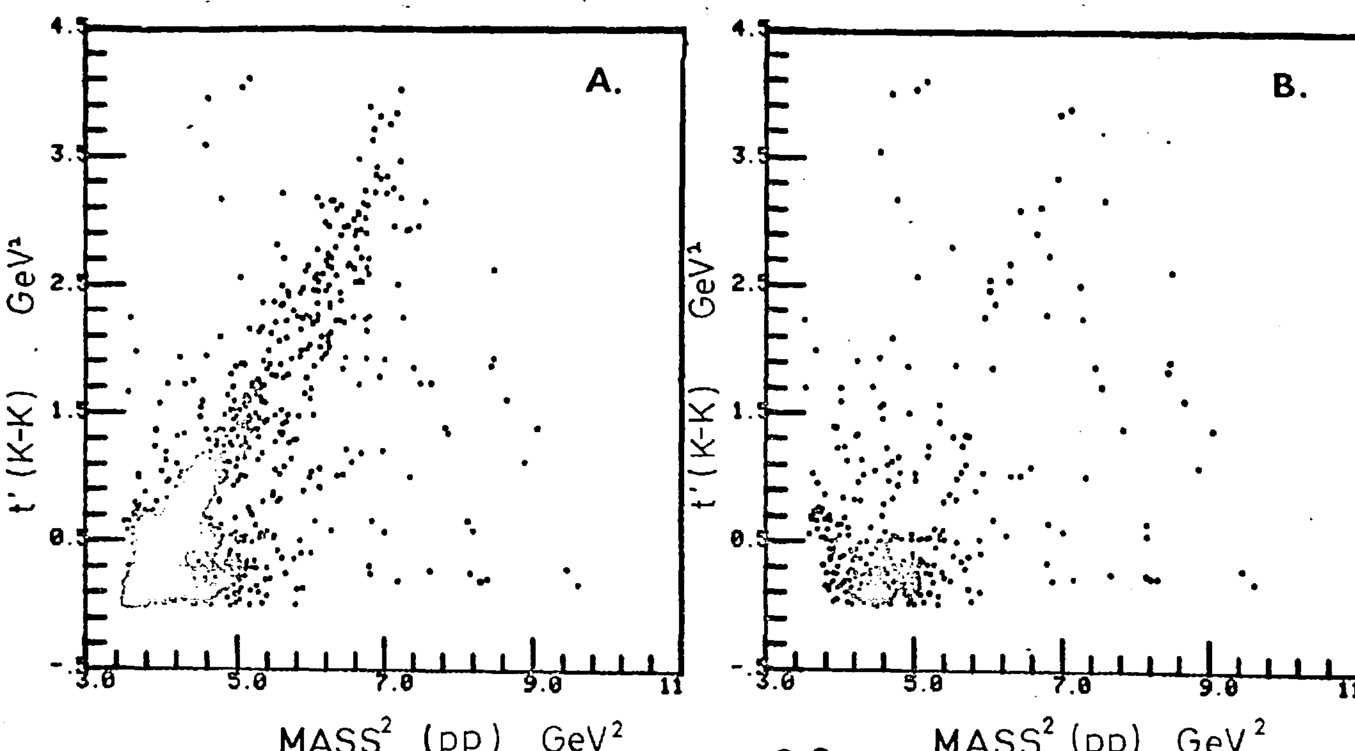
A.
B.
t' (K-K) GeV²
MASS² (pp) GeV²
4.5
3.5
2.5
1.5
0.5
-.5
3.0
5.0
7.0
9.0
11

2.9

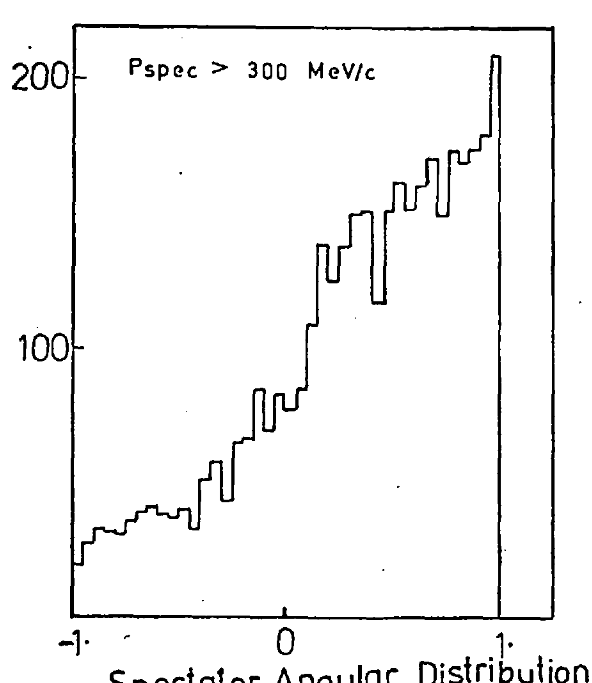
Pspec > 300 MeV/c
200
100
-1
0
1
Spectator Angular Distribution

2.10

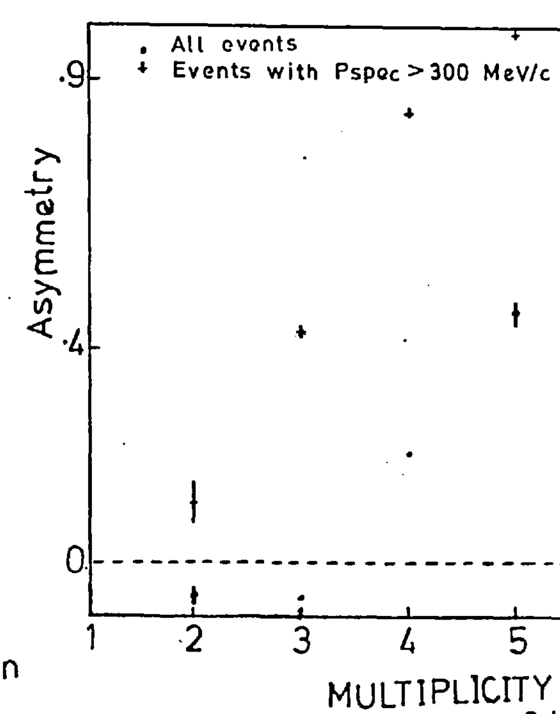
All events
Events with Pspec > 300 MeV/c
Asymmetry
.9
.4
0
1
2
3
4
5
MULTIPLICITY

2.11

$K^+d \to K^0 pp$

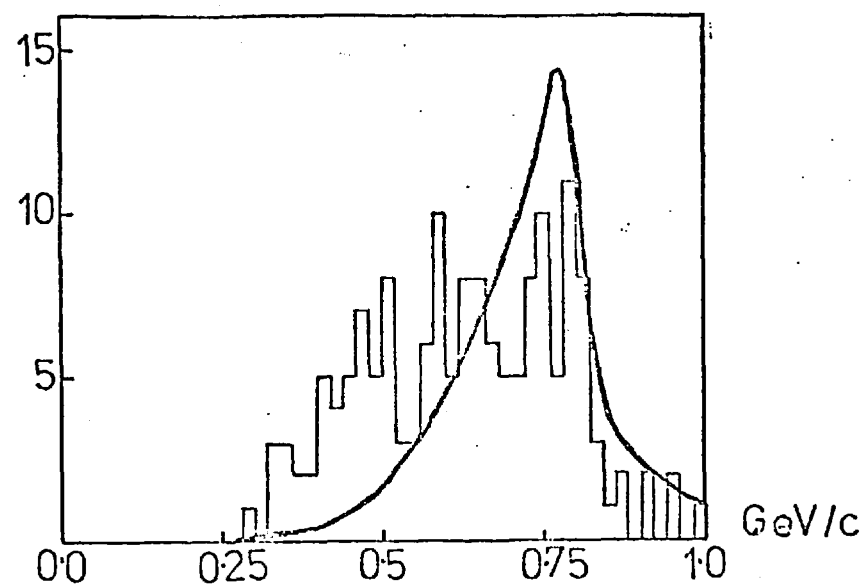

2.12 MOMENTUM OF (PP) IN LABORATORY FRAME

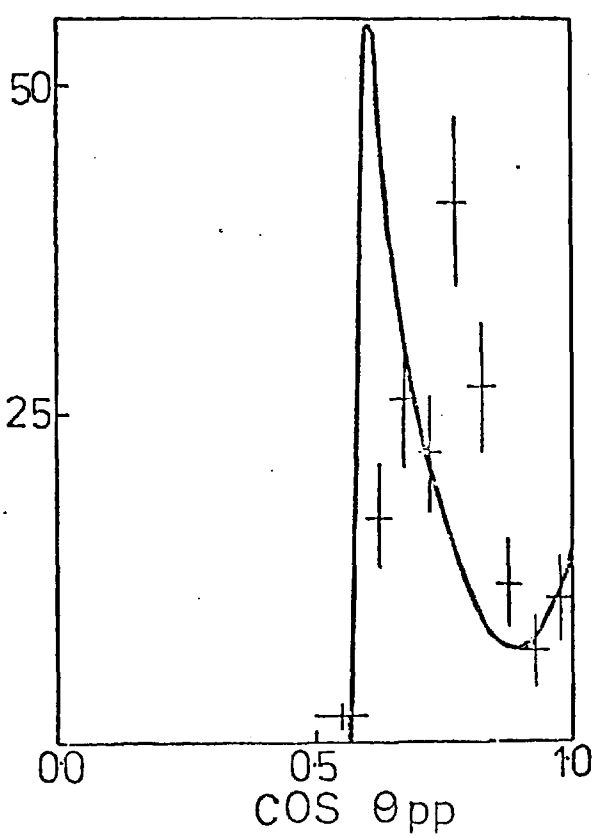

θpp = angle of the pp system wrt. beam direction in laboratory frame.

2.13

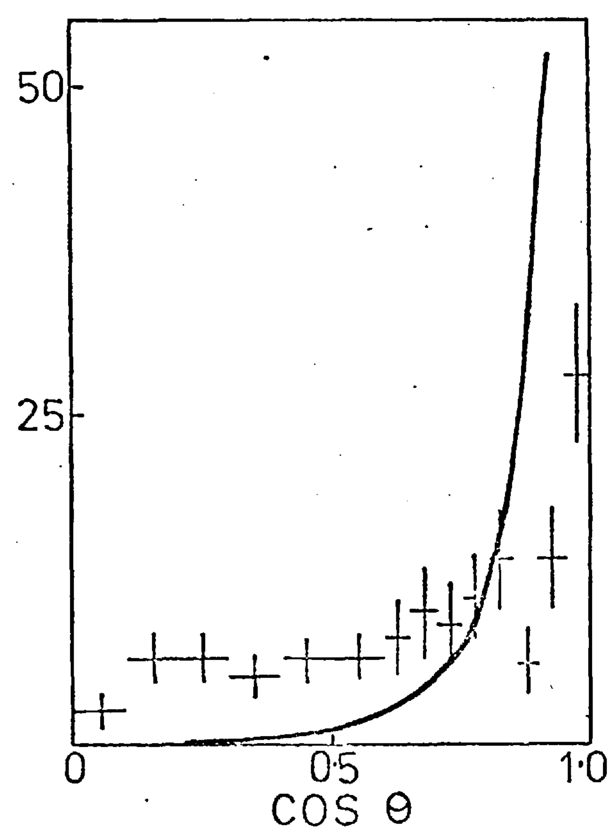

θ = angle of the proton in pp rest frame.

2.14

CHAPTER 3

In this chapter a study of the reaction

$$K^+n \rightarrow K^\circ p \qquad 3.1$$

is presented. The reaction is observed in a deuterium target experiment as

$$K^+d \rightarrow K^\circ pp \qquad 3.2$$

where one of the protons in the final state is a spectator in the interaction of the K^+ meson with the neutron of the deuteron. Only one or two prong events with a visible V_o can give rise to such fits.

3.1 AMBIGUITIES AND SELECTION OF EVENTS

The reaction 3.2 gives a highly constrained kinematic fit, the total number of constraints being 7. The number of constraints however goes down to 6 or 4 when one of the tracks is badly measured, or when the decay vertex cannot be simultaneously fitted to a K^O. The high constraints restrict the contamination with this channel to a minimum. The possible contaminations are

$$K^+n(p) \rightarrow K^\circ\pi^\circ p\,(p) \qquad 3.3$$

$$K^+d \rightarrow K^\circ\pi^+d \qquad 3.4$$

$$K^+d \rightarrow K^\circ\pi^\circ\pi^+d \qquad 3.5$$

$$K^+n(p) \rightarrow K^\circ\pi^\circ\pi^\circ p(p) \qquad 3.6$$

$$K^+n\,(p) \rightarrow K^\circ\eta^\circ\, p\,(p) \qquad 3.7$$

$$K^+n\,(p) \rightarrow K^\circ\eta^\circ\pi^\circ p\,(p) \qquad 3.8$$

$$K^+n\,(p) \rightarrow K^\circ K^+\Lambda^\circ\,(p) \qquad 3.9$$

The reactions 3.6 to 3.8 can be fitted to these two prong events(with a V_o) only when the missing momentum and missing mass are large, since the probability of emitting two slow π^O's is very small. So by suitably choosing restrictions on the missing mass and missing momentum it was possible to eliminate any contamination from those channels. The contamination of the reactions 3.4 and 3.5 is also negligible. This is due to the fact that the pion and proton tracks could be distinguished by bubble density measurements for tracks with momenta less than 1.5 GeV/c. The reaction 3.9 is highly improbable because it involves the production of a pair of strange particles. The cross-section for the corresponding process at this energy has been found to be of the order of 30 μb. So at the present level of statistics, one can safely ignore this process. Furthermore the K^+ and p tracks are distinguishable by bubble density measurement for tracks with momenta below 1.3 GeV/c. Of all the events fitted to the reaction 3.2 only .3% are ambiguous with the hypothesis 3.3. This percentage is fairly uniform over the different beam momenta and this ambiguity only occurs in the case of badly measured events. However, this figure does not give a true picture of the level of contamination at the kinematic fitting stage because during grind choicing it was decided that a 4c fit should always be preferred to a 1c fit except when the confidence level of the later is at least 10 times greater than that of the former, assuming both are consistent with ionisation. The probability distribution (figure 3.3), however, shows no enhancement at low probability, thus justifying the preference of the 4c fits at the Grind choicing stage. The probability distribution shows some excess of events on the higher probability side.

One important feature of the reaction 3.2 is an unusual long tail on the higher momentum side in the laboratory momentum distribution of the slow proton. This has been discussed in some detail in Chapter 2 where this excess of events with large spectator momentum has been attributed to double scattering. As a further check, here the cross-section has been calculated in two ways. The first method consists of rejecting events with "Spectator protons" above 300 MeV/c and then correcting for the loss of events in the forward direction (as described in section 3.3); the second method utilises the t-channel neutron exchange diagram and a Chew-Low extrapolation procedure to the neutron pole (as described in section 3.2). The two methods give compatible results (Table 3.2). So in revealing the other features of the process, a cut is used at the spectator momentum value of 300 MeV/c.

3.2 CHEW-LOW EXTRAPOLATION

The reaction $K^+d \rightarrow K^o pp$ could be explained in terms of t-channel diagrams like fugure 3.4

The contribution of this diagram to the process (2) can be written as

$$\sigma_\tau = \frac{2\pi}{P_{KL} m_d} \int_\tau 4\pi\Gamma^2 \frac{1}{(\Delta^2 - m_n^2)^2} |\langle p_F i | j_n | p_K \rangle|^2 4 m_d m_p (p_s^2 - m_p^2) \frac{d^4 p_s}{(2\pi)^3} \qquad 3.10$$

where P_{KL} = laboratory momentum of the incident K^+ meson.

m_d, m_n, m_p = masses of the deuteron, the neutron and proton respectively.

p_s = four momentum of the spectator proton

Δ^2 = effective mass squared of the t-channel exchanged virtual neutron.

$4\pi\Gamma^2$ = spin average density matrix element squared at the dnp vertex.

$|p_F i\rangle, |p_K\rangle$ = the final and the initial states at the top vertex.

j_n = neutron current.

If one assumes that the residue at the pole is related to the physical process with a neutron on the mass-shell, the two vertex functions can be further simplified at the pole and expressed in terms of some observables

Then

$$4\pi\Gamma^2 = 4\pi \frac{4}{m_p}\left[\frac{\alpha}{1-\alpha r_6}\right] \qquad 3.11$$

$$|\langle p_F i | j_n | p_K \rangle|^2 = \frac{\sigma_{CEX}}{2} \left(\frac{s^2}{4} - \frac{s}{2}(m_K^2 + \Delta^2) + \frac{1}{4}(m_K^2 - \Delta^2)^2\right)^{1/2} \qquad 3.12$$

where s = effective mass squared of the system $K^o p$.

σ_{CEX} = reaction cross-section for the process $K^+n \rightarrow K^0p$.

$1/\alpha$ = deuteron radius.

r_o = effective range for 3S dnp coupling.

Thus

$$\sigma_{CEX} = \frac{1-\alpha r_0}{\alpha} \quad \pi m_d P_{KL} \frac{(\Delta^2 - m_n^2)^2}{[s^2 - 2s(m_K^2+\Delta^2) + (m_K^2-\Delta^2)^2]^{1/2}} \frac{d^2\sigma_t}{ds\,d\Delta^2} \qquad 3.13$$

Near the neutron pole, the process 3.2 is dominantly given by a diagram like 3.4; so σ_t could be replaced by the cross-section for the reaction 3.2 in a limited Δ^2 region. One further assumes that the deuteron is dominantly S-wave so that α = .0456 GeV and r_o = 1.74 fm. The quantity

$$\frac{1-\alpha r_0}{\alpha} \frac{m_d P_L (\Delta^2 - m_n^2)^2}{\int_{s_{low}}^{s_{high}} [s^2 - 2s(m_K^2+\Delta^2) - (m_K^2-\Delta^2)^2]^{1/2} ds} \frac{dN}{d\Delta^2} \qquad 3.14$$

has been plotted against Δ^2, the integral being computed between the two limits of the Chew-Low plot and a straight line extrapolation is made to the neutron mass (figure 3.1). Due to the large statistical error, no other possible extrapolation was attempted. However, when this method of extracting neutron cross-section was tried for other channels, this did not lead to cross-section measurements compatible with those from the direct evaluation.

3.3 CROSS-SECTION

The channel cross-section for the process 3.2 is summarised in table 3.1. The fifth column of this table gives a measurement of cross-section for the process 3.1 based on the two following assumptions, (a) only events with spectator momentum less than 300 MeV/c are due to the process 3.1 and (b) the loss of events in the forward direction can be taken into account by using the formula with the spin flip component of $d\sigma/dt$ for the process 3.1 to be zero in the very forward direction.

The total cross-section for 3.1 has been plotted against the laboratory momentum on diagram 3.2 together with the measurements at other experiments at 1.94 GeV/c (Davies et al., 1972), 2.3 GeV/c (Butterworth et al., 1965a), 2.97 GeV/c (Goldschmidt Clermont et al., 1968), 3.8 GeV/c (Moninger et al., 1973), 3 GeV/c, 4 GeV/c, 6 GeV/c (Diebold et al., 1974), 4.6 GeV/c (Dehm et al., 1973), 5.5 GeV/c (D. Cline et al., 1970) and 12 GeV/c (Firestone et al., 1970). The cross-section follows a Ap^n behaviour with $A = 7.55 \pm 0.50$ mb and $n = -2.10 \pm 0.05$. On the same graph, also the cross-section for the line reversed reaction $K^-p \rightarrow \overline{K}^On$ has been plotted ($n = -1.74 \pm 0.10$). The cross-sections for the two processes should have been equal if they proceed through exchange degenerate Regge pole exchanges. At about 20 GeV/c, the K^+ cross-section is approximately twice the K^- cross-section. However the two cross-sections converge on one another at higher momenta. So either the absorbtion effects are important below $\sim$ 4 GeV/c which die away rapidly at higher momenta or else the exchange degeneracy is not obeyed.

The total cross-section does not show any structure which might have been expected from a narrow Z^* resonance (width$\sim$100MeV) coupled strongly to the elastic channel. To investigate this effect in some greater detail, the centre of mass energy distribution for the process 3.1 has been compared with an estimated distribution based on the assumptions that the total cross-section is constant over the E^* range and the deuteron can be approximated by a S -wave n,p state. In the reaction 3.1, E^* has been defined as the invariant mass of the final state K^Op system. This gives the cross-section as a function of E^* (in diagram 3.5) within an E^* region 2.2 GeV $< E^* <$ 2.6 GeV. This is again consistent with no Z^* production.

The cross-section measurement for the process 3.1 has also been compared with the SU(3) sum rule due to Barger and Cline (1967). The occurence of only 1 and 8 representations of SU(3) for the observed mesons suggests that exchanges of singlet and octetstates should dominate the scattering amplitude. This SU(3) sum rule assumes the octet dominance in the crossed meson channel with an approximate SU(3) invariance for the individual exchange amplitudes. Assuming that the (π,K,η) pseudoscalar mesons form an octet representation of SU(3), the meson nucleon charge exchange amplitudes of definite helicity were expressed in terms of two amplitudes which represent the contributions of $I^G = 1^-$ and $I^G = 1^+$ meson exchanges. This leads to the relation

$$\frac{d\sigma}{dt}(K^+n \to K^0p) = \frac{d\sigma}{dt}(\pi^-p \to \pi^0n) + 3\frac{d\sigma}{dt}(\pi^-p \to \eta^0n) - \frac{d\sigma}{dt}(K^-p \to \bar{K}^0n) \qquad 3.15$$

at any fixed s-value. A corresponding relation for the total cross-section should also be true. It is quite evident from figure 3.7 that this rule is inconsistent with the data at momenta less than $\sim$4 GeV/c. This could not be accounted for by standard Regge pole models and is presumably the reason for the nonapplication of such models at lower energies. However, the sum rule has a better agreement when the relation is tested at a fixed Q value (figure 3.16). Comparisons of the differential cross-sections at a fixed s (figure 3.8) and at a fixed Q (figure 3.17) show that the πN data points are lower than the KN data points at all t-values.

3.4 DIFFERENTIAL CROSS-SECTION

The production angular distribution is shown in figure 3.9 at the three laboratory momenta. All the three distributions are peaked in the forward direction suggesting the t-channel singularity dominance in the total amplitude. The solid lines are fits with a sum of Legendre polynomials

$$\frac{d\sigma}{d\cos\theta} = \sum A_n P_n(\cos\theta) \qquad 3.16$$

The coefficients A_n's has been evaluated by the method of moments and are summarised in table 3.3. Only coefficients up to n=8 have significantly nonzero values. All the events were divided in 9 s-bins and the coefficients evaluated have been plotted in figure 3.10. At some coefficient (A_4,A_5) there seems to be some structure near $E^* = 2.4$ GeV (corresponding to the opening of $K^*(1420)$ channel). But due to large errors in the data, no further attempts could be made to analyse the s-channel effect in this channel.

The $d\sigma/dt$ distributions for the process 3.1 have all been fitted to expressions of the form $d\sigma/dt = A\, e^{Bt}$ in the region 1.5 GeV$^2 > |t| >$ .1 GeV^2 and the values of the parameter B are plotted in fugure 3.11 against the laboratory beam momentum together with similar quantities from other experiments. They are consistent throughout and a shrinkage of the forward peak is clearly evident.

The optical theorem and isospin decomposition relate the forward charge exchange amplitude to the K^+p and K^+n total cross-sections.

$$\mathrm{Im}\, A_{CE}\Big|_{t=0} = \frac{q}{4\pi}\left(\sigma^T_{K^+p} - \sigma^T_{K^+n}\right) \qquad 3.17$$

Abrams et al. (1970) made an accurate measurement of the K^+p and K^+n total cross-section. Using their data the ratio of the imaginary to the real part of the forward scattering amplitude was computed. This ratio (as in Figure 3.6) has been found to be negative and decreasing with the laboratory momentum. A strong exchange degenerate model predicts a purely real amplitude for the process 3.1. So the data suggest that absorbtion effects are present at 2-3 GeV/c.

There is no evidence for a backward peak in the differential cross-section as might have been expected due to hyperon exchange processes in the crossed u-channel. The differential cross-section in the backward direction has been plotted in figure 3.12 together with the data from 1.94 GeV/c experiment. It is found to fall rapidly with increasing momentum.

3.5 COMPARISON WITH THEORETICAL PREDICTION AND CONCLUSION

In explaining the forward peaks in the differential cross-section one generally assumes the amplitude to be dominated by the singularity nearest to the physical region. This leads to one particle exchange models at medium and high energies. However, the one particle exchange models have unsatisfactory energy dependence in the amplitude if they involve the exchange of particles with nonzero spin. This unphysical energy dependence has been tried to be got rid of by adding the contributions of various spin states to the amplitude. If the exchanged particles are infinite in number, the sum can satisfy Froissart bound under restricted conditions. This idea has been developed in Regge pole models which consider the sum of a series of spin states J_o, J_o+2, J_o+4, ... as a singularity in the complex J-plane whose position is a function of t. The contribution of a Regge pole to the t-channel helicity amplitude can be written as

$$A_{H_t}(s,t) = -16\pi(2\alpha(t)+1)\beta_H(t)\frac{(1+\tau\exp(i\pi(\alpha(t)-\nu)))}{2\sin(\pi(\alpha(t)-\nu))}\; d^{\alpha}_{-\lambda\lambda'}(-z_t) \qquad 3.18$$

where $\alpha(t)$ gives the position of the pole, τ its signature (and is +1 or -1), $\beta_H(t)$ the residue at the pole. λ, λ' are the helicity flips at the two vertices, Z_t the t-channel scattering angle and ν is a factor depending on the t-channel exchange particles.

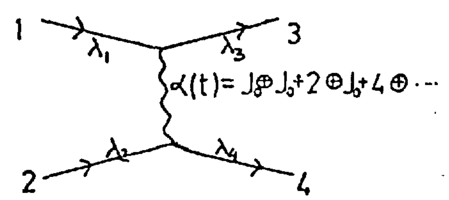

$\lambda = \lambda_1 - \lambda_3$
$\lambda' = \lambda_2 - \lambda_4$

In its simplest manifestation $\alpha(t)$ has been parametrised as a linear function of t. The nature of the residue function is quite unknown and the different models assume different characteristics for this function. One plausible assumption is the so called factorisation, i.e.

$$\beta_H(t) = \gamma_{13}\gamma_{24} \qquad 3.19$$

$\beta_H(t)$ inherits the t-singularities of $A_H(s,t)$. So the t-channel threshold effect would be reflected in $\beta_H(t)$. But the s-channel physical region is far away from the t-channel threshold; so this effect should not be important in the s-channel amplitude. However, the singularities at t=0 in the d^J function is quite important and can be got rid of by making β_H vanish sufficiently fast at t=0. The d^J function gives rise to a branch point $(\alpha - J_0)^{1/2}$ at sense-nonsense points. A vertex is called a sense point if $J_0 > |\lambda|$ and a nonsense point if $J_0 < |\lambda'|$. To kill this singularity one demands

$$\beta_{ss}\beta_{nn} = \beta_{sn}^2 \sim (\alpha - J_0) \qquad 3.20$$

To satisfy this one may choose sense, i.e. $\beta_{nn} \sim (\alpha - J_0)$ and β_{ss} finite, or choose nonsense, i.e. $\beta_{ss} \sim (\alpha - J_0)$ and β_{nn} finite. In the later case one introduces a pole in the nn amplitude and this is usually taken care of by having extra zeroes in the residues.

The contrasting behaviour of the particle and antiparticle processes, introduces a new idea in the Regge pole models. The Regge trajectories of opposite signatures and parity appear in pairsand the residue functions corresponding to these trajectories are very much similar. This is called the exchange degeneracy.

The process 3.1 because of its simple spin structure has been subjected to analysis in several Regge pole models. Though the differential cross-section is quite structureless the models still find it difficult to give a good quantitative agreement with the experimental results. Simple Regge pole ideas have been modified by introducing complexities like absorbtion, Regge cuts, etc. Still there is not one good systematic which can explain the s,t dependence of the elastic scattering of the SU(3) 0^- meson octet and the nucleon octet.

One of the early attempts of these types is one due to Rarita and Schwarzschild (1967). This particular model is meant for only elastic charge exchange scatterings. They assumed the exchange of the ρ, ρ' and A_2 trajectories in the t-channel. The introduction of the nucleon spin demands the vanishing of spin flip residue functions and the ghost killing for the even signature trajectories at α=0. The ghost arises due to the pole at α=0 which corresponds to a negative mass squared. In that particular model these are accomplished by assuming that the nonsense vertices each provide a factor $\sqrt{\alpha}$ for all trajectories and that in the case of A_2 exchange, every vertex provides an additional factor $\sqrt{\alpha}$. The model demands linear but nonexchange degenerate trajectories. As a result it involved 24 parameters (including the SU(3) breaking factors). One particular feature of the model is that it used the Legendre function expansion at smaller energies. It explains our data reasonably well (Figure 3.13) up to t = -1. GeV^2 beyond which the model blows up. However this model needed to introduce a new ρ' trajectory, which seems to be only a means of introducing the extra parameters needed to fit the data. The ρ' parameters vary considerably according to the data fitted. The facts that (1) ρ' is not well established, and (2) polarization data of $\pi^- p \to \pi^0 n$ is not well explained make the model a weak one.

Dass, Michael and Phillips (1969) later made a systematic study in terms of Regge poles. It involves isoscalar as well as isovector exchanges. Thus it covered a lot other reactions. It involved $\rho, \omega, \omega', A_2, P, P'$ trajectories. It again has not built in exchange degeneracy. At α = 0, ρ chooses sense and A_2 chooses nonsense. The residue of t-channel helicity nonflip amplitude was chosen to describe $\pi^- p \to \pi^0 n$ data. The A_2 ghost killing mechanism was however doubtful but that was not important since the model resulted in a flat A_2 trajectory. The fit of our data is quite poor. The theoretical prediction of the cross-section is down by a factor of 2 from the experimental findings (Figure 3.14). However this does not involve the Legendre function expansion.

One useful tool in more recent models is the so called local duality. The s-channel background and resonance effects are results of the t-channel Pomeron and Regge trajectory exchanges. All the recent models make use of this fact and also the exchange degeneracy of odd and even signature trajectories. Also amplitude analysis suggests (Ringland et al. 1971) that the helicity flip amplitudes have the simple Regge pole form with absorption (cuts) playing a minor role whereas the helicity nonflip amplitudes do not have a simple Regge pole form but are significantly affected by absorption. But there is no clearcut way of calculating the absorption. Loos and Matthews (1972) used Harari's (1971) dual absorption model and applied it to all 2 body processes. In this model, the imaginary part of the Regge exchange s-channel helicity nonflip amplitude is assumed to have an approximate 'J_o' behaviour with an absorption zero at the cross-over zero. The helicity flip amplitudes are made to be nearly Regge like in agreement with the polarization data and the differential cross section data for the processes $\pi^- p \rightarrow \pi^0 n$ and $\pi^- p \rightarrow \eta^0 n$. The real part of the helicity non flip amplitude was empirically parametrized by a polynomial and exponential in t. The model explains the experimental data remarkably well at high energy. In our energy region, the model prediction is down by a factor of 2 in the forward direction (Figure 3.15). But near t = 2.0 GeV^2, the model gives a curious reproduction of the experimental structure. This is remarkable since these structures are absent at higher energies.

Hartley and Kane (1973) took into account the s-channel unitarity effects by treating the reactions at high energies to be largely absorptive in nature. The Born term was defined by a reggeon exchange whose intrinsic quantum numbers and symmetry properties characterise the exchange but whose s,t dependence and size are strongly modified by unitarity effects. The Pomeron structure as determined from the consideration of s-channel unitarity effect has got two parts. One is due to the complicated structureless intermediate states, namely the pionisation and the other due to the peripheral terms in the unitarity sum. The absorption effect decreases with energy consequently one should have at high energies the $K^+n \to K^0p$ cross-section larger than $K^-p \to \bar{K}^0 n$ cross-section. This has not been verified since at high energies, no measurement of $K^+n \to K^0 p$ cross-section has yet been done. However the model does not work well at lower energies.

Girardi et al. (1974) put forward a model which incorporates Regge cuts in duality diagrams. A study of the physical amplitudes shows that one should have to add to the exchange degenerate Regge poles corrected by absorption, a contribution which violates exchange degeneracy, exists in exotic s and u channel and contributes to negative signature with central real parts. This contribution comes from a dual description of Regge cuts. The intermediate exotic states in the cut diagrams were avoided. However, this model does not have a good qualitative agreement with data of this experiment.

Though many versions of basically Regge type theory explain most of the higher energy data (though perhaps not all simultaneously), all run into trouble at lower energies. What is needed is a means of extrapolating these basically correct theories to the lower energies where the effects of absorbtion and mass differences become more important.

TABLE 3.1

Beam Momentum GeV/c	No. of events per μb	Deuteron cross-section without any cut in spectator momentum. mb	Deuteron cross-section with a cut in spectator momentum at 300 MeV/c. mb	Neutron cross-section. mb
2.18	$1.86 \pm .05$	$1.63 \pm .11$	$1.38 \pm .10$	$1.49 \pm .11$
2.43	$1.78 \pm .05$	$1.31 \pm .10$	$1.12 \pm .09$	$1.21 \pm .09$
2.70	$1.94 \pm .05$	$1.03 \pm .09$	$0.87 \pm .09$	$0.95 \pm .09$

TABLE 3.2

Beam Momentum GeV/c	Δ^2_{cut} GeV^2	x^2/ND	Prob.	Extrapolated No	σ_{ext}	Neutron Cross-section (from table 3.1) mb
2.18	0.86	1.26	0.26	2960.1 ± 89.3	$1.59 \pm .06$	$1.49 \pm .11$
2.43	0.86	1.10	0.36	2385.2 ± 221.3	$1.34 \pm .13$	$1.21 \pm .09$
2.70	0.86	0.98	0.44	1637.3 ± 119.7	$0.85 \pm .07$	$0.95 \pm .09$

TABLE 3.3

An/Ao/P Beam GeV/c	2.18	2.43	2.70
A1/Ao	$1.86 \pm .04$	$2.05 \pm .05$	$2.24 \pm .04$
A2/Ao	$1.79 \pm .07$	$2.16 \pm .07$	$2.35 \pm .08$
A3/Ao	$0.81 \pm .09$	$1.22 \pm .11$	$1.64 \pm .12$
A4/Ao	$-0.34 \pm .11$	$0.09 \pm .13$	$0.59 \pm .14$
A5/Ao	$-0.90 \pm .12$	$-0.71 \pm .14$	$-0.32 \pm .16$
A6/Ao	$-1.01 \pm .13$	$-1.11 \pm .15$	$-0.95 \pm .17$
A7/Ao	$-0.66 \pm .14$	$-0.92 \pm .16$	$-1.02 \pm .19$
A8/Ao	$-0.52 \pm .16$	$-0.63 \pm .18$	$-1.01 \pm .20$

TABLE 3.4

t GeV^2	2.2 GeV/c (dσ/dt) mb/GeV^2	2.2 GeV/c (dσ/dt) (corrected) mb/GeV^2	2.45 GeV/c (dσ/dt) mb/GeV^2	2.45 GeV/c (dσ/dt) (corrected) mb/GeV^2	2.7 GeV/c (dσ/dt) mb/GeV^2	2.7 GeV/c (dσ/dt) (corrected) mb/GeV^2
$-.025\pm.025$	$1.21\pm.19$	2.01	$1.05\pm.19$	1.79	$0.96\pm.17$	1.55
$-.075\pm.025$	$1.93\pm.25$	2.36	$1.76\pm.24$	2.13	$1.57\pm.22$	1.92
$-.125\pm.025$	$2.36\pm.27$	2.65	$2.29\pm.27$	2.59	$1.38\pm.20$	1.55
$-.175\pm.025$	$2.09\pm.26$	2.26	$1.65\pm.23$	1.79	$1.62\pm.22$	1.75
$-.225\pm.025$	$2.53\pm.28$	2.69	$1.59\pm.23$	1.68	$1.60\pm.22$	1.70
$-.275\pm.025$	$2.15\pm.26$	2.25	$1.40\pm.21$	1.47	$1.36\pm.20$	1.42
$-.325\pm.025$	$1.62\pm.23$	1.68	$1.93\pm.25$	2.00	$1.23\pm.19$	1.28
$-.375\pm.025$	$1.35\pm.21$	1.39	$1.02\pm.18$	1.04	$0.96\pm.17$	0.99
$-.425\pm.025$	$1.27\pm.20$	1.30	$1.37\pm.21$	1.41	$0.78\pm.15$	0.80
$-.475\pm.025$	$1.55\pm.22$	1.58	$1.18\pm.20$	1.20	$0.75\pm.15$	0.76
$-.525\pm.025$	$1.15\pm.19$	1.17	$1.28\pm.20$	1.30	$0.61\pm.14$	0.62
$-.575\pm.025$	$0.78\pm.16$	0.79	$0.72\pm.15$	0.74	$0.61\pm.14$	0.62
$-.625\pm.025$	$0.73\pm.15$	0.74	$0.39\pm.11$	0.39	$0.26\pm.09$	0.26
$-.675\pm.025$	$0.68\pm.15$	0.68	$0.57\pm.14$	0.58	$0.38\pm.11$	0.39
$-.750\pm.050$	$0.48\pm.09$	0.49	$0.20\pm.06$	0.20	$0.25\pm.06$	0.25
$-.850\pm.050$	$0.40\pm.08$	0.40	$0.20\pm.06$	0.20	$0.28\pm.06$	0.28
$-.950\pm.050$	$0.22\pm.06$	0.22	$0.23\pm.06$	0.23	$0.22\pm.06$	0.22
$-1.100\pm.100$	$0.15\pm.03$	0.15	$0.14\pm.03$	0.14	$0.13\pm.03$	0.13
$-1.500\pm.300$	$0.11\pm.02$	0.11	$0.07\pm.01$	0.07	$0.05\pm.01$	0.05
$-2.100\pm.300$	$0.09\pm.02$	0.09	$0.04\pm.01$	0.04	$0.03\pm.01$	0.03
$-2.781\pm.381$	$0.07\pm.01$	0.07	-	-	-	-
$-3.002\pm.602$	-	-	$0.04\pm.01$	0.04	-	-
$-3.248\pm.848$	-	-	-	-	$0.013\pm.003$	0.013

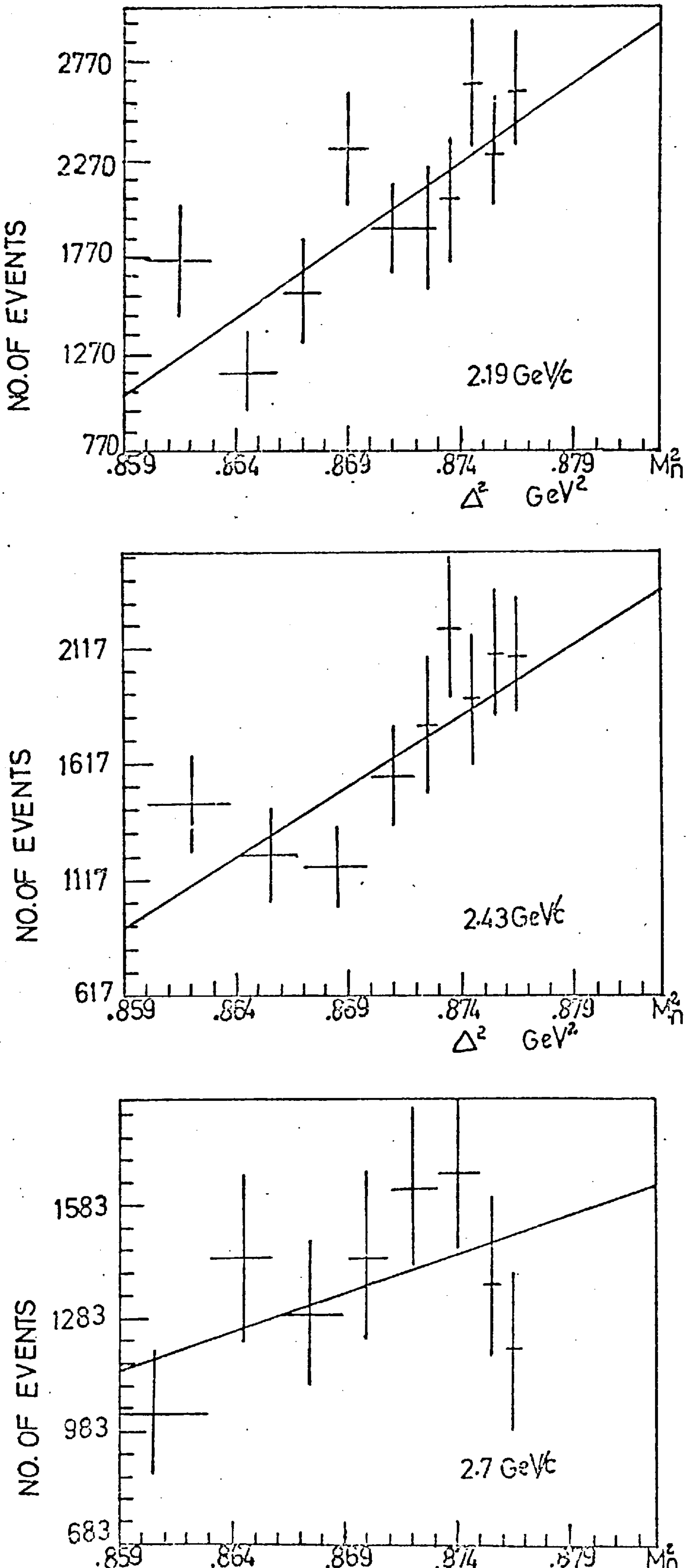
NO.OF EVENTS
2770
2270
1770
1270
770
2.19 GeV/c
.859
.864
.869
.874
.879
M_n^2
Δ^2 GeV^2
NO.OF EVENTS
2117
1617
1117
617
2.43 GeV/c
.859
.864
.869
.874
.879
M_n^2
Δ^2 GeV^2
NO. OF EVENTS
1583
1283
983
683
2.7 GeV/c
.859
.864
.869
.874
.879
M_n^2
Δ^2 GeV^2

3.1

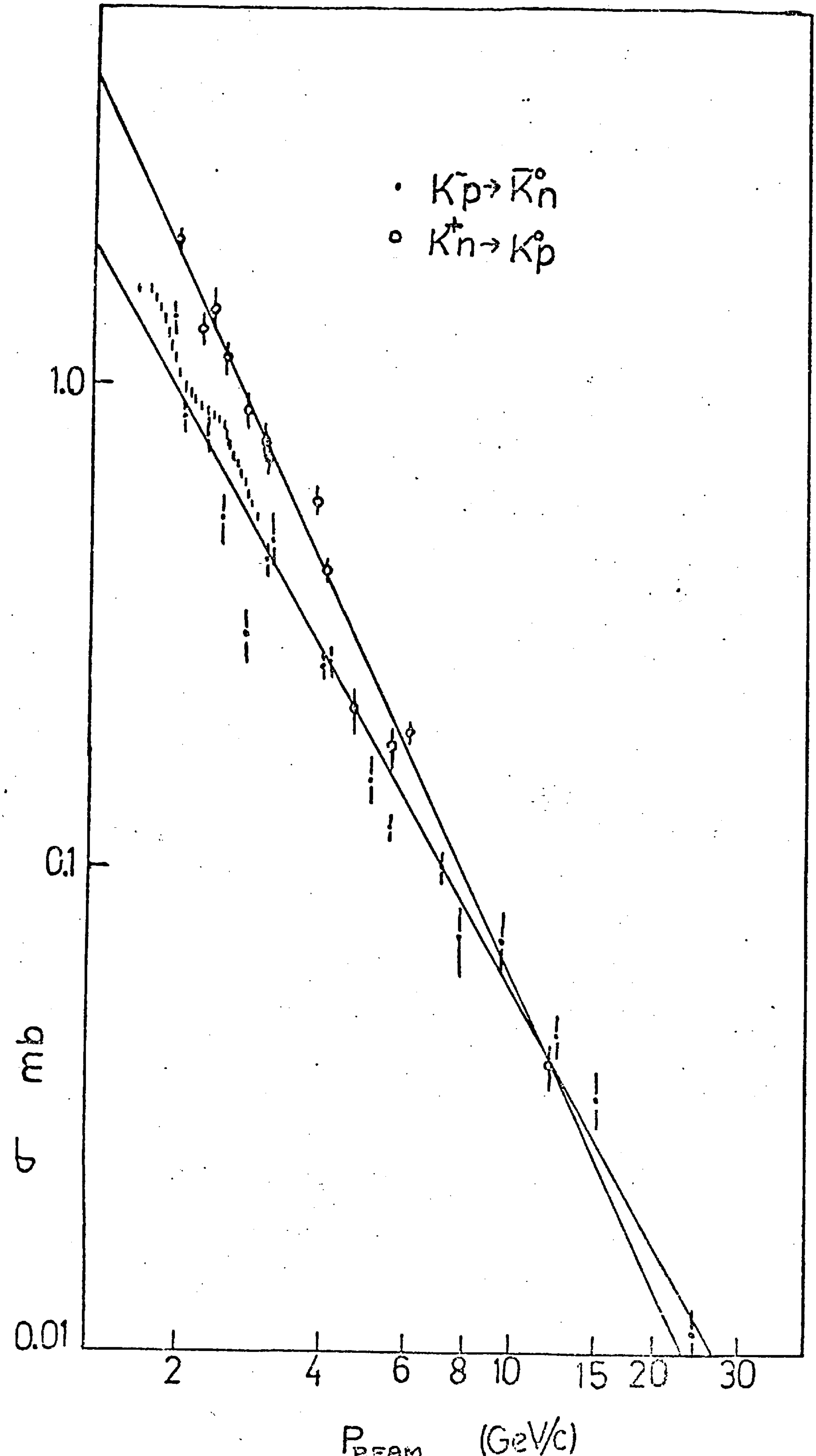

3.2

$K^+ n \rightarrow K^0 p$

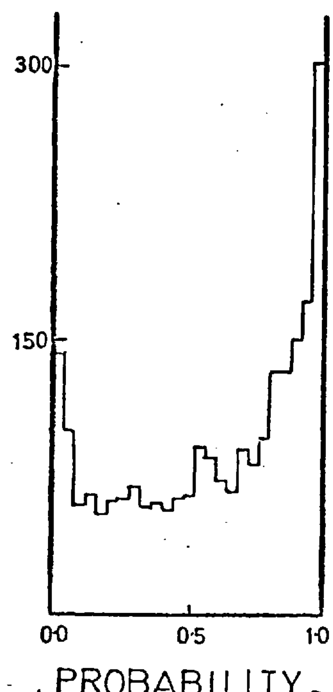

3.3

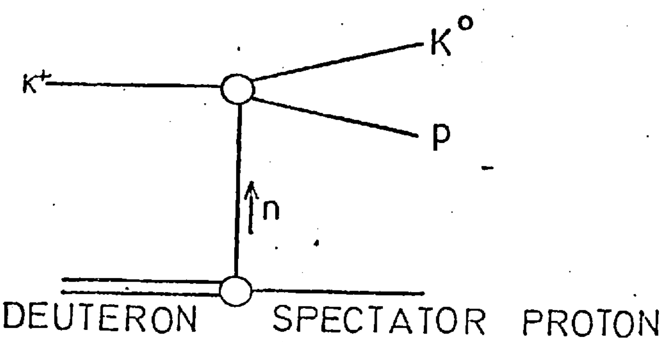

3.4

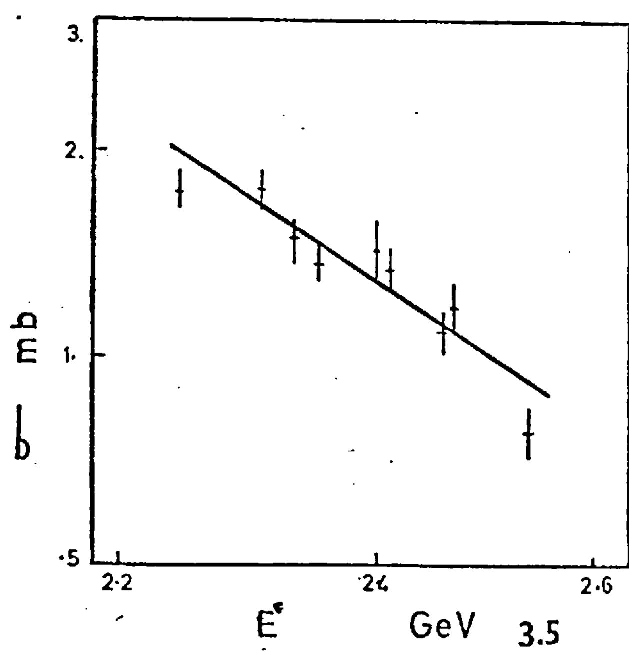

3.5

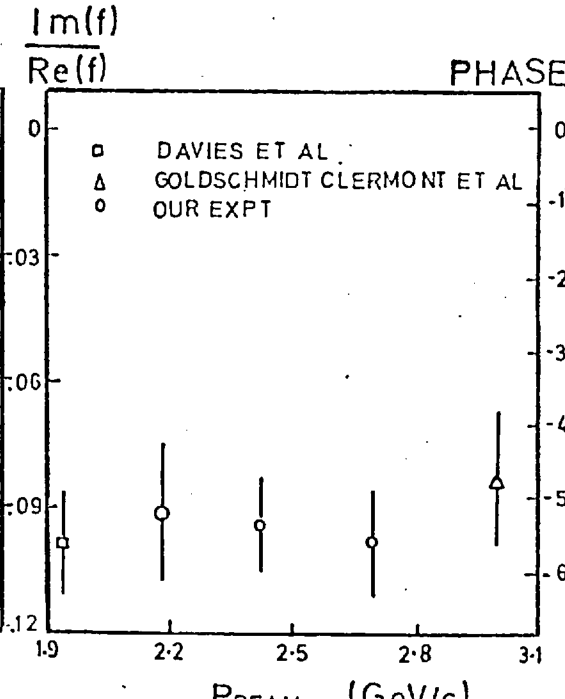

3.6

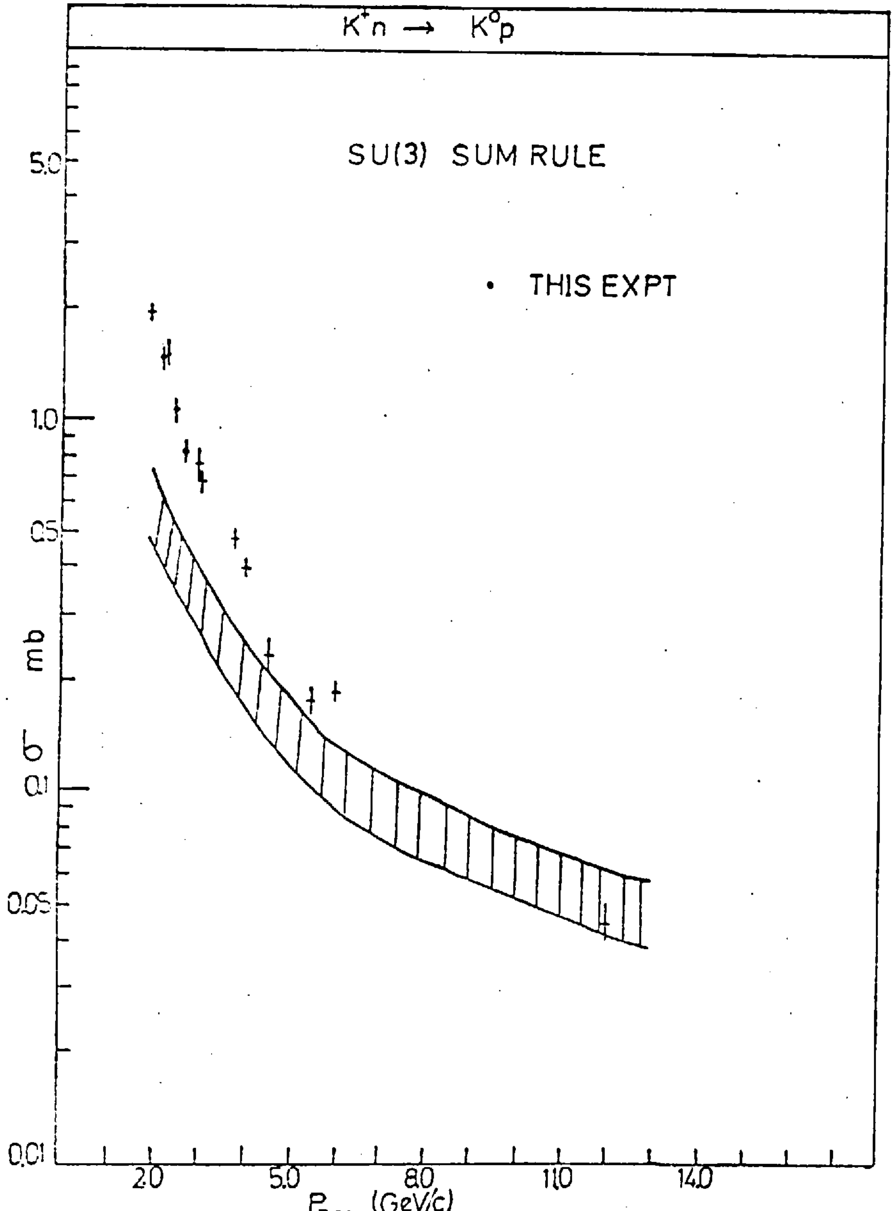

$K^+n \rightarrow K^0p$
SU(3) SUM RULE
• THIS EXPT
5.0
1.0
0.5
0.1
0.05
0.01
σ mb
2.0
5.0
8.0
11.0
14.0
P_{BEAM} (GeV/c)

3.7

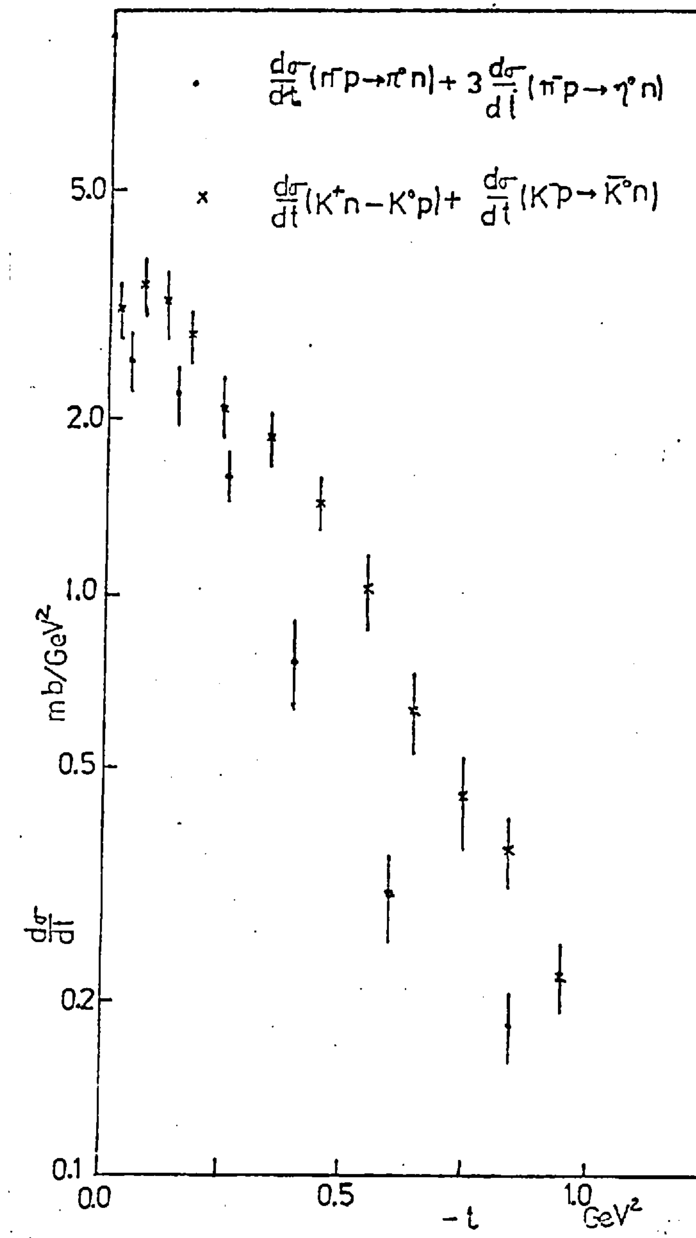

• $\frac{d\sigma}{dt}(\pi^-p\rightarrow\pi^0n)+3\frac{d\sigma}{dt}(\pi^-p\rightarrow\eta^0n)$
× $\frac{d\sigma}{dt}(K^+n-K^0p)+\frac{d\sigma}{dt}(K^-p\rightarrow\bar{K}^0n)$
5.0
2.0
1.0
0.5
0.2
0.1
$\frac{d\sigma}{dt}$ mb/GeV²
0.0
0.5
1.0
−t GeV²

3.8

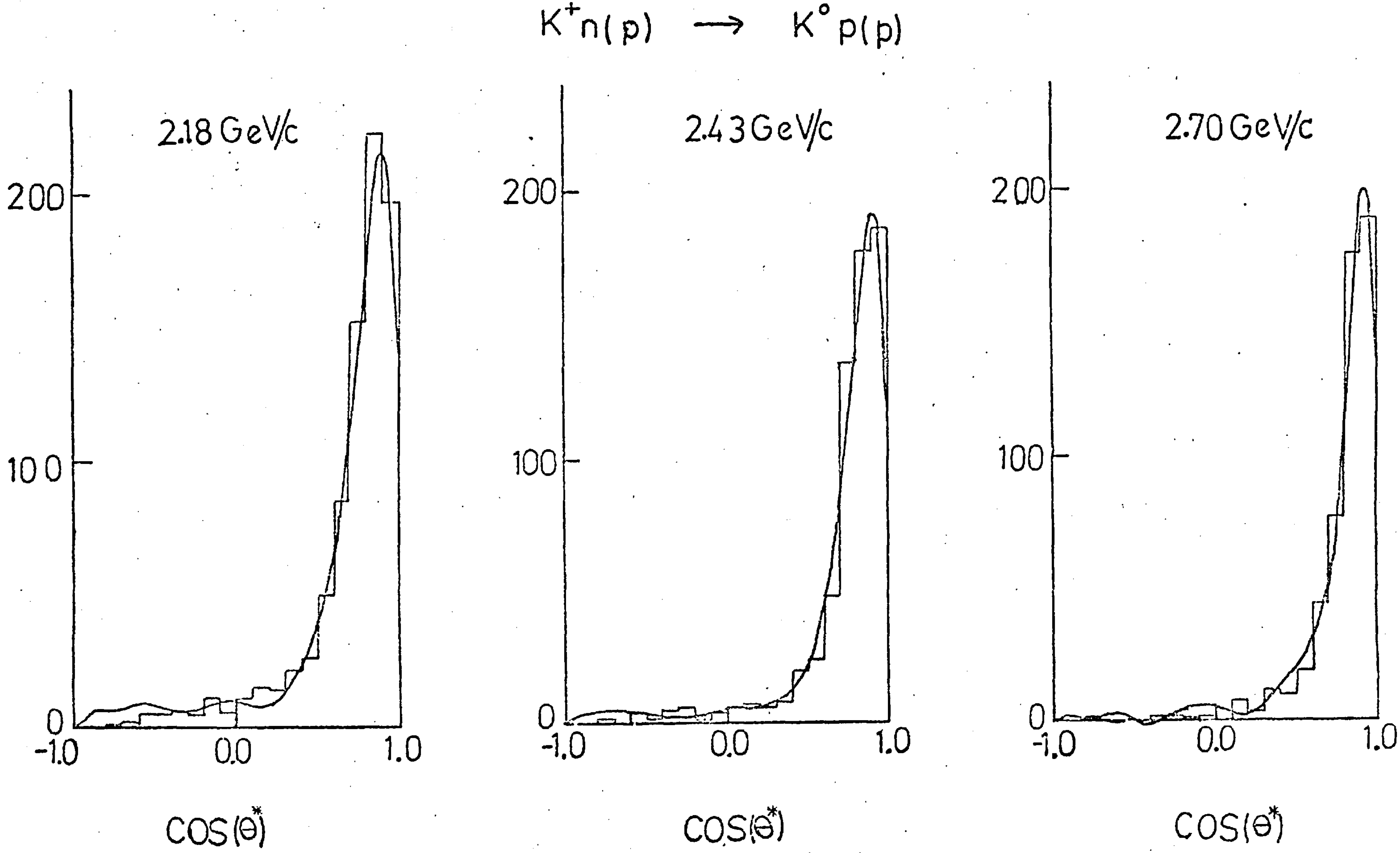
$K^+n(p) \longrightarrow K^\circ p(p)$
2.18 GeV/c
2.43 GeV/c
2.70 GeV/c
200
100
0
-1.0
0.0
1.0
COS(θ^*)
COS(θ^*)
COS(θ^*)

3.9

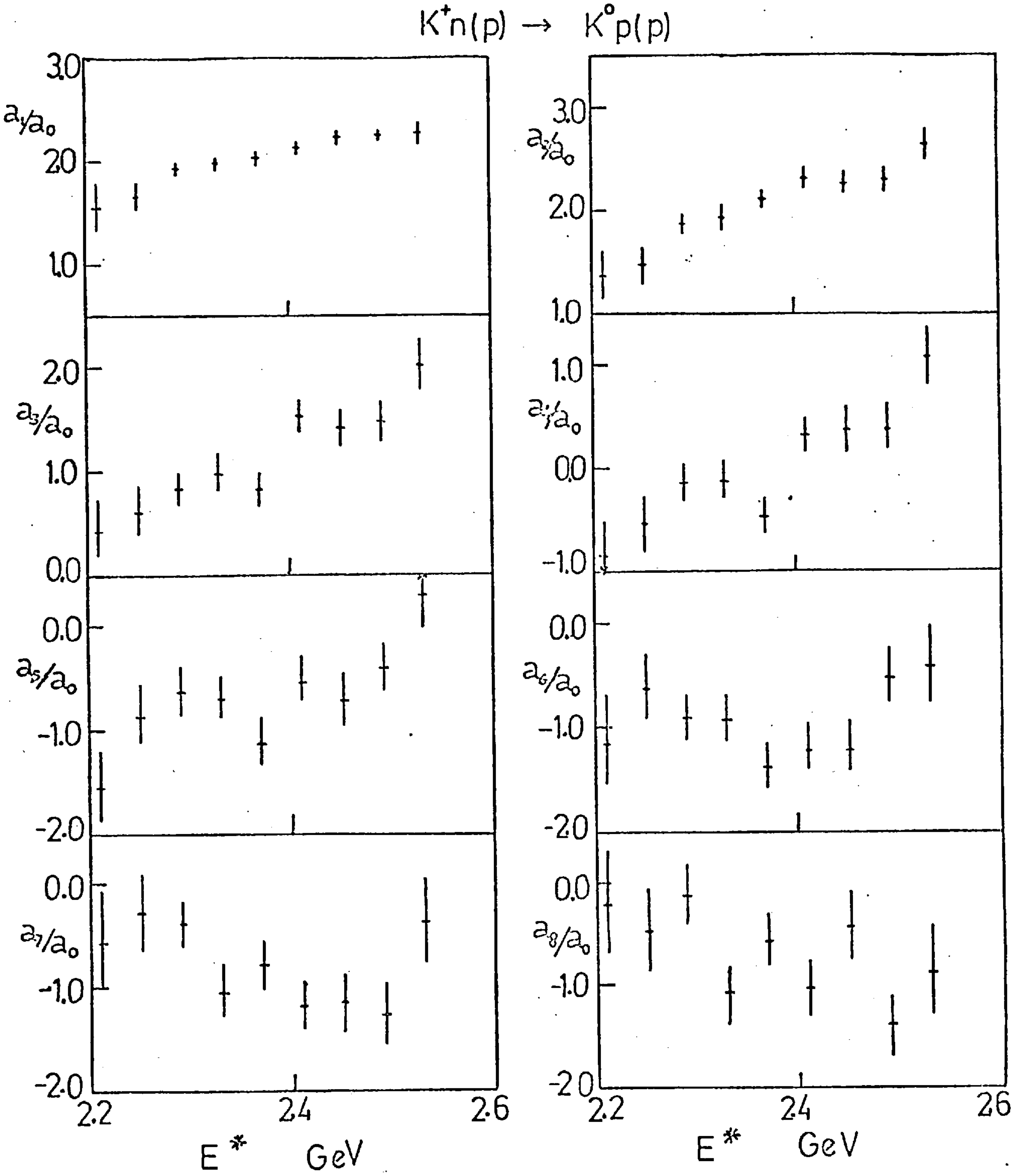

K⁺n(p) → K°p(p)
a_1/a_0
a_2/a_0
a_3/a_0
a_4/a_0
a_5/a_0
a_6/a_0
a_7/a_0
a_8/a_0
3.0
2.0
1.0
0.0
-1.0
-2.0
2.2
2.4
2.6
E* GeV

3.10

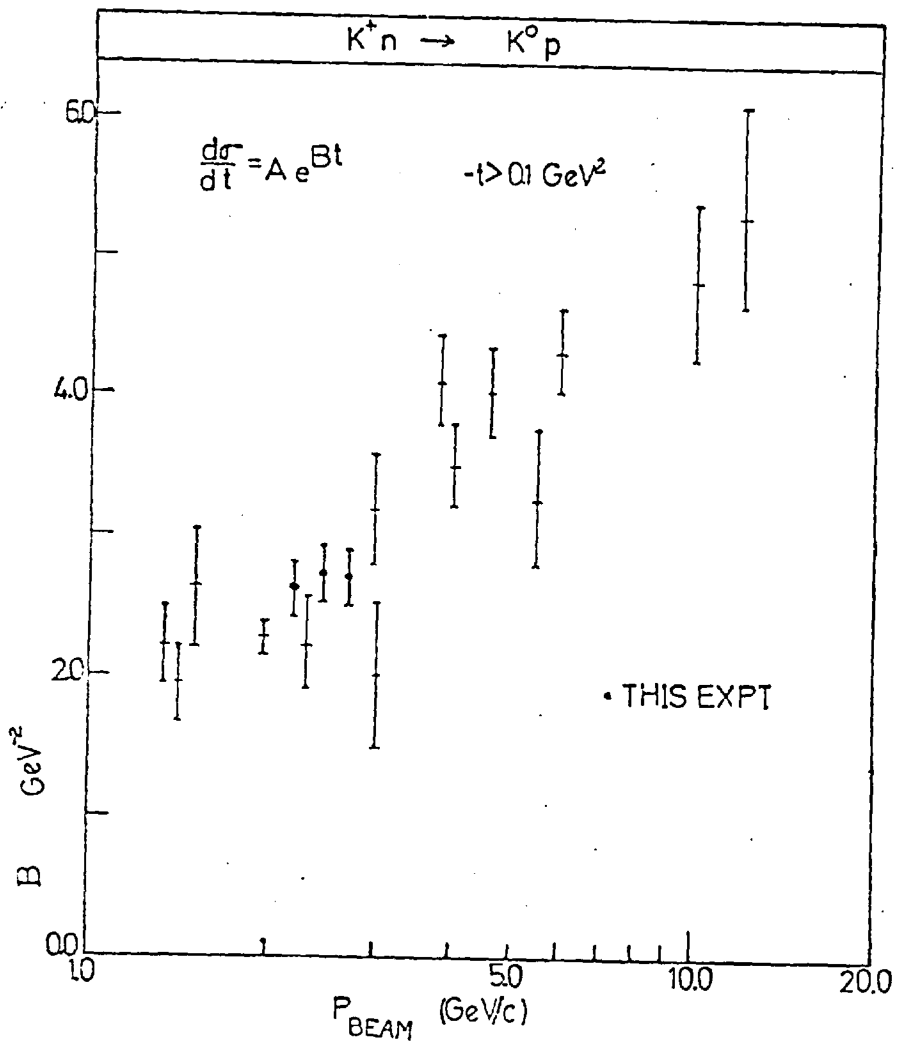

$K^+n \rightarrow K^0p$
$\frac{d\sigma}{dt} = Ae^{Bt}$
$-t > 0.1\ GeV^2$
• THIS EXPT
B GeV^{-2}
6.0
4.0
2.0
0.0
1.0
5.0
10.0
20.0
P_{BEAM} (GeV/c)

3.11

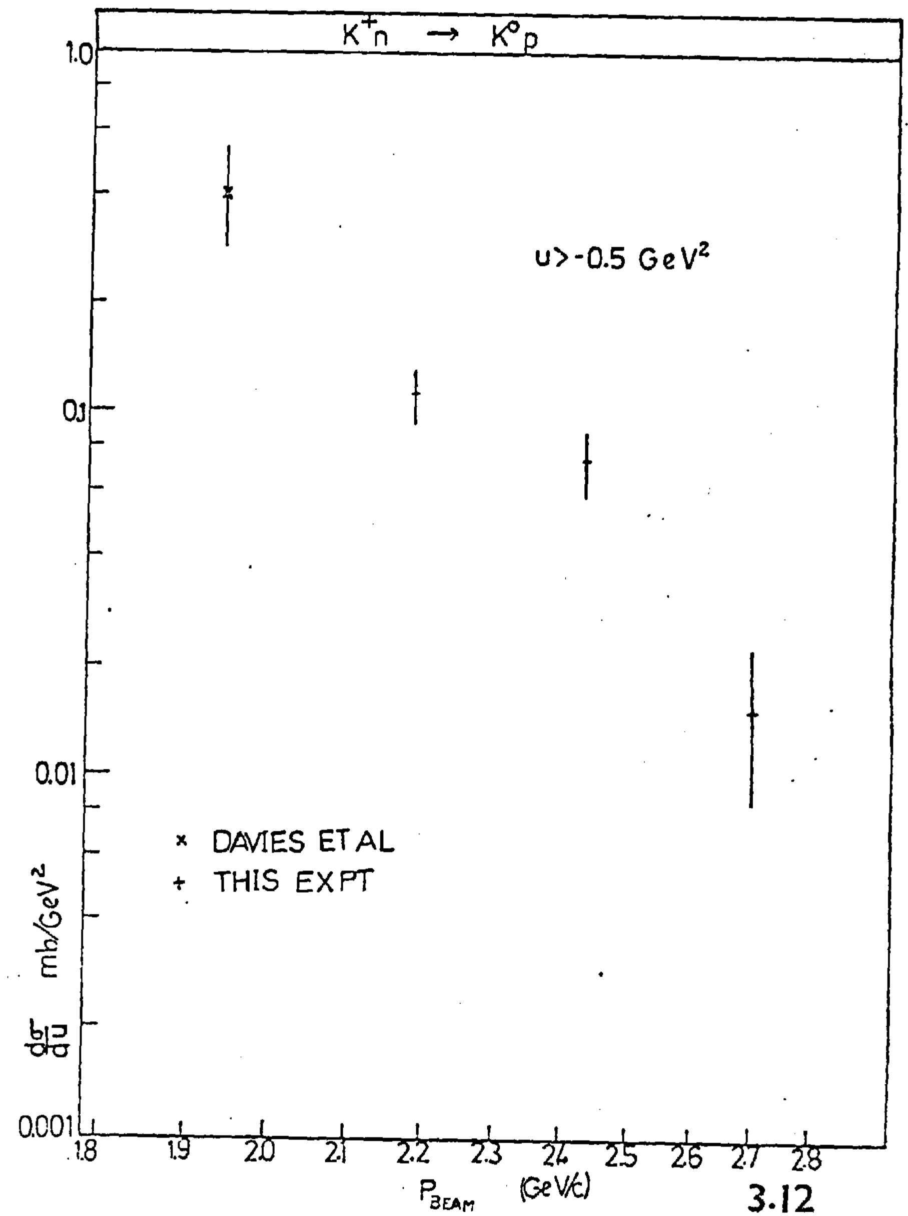

$K^+n \rightarrow K^0p$
$u > -0.5\ GeV^2$
× DAVIES ET AL
+ THIS EXPT
$\frac{d\sigma}{du}$ mb/GeV^2
1.0
0.1
0.01
0.001
1.8
1.9
2.0
2.1
2.2
2.3
2.4
2.5
2.6
2.7
2.8
P_{BEAM} (GeV/c)

3.12

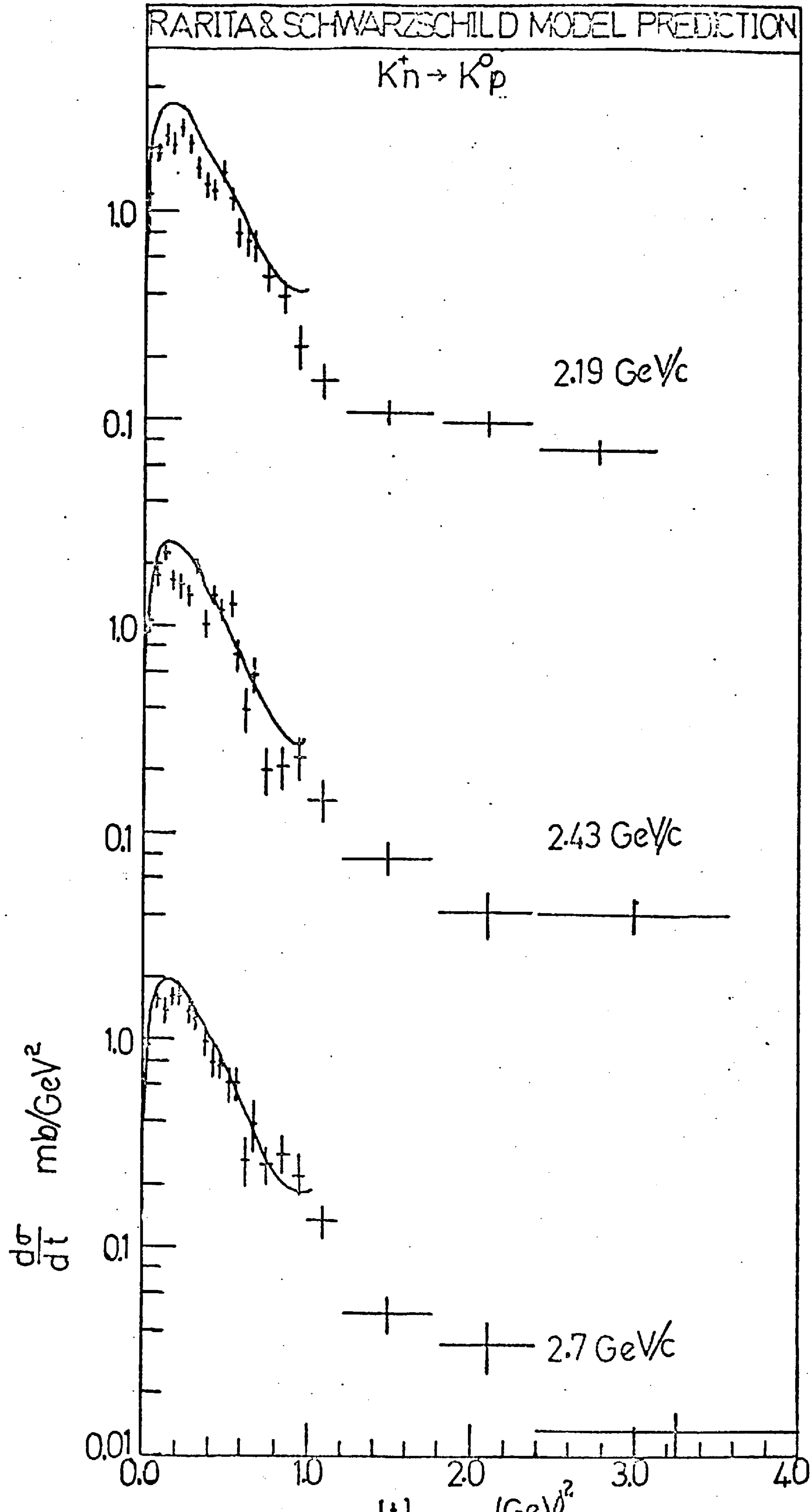

RARITA & SCHWARZSCHILD MODEL PREDICTION
$K^+n \rightarrow K^0p$
2.19 GeV/c
2.43 GeV/c
2.7 GeV/c
1.0
0.1
0.01
$\frac{d\sigma}{dt}$ mb/GeV^2
0.0
1.0
2.0
3.0
4.0
|t| (GeV)^2

3.13

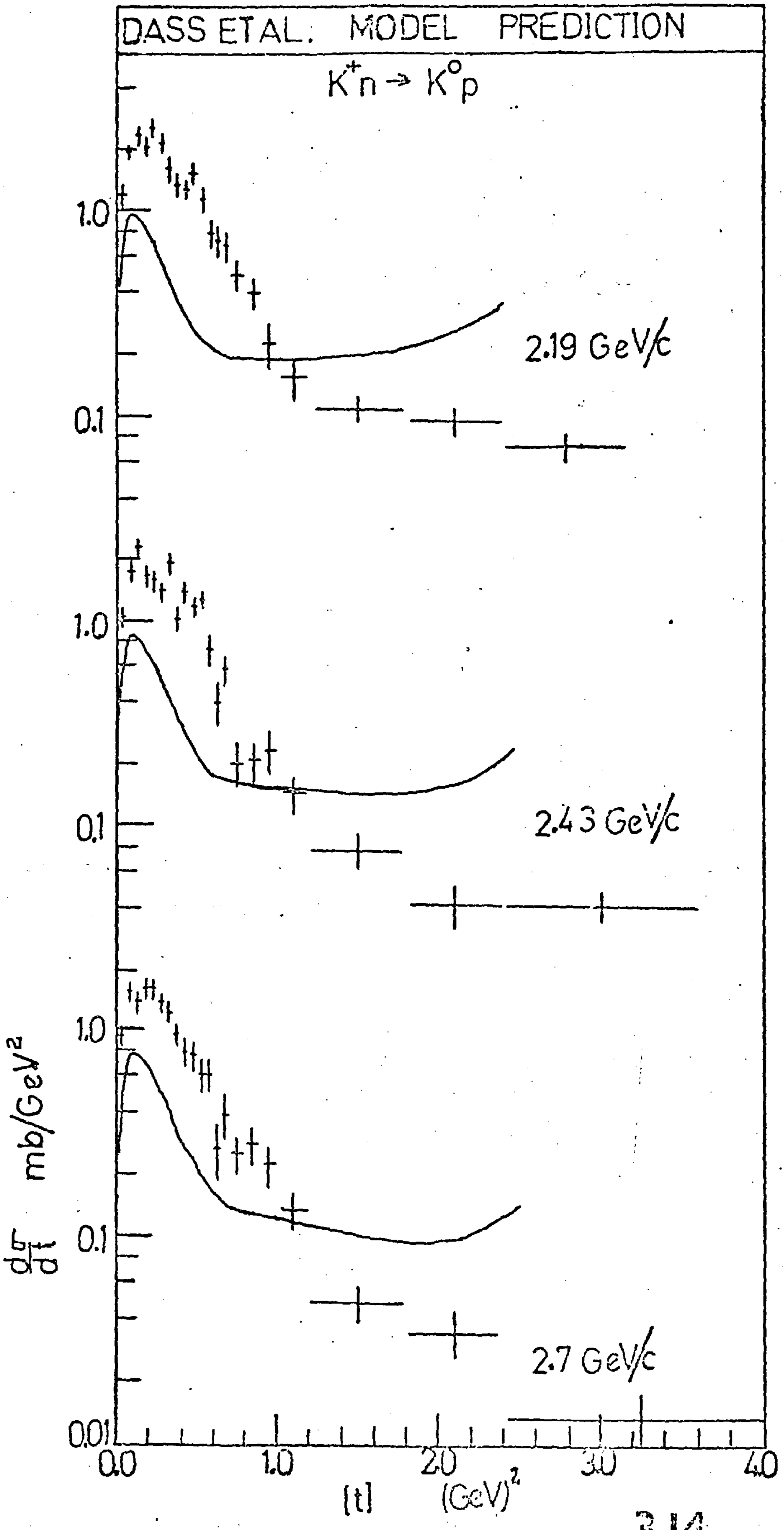
DASS ETAL: MODEL PREDICTION
$K^+n \to K^0p$
2.19 GeV/c
2.43 GeV/c
2.7 GeV/c
1.0
0.1
0.01
$\frac{d\sigma}{dt}$ mb/GeV^2
0.0
1.0
2.0
3.0
4.0
|t| (GeV)^2

3.14

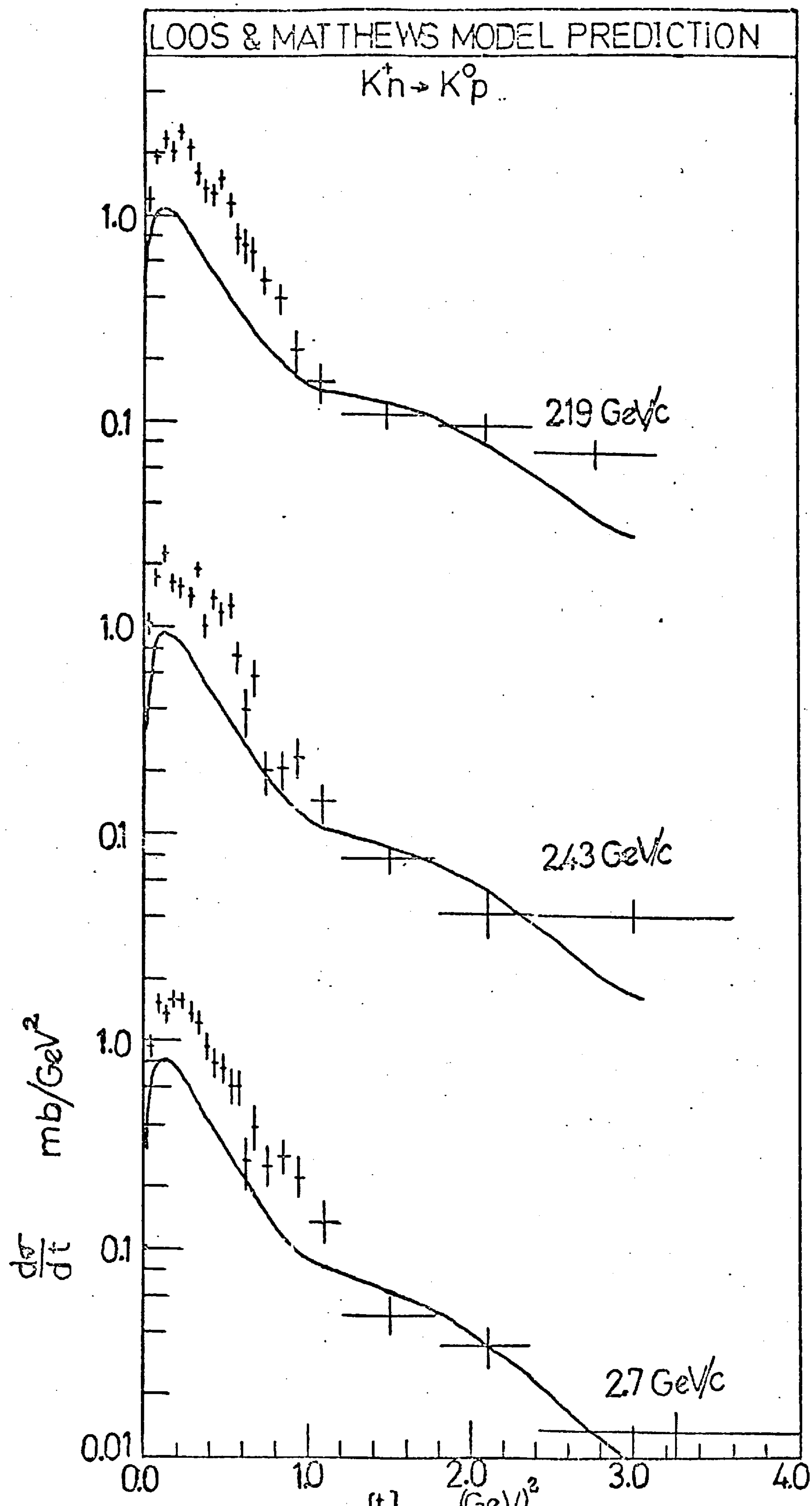

LOOS & MATTHEWS MODEL PREDICTION
$K^+n \to K^0p$
2.19 GeV/c
2.43 GeV/c
2.7 GeV/c
1.0
0.1
0.01
$\frac{d\sigma}{dt}$ mb/GeV^2
0.0
1.0
2.0
3.0
4.0
|t| (GeV)^2

3.15

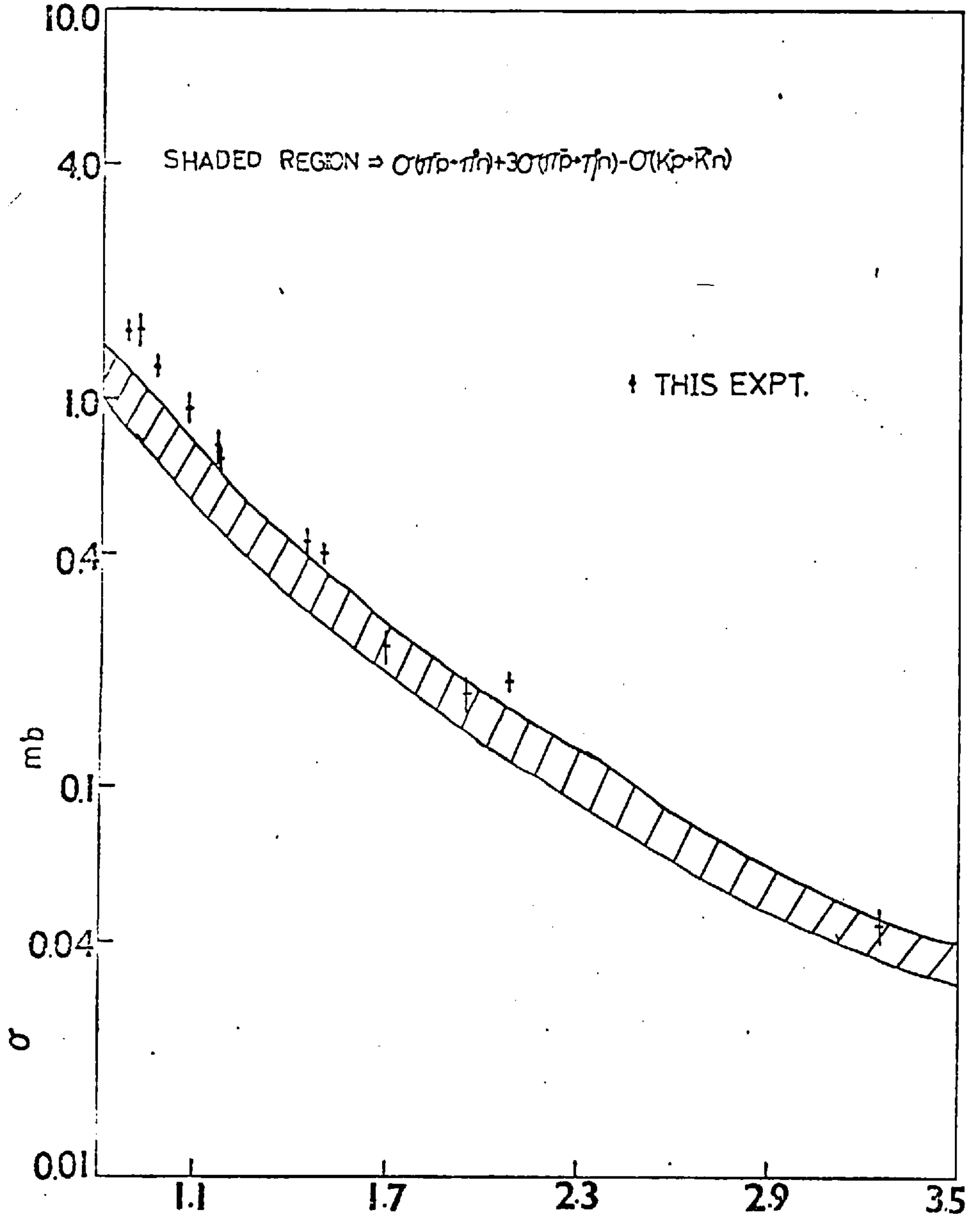
SHADED REGION ⇒ σ(π⁻p→π°n)+3σ(π⁻p→ηn)−σ(K⁻p→K̄°n)
THIS EXPT.
σ mb
Q GeV
10.0
4.0
1.0
0.4
0.1
0.04
0.01
1.1
1.7
2.3
2.9
3.5

3.16

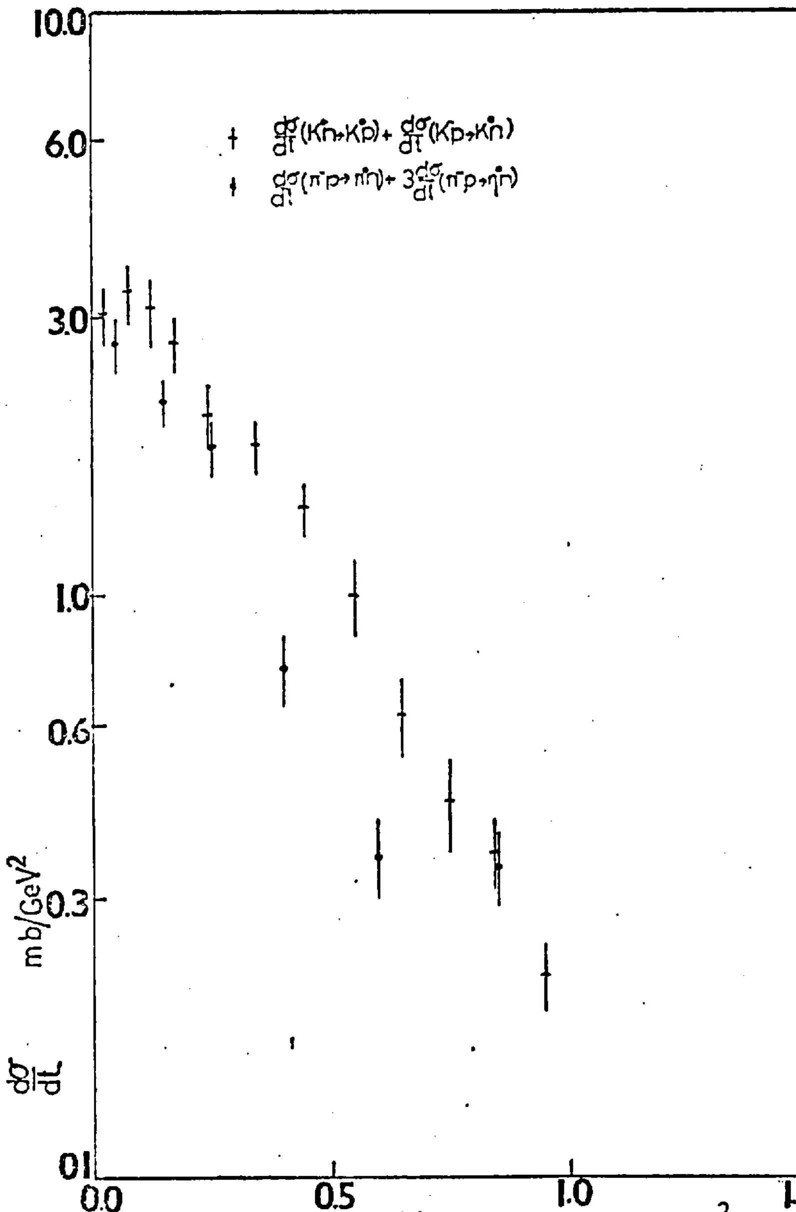
dσ/dt mb/GeV²
|t| GeV²
10.0
6.0
3.0
1.0
0.6
0.3
01
0.0
0.5
1.0
1.5

3.17

CHAPTER 4

The rapidly opening threshold of the $K^*(890)$ production in K^+N reactions has been argued by Aaron et al. (1971) to affect the elastic channel and this would result in the elastic channel going resonant. Similar consideration for the opening up of the $K^*(1420)$ threshold may cause a resonating state in the KN system. The process should be a highly inelastic one and should have been observed in the $KN \longrightarrow K^*(890)N$ reaction. With this motivation one looks at the single pion production processes in this chapter. In this experiment one can observe three such reactions in the K^+n system and one in the K^+p system. They are

$$K^+n \rightarrow K^+\pi^-p \qquad 4.1$$
$$K^+n \rightarrow K^0\pi^0p \qquad 4.2$$
$$K^+n \rightarrow K^0\pi^+n \qquad 4.3$$
$$K^+p \rightarrow K^0\pi^+p \qquad 4.4$$

The other single pion production process in the K^+n system is

$$K^+n \rightarrow K^+\pi^0n \qquad 4.5$$

which is a zero constraint fit among one or two prong events without a visible V_o decay. So this reaction cannot be studied in this experiment. Other such reactions in the K^+p system have not been measured in this experiment as this has been done in some good detail in an earlier experiment (Brunet et al. 1972).

4.1 AMBIGUITY AND SELECTION OF EVENTS

Reactions of type 4.1 are observed in this experiment as

$$K^+n(p) \rightarrow K^+\pi^-p(p) \qquad 4.6$$

They appear as 300 or 400 topology events on the film. These reactions give highly constrained kinematic fits. So the contamination level from other K^+ induced channels is quite low. But the possibility of pion contamination in the beam introduces some problem. It was suggested that at the time of fitting, the corresponding hypothesis.for a pion beam should also have to be considered.

$$\pi^+ n(p) \rightarrow \pi^+\pi^- p(p) \qquad 4.7$$

As a result of this most of the events which give a fit of type 4.6 also are fitted to the hypothesis 4.7 and there is no obvious way of distinguishing the two reactions. One assumes that the production mechanism in the two processes are similar so that the ratio of the number of unique events fitted to the hypotheses 4.6 and 4.7 will give a true ratio of the K^+ and π^+ induced reactions. This assumption leads to the pion contamination in the beam to be 9.5%, 4.1% and 10.5% for beam momenta of 2.18 GeV/C, 2.43 GeV/C and 2.70 GeV/C respectively. However the GRIND fittings to the hypotheses 4.6 and 4.7 depend on the measurement errors and the spread in beam momenta. Further one finds that 77.4% of the ambiguous events has spectator momentum less than 80 MeV/c in the laboratory frame so that the spectators cannot be seen on the film, This makes the estimation of pion contamination to be dubious. The other possible contamination comes from the reaction

$$K^+ n(p) \rightarrow K^+\pi^-\pi^0 p(p) \qquad 4.8$$

But the preference of four constraint fits to one constraint fits make such contamination in the final data sample to a minimum. However, this causes some excess of events at low probabilities for reactions of the type 4.6. So only events with probability greater than 4% were accepted for further analysis .

The reaction 4.2 is observed as

$$K^{+}n(p) \rightarrow K^{0}\pi^{0}p(p) \qquad 4.9$$

and the reactions 4.3 and 4.4 are observed as

$$K^{+}n\,p \rightarrow K^{0}\pi^{+}n\,p \qquad 4.10$$

Both these fits come from one or two prong events with an associated V_{o} decay. A study of the spectator nucleon in these reactions (as described in Section 2.1) suggests that though for the events where one proton is unobserved, fitting of the neutral particle was poor, there has been no serious loss of events in either of the channels. The reaction 4.9 is ambiguous with 4.10 and also with

$$K^{+}n(p) \rightarrow K^{0}p(p) \qquad 4.11$$

$$K^{+}d \rightarrow K^{0}\pi^{+}d \qquad 4.12$$

$$K^{+}d \rightarrow K^{0}\pi^{+}\pi^{0}d \qquad 4.13$$

Both 4.11 and 4.12 give four constraint fits and they are always preferred to the hypothesis 4.9. The level of contamination is however quite small for this process ($\sim$1%). For events where the only existing ambiguity is between 4.9 and 4.10, one weighs each event by the inverse of the number of fittable hypotheses to that event. However in reaction 4.10, the chief ambiguity is with the reaction 4.12. The level of contamination is 2.9% at 2.18 GeV/c and it rises to 3.8% at 2.70 GeV/c. The resolution of this ambiguity has been done by using cuts on the mass and angle of the proton, neutron system. This will be discussed in some detail in Chapter 6. As has been specified earlier only those events which have their spectator momenta less that 300 MeV/c were accepted for final analysis.

4.2 CROSS-SECTION AND RESONANCE FRACTIONS.

Cross-sections of the channels have been summarised in table 4.1 and they have been plotted with the cross-section measurements at other energies on figures 4.1, 4.2, 4.3 and 4.4 respectively. The cross-section for the process 4.1 is falling with laboratory beam momentum at the energy level of this experiment with an energy dependence of the form $A\ P_{lab}^{-n}$ $(n = 1.3 \pm 0.1)$. Also on the same graph are plotted the cross-sections for the process $K^- p \rightarrow K^- \pi^+ n$. The two cross-sections fall more or less on top of each other. This fact supports the exchange of exchange degenerate Regge trajectories (or a single Regge trajectory) which is not so obvious in the case of the elastic charge exchange reaction (Chapter 3). The reactions 4.2, 4.3, 4.4 all have smooth energy dependence. The reaction 4.4 has also been observed in hydrogen target experiments and within errors the result of this experiment fits very well with the hydrogen target experiments. This further supports the selection criterion of the spectator events. All the cross-sections were fitted with an energy dependence proportional to $(P_{lab})^{-n}$. The fitted parameters using cross-sections above 2 GeV/c have been shown on table 4.1. None of the cross-sections within error shows any structure. Thus one cannot see in this experiment the dominance of Z^* production in any of the channels. However, if the resonance is highly inelastic as has been suggested by Aaron (1971), one should get a reasonably smooth cross-sectional behaviour and only a partial wave analysis of the system would show the existence of such a resonance. This has been done in some detail and described in Chapter 5.

The distribution of events on the Dalitz plots have been shown on diagrams 4.5-4.8 for the different reactions at the three different beam momenta. All the reactions show a strong $K^*(890)$ production. However the resonance band becomes broader for a one constraint fit with a final state π^0. The π^0 momenta are poorly determined for events where one of the proton tracks is badly measured or unseen. This causes the broadening and this is more evident at larger beam momenta. The reaction 4.4 shows a strong $\Delta^{++}(1236)$ production. The reaction 4.1 has a broad distribution in the $p\pi^-$ system. An attempt has been made to explain this as a diffractive dissociation of the neutron by Yen et al. (1974) and this is considered in some detail in section 4.3c. The reaction 4.2 and 4.3 show a $\Delta^+(1236)$ signal. However the reaction 4.3 also shows some concentrations of events near $N^*(1520)$ and $N^*(1688)$ masses. There is no significant accumulation of events in the diagonal direction which would have been expected for a resonance in the (KN) system.

To calculate the resonance fractions in the various channels, a maximum likelihood method (G. Thompson, 1971) was used. For each event, the following function was calculated which has got resonant and also nonresonant terms.

$$L_j = \sum_i \frac{\alpha_i (BW)_i \, PH}{N_i} + \frac{1 - \sum_i \alpha_i}{A} \qquad 4.14$$

The first term gives the sum of intensities of the resonances, α_is are the resonance fractions to be fitted. (BW) is the Breit-Wigner factor and it is parametrised as

$$(BW) = \frac{1}{\pi} \frac{m_0 \Gamma(m)}{(m^2 - m_0^2)^2 + m_0^2 \Gamma^2} \qquad 4.15$$

m being the mass of the two particle combination, m_0 the mass of the resonance and Γ the width of the resonance. The energy variation of Γ for two body decay takes the form (Jackson 1964)

$$\Gamma = \Gamma_0 \left[\frac{q}{q_0}\right]^{2l+1} \frac{\rho(m)}{\rho(m_0)} \qquad 4.16$$

The first term in the expression is the central width. The second term is the decay angular momentum barrier, q being the decay particle momentum in the resonance rest frame and l the relative angular momentum of the decay. This factor is normalised to have a value of 1 at $m = m_o$. The factor ρ is a slowly varying function of mass of the resonating system depending on the J^P values of the resonance and also the decay products. For a $J^P = 1^-$ system proceeding via pseudoscalar exchange.

$$\rho(m) = m \tag{4.17}$$

For a $J^P = 1^-$ state proceeding via vector exchange, the right hand side of 4.17 is further multiplied by p^2, the square of the recoil nucleon momentum in the overall cm system. This term is due to a production angular momentum barrier. For a P-wave $J^P = 3/2^+$ state produced via vector exchange

$$\rho(m) = \frac{(m+m_1)^2 - m_2^2}{(m_o+m_1)^2 - m_2^2} \; \frac{m_o}{m} \; p_K^2 \tag{4.18}$$

where m_1, m_2 are the masses of the decay products ($\frac{1}{2}^+$ and 0^- states respectively). The inverse phase space term (PH) was

$$PH = m/p \tag{4.19}$$

This was required to divide the two body phase space so that the final term represents the background while the other terms will represent the resonant contributions only. N_i and A are the relative normalisation integrals. They were made up of the numerator (excluding the factors α_i's) integrated over the phase space. Thus A is simply the area of the Dalitz plot.

The likelihood function which was maximised was given by

$$L = \prod_j w_j L_j \tag{4.20}$$

where w_j is the weight of the event j calculated from the position of the decay vertex and also from the ambiguity resolution criterion. The logarithm of this likelihood function was taken and then inverted in sign. This log likelihood function was then minimised using the CERN MINUIT program. In this process one assumes that there is no appreciable interference among the various resonances. The interference effect should be small in all the reactions except 4.4 which has strong $K^*(890)$ and $\Delta^{++}(1236)$ production. A comparison of number of events in the overlap region with the events in the conjugate region (i.e. the regions produced by the interchange of directions of the two particles in a resonance decay) suggests that this interference effect is also small in this case. One further does not consider the structure in the Dalitz plot due to anisotropic decay of the resonance in its rest frame. This introduces more adjustable parameters in the fits thus increasing the errors in the fraction, but it does not improve the quality of the fit or vary the fractions appreciably. So they have not been used in the final fits.

In all the reactions 4.1 - 4.4, one assumes $K^*(890)$ and $\Delta(1236)$ production, $K^*(890)$ has been assumed to be in a pure $J^P = 1^-$ state and it is produced by pseudoscalar and vector exchanges in the case of the neutral and the charged modes. Δ (1236) is assumed to be a $J^P = 3/2^+$ state produced by vector exchange. The fit of the reaction 4.3 also involved D13N^*(1520) and F15 N^*(1688) states in the $n\pi^+$ system. For both of these the width was assumed to be mass independent. The mass and width of Δ and N^*'s were fixed during the fit except in the case of reaction 4.4 where the Δ signal was strong. In the reaction 4.2, the width of K^* was also fixed, otherwise the unseen spectator events severely distort the likelihood function and the convergence criterion cannot be obtained.

The quality of the fits is shown on diagrams 4.9-4.12 which show the effective mass distributions for all the reactions at the three beam momenta. The results have been summarised on tables 4.2 and 4.3. The errors quoted correspond to a change of 0.5 in the log likelihood function. To check the quality of the fit, the ratio of the cross-sections for $K^+n \to K^*(890)p$, $K^* \to K^+\pi^-$ and $K^+n \to K^*(890)p$, $K^* \to K^0\pi^0$ has been compared with the prediction from isospin Clebsch-Gordan coefficients. The experimental value is in good agreement at each beam momentum.

The cross-sections for the resonance production of the $K^*(890)$ state in the reaction $K^+n \to K^{*0}p$ have been plotted on figure 4.13 with similar measurements at 2.3 GeV/c, (I. Butterworth et al., 1965b), 3.0 GeV/c (Bass ompierre et al. 1970), 4.6 GeV/c (Buchner et al. 1972), 9.0 GeV/c (D. Cords et al., 1971) and 12.0 GeV/c (A. Firestone et al. 1971). The measured cross-section in this experiment is in good agreement with the other results and it shows an energy dependence $\sim P_{lab}^{-n}$ with $n = 2.5 \pm 0.2$. In crude Regge picture, the energy dependence of cross-section should be like $s^{2(\alpha(0)-1)}$ i.e. $P_{lab}^{2\alpha(0)-2}$ where s is the total centre of mass energy squared and $\alpha(0)$ is the intercept of the dominant trajectory. This measurement shows that the dominant trajectory for this process should have an intercept -0.25 ± 0.10. The dominant mechanism in the $K^{*0}(890)$ production is the exchange of the pion trajectory. This value is then comparable to the intercept -0.02 which should be obtained for a linear pion trajectory with a unit slope. On the same graph, the cross-sections for the line reversed reaction $K^-p \to \overline{K^{*0}}(890)n$ have been plotted. Both the processes proceed via pion exchange. So one usually expects the same sort of energy dependence in the two processes. But the cross-section of the line reversed process is smaller than the $K^+n \to K^{*0}p$ cross-section at smaller energies (round about 3 GeV/c). However, it has also got a slower energy variation so that at larger beam momenta the two cross-sections agree within errors. This discrepancy can be removed by assuming contributions from ρ and A_2 trajectories which become important at larger momentum transfers. Also absorption is important at lower energies.

Figure 4.14 shows a plot of the resonance cross-section of the Δ^{++} production in the reaction 4.4. The plot also includes data from hydrogen target experiments at 2.97 GeV/c, (Bassompierre et al., 1970), 3.5 GeV/c (Pape et al. 1968), 5.0 GeV/c (Particle Data Book), 9.0 GeV/c (Lind et al. 1969), 10.0 GeV/c (Barnham et al. 1971) and 12.7 GeV/c (Berlinghieri et al. 1968). The results of this experiment are consistent with the other results and this produces a P_{lab}^{-n} behaviour with n = 1.9$\pm$0.2. The Δ^{++} production have been explained in Regge pole models by ρ and A_2 exchanges. The process $K^- n \rightarrow \overline{K^\circ} \Delta^-$ also involves ρ and A_2 exchanges, but the amplitudes have got opposite signs. So a comparison of these two processes would test the exchange degeneracy of those two trajectories. On the same plot, the cross-sections for the process $K^- n \rightarrow \overline{K^\circ} \Delta^-$ have been plotted and they are markedly different from the cross-section of the process $K^+ p \rightarrow K^\circ \Delta^{++}$ over the entire energy region (n is 1.6$\pm$0.2). There are two obvious ways of explaining this inequality. The first explanation involves diagrams like 4.15 for Δ production. Then the difference of the two cross-sections would result from the inequalities of the cross-sections for the process $K^+ n \rightarrow K^\circ p$ and $K^- p \rightarrow \overline{K^\circ} n$. This would then imply the Δ production cross-sections in the K^+ and K^- system would tend to become closer at larger energy. However, the data in the figure 4.14 does not support this view. The other explanation involves some coherent interference between the resonant and the nonresonant parts of the amplitudes. The slopes n of the $K^+ n \rightarrow K^\circ p$ and $K^- p \rightarrow \overline{K^\circ} n$ cross-sections in $\sigma - P_{lab}$ distribution are 2.10$\pm$0.05 and 1.74$\pm$0.10 respectively which are similar to those for Δ production processes.

Since strong interactions conserve isotopic spin as well as its z component it is possible to separate the isospin 1 component from the isospin zero component in the reaction $K^+ N \rightarrow K^*(890) N$. The formulae one uses are

$$\sigma_1 = \sigma\,(K^+p \to K^{*+}p) \qquad 4.21$$

$$\sigma_5 = 2[\sigma\,(K^+n - K^{*+}n) + \sigma(K^+n - K^{*0}p)] - \sigma(K^+p - K^{*+}p) \qquad 4.22$$

The cross-sections thus evaluated have been listed in table 4.3 and also plotted on Figure 4.16 together with other experimental results. Both the cross-sections are observed to fall smoothly at the energy of the present experiment. The parameters of $A\,P_{lab}^{-n}$ fits are quoted in table 4.3.

4.3 A STUDY OF THE REACTION $K^+n \to K^+\pi^-p$.

4.3 A) General Features of $K^*(890)$ production:

The main feature of the $K^+\pi^-$ system is that it shows a strong $K^*(890)$ signal in the mass plot. Quark models (Bialas et al. 1968) for hadrons which include quark spins can relate the $K^*(890)$ production cross-section and differential cross-sections to those of other two or quasi two body processes. These are essentially based on several assumptions. The most fundamental of these assumptions is the so called additivity assumption which states that the amplitude for each particle particle scattering is a sum of one quark-one quark scattering amplitudes without baryon number exchanges. This assumption rules out more than one unit of charge/strangeness exchange and also baryon exchange which is clearly not true at low energies. But it is a good approximation at high energies. Also exact U(3) symmetries of quarks or antiquarks alone are assumed and the breaking of this symmetry by exchanged particles lead to relations between several reactions, the one relevant here is

$$\bar{\sigma}\,(\pi^-p \to \omega^0 n) + \bar{\sigma}(\pi^-p \to \phi n) + \bar{\sigma}(\pi^-p \to \rho^0 n) = \bar{\sigma}(K^-p \to \bar{K}^{*0}n) + \bar{\sigma}(K^+n \to K^{*0}p) \qquad 4.23$$

where

$$\bar{\sigma} = s\,\frac{P_{in}}{P_{out}}\,\sigma \qquad 4.24$$

s being the total centre of mass energy squared, p_{in}, p_{out} are the momenta of incoming and outgoing particles in the centre of mass frame. However, the limited data for the reaction $\pi^- p \rightarrow \omega n$ restricts the testing of this formula at the energy of this experiment.

One other useful assumption is the equivalence of the quarks constituting mesons and the quarks constituting baryons and antibaryons. This together with the charge conjugation invariance leads to the following formulae

$$\sigma(K^+n \rightarrow K^{*0}p) = \frac{3}{8}\sigma(K^+p \rightarrow K^{*0}\Delta^+) + \frac{25}{24}\sigma(K^+p \rightarrow K^{*0}\Delta^{++}) \quad 4.25$$

$$\sigma(K^+n \rightarrow K^{*0}p) = \frac{3}{8}\sigma(pp \rightarrow n\Delta^{++}) \quad 4.26$$

It can be seen from figures 4.17A and 4.17B that these rules are not valid at this energy. One should however remember that at the energy of this experiment, the additivity assumption is not strictly true.

$K^*(890)$ events were selected using a mass cut from 0.84 to 0.94 and the t-distribution has been shown in figure 4.18. The distribution shows a forward dip near $t = -0.01 GeV^2$. This is probably a kinematic effect and the $t'(=t-t_{min})$ distribution (figure 4.20) does not show any sign of forward dip at all. The t-distribution clearly shows a change of slope near $|t| = 0.6\ GeV^2$ which is also observed at 3.0 GeV/c and 4.6 GeV/c. This might suggest that different t regions are produced differently and it will be discussed later. The t' distribution has been fitted with an exponential up to $t' = 0.3\ GeV^2$ and the slopes have been quoted in table 4.4. The slope parameters have been plotted on figure 4.19 along with those from other experiments. The slope stays practically constant over the entire energy region. In a pure Regge pole exchange model, the slope of the t-distribution can be expressed as

$$B = B_0 + 2\alpha' \ln s \quad 4.27$$

where α' is the slope of the dominant trajectory exchanged. The variation of $\ln s$ in the entire energy range is approximately 1.5. This leads to $\alpha' \sim 0.5\ GeV^{-2}$ But this reaction involves more than one exchange; this complicates the relation 4.27. So no clear conclusion can be made in this respect.

4.3 B) Decay characteristics of $K^*(890)$:

To look at the J^P states involved for that large $K^+\pi^-$ mass bump near 0.9 GeV one should utilise the angular distribution information . The decay distribution can be expanded in terms of the spherical harmonics as

$$W(\theta,\phi) = \sum_{l,m} a^l_m Y_{lm}(\theta,\phi) \qquad 4.28$$

Thus one obtains the coefficients of the spherical harmonics as

$$a^l_m = \int W(\theta,\phi) Y^*_{lm}(\theta,\phi) d\cos\theta d\phi = \langle Y^*_{lm} \rangle \qquad 4.29$$

The decay distributions are generally studied in the resonance rest frame. The z-axis can be chosen in various ways, two of which are commonly used. One is the direction of the beam (or the target) in the resonance rest frame and this system is called the t-channel frame or the Gottfried Jackson frame. In the other, known as the helicity or the s-channel frame, the z-axis is given by the direction of the resonance particle. In both the cases, y-axis is defined by the direction of the normal to the production plane.

Using the angular distributions in the s-channel or the helicity frame, the real and the imaginary parts of the coefficients have been evaluated using the method of moments at various masses of the $K^+\pi^-$ system. The imaginary parts were found to be consistent with zero. The real parts of the coefficients have been plotted as a function of the $K^+\pi^-$ mass on diagram 4.22. The coefficients higher than $l \geqslant 3$ are consistent with zero throughout implying that partial waves higher than L=1 (P-wave) are not required in this mass range. However, a_{30} has some nonzero value in $K^*(890)$ mass range which could be possibly due to a PD wave interference effect. But this effect is small and neglected here. All the coefficients with $l \leqslant 2$ show structures in the mass region 0.80 GeV < Mass $(K^+\pi^-)$ < 1.00 GeV which suggests that in addition to the P-wave, there is some S-wave present as well. From the interference of the S and P waves, the phase shift analysis of the $K^+\pi^-$ system could be done. This has been done elsewhere (S.L. Baker et al. 1974) where one may obtain a possible resonance in S-wave at the same mass as $K^*(890)$.

The decay polar and azimuthal angular distribution in the Gottfried-Jackson frame of the $K^+\pi^-$ system (in the mass range 0.84 - 0.94 GeV) have been shown in figure 4.23. The azimuthal angular distribution shows an approximately flat distribution whereas the polar angular distribution takes an approximate $\cos^2\theta$ shape suggesting dominance of P-wave production by unnatural parity exchange. A pure P-wave would give a symmetric polar distribution. But the polar distribution has clearly got a larger forward peak than a backward peak. So one has to assume S and P waves to be present in this mass range. Thus one gets a hermitian positive 4 x 4 density matrix

$$\begin{pmatrix} \rho_{11} & \rho_{10} & \rho_{1-1} & \rho_{1S} \\ \rho_{10}^* & \rho_{00} & -\rho_{10}^* & \rho_{0S} \\ \rho_{1-1} & -\rho_{10} & \rho_{11} & -\rho_{1S} \\ \rho_{1S}^* & \rho_{0S}^+ & -\rho_{1S}^* & \rho_{SS} \end{pmatrix} \qquad 4.30$$

The decay angular distribution expressed in terms of the density matrix elements looks like

$$W(\cos\theta,\phi) = \tfrac{1}{4\pi}[1+(\rho_{00}-\rho_{11})(3\cos^2\theta-1) - 3\rho_{1-1}\sin^2\theta\cos2\phi$$
$$-3\sqrt{2}\,\mathrm{Re}\,\rho_{10}\sin2\theta\cos\phi + 2\sqrt{3}\,\mathrm{Re}\,\rho_{0S}\cos\theta - 2\sqrt{6}\,\mathrm{Re}\,\rho_{1S}\sin\theta\cos\phi\,] \qquad 4.31$$

with projected distributions

$$W(\cos\theta) = 1/2\,[1 + (\rho_{00} - \rho_{11})(3\cos^2\theta - 1) + 2\sqrt{3}\,\mathrm{Re}\,\rho_{0s}\cos\theta] \qquad 4.32$$

$$W(\phi) = 1/2\pi\,[(1 - 2\rho_{1-1}) - 4\rho_{1-1}\cos^2\phi - \sqrt{6}/2\ \mathrm{Re}\,\rho_{1s}\cos\phi] \qquad 4.33$$

Thus there are only five observables namely

$$\rho_{00} - \rho_{11} = (15\langle\cos^2\theta\rangle - 5)/4 \qquad 4.34$$

$$\rho_{1-1} = 5/4\,\langle\sin^2\theta\cos 2\phi\rangle \qquad 4.35$$

$$\mathrm{Re}\,\rho_{10} = -5\sqrt{2}/8\ \langle\sin 2\theta\cos\phi\rangle \qquad 4.36$$

$$\mathrm{Re}\,\rho_{1s} = -\sqrt{6}/4\ \langle\sin\theta\cos\phi\rangle \qquad 4.37$$

$$\mathrm{Re}\,\rho_{0s} = \sqrt{3}/2\ \langle\cos\theta\rangle \qquad 4.38$$

with four real variables (ρ_{11}, $\mathrm{Im}\,\rho_{10}$, $\mathrm{Im}\,\rho_{0s}$, $\mathrm{Im}\,\rho_{1s}$) unmeasured. These five observables were measured for the decay of the $K^+\pi^-$ system in the K^*(890) mass range at the three different beam momenta and at various t-bins in both the s- and t-channel frames. This was done by the method of moments and they are listed in table 4.5. In the t-channel frame, $\rho_{00} - \rho_{11}$ decreases as t increases. This suggests that at low t, π exchange is the dominant feature of the process, but at large t some other exchanges will be present. The fact that ρ_{1-1} is small over the entire t-range suggests that the exchanges of negative and positive parity states will be present in equal proportions.

The quark model as referred earlier relates K^* density matrix elements to those Δ^{++} produced in the reaction $pp \to n\Delta^{++}$. This assumes a pure P-wave in the K^*(890) mass region and gives the following relations.

$$(\rho_{11} + \rho_{1-1})_{K^{*0}} = (4/3\ \rho_{33} + 4/\sqrt{3}\ \rho_{3-1})_{\Delta^{++}} \qquad 4.39$$

$$(\rho_{11} - \rho_{1-1})_{K^{*0}} = (4/3\ \rho_{33} - 4/\sqrt{3}\ \rho_{3-1})_{\Delta^{++}} \qquad 4.40$$

$$\mathrm{Re}\,\rho_{10\,K^{*0}} = 4/\sqrt{6}\ \mathrm{Re}\,\rho_{31\,\Delta^{++}} \qquad 4.41$$

The three beam momenta have been combined as there is no appreciable variation of the density matrix elements over the energy regions and the values obtained were compared with the results from a pp experiment at 2.8 GeV/c (Bacon et al.) (Figures 4.17C,D,E). The agreement is rather poor. However these relations are much better obeyed at higher energies (Barger 1974).

From the above analyses one thus can conclude that the $K^+\pi^-$ system in the $K^*(890)$ mass region is produced by a mixture of S and P waves and it involves several Regge trajectories exchanges. The low t-region ($|t| < 0.4\ GeV^2$) is dominated by π-exchange whereas large t-region is produced by other exchanges in equal parity mixtures. Further the reaction cross-section for the process $K^+n \rightarrow K^{*0}p$ is larger than the cross-section for the line reversed reaction and also the differential cross-section for the process $K^+n \rightarrow K^{*0}p$ shows much more peripheralism than the other reaction. This could be explained by assuming that the small momentum transfer region has been absorbed differently in the two processes. All these facts need an absorption type Regge model which involves π, ρ and A_2 trajectory exchanges. One such model has been suggested by G.C. Fox and others (1971) which assumes vector dominance at large t-values and the absorbtion effect arising due to the interference of the ρ Regge pole with the strong cut correction to π exchange. The differential cross-section for this process has been compared with the model prediction on figure 4.24. The quality of the fit is remarkable even at the energy of this experiment. However the model cannot explain the large $|t|$ data adequately, probably due to omission of the B-trajectory.

4.3 C) Study of the $p\pi^-$ system

The effective mass spectrum of the $p\pi^-$ system (as shown in figure 4.9) shows a broad mass enhancement from 1.1 GeV to 1.6 GeV. This is not a pure kinematic effect and also has been observed at 9 GeV/c (Yen et al. 1974) and 12 GeV/c (Lissauer et al. 1972). The production of this $p\pi^-$ system is peripheral in nature and the peripherality increases as one goes to the lower mass region. The t' distribution (from K to K) has been shown on figure 4.21 for various mass cuts of the $p\pi^-$ system. These t' distributions were fitted with exponentials having slopes $B = -7.2 \pm 0.2, -6.0 \pm 0.2, -5.2 \pm 0.2, -3.2 \pm 0.2, -1.9 \pm 0.2\ GeV^{-2}$ for the five Mass ($p\pi^-$) bins defined by (a) $1.1 < M(p\pi^-) < 1.2$ GeV, (b) $1.2 < M(p\pi^-) < 1.3$ GeV, (c) $1.3 < M(p\pi^-) < 1.4$ GeV, (d) $1.4 < M(p\pi^-) < 1.5$ GeV, (e) $1.5 < M(p\pi^-) < 1.6$ GeV . A similar shaped enhancement is also observed in the $p\pi^-$ system in the reaction $pn \rightarrow pp\pi^-$. The strong variation of the slope with the mass of the $p\pi^-$ system suggests that there are more than one mechanism responsible for the production of the $p\pi^-$ system. An estimate of $\Delta^0(1236)$ production has been made from the reaction cross-section of the process $K^+p \rightarrow K^0\Delta^{++}$ and this estimate has been found to be less than 6%. So this broad enhancement is principally due to isospin $\frac{1}{2}$ states of the $p\pi^-$ system. This is not a reflection of the $K^*(890)$ resonance production in the $K^+\pi^-$ system as can be seen from the Dalitz plot (figure 4.5). Also antiselection of the $K^*(890)$ events using a mass cut does not affect the above features at all. Lissauer et al. (1972) went through a partial wave type analysis in the $p\pi^-$ system and identified this enhancement as a joint effect of a D13 $N^*(1520)$ and F15 $N^*(1680)$ production with a strong P11 wave in the $p\pi^-$ system in the low t' region. The P11 wave has been found to be peaked at 1250 MeV and has a width of 300 MeV and also it is very similar to the $N^*(1470)$ state.

The strong t dependence of the process also suggests some Regge-exchange process responsible for the production of this system. The Deck effect originally introduced to improve the calculation of the phase space in the construction of the scattering amplitude has been developed to incorporate Regge trajectories and these types of models have been largely used to describe successfully the three particle final states. There are several such Deck diagrams which will be important only in some selected region of the phase space. In a triangular plot of the longitudinal momenta of the three final state particles one can select out six regions and can associate the final state particles with the various vertices in these regions (illustrated in figure 4.25). A large fraction of events in the enhancement including the K^*s (~35%) lies in the region corresponding to the Vanhove angle w (figure 4.25) between 120° and 180°. So one can have a Reggeised diagram like figure 4.26 to explain the data in this region. The total amplitude is thus factorised into 3 components, an off shell $K^+\pi^-$ scattering term, a pion propagator and a pomeron, nucleon scattering amplitude by pion exchange. According to Berger (1969), the squared amplitude of such a diagram can be written as

$$|M|^2 \sim |R_\pi(t_{np})|^2 \left(\frac{\bar{s}_{p\pi}}{\bar{s}_{0\pi}}\right)^{2\alpha_\pi} |R_P(t_{KK})|^2 \left(\frac{\bar{s}_{K\pi}}{\bar{s}_{0P}}\right)^2 \qquad 4.42$$

$$|R_\pi(t_{np})|^2 = \frac{t_{np}}{1-\cos\pi\alpha_\pi}\, \exp(\lambda_1 t_{np}) \qquad 4.43$$

$$|R_P(t_{KK})|^2 = \exp(\lambda_2 t_{KK}) \qquad 4.44$$

$$\bar{s}_{p\pi} = M^2(p\pi) - t_{KK} - m_\pi^2 - 0.5(m_\pi^2 - t_{np} - t_{KK}) \qquad 4.45$$

$$\bar{s}_{K\pi} = M^2(K\pi) - t_{np} - m_K^2 - 05(m_\pi^2 - t_{KK} - t_{np}) \qquad 4.46$$

$$\alpha_\pi = \alpha'_\pi(t_{np} - m_\pi^2) \qquad 4.47$$

One uses $\bar{s}_{0\pi} = 0.7\ GeV^2$, $\bar{s}_{0P} = 1.0\ GeV^2$ and $\alpha'_\pi = 1.2\ GeV^{-2}$. A comparison with the experimental distributions have been made in figure 4.29 by generating events using the CERN monte carlo phase space program FOWL and weighting each event by a factor $|M|^2$. The experimental data and the fit both use the same kinematic cuts $120° < w < 180°$, mass of the $K^+\pi^-$ system > 1.0 GeV and $|t_{np}| > 0.8\ GeV^2$. The parameters λ_1 and λ_2 have been adjusted by looking at the fitted distribution and the fits are rather insensitive to these values.

The values of λ_1 and λ_2 used here are 2.5 and 4.3 GeV^{-2} respectively. The fits to the data are reasonably good.

Thus the process $K^+n \rightarrow K^+\pi^-p$ is dominated by $K^{*o}(890)$ production and also some diffraction dissociation of the neutron is present.

4.4 $K^*(890)$ PRODUCTION AND DECAY IN THE REACTIONS 4.2, 4.3 and 4.4

The production of the $K^*(890)$ state is the most dominant feature in the reactions 4.2, 4.3 and 4.4. However, in reaction 4.4 there is also some evidence for strong production of the $\Delta^{++}(1236)$ state. But the interference of the K^{*+} and Δ^{++} has been found to be small. So a cut in the mass plot $0.84 < M(K\pi) < 0.94$ GeV has been used to select out $K^*(890)$ events for further analysis.

The t' distributions from K^+ to K^{*o} have been plotted for the process 4.2 on figure 4.30 at the three different beam momenta. All of them agree with an exponential distribution with slopes 5.2 ± 1.0, 5.3 ± 1.0 and 5.9 ± 1.0 GeV^{-2} respectively. These values are somewhat smaller than the slopes obtained for the K^{*o} production process in $K^+\pi^-p$ final state. There is some evidence of shrinkage of the forward peak and using the data at 4.6 GeV/c (Buchner et al. 1972), the estimated slope of the exchange trajectory has been found to be 3.0 ± 1.0 GeV^{-2}.

The t' distribution for the K^{*+} production in the reactions 4.3 and 4.4 have been shown on diagrams 4.31 and 4.32 respectively. These reactions have been found to be less peripheral than the K^{*o} production processes. The exponential fits yield slopes 3.1 ± 0.5, 3.3 ± 0.6, 3.7 ± 0.6 GeV^{-2} respectively for K^{*+} production in the reaction 4.3 and 2.7 ± 0.5, 3.0 ± 0.5, 2.9 ± 0.5 GeV^{-2} respectively for K^{*+} production in 4.4. They agree well within errors and are compatible with the hydrogen target experiments. The difference in the t' distribution for K^{*o} and K^{*+} production suggests different production mechanisms in the two processes. This could be studied in further detail by looking at the decay distribution of the $K^*(890)$.

Figures 4.34, 4.35 and 4.36 show the decay polar and azimuthal angular distributions of the $K^*(890)$ for the reaction 4.2, 4.3 and 4.4 respectively. All the polar angular distributions show some forward-backward asymmetry. A pure P-wave decay to the $K\pi$ system would give rise to a symmetric distribution. So there is some S-wave present and this has been observed in all previous experiments with a deuteron target. However other hydrogen target experiments did not observe such effects. This is not due to the presence of Δ^{++} events in the sample. The overlap region of the Dalitz plot can be removed and replaced by events from conjugate region using Eberhard-Pripstein prescription and still the same effect has been observed. The azimuthal angular distribution for K^{*o} decay is essentially flat and the polar angular distribution has taken a $\cos^2\theta$ form suggesting pseudoscalar exchange to be dominant. The polar angular distribution for the decay of the K^{*+} state takes a $\sin^2\theta$ form suggesting vector dominance.

From these decay distributions the decay density matrix elements were calculated by the method of moments and they have been listed in tables 4.7, 4.8 and 4.9 respectively as a function of t'. The smooth curves on the plots are the estimated distribution from these density matrix elements. The matrix elements of the K^{*+} production with proton and neutron targets have similar features suggesting similar reaction mechanisms in the two processes. However no single exchange is dominant in any of these reactions. The largeness of ρ_{00} at low t' for reactions 4.3 and 4.4 suggests that pseudoscalar exchange could be present at low t' - but natural parity vector exchange becomes important at large t'. The K^{*o} decay density matrix elements are similar to those in the reaction 4.1, namely ρ_{00} is large specially at low t' values suggesting that pseudoscalar exchange is dominant and ρ_{1-1} is small suggesting natural and unnatural parity exchanges are equally present. The dominance of π over ρ-A_2 trajectories in K^{*o} production might imply isoscalar exchange to be dominant in K^{*+} production. One usually assumes natural parity isoscalar exchange to be w and f trajectories. Using the slopes of t' distribution of this experiment with those in other proton target experiments (Fu et al. 1971, Baere et al. 1970) one finds the slope of the trajectory to be 0.7 ± 0.2.

4.5 $\Delta^{++}(1236)$ PRODUCTION AND DECAY IN THE REACTION 4.4

The Δ^{++} events were selected using a mass cut in the Dalitz plot $1.13 < M(p\pi^+) < 1.33$ GeV. The t' distributions from K to K^0 have been shown on figure 4.33 for these events at the three beam momenta. This shows a forward dip which is expected in ρ-A_2 exchanges. Except for this dip, the t' distribution shows no other structure. The events with t' between 0.15 GeV^2 and 0.75 GeV^2 are well explained by an exponential t' distribution. The exponential distribution yields the values of the slopes to be 2.75 ± 0.50, 2.84 ± 0.50 and 3.03 ± 0.50 GeV^{-2} at the three beam momenta, respectively. Together with the slopes at other hydrogen target experiments, 4.2 ± 0.4 GeV^{-2} at 3.5 GeV/c (Baere et al. 1970), 4.9 ± 0.6 GeV^{-2} at 4.6 GeV/c (Fu et al. 1971). 5.3 ± 0.7 GeV^{-2} at 8.25 GeV/c (Baere et al. 1970), one can clearly see a shrinkage on the forward peak of the differential cross section. From a Regge analogy

$$B = B_0 + \alpha' \ln s \qquad 4.48$$

So one gets $\alpha' = 1.0 \pm 0.2$ GeV^{-2} for the effective exchange trajectory which is close to the accepted value of ρ-A_2 trajectory (0.9 GeV^{-2}).

The decay polar and azimuthal angular distribution of the Δ^{++} system have been shown in figure 4.37. The decay of a $J^P = 3/2^+$ state to a $J^P = 0^-, \frac{1}{2}^+$ states in a relative P-wave state can be explained in terms of a density matrix as following

$$W(\cos\theta,\phi) = \tfrac{3}{4\pi}\,[\,(1+4\rho_{33})/6 + (1-4\rho_{33})\cos^2\theta/2 - 2\,\mathrm{Re}\,\rho_{3-1}\sin^2\theta\cos 2\phi/\sqrt{3} - 2\,\mathrm{Re}\,\rho_{31}\sin 2\theta\cos\phi/\sqrt{3}\,] \qquad 4.49$$

with the projected distributions as

$$W(\cos\theta) = [(1+4\rho_{33})+3(1-4\rho_{33})\cos^2\theta]/4 \qquad 4.50$$

$$W(\phi) = [(1+4\mathrm{Re}\,\rho_{3-1}/\sqrt{3})-8\mathrm{Re}\,\rho_{3-1}\cos^2\phi/\sqrt{3}\;]/2\pi \qquad 4.51$$

Thus it is possible to evaluate three of the density matrix elements among the possible six real variables. The matrix elements have been calculated by the method of moments and have been summarised in table 4.11. The t-dependence of the matrix elements has been found to be small. ρ_{33} is not consistent with zero and hence spin zero exchange is not large. However Reρ_{31} is consistent with zero all over the t-range. Stodolsky and Sakurai (1963) suggested that Δ^{++} should be produced by ρ-exchange and calculated the density matrix elements for Δ decay by considering the $N\rho\Delta$ vertex in analogy with $N\gamma\Delta$ vertex in pion photoproduction, ρ and γ having the same quantum numbers. This gives a prediction of the density matrix elements $\rho_{33} = 0.375$, Re$\rho_{3-1} = 0.216$, Re$\rho_{31} = 0.0$ which is in excellent agreement with the results of this experiment.

An approximate SU(3) invariance and the dominance of the octet state exchange in pseudoscalar meson-baryon scattering process would relate several differential cross-sections. This sum rule has been formulated by Barger and Cline (1967) and for the proces $K^+p \rightarrow K^0\Delta^{++}$, it looks like

$$\frac{d\sigma}{dt}(\pi^+p\rightarrow\pi^0\Delta^{++})+3\frac{d\sigma}{dt}(\pi^+p\rightarrow\eta^0\Delta^{++}) = \frac{d\sigma}{dt}(K^+p\rightarrow K^0\Delta^{++})+\frac{d\sigma}{dt}(K^-n\rightarrow K^0\Delta^-) \qquad 4.52$$

On figure 4.27 one plots the calculated values of the left hand side and the right hand side of equation 4.52 as a function of t at about $E^* \sim 2.5$ GeV. This shows an excellent agreement of the sum rule specially at very small t-values. It is to be noted that the sum rule does not work well at this energy for a nucleon in the final state.

The strong cut Reggeised absorption model described by Fox et al. (1971) has been developed by Johnson et al. (1972) to describe the Δ production data. This involves exchange of degenerate ρ and A_2 trajectories modified by strong absorption corrections due to elastic scattering in the initial and the final states. This model simultaneously explain π and K induced reactions (using an SU(3) breaking factor). The fit to the data of this experiment has been shown on figure 4.28 which is reasonable considering the low centre of mass energy of this experiment.

TABLE 4.1

Channel	Beam Momentum	Cross Section	Parameters for the fit $A\ P_{lab}^{-n}$	
	GeV/c	mb	A mb	n
	2.18	2.73 ± 0.08		
$K^+n \rightarrow K^+\pi^-p$	2.43	2.63 ± 0.08	7.9 ± 0.8	1.3 ± 0.1
	2.70	2.53 ± 0.08		
$K^+n \rightarrow K^o\pi^o p$	2.18	2.22 ± 0.10		
	2.43	1.94 ± 0.10	9.7 ± 1.6	1.8 ± 0.2
	2.70	1.80 ± 0.10		
	2.18	1.86 ± 0.08		
$K^+n \rightarrow K^o\pi^+n$	2.43	1.47 ± 0.08	7.7 ± 1.4	1.7 ± 0.2
	2.70	1.50 ± 0.08		
	2.18	3.61 ± 0.18		
$K^+p \rightarrow K^o\pi^+p$	2.43	2.77 ± 0.15	13.1 ± 1.0	1.5 ± 0.2
	2.70	2.68 ± 0.15		

TABLE 4.2

Channel	Resonance	Beam Momementum GeV/c	Mass MeV	Width GeV	Fraction
$K^+n \rightarrow K^+\pi^-p$	$K^*(890)$	2.18	0.901 ± 0.002	0.064 ± 0.0001	0.641 ± 0.016
		2.43	0.898 ± 0.002	0.063 ± 0.003	0.542 ± 0.014
		2.70	0.897 ± 0.002	0.061 ± 0.002	0.467 ± 0.039
	$\Delta(1236)$	2.18	$1.236^\dagger$	$0.120^\dagger$	0.092 ± 0.009
		2.43	$1.236^\dagger$	$0.120^\dagger$	0.097 ± 0.008
		2.70	$1.236^\dagger$	$0.120^\dagger$	0.123 ± 0.010
$K^+n \rightarrow K^0\pi^0p$	$K^*(890)$	2.18	0.902 ± 0.004	$0.065^\dagger$	0.386 ± 0.029
		2.43	0.900 ± 0.002	$0.065^\dagger$	0.417 ± 0.031
		2.70	0.917 ± 0.003	$0.065^\dagger$	0.334 ± 0.023
	$\Delta(1236)$	2.18	$1.236^\dagger$	$0.120^\dagger$	0.121 ± 0.021
		2.43	$1.236^\dagger$	$0.120^\dagger$	0.148 ± 0.010
		2.70	$1.236^\dagger$	$0.120^\dagger$	0.119 ± 0.014
$K^+n \rightarrow K^0\pi^+n$	$K^*(890)$	2.18	0.900 ± 0.002	0.073 ± 0.003	0.517 ± 0.031
		2,43	0.895 ± 0.001	0.066 ± 0.002	0.487 ± 0.024
		2.70	0.896 ± 0.002	0.083 ± 0.004	0.472 ± 0.021
	$\Delta(1236)$	2.18	$1.236^\dagger$	$0.120^\dagger$	0.127 ± 0.015
		2.43	$1.236^\dagger$	$0.120^\dagger$	0.116 ± 0.010
		2.70	$1.236^\dagger$	$0.120^\dagger$	0.142 ± 0.013
	$N^*(1520)$	2.18	$1.520^\dagger$	$0.125^\dagger$	0.126 ± 0.023
		2.43	$1.520^\dagger$	$0.125^\dagger$	0.160 ± 0.026
		2.70	$1.520^\dagger$	$0.125^\dagger$	0.067 ± 0.011
	$N^*(1688)$	2.18	$1.688^\dagger$	$0.140^\dagger$	0.179 ± 0.021
		2.43	$1.688^\dagger$	$0.140^\dagger$	0.208 ± 0.019
		2.70	$1.688^\dagger$	$0.140^\dagger$	0.264 ± 0.020
$K^+p \rightarrow K^0\pi^+p$	$K^*(890)$	2.18	0.904 ± 0.002	0.080 ± 0.002	0.502 ± 0.011
		2.43	0.907 ± 0.002	0.093 ± 0.003	0.518 ± 0.023
		2.70	0.898 ± 0.001	0.075 ± 0.001	0.476 ± 0.019
	$\Delta(1236)$	2.18	1.237 ± 0.002	0.146 ± 0.005	0.377 ± 0.016
		2.43	1.233 ± 0.001	0.136 ± 0.002	0.366 ± 0.018
		2.70	1.230 ± 0.002	0.127 ± 0.003	0.358 ± 0.014

†Parameters fixed during the minimisation procedure.

<u>TABLE 4.3</u>

Channel	Beam momentum GeV/c	Cross-section mb	Parameters of the fit $A\,P_{lab}^{-n}$ A mb	n
$K^+n\to K^{*o}(890)p$	2.18	1.75 ± 0.15		
$\hookrightarrow K^+\pi^-$	2.43	1.43 ± 0.14	13.7 ± 1.5	2.5 ± 0.2
	2.70	1.19 ± 0.10		
$K^+n\to K^{*o}(890)p$	2.18	0.86 ± 0.07		
$\hookrightarrow K^o\pi^o$	2.43	0.81 ± 0.08		
	2.70	0.60 ± 0.06		
$K^+n\to K^{*+}(890)n$	2.18	0.96 ± 0.09		
$\hookrightarrow K^o\pi^+$	2.43	0.72 ± 0.06		
	2.70	0.71 ± 0.06		
$K^+p\to K^{*+}(890)p$	2.18	1.81 ± 0.12		
$\hookrightarrow K^o\pi^+$	2.43	1.44 ± 0.10		
	2.70	1.28 ± 0.10		
$K^+N\to K^*(890)\ N$	2.18	2.72 ± 0.18		
I=1	2.43	2.15 ± 0.15	14.3 ± 2.0	2.0 ± 0.2
	2.70	1.91 ± 0.16		
$K^+N\to K^*(890)N$	2.18	4.82 ± 0.50		
I=0	2.43	4.25 ± 0.44	24.9 ± 5.0	2.0 ± 0.2
	2.70	3.77 ± 0.40		
$K^+n\to K^+\Delta^o(1236)$	2.18	0.25 ± 0.03		
$\downarrow p\pi^-$	2.43	0.26 ± 0.03		
	2.70	0.31 ± 0.03		
$K^+n\to K^o\Delta^+(1236)$	2.18	0.27 ± 0.03		
$\downarrow p\pi^o$	2.43	0.29 ± 0.03		
	2.70	0.21 ± 0.02		
$K^+n\to K^o\Delta^+(1236)$	2.18	0.24 ± 0.02		
$\downarrow n\pi^+$	2.43	0.17 ± 0.02		
	2.70	0.21 ± 0.02		
$K^+p\to K^o\Delta^{++}(1236)$	2.18	1.36 ± 0.14		
$\downarrow p\pi^+$	2.43	1.01 ± 0.10	5.8 ± 0.4	1.9 ± 0.2
	2.70	0.96 ± 0.10		
$K^+n\to K^oN^{*+}(1520)$	2.18	0.23 ± 0.03		
$\downarrow n\pi^+$	2.43	0.23 ± 0.03		
	2.70	0.10 ± 0.01		
$K^+n\to K^oN^{*+}(1688)$	2.18	0.33 ± 0.03		
$\downarrow n\pi^+$	2.43	0.31 ± 0.03		
	2.70	0.40 ± 0.03		

TABLE 4.4

Channel	Beam Momentum GeV/c	t' range used GeV^2	slope of the exponential fit B GeV^{-2}
$K^+n \to K^{*o}p$, $\hookrightarrow K^+\pi^-$	2.18	0.0 - 0.3	7.05 ± 0.24
	2.43	0.0 - 0.3	7.51 ± 0.28
	2.70	0.0 - 0.3	8.10 ± 0.32
$K^+n \to K^{*o}p$, $\hookrightarrow K^o\pi^o$	2.18	0.0 - 0.5	5.2 ± 1.0
	2.43	0.0 - 0.5	5.3 ± 1.0
	2.70	0.0 - 0.5	5.9 ± 1.0
$K^+n \to K^{*+}p$, $\hookrightarrow K^o\pi^+$	2.18	0.0 - 1.0	3.1 ± 0.5
	2.43	0.0 - 1.0	3.3 ± 0.6
	2.70	0.0 - 1.0	3.7 ± 0.6
$K^+p - K^{*+}p$, $\hookrightarrow K^o\pi^+$	2.18	0.0 - 0.75	2.7 ± 0.5
	2.43	0.0 - 0.75	3.0 ± 0.5
	2.70	0.0 - 0.75	2.9 ± 0.5
$K^+p \to K^o\Delta^{++}$, $\hookrightarrow p\pi^+$	2.18	0.15 - 0.75	2.75 ± 0.50
	2.43	0.15 - 0.75	2.84 ± 0.50
	2.70	0.15 - 0.75	3.03 ± 0.80

TABLE 4.5

t interval in GeV^2		$d\sigma/dt$ for the process $K^+n \to K^{*o}(890)p$ in mb/GeV^2 2.18 GeV/c	2.43 GeV/c	2.70 GeV/c
0.0	0.02	0.51 ± 0.15	1.62 ± 0.27	2.34 ± 0.31
0.02	0.04	12.39 ± 0.73	10.40 ± 0.68	10.16 ± 0.65
0.04	0.06	10.37 ± 0.69	9.68 ± 0.65	9.83 ± 0.64
0.06	0.08	9.49 ± 0.68	7.29 ± 0.57	6.79 ± 0.53
0.08	0.10	8.94 ± 0.64	7.34 ± 0.57	5.76 ± 0.49
0.10	0.12	7.65 ± 0.59	6.30 ± 0.53	4.65 ± 0.44
0.12	0.14	6.91 ± 0.58	5.58 ± 0.51	4.24 ± 0.42
0.14	0.16	6.04 ± 0.53	4.28 ± 0.44	3.00 ± 0.35
0.16	0.18	5.30 ± 0.49	3.47 ± 0.39	2.92 ± 0.35
0.18	0.20	4.47 ± 0.45	2.93 ± 0.37	2.76 ± 0.34
0.20	0.24	4.01 ± 0.30	2.93 ± 0.25	2.32 ± 0.22
0.24	0.28	2.70 ± 0.25	2.09 ± 0.22	1.48 ± 0.17
0.28	0.32	2.79 ± 0.25	1.55 ± 0.19	1.03 ± 0.15
0.32	0.36	1.61 ± 0.19	1.49 ± 0.18	1.30 ± 0.16
0.36	0.40	1.59 ± 0.19	1.22 ± 0.16	0.97 ± 0.14
0.40	0.44	1.31 ± 0.17	0.99 ± 0.15	0.93 ± 0.14
0.44	0.48	1.18 ± 0.16	0.97 ± 0.15	0.53 ± 0.10
0.48	0.52	0.94 ± 0.15	0.59 ± 0.11	0.51 ± 0.10
0.52	0.56	0.69 ± 0.13	0.61 ± 0.12	0.56 ± 0.11
0.56	0.60	0.58 ± 0.12	0.74 ± 0.14	0.56 ± 0.11
0.60	0.68	0.62 ± 0.08	0.46 ± 0.07	0.43 ± 0.07
0.68	0.76	0.58 ± 0.08	0.44 ± 0.07	0.21 ± 0.05
0.76	0.84	0.52 ± 0.08	0.32 ± 0.06	0.24 ± 0.05
0.84	0.92	0.40 ± 0.07	0.28 ± 0.06	0.24 ± 0.05
0.92	1.00	0.35 ± 0.06	0.26 ± 0.05	0.21 ± 0.05

TABLE 4.6

Decay density matrix for the process $K^+ n \to K^{*o}(890)p$, $K^{*o} \to K^+\pi^-$

t' range in GeV^2.	P_{LAB} GeV^2	$\rho_{oo}-\rho_{11}$ G.J. FRAME	$\rho_{oo}-\rho_{11}$ HELICITY FRAME	ρ_{1-1} G.J. FRAME	ρ_{1-1} HELICITY FRAME	Re ρ_{10} G.J. FRAME	Re ρ_{10} HELICITY FRAME	Re ρ_{0s} G.J. FRAME	Re ρ_{0s} HELICITY FRAME	Re ρ_{1s} G.J. FRAME	Re ρ_{1s} HELICITY FRAME
	2.18	0.40±0.06	0.47±0.06	0.02±0.03	0.03±0.03	-0.07±0.02	0.02±0.02	0.08±0.03	0.10±0.03	-0.04±0.02	-0.02±0.02
0.0-0.025	2.43	0.50±0.06	0.53±0.06	0.00±0.03	0.02±0.03	-0.10±0.03	0.01±0.03	0.13±0.03	0.14±0.03	-0.03±0.02	0.00±0.02
	2.70	0.45±0.06	0.50±0.06	-0.03±0.03	-0.01±0.03	-0.08±0.03	0.03±0.03	0.15±0.03	0.15±0.03	0.00±0.02	0.03±0.02
	2.18	0.40±0.07	0.42±0.06	0.00±0.03	-0.01±0.03	-0.08±0.03	0.09±0.03	0.11±0.03	0.14±0.03	-0.06±0.02	-0.01±0.02
0.025-0.050	2.43	0.53±0.07	0.67±0.07	-0.05±0.03	-0.02±0.03	-0.18±0.03	0.08±0.03	0.11±0.04	0.12±0.04	-0.03±0.02	0.02±0.02
	2.70	0.50±0.07	0.51±0.07	0.04±0.03	0.05±0.03	-0.15±0.03	0.11±0.03	0.16±0.03	0.18±0.03	-0.06±0.02	0.01±0.02
	2.18	0.26±0.07	0.40±0.07	-0.03±0.04	0.00±0.04	-0.14±0.03	0.07±0.03	0.11±0.03	0.14±0.03	-0.06±0.02	0.01±0.02
0.050-0.075	2.43	0.47±0.08	0.71±0.08	-0.09±0.04	0.00±0.03	-0.24±0.03	0.10±0.03	0.07±0.04	0.11±0.04	-0.06±0.02	-0.01±0.02
	2.70	0.36±0.08	0.62±0.08	-0.08±0.04	0.00±0.04	-0.21±0.03	0.08±0.04	0.16±0.04	0.14±0.04	-0.01±0.02	0.07±0.02
	2.18	0.46±0.08	0.58±0.07	-0.07±0.04	-0.02±0.04	-0.22±0.03	0.16±0.03	0.10±0.04	0.11±0.04	-0.04±0.02	0.03±0.02
0.075-0.100	2.43	0.46±0.08	0.38±0.09	0.06±0.04	0.05±0.04	-0.18±0.03	0.20±0.03	0.10±0.04	0.09±0.04	-0.02±0.02	0.04±0.02
	2.70	0.48±0.10	0.53±0.09	-0.01±0.04	-0.02±0.04	-0.19±0.04	0.19±0.04	0.26±0.04	0.23±0.04	-0.05±0.03	0.11±0.02
	2.18	0.40±0.07	0.43±0.06	-0.09±0.03	-0.05±0.03	-0.19±0.03	0.16±0.03	0.10±0.03	0.11±0.03	-0.05±0.02	0.03±0.02
0.10-0.15	2.43	0.39±0.07	0.51±0.07	-0.01±0.04	0.03±0.04	-0.27±0.03	0.22±0.03	0.13±0.03	0.14±0.03	-0.07±0.02	0.04±0.02
	2.70	0.33±0.08	0.28±0.07	-0.02±0.04	-0.03±0.04	-0.15±0.03	0.15±0.03	0.11±0.04	0.12±0.04	-0.04±0.02	0.05±0.02
	2.18	0.25±0.07	0.43±0.08	-0.06±0.04	0.00±0.03	-0.24±0.03	0.20±0.03	0.12±0.03	0.13±0.04	-0.06±0.02	0.05±0.02
0.15-0.20	2.43	0.29±0.09	0.40±0.09	-0.04±0.04	-0.01±0.04	-0.24±0.03	0.21±0.03	0.08±0.04	0.08±0.04	-0.03±0.03	0.04±0.02
	2.70	0.32±0.09	0.45±0.09	-0.10±0.04	-0.06±0.05	-0.23±0.04	0.19±0.03	0.16±0.04	0.14±0.04	-0.06±0.03	0.07±0.03
	2.18	0.27±0.09	0.29±0.09	-0.02±0.05	-0.02±0.05	-0.25±0.03	0.25±0.03	0.06±0.04	0.07±0.04	-0.04±0.03	0.03±0.03
0.20-0.25	2.43	0.62±0.12	0.05±0.11	0.01±0.05	-0.18±0.06	-0.19±0.04	0.29±0.04	0.13±0.06	0.09±0.05	-0.03±0.03	0.08±0.04
	2.70	0.22±0.11	0.29±0.11	-0.02±0.06	0.01±0.06	-0.23±0.04	0.22±0.04	0.09±0.05	0.10±0.05	-0.05±0.03	0.04±0.03
	2.18	0.18±0.11	0.17±0.11	-0.03±0.05	-0.05±0.06	-0.18±0.04	0.19±0.04	-0.02±0.05	0.10±0.05	-0.08±0.03	-0.04±0.08
0.25-0.30	2.43	0.44±0.12	0.04±0.12	0.00±0.06	-0.13±0.06	-0.18±0.05	0.23±0.04	0.10±0.06	0.07±0.05	-0.02±0.03	0.07±0.04
	2.70	0.66±0.14	0.22±0.14	-0.11±0.07	-0.24±0.07	-0.29±0.05	0.34±0.05	0.11±0.07	0.08±0.07	-0.04±0.04	0.06±0.05
	2.18	0.05±0.11	0.24±0.12	-0.06±0.06	-0.01±0.06	-0.22±0.04	0.19±0.04	0.09±0.05	-0.01±0.05	0.02±0.04	0.07±0.03
0.30-0.35	2.43	0.15±0.13	0.20±0.13	-0.11±0.07	-0.06±0.06	-0.20±0.05	0.18±0.05	0.00±0.06	-0.01±0.06	0.00±0.04	0.00±0.04
	2.70	0.32±0.13	0.01±0.13	0.06±0.06	-0.04±0.07	-0.26±0.04	0.29±0.04	0.11±0.07	0.01±0.06	0.00±0.04	0.07±0.04
	2.18	0.24±0.09	-0.19±0.08	0.10±0.05	-0.05±0.05	-0.20±0.04	0.22±0.03	0.12±0.04	0.05±0.04	-0.03±0.03	0.08±0.03
0.35-0.45	2.43	0.10±0.10	0.07±0.10	-0.04±0.06	-0.03±0.06	-0.19±0.04	0.17±0.04	0.05±0.05	0.00±0.04	0.01±0.03	0.03±0.03
	2.70	0.38±0.13	0.01±0.11	-0.06±0.05	-0.18±0.07	-0.22±0.05	0.24±0.04	-0.07±0.06	-0.04±0.05	0.02±0.04	-0.05±0.04

t' range in GeV^2	P_{LAB} GeV/c	$\rho_{00}-\rho_{11}$		ρ_{1-1}		Reρ_{10}		Reρ_{0s}		Reρ_{1s}	
		G.J. FRAME	HELICITY FRAME	G.J. FRAME	HELICITY FRAME	G.J. FRAME	HELICITY FRAME	G.J. FRAME	HELICITY FRAME	G.J. FRAME	HELICITY FRAME
0.45-0.55	2.18	0.02 ± 0.12	0.00 ± 0.13	-0.01 ± 0.08	0.01 ± 0.07	-0.13 ± 0.05	0.11 ± 0.05	0.11 ± 0.05	0.03 ± 0.06	-0.02 ± 0.04	0.08 ± 0.04
	2.43	0.01 ± 0.13	0.19 ± 0.12	-0.15 ± 0.07	-0.07 ± 0.07	-0.14 ± 0.06	0.14 ± 0.06	-0.02 ± 0.06	0.01 ± 0.06	-0.01 ± 0.05	-0.01 ± 0.04
	2.70	-0.03 ± 0.12	0.04 ± 0.13	0.00 ± 0.08	0.01 ± 0.07	-0.13 ± 0.06	0.12 ± 0.06	0.06 ± 0.06	-0.02 ± 0.06	0.01 ± 0.04	0.04 ± 0.04
0.55-0.65	2.18	0.30 ± 0.14	-0.22 ± 0.13	0.00 ± 0.07	-0.16 ± 0.08	-0.18 ± 0.05	0.15 ± 0.05	0.02 ± 0.07	-0.05 ± 0.05	0.03 ± 0.04	0.01 ± 0.05
	2.43	-0.03 ± 0.13	-0.09 ± 0.15	0.05 ± 0.09	0.04 ± 0.08	-0.08 ± 0.06	0.08 ± 0.06	0.02 ± 0.07	0.04 ± 0.06	-0.02 ± 0.05	0.02 ± 0.05
	2.70	-0.37 ± 0.13	0.36 ± 0.18	-0.12 ± 0.11	0.11 ± 0.09	-0.13 ± 0.06	0.15 ± 0.07	0.06 ± 0.06	0.06 ± 0.08	-0.05 ± 0.06	0.05 ± 0.04
0.65-0.85	2.18	-0.03 ± 0.10	-0.02 ± 0.10	-0.03 ± 0.06	-0.04 ± 0.06	-0.09 ± 0.04	0.10 ± 0.05	-0.02 ± 0.05	0.05 ± 0.05	-0.04 ± 0.03	-0.01 ± 0.03
	2.43	-0.12 ± 0.12	0.00 ± 0.13	-0.01 ± 0.08	0.00 ± 0.08	-0.12 ± 0.05	0.13 ± 0.05	-0.03 ± 0.05	0.06 ± 0.06	-0.04 ± 0.04	-0.01 ± 0.04
	2.70	-0.29 ± 0.12	0.04 ± 0.14	0.00 ± 0.09	0.11 ± 0.08	-0.17 ± 0.06	0.20 ± 0.06	0.09 ± 0.05	0.04 ± 0.06	-0.04 ± 0.05	0.07 ± 0.04
0.85-1.05	2.18	0.00 ± 0.15	-0.18 ± 0.13	0.13 ± 0.08	0.04 ± 0.09	-0.03 ± 0.05	0.01 ± 0.05	0.08 ± 0.06	0.10 ± 0.06	-0.09 ± 0.04	0.08 ± 0.04
	2.43	-0.16 ± 0.13	-0.02 ± 0.13	-0.03 ± 0.09	0.02 ± 0.08	-0.10 ± 0.05	0.11 ± 0.06	0.11 ± 0.06	0.01 ± 0.06	-0.03 ± 0.05	0.07 ± 0.04
	2.70	0.05 ± 0.17	-0.29 ± 0.16	0.11 ± 0.09	-0.03 ± 0.10	-0.09 ± 0.06	0.04 ± 0.06	0.09 ± 0.07	-0.05 ± 0.06	0.02 ± 0.05	0.06 ± 0.06
1.05-1.45	2.18	0.01 ± 0.11	-0.14 ± 0.11	0.10 ± 0.06	0.07 ± 0.06	-0.01 ± 0.04	-0.04 ± 0.04	0.07 ± 0.05	-0.04 ± 0.05	0.01 ± 0.03	0.03 ± 0.03
	2.43	-0.22 ± 0.11	-0.13 ± 0.12	-0.02 ± 0.08	0.03 ± 0.08	-0.11 ± 0.05	0.15 ± 0.05	0.02 ± 0.05	-0.01 ± 0.05	0.00 ± 0.04	0.02 ± 0.04
	2.70	0.07 ± 0.16	0.03 ± 0.16	-0.03 ± 0.09	-0.02 ± 0.09	-0.01 ± 0.07	-0.01 ± 0.06	-0.01 ± 0.07	0.12 ± 0.07	-0.09 ± 0.05	0.03 ± 0.05
1.45-1.85	2.18	-0.09 ± 0.11	-0.18 ± 0.10	0.10 ± 0.07	0.07 ± 0.07	-0.04 ± 0.04	-0.01 ± 0.04	0.13 ± 0.05	0.01 ± 0.05	-0.10 ± 0.03	0.13 ± 0.03
	2.43	-0.20 ± 0.11	-0.25 ± 0.11	0.14 ± 0.08	0.11 ± 0.08	-0.05 ± 0.04	0.03 ± 0.04	0.10 ± 0.05	-0.02 ± 0.05	-0.04 ± 0.04	0.08 ± 0.04
	2.70	-0.31 ± 0.15	-0.25 ± 0.15	0.02 ± 0.11	0.04 ± 0.10	-0.13 ± 0.06	0.15 ± 0.06	0.16 ± 0.05	0.05 ± 0.07	-0.12 ± 0.05	0.16 ± 0.05
1.85-2.25	2.18	0.02 ± 0.20	-0.04 ± 0.16	0.09 ± 0.09	0.11 ± 0.06	0.02 ± 0.06	-0.02 ± 0.08	0.12 ± 0.08	-0.12 ± 0.08	0.00 ± 0.05	0.03 ± 0.06
	2.43	-0.20 ± 0.13	-0.29 ± 0.12	0.14 ± 0.08	0.11 ± 0.08	-0.06 ± 0.05	0.01 ± 0.05	0.09 ± 0.05	-0.04 ± 0.05	-0.03 ± 0.04	0.06 ± 0.04
	2.70	-0.15 ± 0.14	-0.60 ± 0.08	0.10 ± 0.09	-0.05 ± 0.10	-0.23 ± 0.04	0.02 ± 0.06	0.03 ± 0.06	-0.01 ± 0.05	-0.01 ± 0.04	0.02 ± 0.05
2.25-2.75	2.18	-	-	-	-	-	-	-	-	-	-
	2.43	0.01 ± 0.19	-0.30 ± 0.16	-0.01 ± 0.11	-0.11 ± 0.13	-0.15 ± 0.09	-0.05 ± 0.09	0.29 ± 0.08	-0.13 ± 0.08	-0.11 ± 0.06	0.19 ± 0.06
	2.70	-0.25 ± 0.14	-0.36 ± 0.13	0.05 ± 0.10	0.02 ± 0.09	-0.08 ± 0.05	0.06 ± 0.06	0.11 ± 0.06	-0.08 ± 0.07	-0.01 ± 0.05	0.04 ± 0.05
all events	2.18	0.27 ± 0.02	0.28 ± 0.02	-0.01 ± 0.01	-0.01 ± 0.01	-0.14 ± 0.01	0.11 ± 0.01	0.09 ± 0.01	0.08 ± 0.01	-0.04 ± 0.01	0.02 ± 0.01
	2.43	0.30 ± 0.02	0.32 ± 0.02	-0.01 ± 0.01	0.00 ± 0.01	-0.17 ± 0.01	0.13 ± 0.01	0.09 ± 0.01	0.08 ± 0.01	-0.03 ± 0.01	0.03 ± 0.01
	2.70	0.28 ± 0.02	0.29 ± 0.02	-0.02 ± 0.01	-0.01 ± 0.01	-0.16 ± 0.01	0.13 ± 0.01	0.12 ± 0.01	0.11 ± 0.01	-0.03 ± 0.01	0.04 ± 0.01

TABLE 4.7

Density matrix for the process $K^+ n \to K^{*o}(890)p$, $\hookrightarrow K^{o}\pi^{o}$

t' range in GeV^2	P_{LAB} GeV/c	$\rho_{oo}-\rho_{11}$ G.J. FRAME	$\rho_{oo}-\rho_{11}$ HELICITY FRAME	ρ_{1-1} G.J. FRAME	ρ_{1-1} HELICITY FRAME	Re ρ_{1o} G.J. FRAME	Re ρ_{1o} HELICITY FRAME	Re ρ_{os} G.J. FRAME	Re ρ_{os} HELICITY FRAME	Re ρ_{1s} G.J. FRAME	Re ρ_{1s} HELICITY FRAME
	2.18	0.59±0.12	0.63±0.13	0.05±0.06	0.02±0.06	-0.09±0.05	0.09±0.05	-0.08±0.06	-0.07±0.06	-0.01±0.03	-0.04±0.03
0.0-0.05	2.43	0.51±0.13	0.49±0.11	-0.03±0.06	-0.03±0.05	-0.08±0.05	0.03±0.06	0.14±0.06	0.12±0.06	0.01±0.03	0.03±0.03
	2.70	0.52±0.13	0.61±0.12	-0.02±0.06	0.00±0.06	-0.16±0.06	-0.01±0.06	-0.11±0.07	-0.10±0.07	0.02±0.04	-0.01±0.04
	2.18	0.23±0.14	0.33±0.14	0.00±0.07	0.05±0.07	-0.14±0.06	0.06±0.06	0.01±0.07	-0.02±0.07	0.01±0.04	0.02±0.04
0.05-0.10	2.43	0.21±0.15	0.45±0.16	-0.07±0.07	0.00±0.07	-0.18±0.06	0.05±0.06	-0.05±0.07	-0.04±0.07	0.00±0.04	-0.03±0.04
	2.70	0.46±0.16	0.42±0.16	-0.07±0.07	-0.03±0.07	-0.12±0.06	0.09±0.06	-0.03±0.08	0.05±0.08	-0.07±0.04	-0.08±0.04
	2.18	0.08±0.13	0.54±0.13	-0.19±0.06	-0.05±0.06	-0.19±0.05	0.06±0.05	0.11±0.06	0.18±0.06	-0.10±0.04	0.01±0.04
0.10-0.20	2.43	0.14±0.13	0.37±0.15	-0.04±0.08	0.01±0.07	-0.15±0.06	0.09±0.05	0.07±0.06	0.14±0.07	-0.07±0.04	0.00±0.04
	2.70	0.57±0.13	0.17±0.14	0.09±0.06	-0.03±0.07	-0.15±0.05	0.26±0.05	-0.07±0.07	-0.12±0.06	0.07±0.03	-0.01±0.04
	2.18	0.43±0.16	0.14±0.15	-0.04±0.07	-0.07±0.08	-0.22±0.05	0.24±0.05	-0.04±0.07	-0.11±0.07	0.05±0.04	-0.04±0.05
0.20-0.30	2.43	0.14±0.16	-0.07±0.14	0.05±0.08	-0.02±0.09	-0.10±0.06	0.10±0.06	0.00±0.07	0.00±0.07	0.00±0.05	0.01±0.05
	2.70	0.48±0.22	0.05±0.19	-0.04±0.09	-0.16±0.10	-0.17±0.07	0.23±0.07	0.07±0.10	0.02±0.09	-0.02±0.06	0.05±0.07
	2.18	0.14±0.15	0.28±0.17	-0.16±0.08	-0.11±0.08	-0.25±0.08	0.28±0.07	0.08±0.08	0.05±0.09	-0.03±0.06	0.04±0.06
0.30-0.40	2.43	0.11±0.18	0.17±0.17	-0.08±0.10	-0.07±0.10	-0.16±0.09	0.15±0.09	0.04±0.09	0.02±0.09	0.03±0.06	0.04±0.06
	2.70	0.01±0.22	0.46±0.22	-0.11±0.11	-0.02±0.10	-0.27±0.09	0.25±0.09	-0.02±0.10	0.11±0.11	-0.07±0.07	-0.01±0.06
	2.18	-0.27±0.21	-0.02±0.21	0.11±0.16	0.21±0.18	-0.15±0.14	0.14±0.13	0.01±0.12	0.12±0.13	-0.10±0.09	0.00±0.08
0.40-0.50	2.43	0.22±0.23	0.36±0.23	-0.32±0.12	-0.22±0.11	-0.02±0.11	0.03±0.12	0.08±0.11	0.09±0.11	-0.05±0.08	0.06±0.07
	2.70	0.32±0.40	-0.13±0.23	-0.05±0.14	-0.16±0.22	0.06±0.14	-0.08±0.14	-0.19±0.15	0.28±0.11	-0.20±0.08	-0.16±0.11
	2.18	-0.54±0.12	0.02±0.02	0.18±0.14	0.31±0.09	-0.11±0.08	0.11±0.08	0.00±0.08	-0.04±0.10	0.01±0.07	0.04±0.06
0.50-0.70	2.43	0.14±0.30	-0.04±0.30	-0.07±0.13	-0.17±0.13	-0.07±0.08	0.09±0.08	0.11±0.12	0.06±0.12	-0.04±0.09	0.09±0.09
	2.70	0.23±0.27	-0.11±0.23	-0.12±0.12	-0.16±0.15	-0.12±0.11	0.12±0.11	0.05±0.12	0.11±0.11	-0.09±0.08	-0.04±0.09
	2.18	-0.08±0.19	-0.03±0.19	0.04±0.12	-0.05±0.10	-0.08±0.08	0.10±0.09	0.12±0.08	0.14±0.08	-0.12±0.06	0.13±0.07
0.70-1.00	2.43	-0.57±0.20	0.33±0.31	-0.12±0.17	0.19±0.15	0.01±0.11	0.09±0.10	-0.13±0.09	-0.05±0.14	0.07±0.10	-0.10±0.07
	2.70	-0.10±0.21	0.39±0.23	-0.27±0.14	0.01±0.12	-0.14±0.09	0.22±0.09	0.10±0.09	-0.13±0.12	0.06±0.09	0.03±0.07
	2.18	-0.25±0.17	-0.23±0.18	0.06±0.11	0.06±0.11	-0.17±0.06	0.16±0.06	-0.11±0.07	-0.11±0.07	0.09±0.05	-0.08±0.06
1.00-1.50	2.43	-0.23±0.18	-0.02±0.23	0.02±0.15	0.13±0.11	-0.02±0.09	0.06±0.08	0.00±0.09	0.00±0.10	0.00±0.07	-0.01±0.07
	2.70	-0.35±0.30	-0.02±0.30	0.21±0.16	0.30±0.16	0.07±0.12	-0.01±0.11	-0.14±0.11	-0.02±0.14	0.06±0.09	-0.10±0.07
	2.18	-0.19±0.19	-0.19±0.19	0.10±0.14	0.10±0.14	-0.06±0.07	0.02±0.04	0.10±0.08	-0.08±0.08	0.00±0.06	0.05±0.06
1.50-2.00	2.43	-0.02±0.23	-0.07±0.24	0.23±0.13	0.19±0.13	-0.04±0.03	-0.02±0.07	0.12±0.09	-0.04±0.10	-0.04±0.06	0.11±0.06
	2.70	-0.16±0.37	-0.39±0.22	0.22±0.21	0.17±0.22	-0.09±0.09	0.01±0.15	0.26±0.12	-0.15±0.13	-0.01±0.11	0.14±0.10
	2.18	–	–	–	–	–	–	–	–	–	–
2.00-3.00	2.43	-0.27±0.24	-0.36±0.22	0.21±0.14	0.16±0.16	-0.08±0.08	0.02±0.07	0.24±0.08	-0.26±0.07	0.08±0.07	0.01±0.08
	2.70	-0.24±0.19	-0.01±0.30	0.06±0.17	0.12±0.14	0.01±0.11	0.12±0.07	0.25±0.08	-0.14±0.10	-0.06±0.08	0.12±0.07
	2.18	0.15±0.05	0.26±0.05	-0.02±0.03	0.01±0.03	-0.15±0.02	0.12±0.02	0.02±0.02	0.00±0.02	-0.02±0.02	0.01±0.02
All events	2.43	0.16±0.06	0.28±0.06	-0.02±0.03	0.00±0.03	-0.10±0.02	0.06±0.02	0.06±0.03	0.03±0.03	-0.01±0.02	0.02±0.02
	2.70	0.32±0.06	0.28±0.06	-0.01±0.03	-0.01±0.03	-0.13±0.02	0.13±0.02	-0.02±0.03	-0.04±0.03	-0.01±0.02	-0.01±0.02

TABLE 4.8 DENSITY MATRIX FOR THE PROCESS $K^+n \rightarrow K^{*+}(890)\,n$, $K^{*+} \rightarrow K^0\pi^+$

t' range in GeV^2	P_{LAB} GeV/c	$\rho_{00}-\rho_{11}$ G.J. FRAME	$\rho_{00}-\rho_{11}$ HELICITY FRAME	ρ_{1-1} G.J. FRAME	ρ_{1-1} HELICITY FRAME	$-\mathrm{Re}\,\rho_{10}$ G.J. FRAME	$-\mathrm{Re}\,\rho_{10}$ HELICITY FRAME	$\mathrm{Re}\,\rho_{0s}$ G.J. FRAME	$\mathrm{Re}\,\rho_{0s}$ HELICITY FRAME	$\mathrm{Re}\,\rho_{1s}$ G.J. FRAME	$\mathrm{Re}\,\rho_{1s}$ HELICITY FRAME
	2.18	0.46±0.13	0.44±0.15	-0.07±0.06	0.02±0.07	-0.17±0.06	0.00±0.05	0.12±0.07	0.18±0.07	-0.10±0.04	-0.06±0.04
0.00-0.05	2.43	0.45±0.15	0.35±0.14	0.01±0.05	-0.08±0.06	-0.02±0.05	0.12±0.06	0.18±0.07	0.16±0.07	-0.02±0.04	0.03±0.04
	2.70	0.30±0.14	0.29±0.14	-0.11±0.06	-0.04±0.07	-0.12±0.05	-0.04±0.05	0.11±0.06	0.14±0.06	-0.09±0.04	-0.05±0.04
	2.18	0.07±0.15	0.31±0.18	-0.03±0.08	0.02±0.08	-0.11±0.07	0.01±0.06	0.10±0.07	0.13±0.08	-0.03±0.05	0.03±0.04
0.05-0.10	2.43	0.35±0.16	0.30±0.17	0.06±0.08	0.04±0.08	-0.11±0.06	0.11±0.06	0.07±0.08	0.12±0.08	-0.08±0.04	-0.03±0.05
	2.70	-0.06±0.15	0.21±0.17	0.09±0.09	0.13±0.09	-0.12±0.06	0.01±0.06	0.10±0.07	0.14±0.07	-0.06±0.05	0.01±0.04
	2.18	-0.11±0.10	-0.04±0.11	0.16±0.06	0.18±0.06	0.18±0.06	-0.06±0.04	0.01±0.05	-0.04±0.05	0.03±0.03	-0.01±0.03
0.10-0.20	2.43	-0.39±0.10	0.12±0.13	0.13±0.08	0.30±0.06	-0.13±0.05	-0.03±0.05	0.05±0.05	0.08±0.06	-0.06±0.04	0.01±0.03
	2.70	-0.24±0.11	0.09±0.12	0.07±0.07	0.17±0.07	-0.10±0.05	0.00±0.05	0.05±0.05	0.08±0.06	-0.04±0.04	0.01±0.03
	2.18	-0.11±0.12	-0.27±0.11	0.22±0.07	0.14±0.07	0.00±0.04	0.06±0.04	0.06±0.05	0.12±0.05	-0.07±0.03	-0.01±0.04
0.20-0.30	2.43	-0.32±0.12	-0.02±0.12	0.23±0.07	0.33±0.06	-0.11±0.04	0.06±0.04	-0.01±0.05	-0.03±0.06	0.02±0.04	0.01±0.03
	2.70	-0.18±0.13	-0.39±0.13	0.36±0.08	0.30±0.08	-0.06±0.04	0.06±0.05	0.02±0.06	0.03±0.06	-0.01±0.04	0.02±0.04
	2.18	-0.49±0.10	0.01±0.14	0.19±0.09	0.40±0.07	-0.15±0.05	0.10±0.04	0.00±0.05	0.09±0.06	-0.05±0.04	0.00±0.03
0.30-0.40	2.43	0.20±0.22	-0.35±0.19	0.26±0.11	0.03±0.12	-0.06±0.06	0.13±0.06	0.09±0.10	0.17±0.07	-0.13±0.04	0.04±0.07
	2.70	-0.20±0.18	-0.22±0.17	0.33±0.10	0.25±0.11	-0.14±0.05	0.17±0.05	-0.13±0.07	0.07±0.07	-0.06±0.05	-0.09±0.05
	2.18	-0.24±0.15	-0.10±0.17	0.19±0.10	0.28±0.09	-0.10±0.07	0.05±0.07	0.08±0.07	0.03±0.08	0.00±0.06	0.04±0.05
0.40-0.50	2.43	-0.21±0.16	-0.40±0.12	0.34±0.08	0.26±0.11	-0.04±0.06	0.06±0.06	-0.03±0.07	-0.04±0.07	0.03±0.05	-0.02±0.05
	2.70	-0.08±0.17	-0.32±0.16	0.24±0.10	0.15±0.11	-0.08±0.06	0.08±0.06	0.04±0.08	0.05±0.07	-0.04±0.05	0.02±0.06
	2.18	-0.38±0.11	-0.54±0.12	0.43±0.08	0.33±0.09	-0.08±0.05	0.10±0.05	0.01±0.06	0.05±0.05	-0.04±0.04	0.02±0.04
0.50-0.70	2.43	-0.59±0.15	-0.44±0.16	0.39±0.11	0.35±0.12	0.00±0.04	0.05±0.05	0.00±0.06	0.06±0.06	0.00±0.05	0.04±0.05
	2.70	-0.53±0.14	-0.28±0.15	0.36±0.10	0.47±0.09	-0.06±0.06	0.07±0.06	-0.06±0.06	-0.02±0.08	0.01±0.05	-0.05±0.04
	2.18	-0.30±0.11	-0.10±0.15	0.12±0.11	0.21±0.09	-0.07±0.08	0.10±0.08	0.02±0.07	-0.07±0.08	0.06±0.06	-0.01±0.05
0.70-1.00	2.43	-0.25±0.15	-0.16±0.19	0.16±0.13	0.24±0.09	-0.09±0.08	0.08±0.07	-0.03±0.08	0.08±0.09	-0.03±0.06	0.02±0.06
	2.70	-0.51±0.20	-0.21±0.26	0.25±0.17	0.36±0.15	-0.03±0.09	0.05±0.08	-0.12±0.08	0.01±0.11	0.03±0.08	-0.07±0.07
	2.18	0.05±0.17	-0.38±0.16	0.17±0.11	-0.02±0.13	-0.10±0.08	0.02±0.07	0.10±0.08	-0.03±0.07	-0.02±0.05	0.06±0.06
1.00-1.50	2.43	-0.65±0.17	-0.37±0.28	0.18±0.21	0.20±0.22	-0.21±0.10	0.29±0.08	0.02±0.10	0.23±0.10	-0.17±0.09	0.10±0.09
	2.70	-0.65±0.25	0.59±0.49	-0.12±0.30	0.17±0.20	0.15±0.09	0.18±0.10	0.05±0.11	-0.19±0.19	0.10±0.14	-0.05±0.09
	2.18	-0.02±0.23	0.02±0.24	-0.11±0.15	0.00±0.14	0.02±0.10	0.03±0.10	0.14±0.10	-0.12±0.10	0.01±0.08	0.04±0.07
1.50-2.00	2.43	-0.25±0.27	-0.38±0.24	-0.01±0.18	-0.11±0.17	-0.15±0.10	0.16±0.12	-0.21±0.11	-0.08±0.11	0.14±0.09	-0.25±0.08
	2.70	-0.07±0.10	-0.07±0.33	0.29±0.23	0.32±0.18	0.04±0.10	-0.14±0.14	0.24±0.13	-0.13±0.16	0.04±0.09	0.09±0.07
	2.18	-0.01±0.30	-0.09±0.33	0.28±0.25	0.32±0.18	0.03±0.13	-0.04±0.12	0.11±0.15	-0.12±0.15	0.15±0.08	-0.07±0.09
2.00-3.00	2.43	0.01±0.32	-0.25±0.30	0.05±0.20	-0.08±0.21	-0.08±0.14	-0.08±0.11	0.23±0.12	-0.13±0.12	0.00±0.09	0.09±0.10
	2.70	0.06±0.11	-0.30±0.18	0.16±0.13	0.27±0.11	0.08±0.07	0.11±0.08	0.15±0.08	-0.11±0.10	-0.02±0.07	0.10±0.05
	2.18	-0.10±0.04	-0.06±0.05	0.14±0.03	0.17±0.03	-0.08±0.02	0.05±0.02	0.05±0.02	0.05±0.02	-0.03±0.01	0.01±0.01
all	2.43	-0.11±0.05	-0.03±0.05	0.16±0.03	0.17±0.03	-0.08±0.02	0.07±0.02	0.05±0.02	0.06±0.02	-0.03±0.02	0.00±0.02
events	2.70	-0.14±0.05	-0.01±0.05	0.15±0.03	0.19±0.03	-0.07±0.02	0.04±0.02	0.05±0.02	0.05±0.02	-0.03±0.02	-0.01±0.01

TABLE 4.9 DENSITY MATRIX ELEMENTS FOR THE PROCESS $K^+p \rightarrow K^*(890)\,p$, $K^* \rightarrow K^0\pi^+$

t' range in GeV^2	P_{LAB} GeV/c	$\rho_{00}-\rho_{11}$ G.J. FRAME	$\rho_{00}-\rho_{11}$ HELICITY FRAME	ρ_{1-1} G.J. FRAME	ρ_{1-1} HELICITY FRAME	Reρ_{10} G.J. FRAME	Reρ_{10} HELICITY FRAME	Reρ_{0s} G.J. FRAME	Reρ_{0s} HELICITY FRAME	Reρ_{1s} G.J. FRAME	Reρ_{1s} HELICITY FRAME
	2.18	0.39±0.11	0.49±0.11	0.08±0.05	0.09±0.05	-0.08±0.04	0.04±0.05	0.09±0.05	0.09±0.06	0.00±0.03	0.03±0.03
0.00-0.05	2.43	0.17±0.12	0.36±0.13	0.04±0.07	0.10±0.06	-0.13±0.05	-0.02±0.05	0.07±0.06	0.12±0.06	-0.07±0.04	-0.05±0.03
	2.70	0.31±0.11	0.27±0.10	-0.01±0.05	0.01±0.05	-0.04±0.05	0.06±0.05	0.13±0.05	0.10±0.05	0.04±0.03	0.07±0.03
	2.18	0.29±0.11	0.26±0.11	0.16±0.05	0.14±0.05	-0.13±0.04	0.18±0.04	0.06±0.05	0.08±0.05	-0.02±0.03	0.01±0.03
0.05-0.10	2.43	-0.06±0.13	0.12±0.12	0.20±0.07	0.29±0.07	-0.15±0.04	0.02±0.05	0.12±0.05	0.09±0.06	-0.02±0.04	0.05±0.03
	2.70	0.03±0.12	0.09±0.11	0.15±0.06	0.24±0.06	-0.11±0.04	0.04±0.04	-0.01±0.05	0.05±0.05	-0.05±0.03	-0.05±0.03
	2.18	-0.08±0.09	-0.14±0.08	0.30±0.05	0.30±0.05	-0.09±0.03	0.10±0.03	0.10±0.04	0.13±0.04	-0.06±0.02	0.03±0.02
0.10-0.20	2.43	-0.12±0.09	0.07±0.08	0.24±0.04	0.33±0.04	-0.16±0.03	0.09±0.03	0.17±0.04	0.24±0.04	-0.13±0.02	0.04±0.02
	2.70	-0.14±0.09	0.07±0.09	0.20±0.05	0.22±0.05	-0.09±0.03	0.09±0.03	0.05±0.04	0.04±0.04	-0.03±0.03	0.00±0.02
	2.18	-0.04±0.10	0.00±0.08	0.10±0.05	0.10±0.05	-0.10±0.04	0.10±0.04	0.01±0.04	0.19±0.04	-0.14±0.03	-0.03±0.03
0.20-0.30	2.43	-0.36±0.09	0.22±0.11	0.13±0.07	0.30±0.05	-0.20±0.03	0.11±0.04	0.10±0.04	0.14±0.05	-0.08±0.03	0.02±0.03
	2.70	-0.32±0.10	-0.22±0.09	0.33±0.06	0.33±0.06	-0.09±0.04	0.06±0.04	-0.04±0.04	0.00±0.04	-0.01±0.03	-0.02±0.03
	2.18	-0.45±0.09	-0.17±0.10	0.34±0.06	0.41±0.06	-0.09±0.04	0.07±0.03	0.00±0.04	0.17±0.04	-0.11±0.03	-0.01±0.03
0.30-0.40	2.43	-0.35±0.11	0.03±0.11	0.17±0.06	0.26±0.06	-0.10±0.04	0.09±0.05	0.07±0.05	0.10±0.06	-0.06±0.04	0.05±0.03
	2.70	-0.36±0.09	-0.05±0.11	0.23±0.07	0.26±0.07	-0.07±0.05	0.08±0.05	0.09±0.05	0.05±0.06	-0.04±0.04	0.05±0.03
	2.18	-0.51±0.11	-0.20±0.11	0.28±0.07	0.35±0.07	-0.05±0.04	0.07±0.04	0.01±0.05	0.14±0.05	-0.10±0.04	0.00±0.03
0.40-0.50	2.43	-0.38±0.14	-0.15±0.15	0.23±0.09	0.29±0.08	0.00±0.05	0.00±0.05	-0.05±0.06	0.06±0.07	-0.06±0.05	-0.05±0.04
	2.70	-0.20±0.12	-0.23±0.11	0.22±0.07	0.21±0.07	0.03±0.05	-0.03±0.04	0.03±0.05	0.14±0.05	-0.10±0.04	0.02±0.04
	2.18	-0.30±0.10	-0.04±0.11	0.14±0.06	0.21±0.06	-0.05±0.04	0.06±0.04	0.05±0.04	0.09±0.04	-0.06±0.03	0.04±0.03
0.50-0.70	2.43	-0.36±0.11	-0.15±0.11	0.21±0.07	0.29±0.07	-0.01±0.04	-0.01±0.04	0.10±0.05	0.14±0.05	-0.11±0.04	0.08±0.03
	2.70	-0.43±0.12	-0.09±0.14	0.22±0.08	0.34±0.08	-0.03±0.05	0.02±0.05	-0.04±0.05	0.14±0.06	-0.09±0.04	-0.04±0.04
	2.18	-0.32±0.12	-0.14±0.11	0.16±0.08	0.23±0.08	0.03±0.05	0.02±0.05	-0.10±0.05	0.19±0.05	-0.13±0.04	0.04±0.04
0.70-1.00	2.43	-0.32±0.13	-0.18±0.13	0.18±0.09	0.20±0.09	-0.08±0.06	0.08±0.06	-0.03±0.06	0.23±0.06	-0.14±0.04	0.02±0.05
	2.70	-0.23±0.14	-0.24±0.13	0.21±0.08	0.20±0.09	-0.04±0.05	0.03±0.05	-0.11±0.06	0.07±0.06	-0.02±0.04	-0.07±0.04
	2.18	-0.15±0.14	-0.16±0.12	0.18±0.08	0.17±0.09	0.05±0.05	-0.03±0.06	-0.14±0.06	0.23±0.06	-0.12±0.04	0.00±0.05
1.00-1.50	2.43	-0.34±0.14	-0.38±0.14	0.15±0.11	0.13±0.11	-0.16±0.07	0.12±0.06	-0.04±0.07	0.11±0.06	-0.07±0.05	-0.01±0.06
	2.70	0.00±0.15	-0.07±0.14	0.19±0.08	0.19±0.09	0.12±0.06	-0.13±0.06	-0.12±0.07	0.13±0.07	-0.07±0.05	-0.04±0.05
	2.18	-0.17±0.15	-0.01±0.16	-0.02±0.10	0.01±0.10	-0.02±0.06	0.01±0.06	0.01±0.07	0.09±0.07	-0.09±0.05	0.07±0.05
1.50-2.00	2.43	-0.01±0.26	-0.05±0.20	0.00±0.15	-0.05±0.13	-0.10±0.09	-0.03±0.11	-0.06±0.11	0.17±0.10	-0.08±0.08	0.06±0.08
	2.70	-0.05±0.21	-0.11±0.24	0.34±0.11	0.25±0.13	0.09±0.09	-0.11±0.07	0.00±0.10	0.08±0.10	-0.06±0.06	0.04±0.06
	2.18	-0.73±0.20	0.02±0.34	-0.11±0.23	0.15±0.13	0.22±0.10	0.36±0.09	-0.09±0.09	0.27±0.12	-0.18±0.11	0.11±0.09
2.00-3.00	2.43	0.14±0.19	0.04±0.19	0.15±0.10	0.11±0.11	0.02±0.07	-0.10±0.07	-0.07±0.09	0.09±0.09	-0.04±0.05	0.00±0.06
	2.70	-0.29±0.18	-0.05±0.19	-0.02±0.11	0.05±0.11	0.02±0.07	0.06±0.08	-0.08±0.08	0.18±0.08	-0.16±0.06	0.09±0.06
	2.18	-0.11±0.04	0.01±0.03	0.18±0.02	0.21±0.02	-0.06±0.01	0.08±0.01	0.02±0.02	0.14±0.02	-0.08±0.01	0.01±0.01
all	2.43	-0.19±0.04	0.04±0.04	0.17±0.02	0.24±0.02	-0.11±0.01	0.05±0.01	0.07±0.02	0.15±0.02	-0.08±0.01	0.02±0.01
events	2.70	-0.13±0.04	-0.02±0.04	0.18±0.02	0.21±0.02	-0.04±0.01	0.04±0.01	0.01±0.02	0.07±0.02	-0.04±0.01	0.00±0.01

TABLE 4.10

t' range in GeV^2	$d\sigma/dt$ for the process $K^+p \to K^o \Delta^{++}$ mb/GeV^2 at 2.18 GeV/c	at 2.43 GeV/c	at 2.70 GeV/c
0.0-0.05	1.73 ± 0.21	1.48 ± 0.18	1.67 ± 0.18
0.05-0.10	2.72 ± 0.29	1.80 ± 0.20	1.93 ± 0.20
0.10-0.15	2.58 ± 0.27	1.93 ± 0.21	1.89 ± 0.20
0.15-0.20	2.08 ± 0.22	2.02 ± 0.21	1.42 ± 0.17
0.20-0.25	2.20 ± 0.24	1.57 ± 0.19	1.44 ± 0.17
0.25-0.30	1.81 ± 0.22	1.55 ± 0.19	1.26 ± 0.16
0.30-0.35	1.71 ± 0.21	1.05 ± 0.15	1.14 ± 0.15
0.35-0.40	1.54 ± 0.19	1.01 ± 0.15	0.87 ± 0.13
0.40-0.45	1.46 ± 0.19	0.97 ± 0.15	0.63 ± 0.11
0.45-0.50	1.14 ± 0.17	0.97 ± 0.15	0.69 ± 0.12
0.50-0.60	0.78 ± 0.10	0.70 ± 0.08	0.52 ± 0.07
0.60-0.70	0.56 ± 0.08	0.46 ± 0.07	0.47 ± 0.07
0.70-0.80	0.53 ± 0.08	0.30 ± 0.06	0.33 ± 0.06
0.80-0.90	0.28 ± 0.06	0.13 ± 0.04	0.17 ± 0.04
0.90-1.00	0.28 ± 0.06	0.17 ± 0.04	0.15 ± 0.04
1.00-1.20	0.19 ± 0.03	0.13 ± 0.03	0.09 ± 0.02
1.20-1.40	0.17 ± 0.03	0.07 ± 0.02	0.12 ± 0.02
1.40-1.60	0.17 ± 0.03	0.04 ± 0.01	0.08 ± 0.02
1.60-1.80	0.06 ± 0.02	0.07 ± 0.02	0.06 ± 0.02
1.80-2.00	0.09 ± 0.02	0.05 ± 0.02	0.06 ± 0.02

TABLE 4.11 DENSITY MATRIX ELEMENTS FOR THE PROCESS $K^+p\to K^0\Delta^{++}$

t' range GeV^2	P_{LAB} GeV/c	ρ_{33} G.J. FRAME	ρ_{33} HELICITY FRAME	ρ_{3-1} G.J. FRAME	ρ_{3-1} HELICITY FRAME	ρ_{31} G.J. FRAME	ρ_{31} HELICITY FRAME
0.00-0.05	2.18	0.26±0.07	0.32±0.07	0.14±0.07	0.10±0.08	0.06±0.03	0.01±0.03
	2.43	0.32±0.07	0.40±0.05	0.12±0.07	0.12±0.07	0.04±0.03	-0.01±0.03
	2.70	0.23±0.06	0.28±0.05	0.09±0.06	0.16±0.06	0.05±0.03	0.04±0.03
0.05-0.10	2.18	0.18±0.05	0.46±0.05	0.20±0.05	0.07±0.06	0.06±0.02	0.05±0.02
	2.43	0.28±0.06	0.43±0.05	0.26±0.05	0.17±0.06	0.02±0.03	0.02±0.02
	2.70	0.26±0.06	0.35±0.05	0.14±0.06	0.13±0.06	-0.01±0.02	0.02±0.03
0.10-0.20	2.18	0.20±0.04	0.44±0.03	0.22±0.04	0.09±0.04	0.03±0.02	0.03±0.02
	2.43	0.27±0.04	0.44±0.03	0.20±0.04	0.12±0.05	0.05±0.02	-0.01±0.02
	2.70	0.22±0.04	0.40±0.03	0.18±0.04	0.11±0.04	0.00±0.02	0.04±0.02
0.20-0.30	2.18	0.29±0.04	0.40±0.04	0.19±0.09	0.15±0.05	0.03±0.02	-0.02±0.02
	2.43	0.32±0.04	0.43±0.04	0.26±0.04	0.20±0.05	-0.07±0.02	0.09±0.02
	2.70	0.28±0.04	0.40±0.04	0.18±0.05	0.13±0.05	0.02±0.02	-0.03±0.02
0.30-0.40	2.18	0.42±0.04	0.36±0.05	0.24±0.05	0.26±0.05	0.02±0.02	-0.01±0.02
	2.43	0.32±0.05	0.31±0.05	0.08±0.06	0.12±0.06	-0.02±0.03	0.01±0.03
	2.70	0.30±0.06	0.36±0.05	0.17±0.05	0.14±0.06	0.00±0.02	0.00±0.03
0.40-0.50	2.18	0.33±0.05	0.49±0.05	0.25±0.05	0.16±0.06	-0.01±0.02	-0.02±0.02
	2.43	0.28±0.06	0.37±0.05	0.17±0.06	0.13±0.06	0.01±0.03	0.00±0.03
	2.70	0.23±0.07	0.49±0.05	0.28±0.06	0.17±0.07	-0.08±0.03	0.03±0.03
0.50-0.70	2.18	0.36±0.05	0.37±0.05	0.23±0.05	0.23±0.05	0.02±0.02	-0.03±0.02
	2.43	0.35±0.05	0.41±0.05	0.20±0.05	0.16±0.06	-0.02±0.02	0.01±0.02
	2.70	0.32±0.05	0.43±0.05	0.18±0.05	0.11±0.06	-0.04±0.03	0.03±0.02
0.70-1.00	2.18	0.32±0.06	0.38±0.06	0.24±0.06	0.18±0.06	0.01±0.03	-0.03±0.02
	2.43	0.46±0.06	0.55±0.06	0.38±0.07	0.36±0.08	-0.02±0.03	-0.04±0.02
	2.70	0.43±0.05	0.41±0.06	0.13±0.08	0.14±0.07	-0.03±0.03	0.07±0.03
1.00-1.50	2.18	0.44±0.05	0.48±0.05	0.30±0.06	0.24±0.06	-0.03±0.02	-0.01±0.03
	2.43	0.46±0.08	0.43±0.07	0.31±0.08	0.34±0.08	0.00±0.03	-0.01±0.03
	2.70	0.51±0.06	0.39±0.07	0.22±0.08	0.30±0.07	0.05±0.03	0.04±0.03
1.50-2.00	2.18	0.22±0.10	0.30±0.09	0.23±0.08	0.17±0.10	-0.01±0.04	-0.05±0.05
	2.43	0.26±0.11	0.17±0.10	0.14±0.11	0.16±0.10	0.03±0.05	0.01±0.05
	2.70	0.41±0.10	0.36±0.09	0.22±0.11	0.20±0.10	-0.01±0.04	0.04±0.05
2.00-3.00	2.18	0.24±0.09	0.24±0.10	0.35±0.09	0.35±0.08	0.06±0.04	0.02±0.05
	2.43	0.36±0.08	0.30±0.08	0.14±0.10	0.18±0.09	0.08±0.04	0.06±0.04
	2.70	0.21±0.07	0.19±0.07	0.13±0.07	0.15±0.06	0.07±0.04	0.03±0.04
All events	2.18	0.30±0.02	0.41±0.02	0.23±0.02	0.16±0.02	0.02±0.01	0.00±0.01
	2.43	0.32±0.02	0.40±0.02	0.20±0.02	0.17±0.02	0.00±0.01	0.01±0.01
	2.70	0.29±0.02	0.38±0.02	0.17±0.02	0.15±0.02	0.00±0.01	0.02±0.01

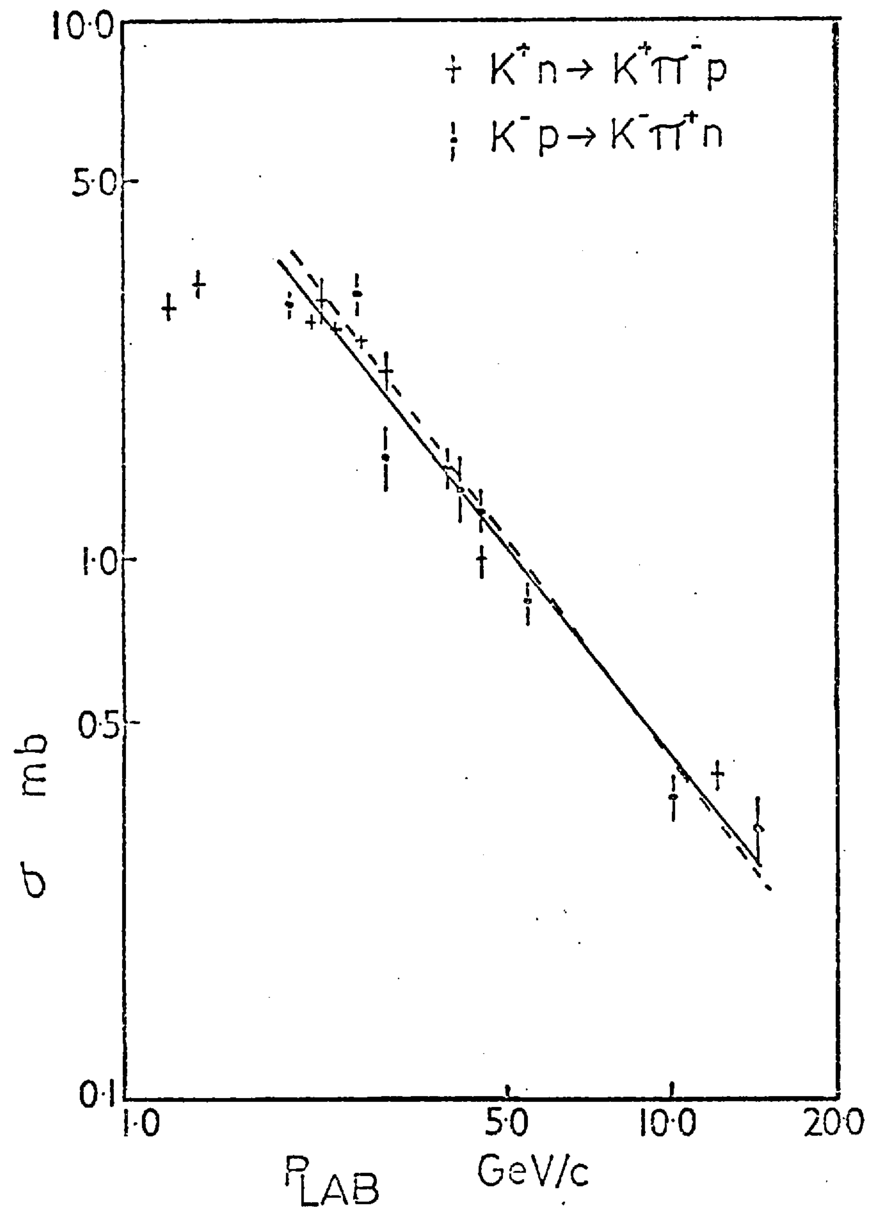
$K^+n \to K^+\pi^-p$
$K^-p \to K^-\pi^+n$
10·0
5·0
1·0
0·5
0·1
σ mb
1·0
5·0
10·0
20·0
P_{LAB} GeV/c
4.1

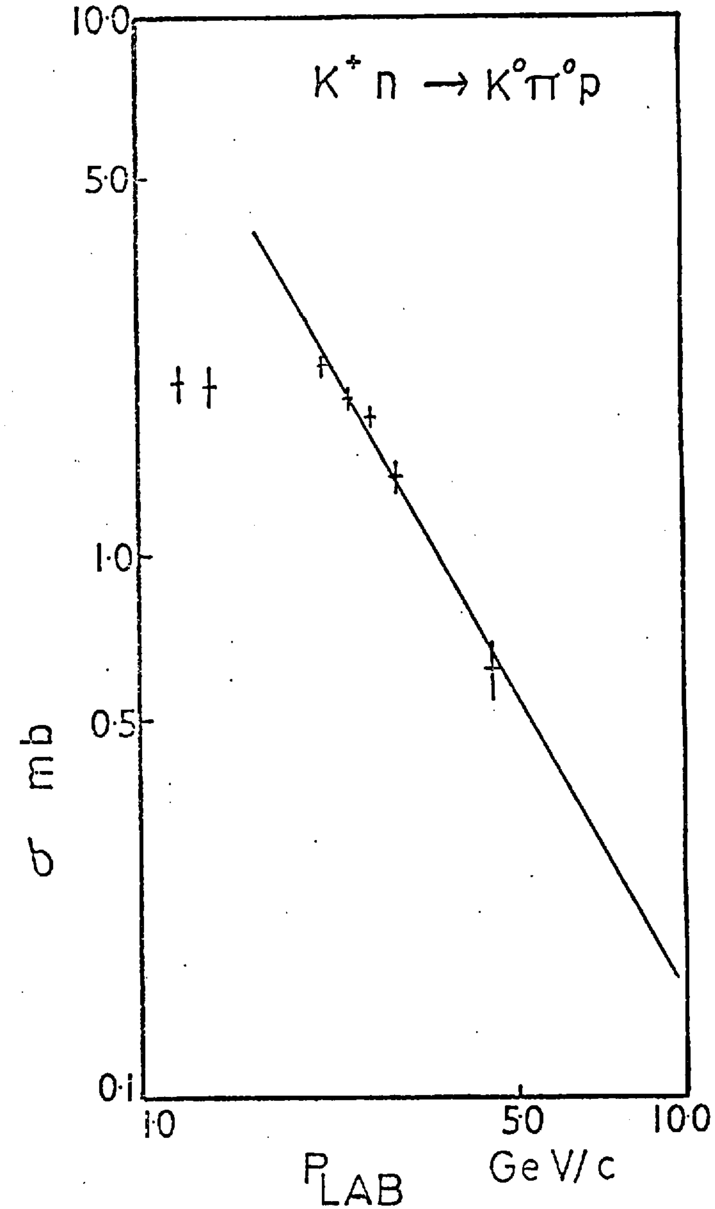
$K^+n \to K^0\pi^0p$
10·0
5·0
1·0
0·5
0·1
σ mb
1·0
5·0
10·0
P_{LAB} GeV/c
4.2

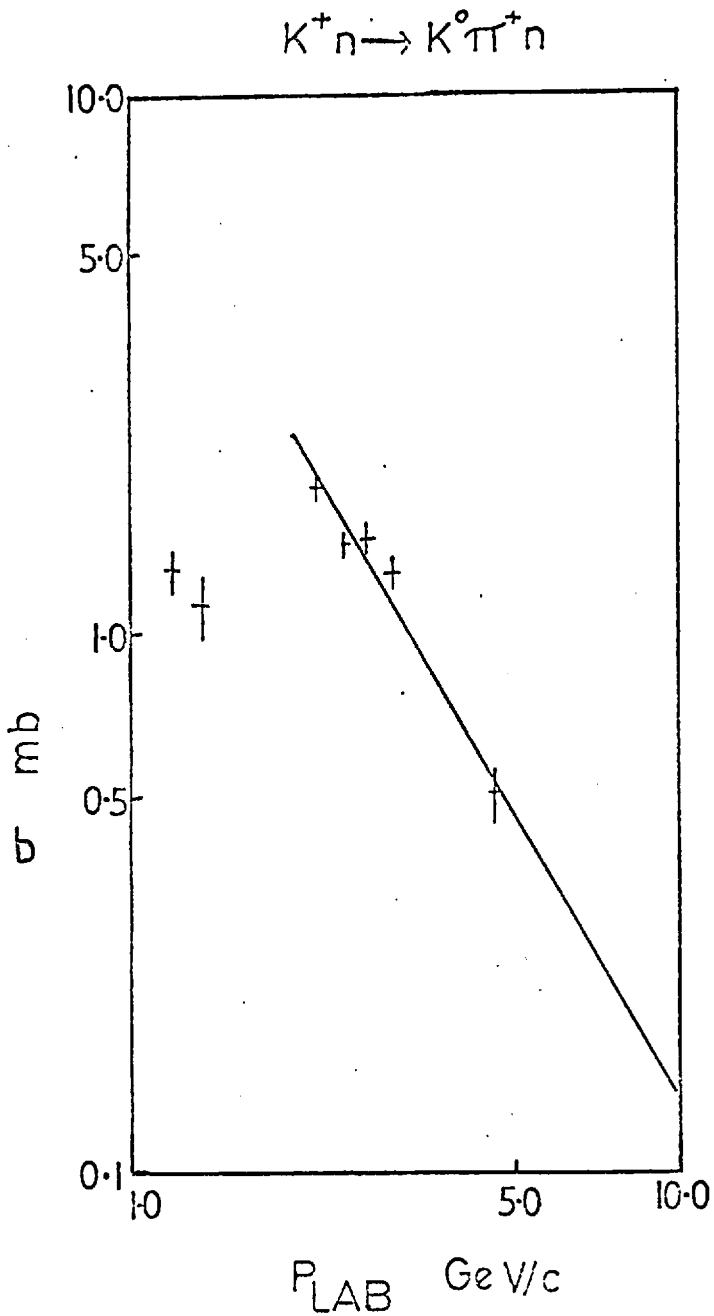
K⁺n ⟶ K°π⁺n
10·0
5·0
1·0
0·5
0·1
σ mb
1·0
5·0
10·0
P_LAB GeV/c

4.3

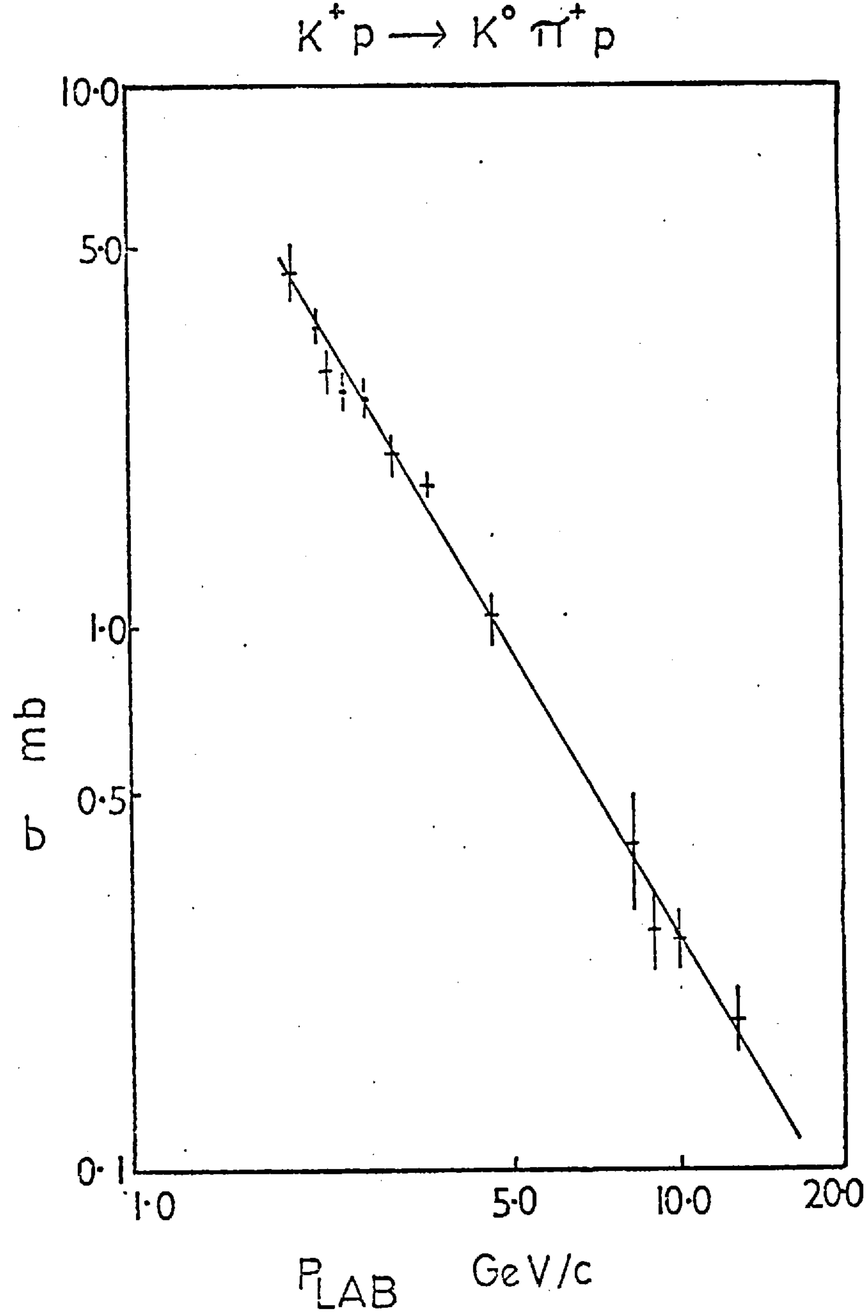
K⁺p ⟶ K° π⁺p
10·0
5·0
1·0
0·5
0·1
σ mb
1·0
5·0
10·0
20·0
P_LAB GeV/c

4.4

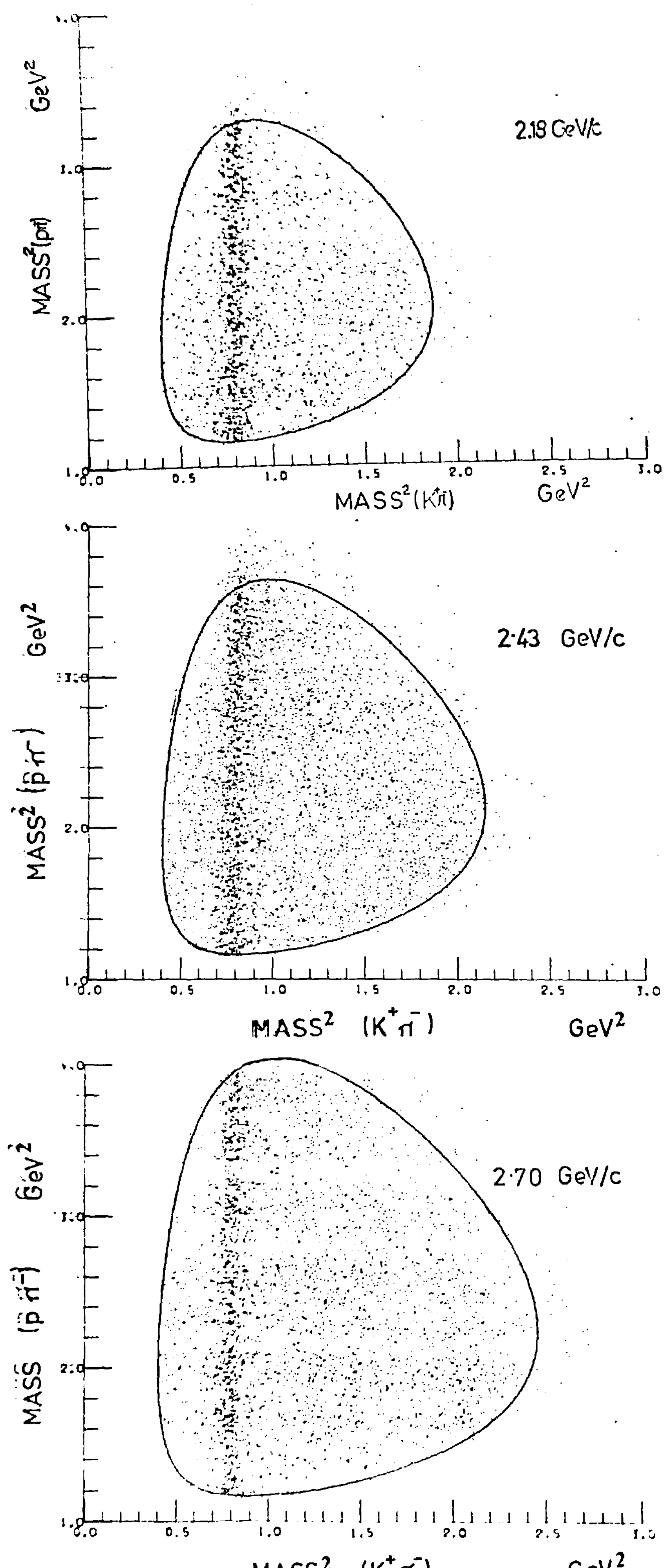

2.18 GeV/c
MASS²(pπ̄) GeV²
MASS²(K⁺π̄) GeV²
2·43 GeV/c
MASS² (p̄π⁻) GeV²
MASS² (K⁺π⁻) GeV²
2·70 GeV/c
MASS (p̄π⁻) GeV²
MASS² (K⁺π⁻) GeV²
0.0
0.5
1.0
1.5
2.0
2.5
3.0

4.5

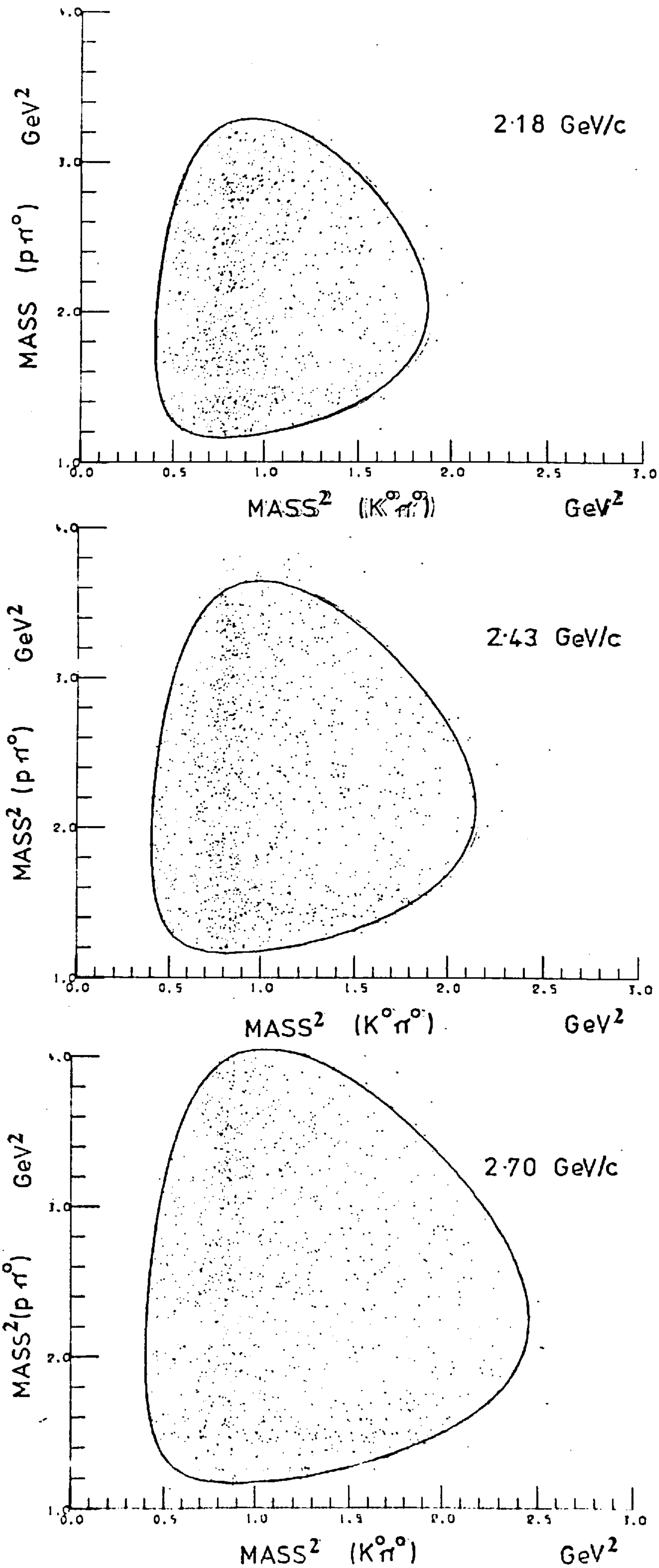
2·18 GeV/c
MASS (p π°) GeV²
MASS² (K°π°) GeV²
2·43 GeV/c
MASS² (p π°) GeV²
MASS² (K°π°) GeV²
2·70 GeV/c
MASS²(p π°) GeV²
MASS² (K°π°) GeV²
0.0 0.5 1.0 1.5 2.0 2.5 3.0
1.0 2.0 3.0 4.0

4.6

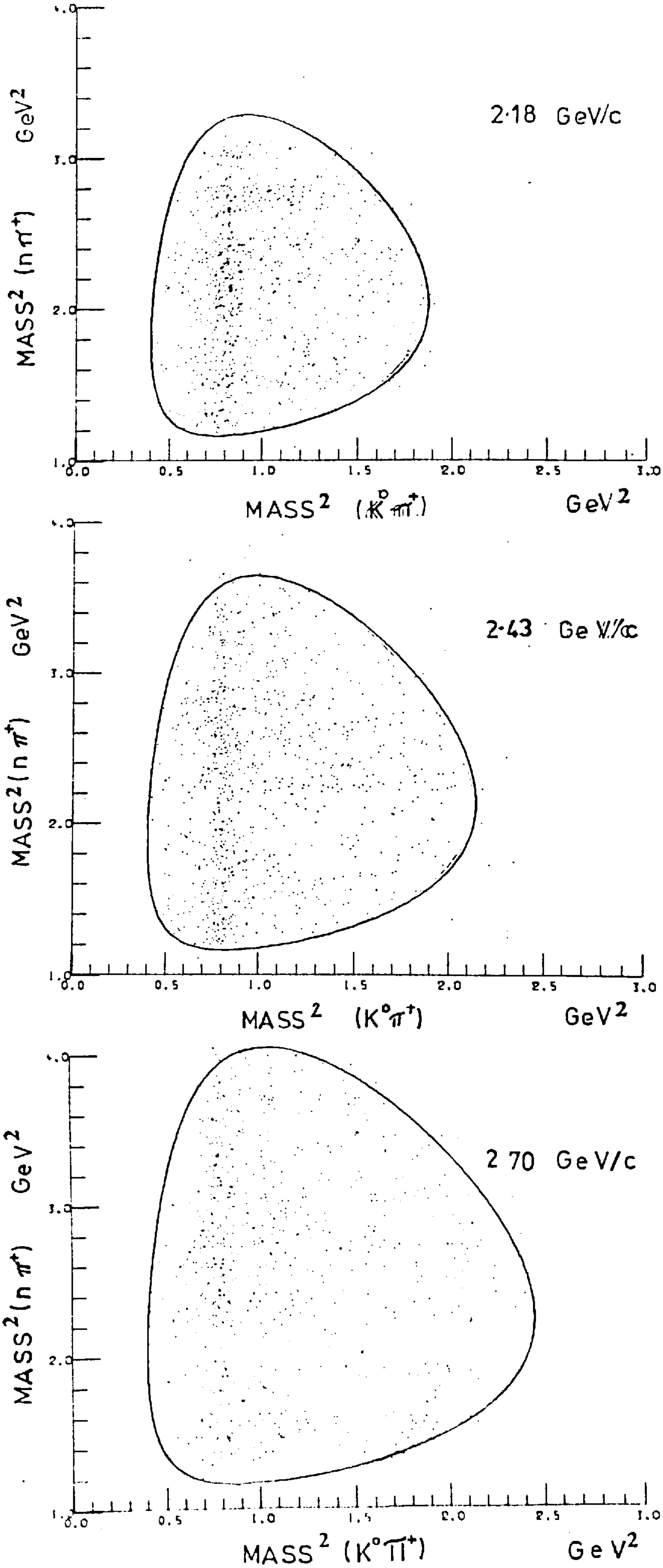
2·18 GeV/c
MASS^2 ($n\pi^+$) GeV^2
MASS^2 ($K^0\pi^+$) GeV^2
2·43 GeV/c
MASS^2 ($n\pi^+$) GeV^2
MASS^2 ($K^0\pi^+$) GeV^2
2 70 GeV/c
MASS^2 ($n\pi^+$) GeV^2
MASS^2 ($K^0\pi^+$) GeV^2

4.7

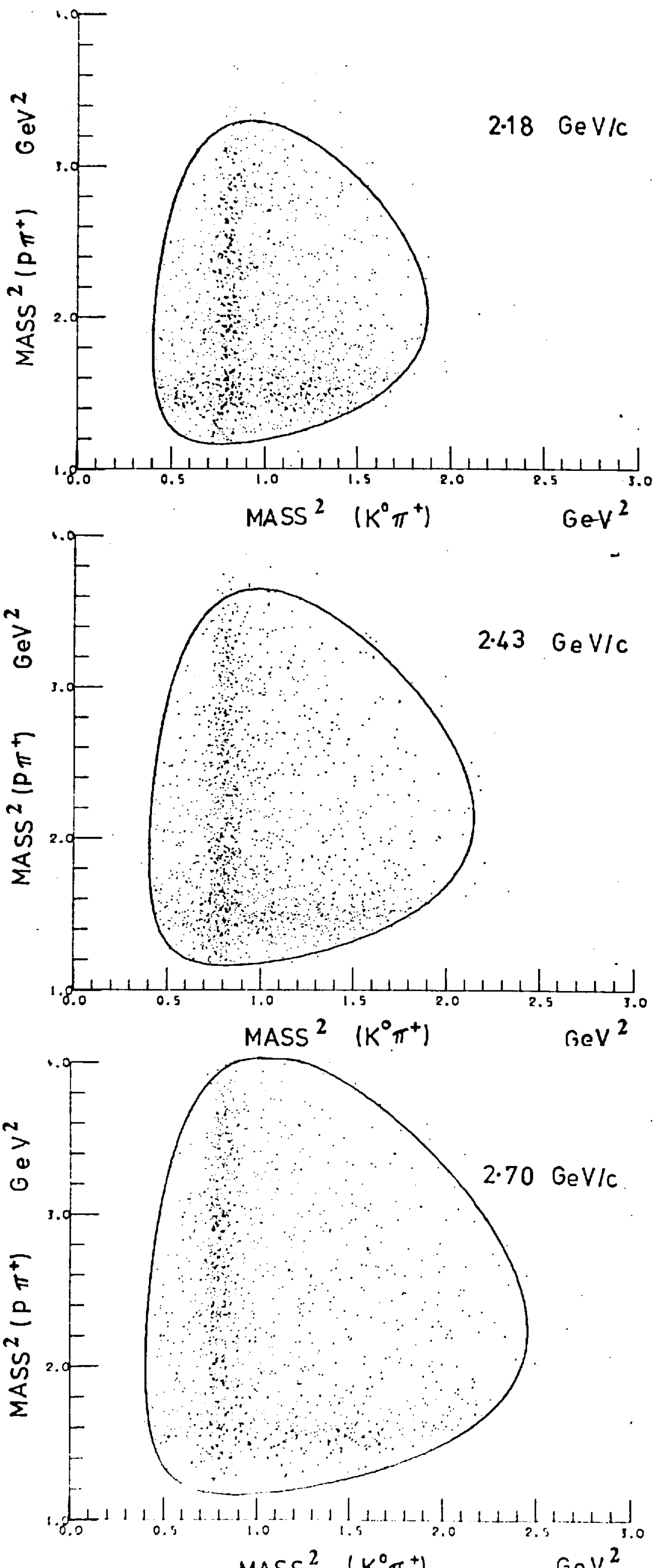
2·18 GeV/c
MASS² (pπ⁺) GeV²
MASS² (K°π⁺) GeV²
2·43 GeV/c
MASS² (pπ⁺) GeV²
MASS² (K°π⁺) GeV²
2·70 GeV/c
MASS² (pπ⁺) GeV²
MASS² (K°π⁺) GeV²

4.8

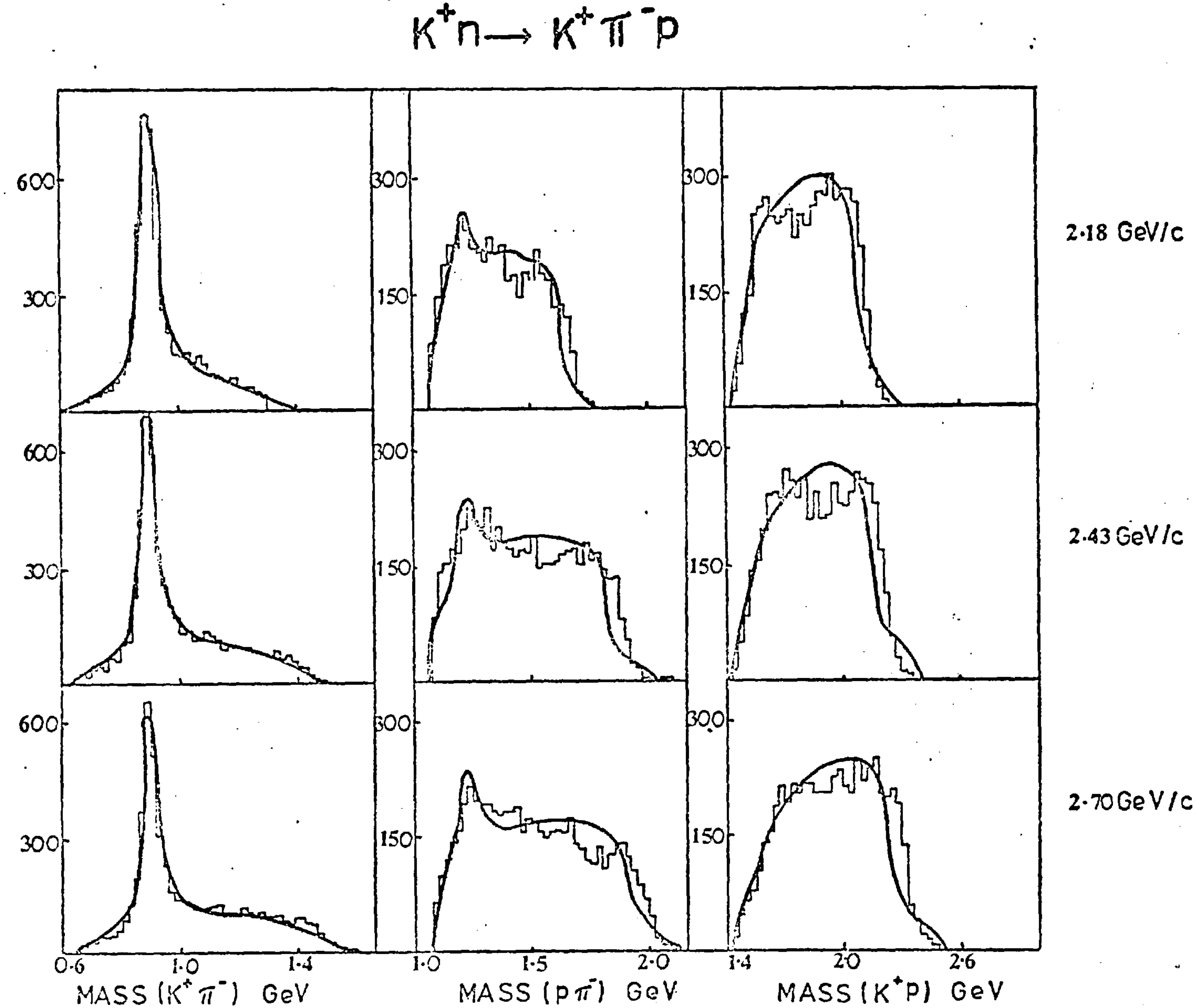

K⁺n ⟶ K⁺π⁻p
600
300
300
150
2·18 GeV/c
2·43 GeV/c
2·70 GeV/c
0·6
1·0
1·4
1·5
2·0
2·6
MASS (K⁺π⁻) GeV
MASS (pπ⁻) GeV
MASS (K⁺p) GeV

$K^+ n \to K^0 \pi^0 p$

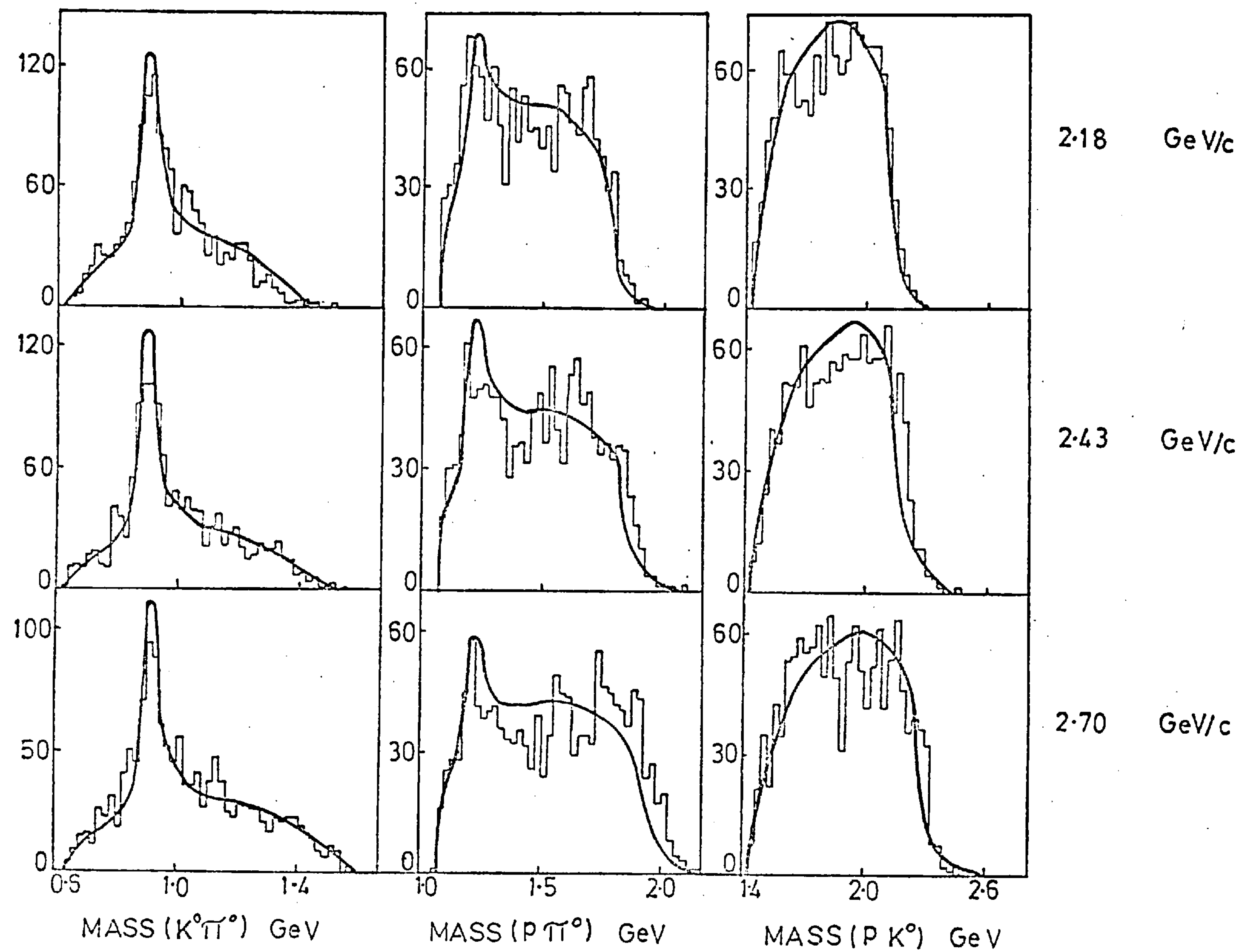

4.10

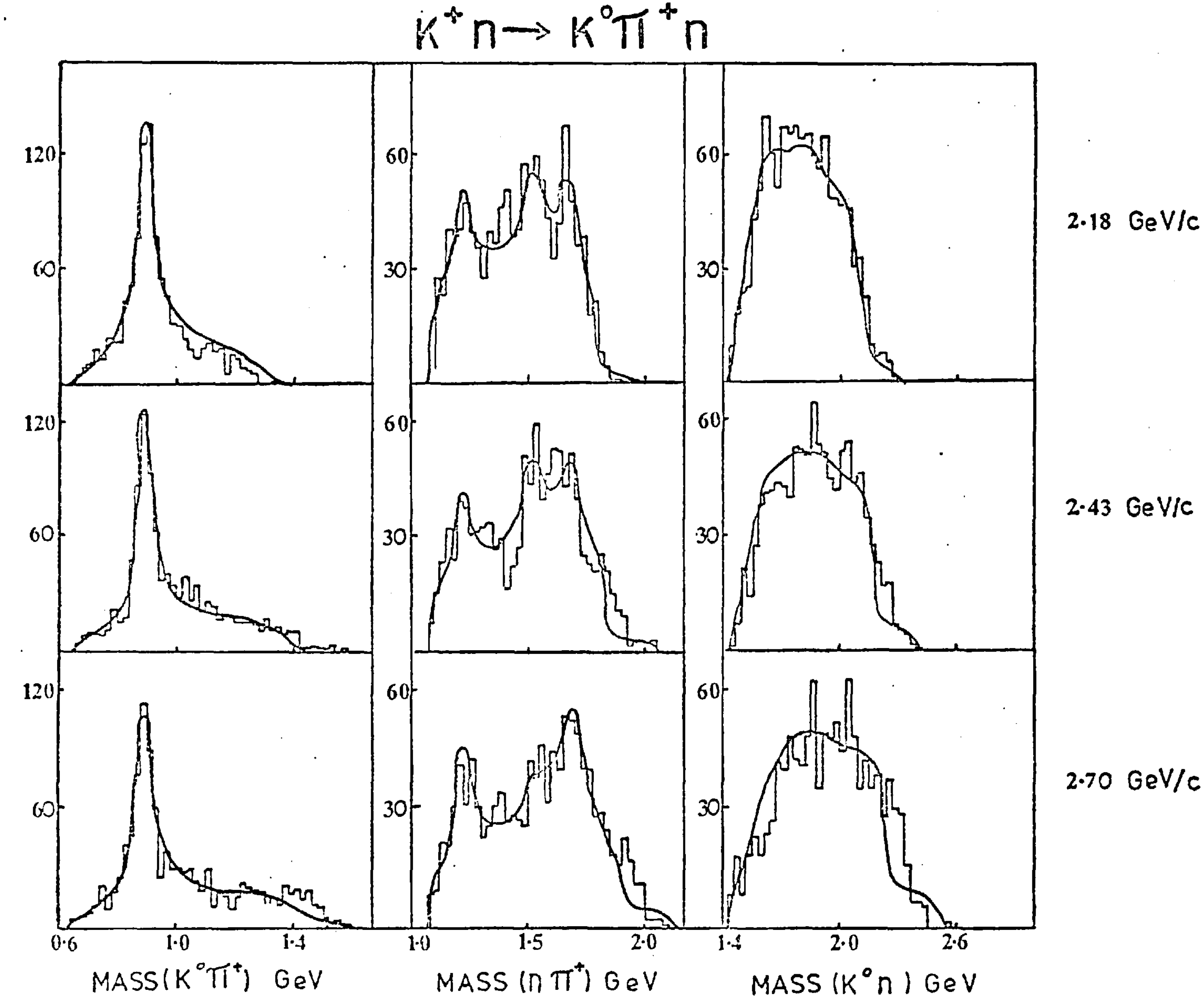
K⁺n → K°π⁺n
120
60
60
30
2·18 GeV/c
2·43 GeV/c
2·70 GeV/c
0·6
1·0
1·4
1·5
2·0
2·6
MASS(K°π⁺) GeV
MASS (nπ⁺) GeV
MASS (K°n) GeV

4.11

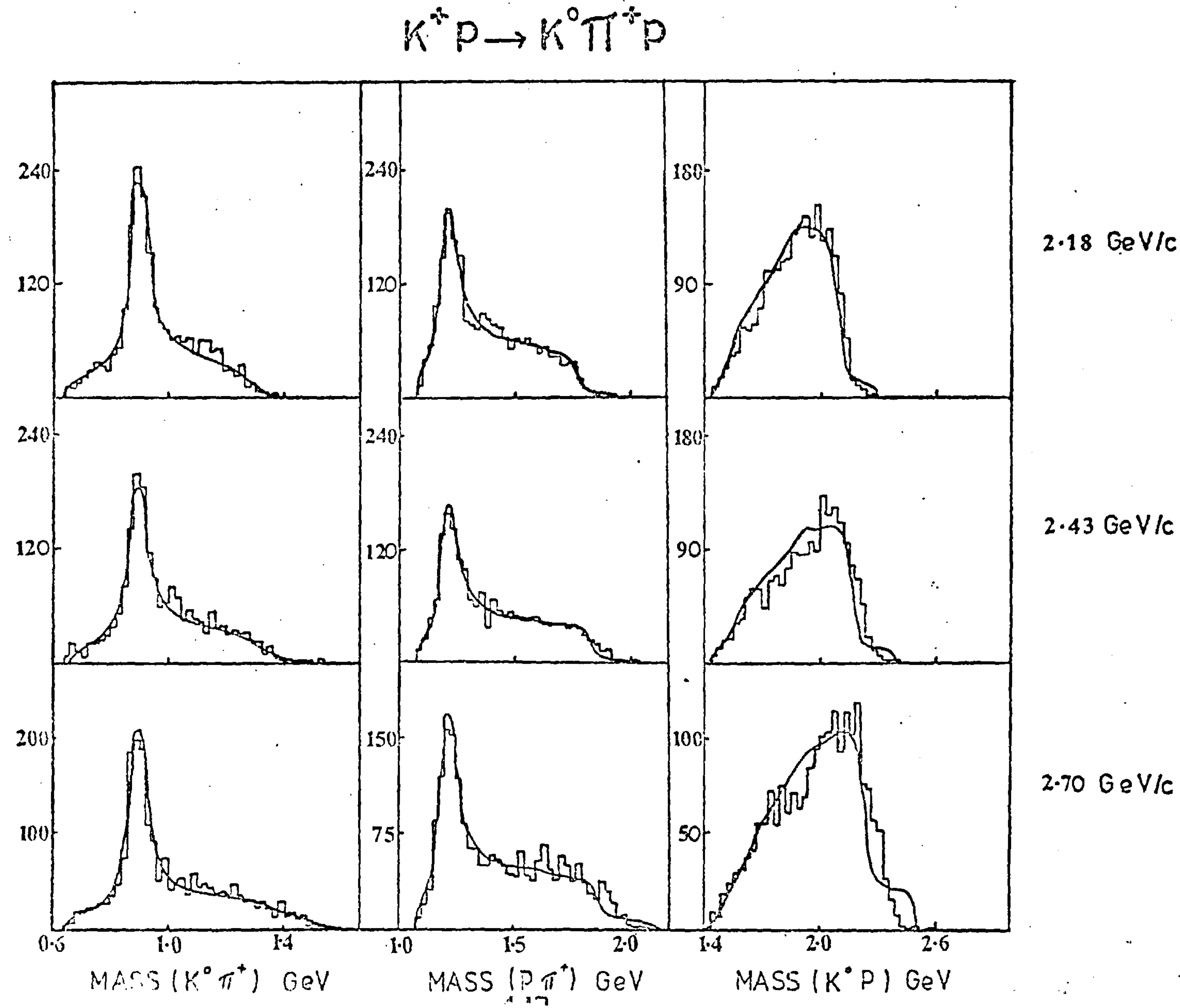

$K^+p \rightarrow K^0\pi^+p$
2·18 GeV/c
2·43 GeV/c
2·70 GeV/c
MASS ($K^0\pi^+$) GeV
MASS ($P\pi^+$) GeV
MASS (K^0P) GeV

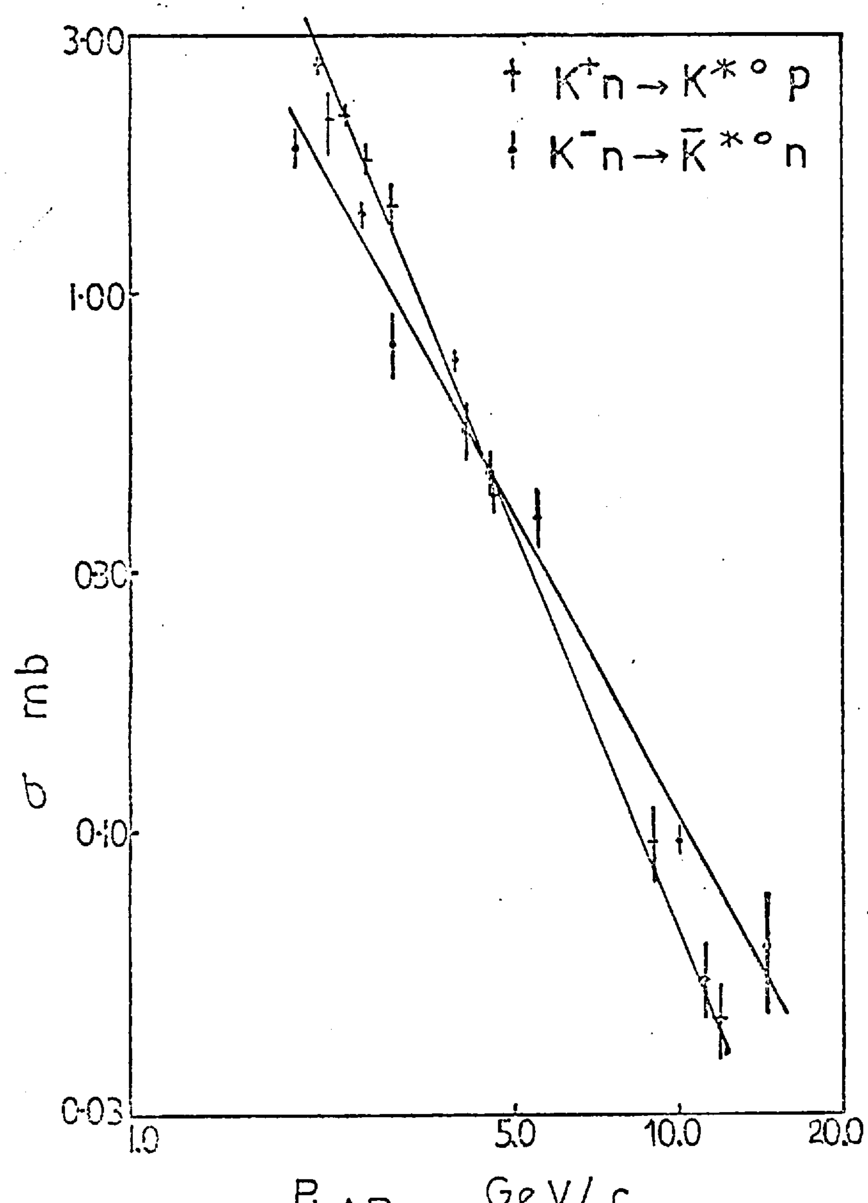

K⁺n → K*° p
K⁻n → K̄*° n
3·00
1·00
0·30
0·10
0·03
σ mb
1.0
5.0
10.0
20.0
P LAB GeV/c

4.13

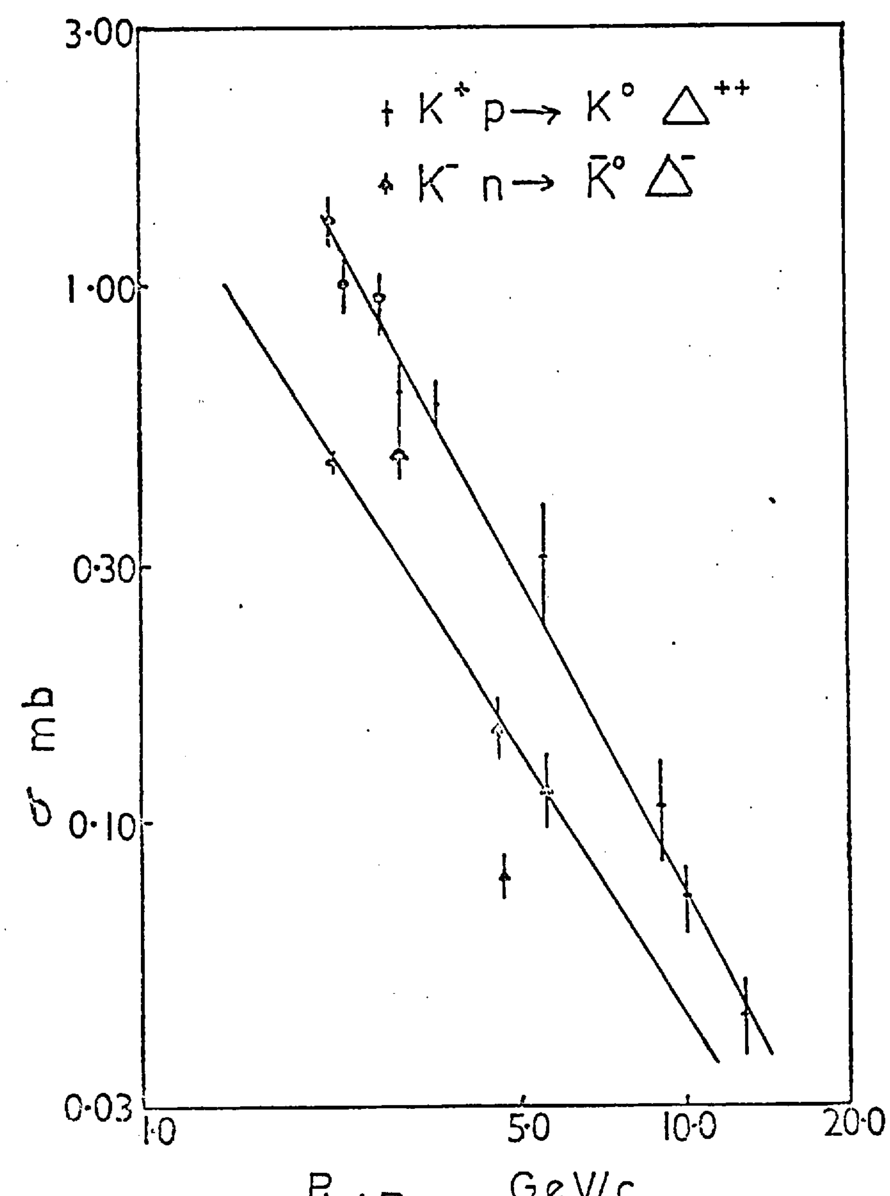

K⁺p → K° Δ⁺⁺
K⁻ n → K̄° Δ⁻
3·00
1·00
0·30
0·10
0·03
σ mb
1·0
5·0
10·0
20·0
P LAB GeV/c

4.14

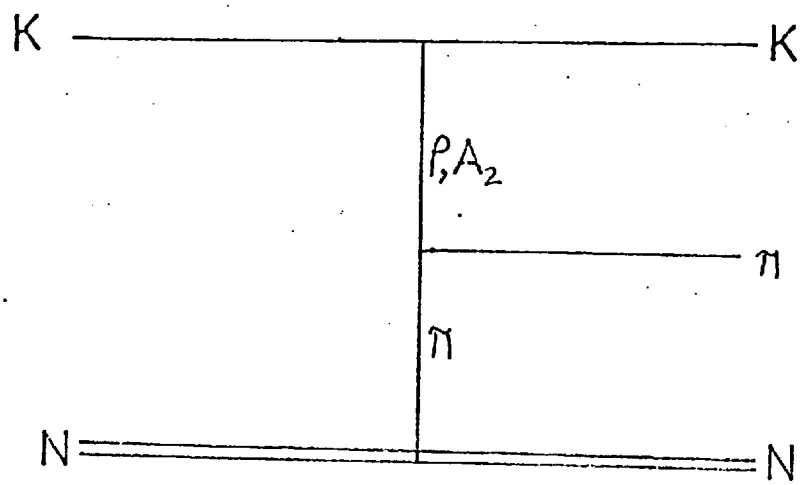

A

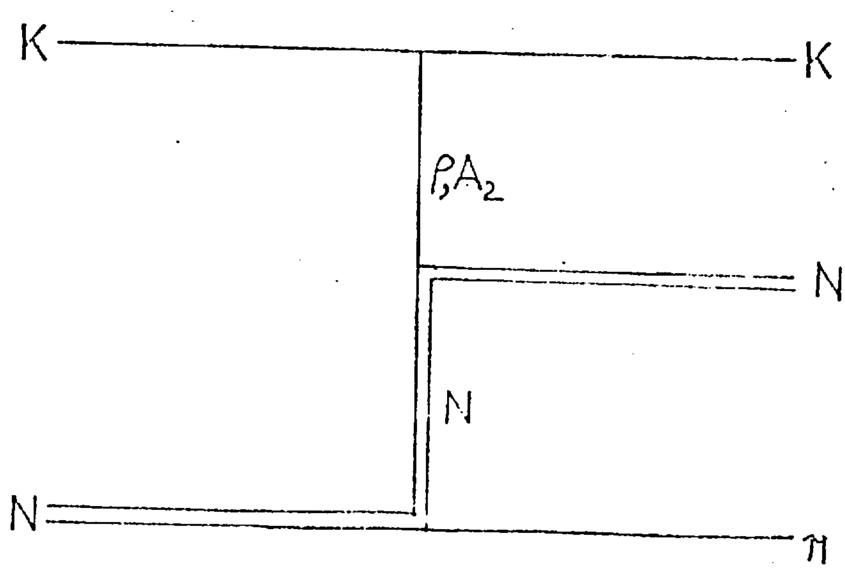

B

4.15

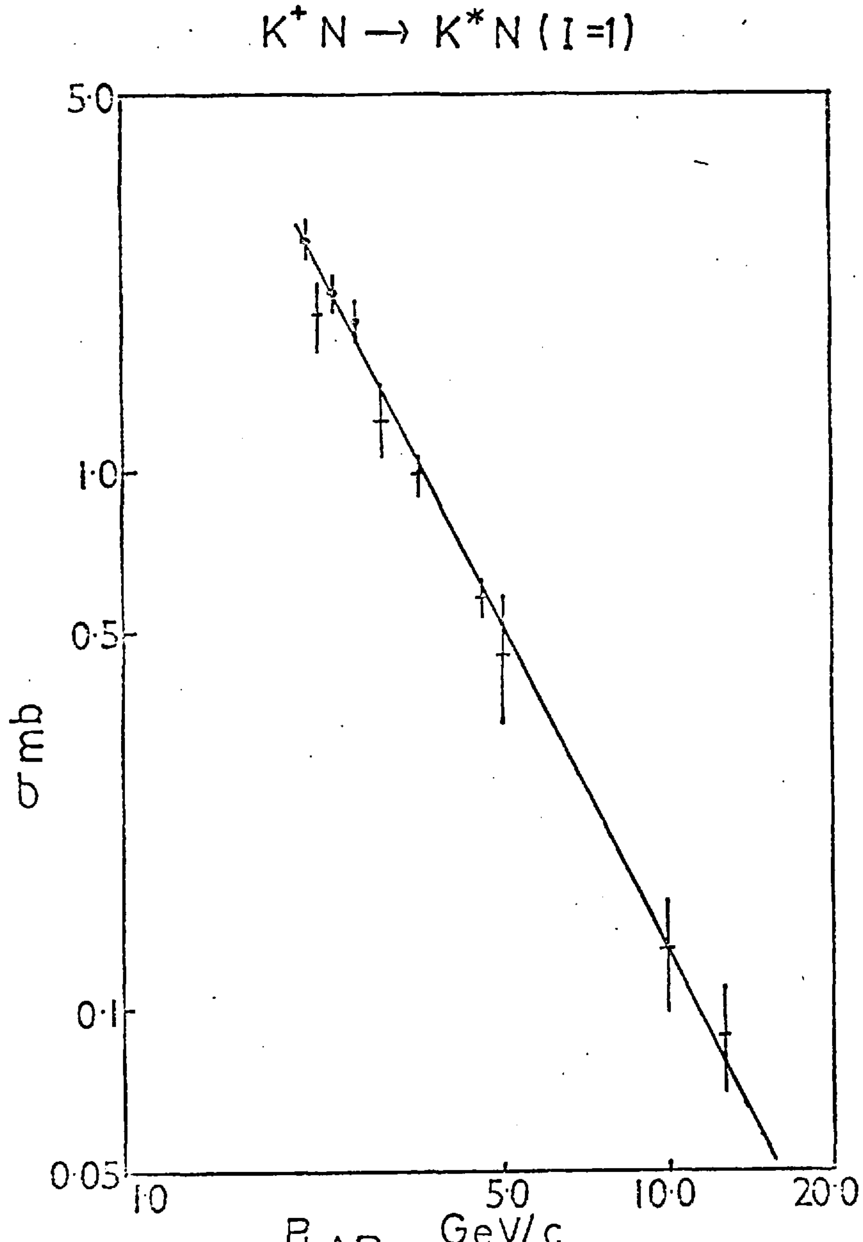

$K^+ N \rightarrow K^* N$ (I=1)
5·0
1·0
0·5
0·1
0·05
σ mb
1·0
5·0
10·0
20·0
P_{LAB} GeV/c

A.

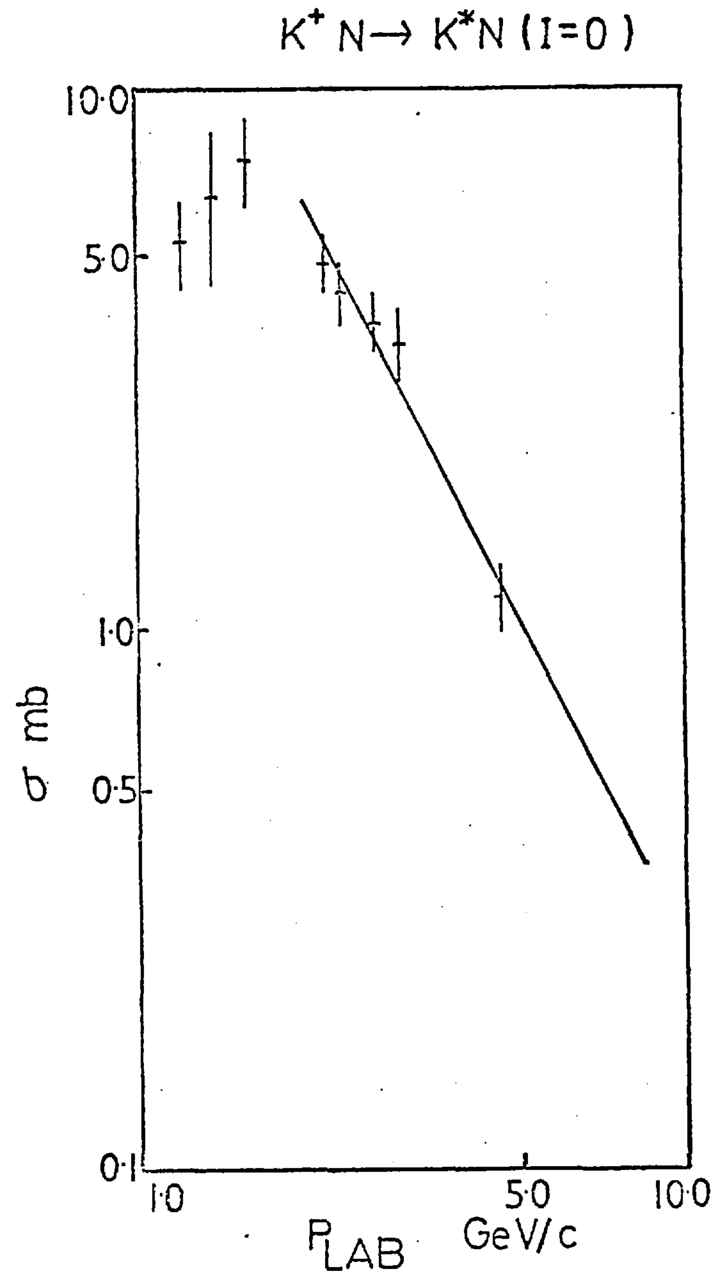

$K^+ N \rightarrow K^* N$ (I=0)
10·0
5·0
1·0
0·5
0·1
σ mb
1·0
5·0
10·0
P_{LAB} GeV/c

B.

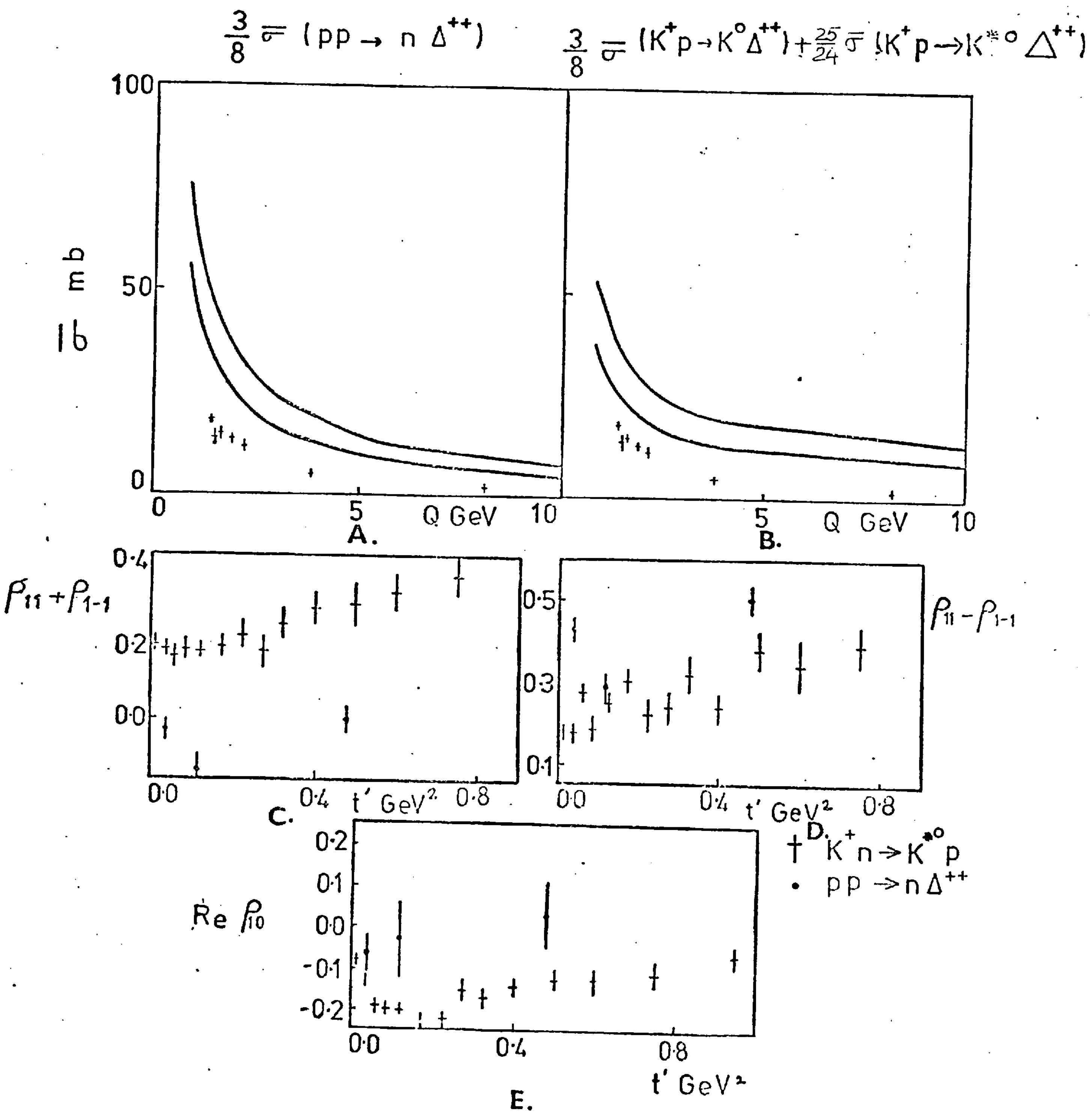

4.17 Comparison with quark model prediction .

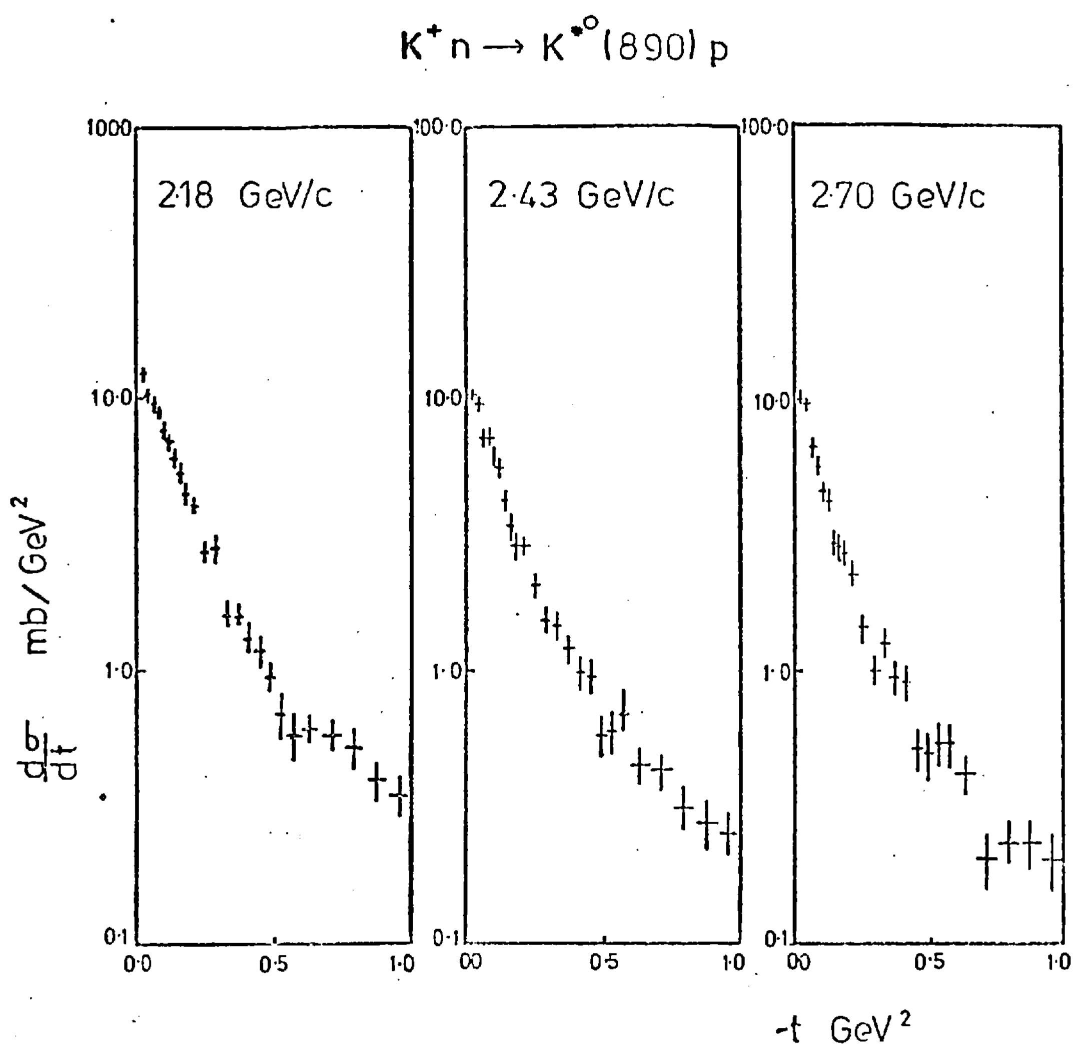
K⁺n → K*⁰(890) p
2·18 GeV/c
2·43 GeV/c
2·70 GeV/c
1000
100·0
100·0
10·0
10·0
10·0
1·0
1·0
1·0
0·1
0·1
0·1
0·0
0·5
1·0
0·0
0·5
1·0
0·0
0·5
1·0
dσ/dt mb/GeV²
-t GeV²

4.18

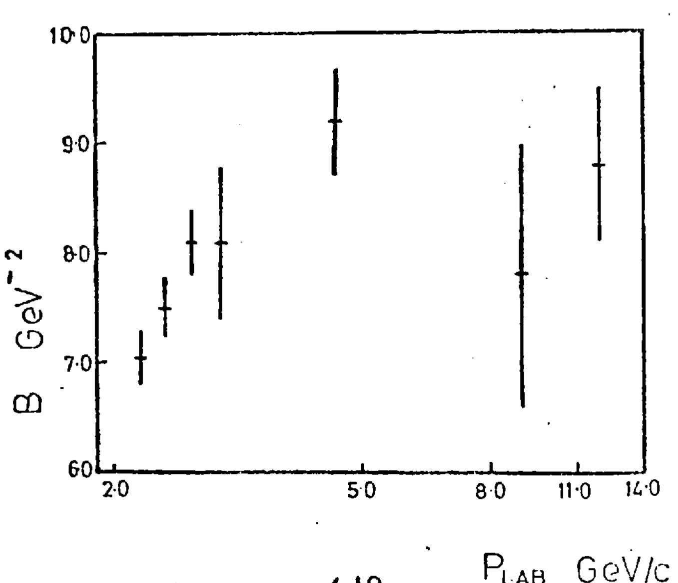
10·0
9·0
8·0
7·0
6·0
B GeV⁻²
2·0
5·0
8·0
11·0
14·0
P_LAB GeV/c

4.19

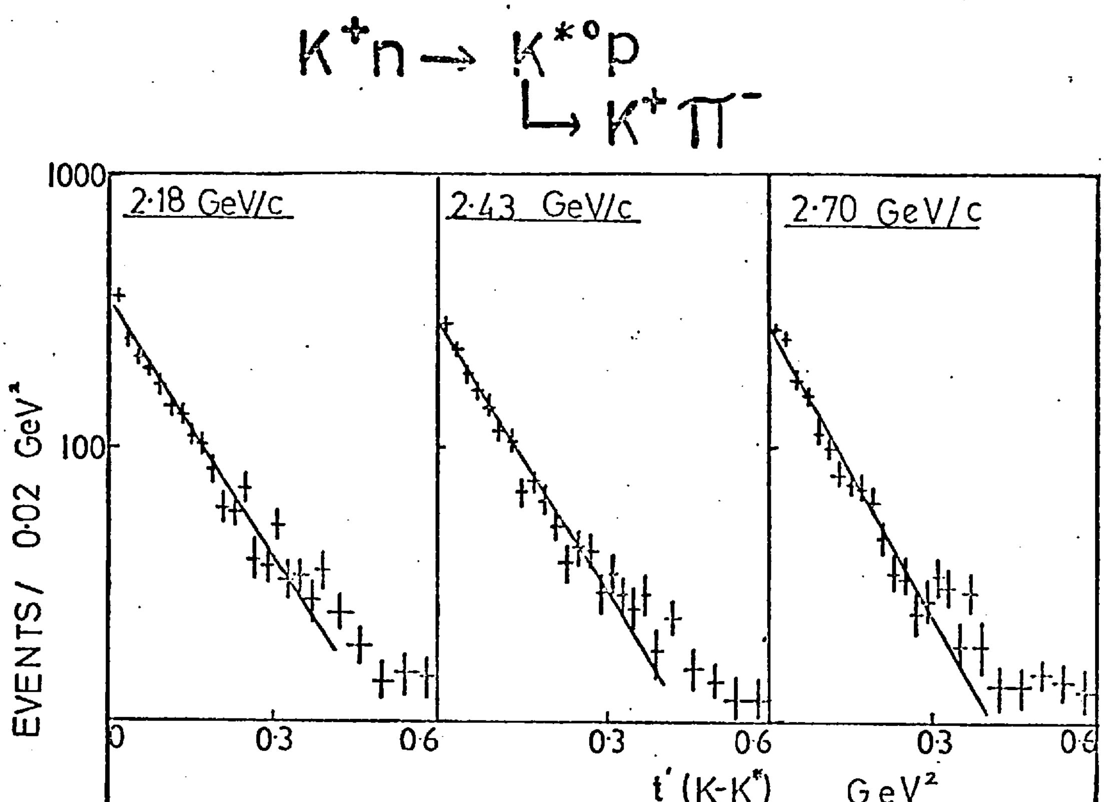
$K^+n \to K^{*0}p$
$\hookrightarrow K^+\pi^-$
2·18 GeV/c
2·43 GeV/c
2·70 GeV/c
EVENTS/ 0·02 GeV²
1000
100
0
0·3
0·6
t' (K-K*) GeV²

4.20

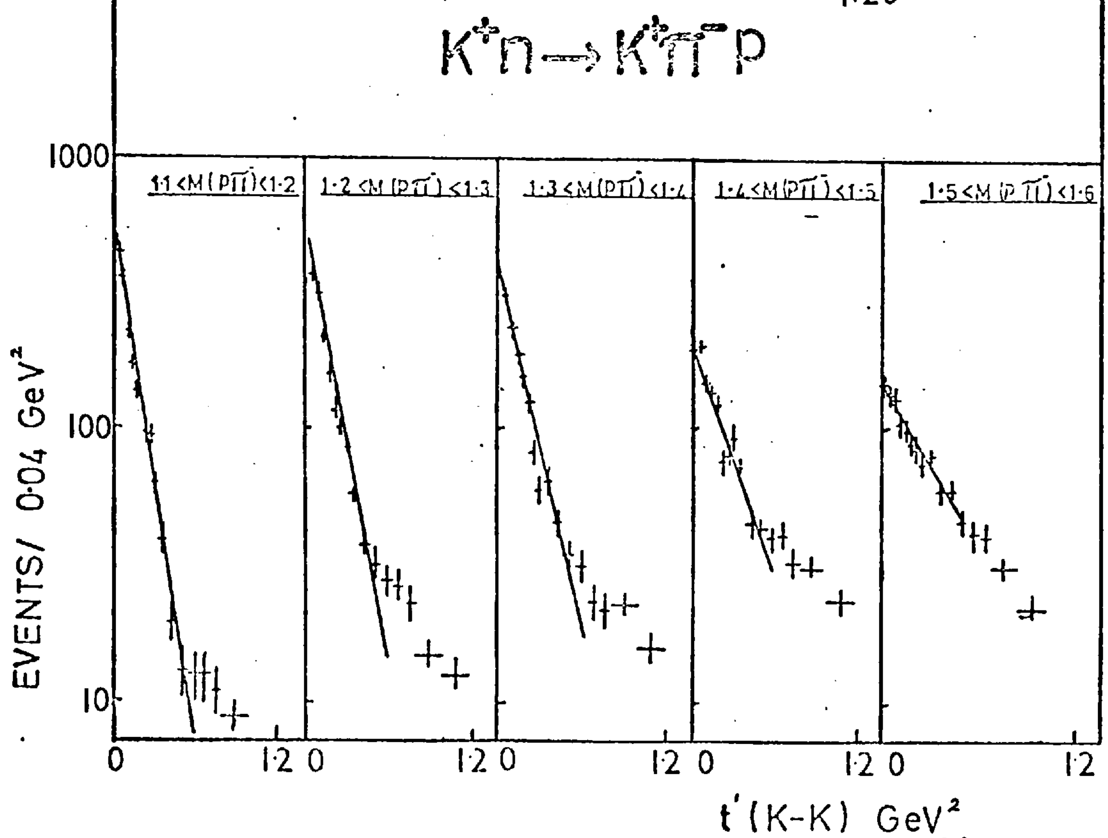
$K^+n \to K^+\pi^-p$
1·1 <M(Pπ⁻)<1·2
1·2 <M(Pπ⁻)<1·3
1·3 <M(Pπ⁻)<1·4
1·4 <M(Pπ⁻)<1·5
1·5 <M(Pπ⁻)<1·6
EVENTS/ 0·04 GeV²
1000
100
10
0
1·2
t' (K-K) GeV²

4.21

$K^+\pi^-$ MOMENTS IN THE HELICITY FRAME

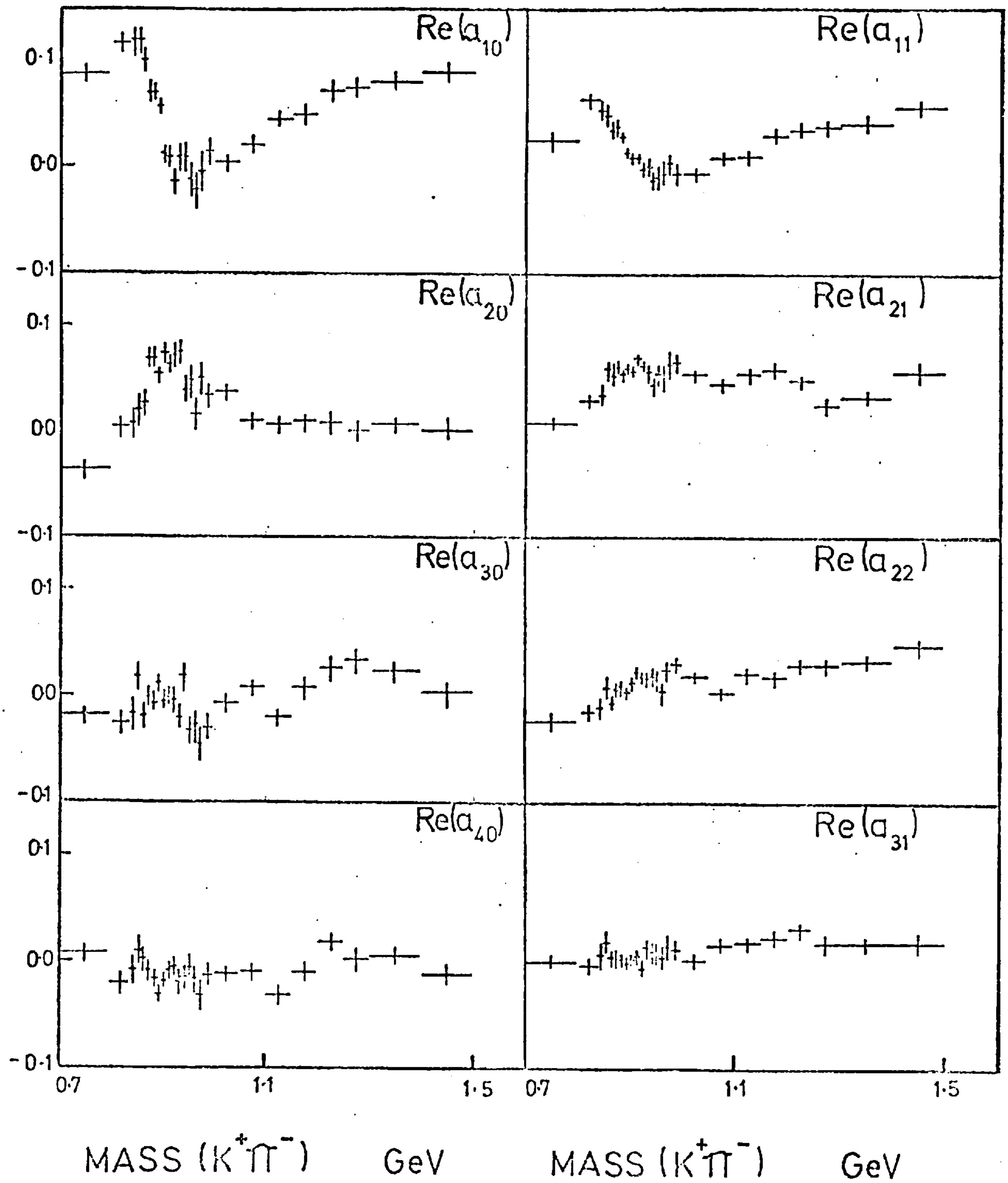

4.22

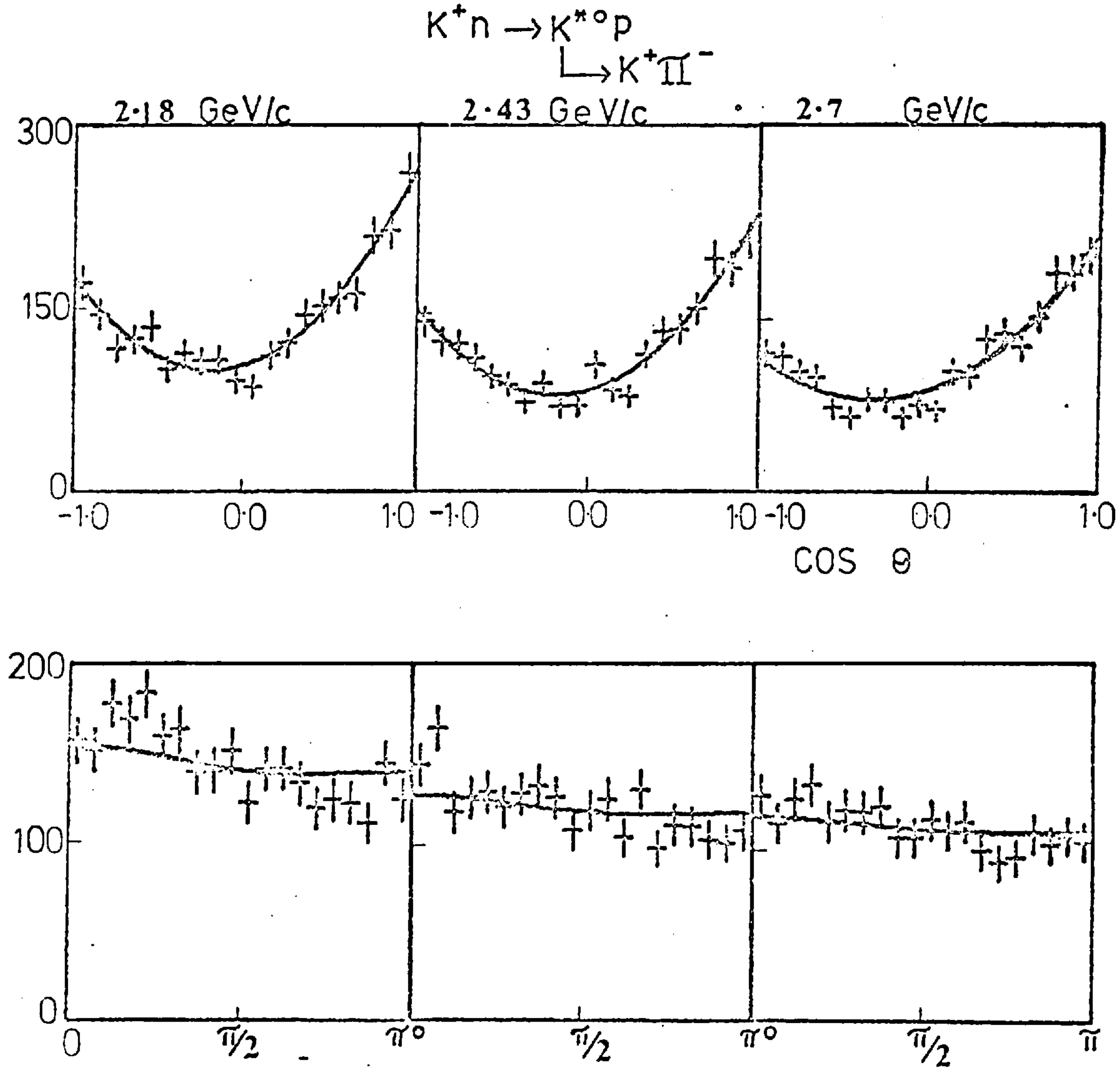

$K^+n \rightarrow K^{*0}p$
$\hookrightarrow K^+\pi^-$
2·18 GeV/c
2·43 GeV/c
2·7 GeV/c
300
150
0
-1·0
0·0
1·0
COS θ
200
100
0
π/2
π
ϕ

4.23

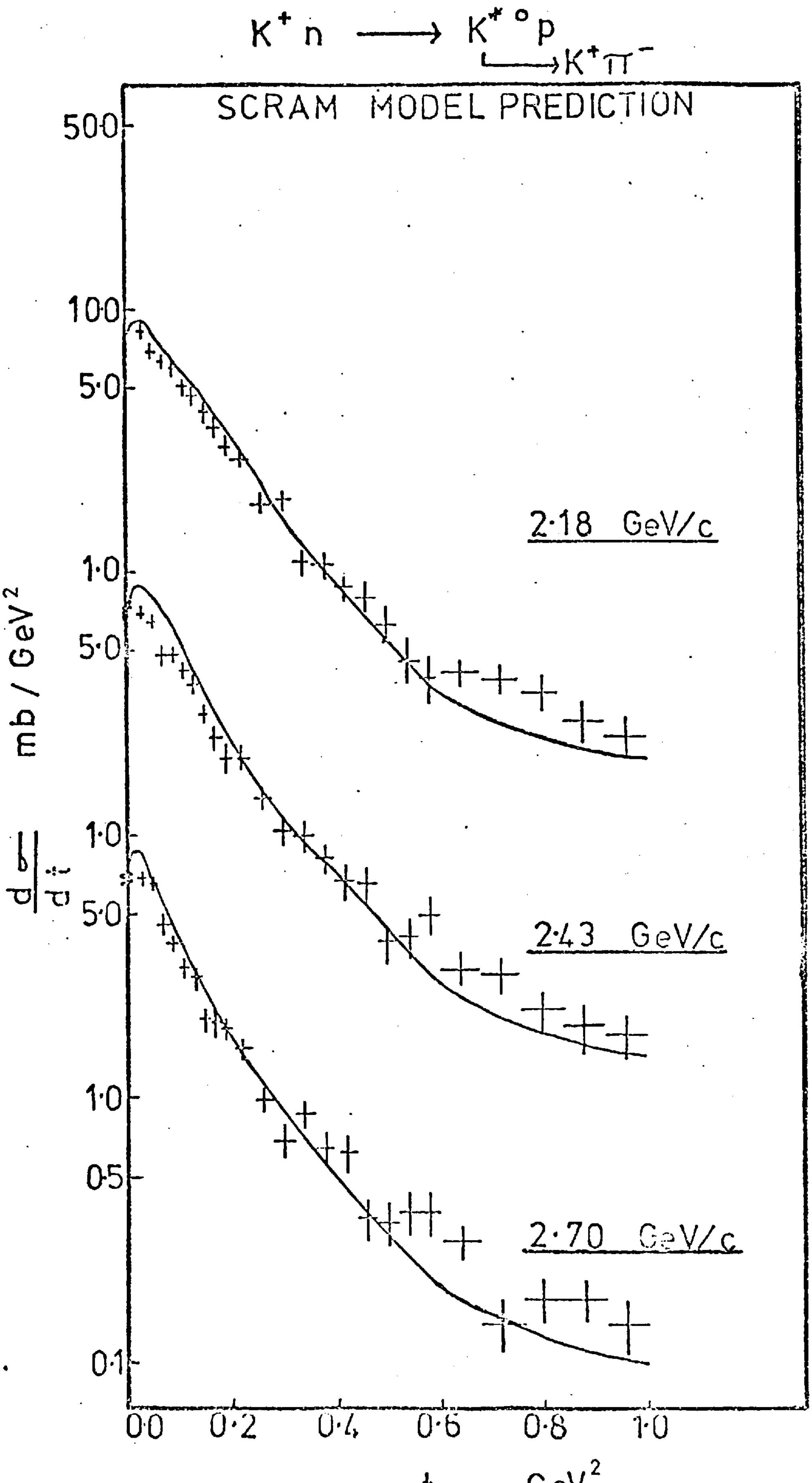

K⁺ n ⟶ K*° p
⟶ K⁺π⁻
SCRAM MODEL PREDICTION
50·0
10·0
5·0
1·0
5·0
1·0
5·0
1·0
0·5
0·1
dσ/dt mb / GeV²
2·18 GeV/c
2·43 GeV/c
2·70 GeV/c
0·0
0·2
0·4
0·6
0·8
1·0
t GeV²

4.24

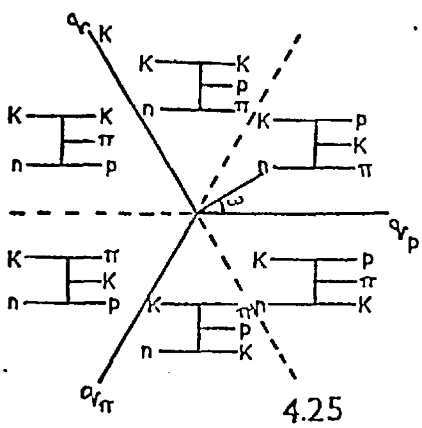

4.25

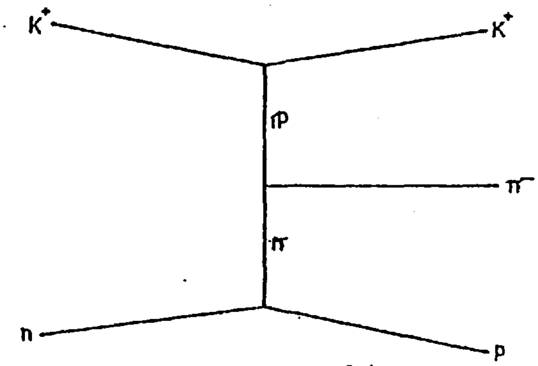

4.26

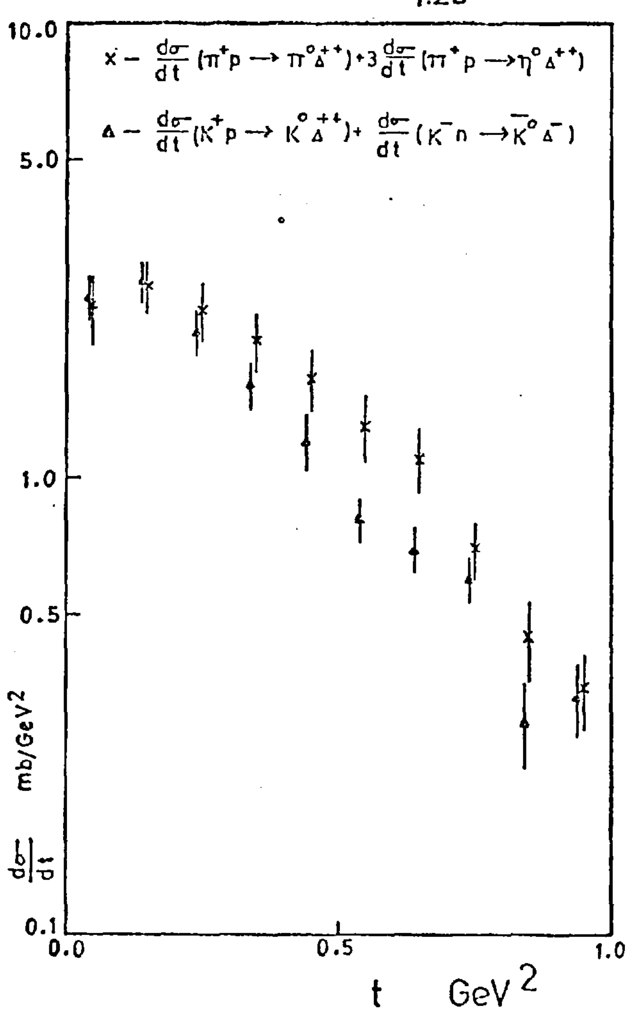

4.27

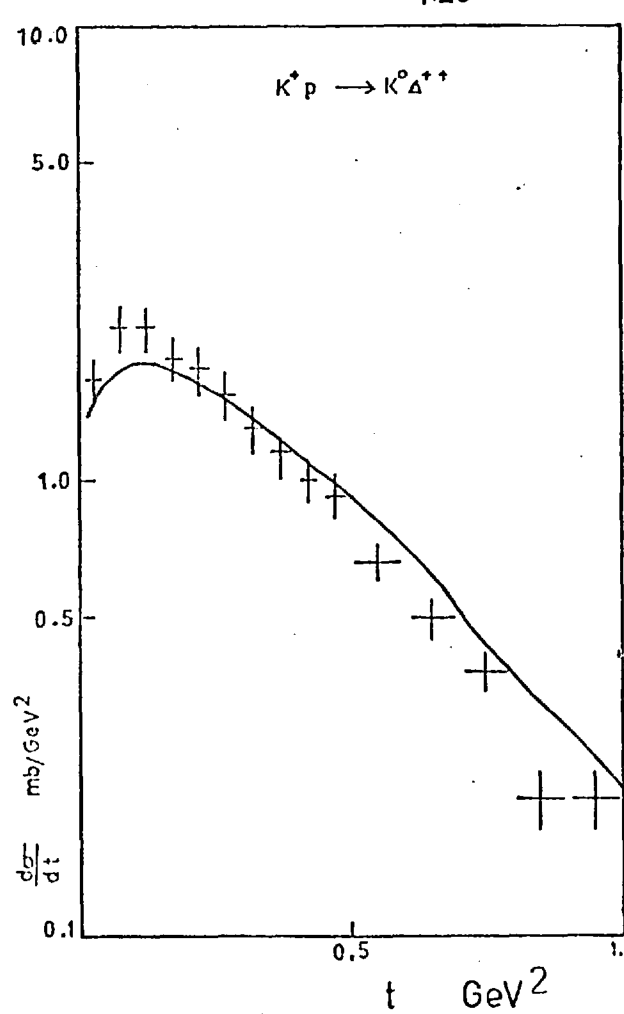

4.28

$K^+n \rightarrow K^+\pi^-p$

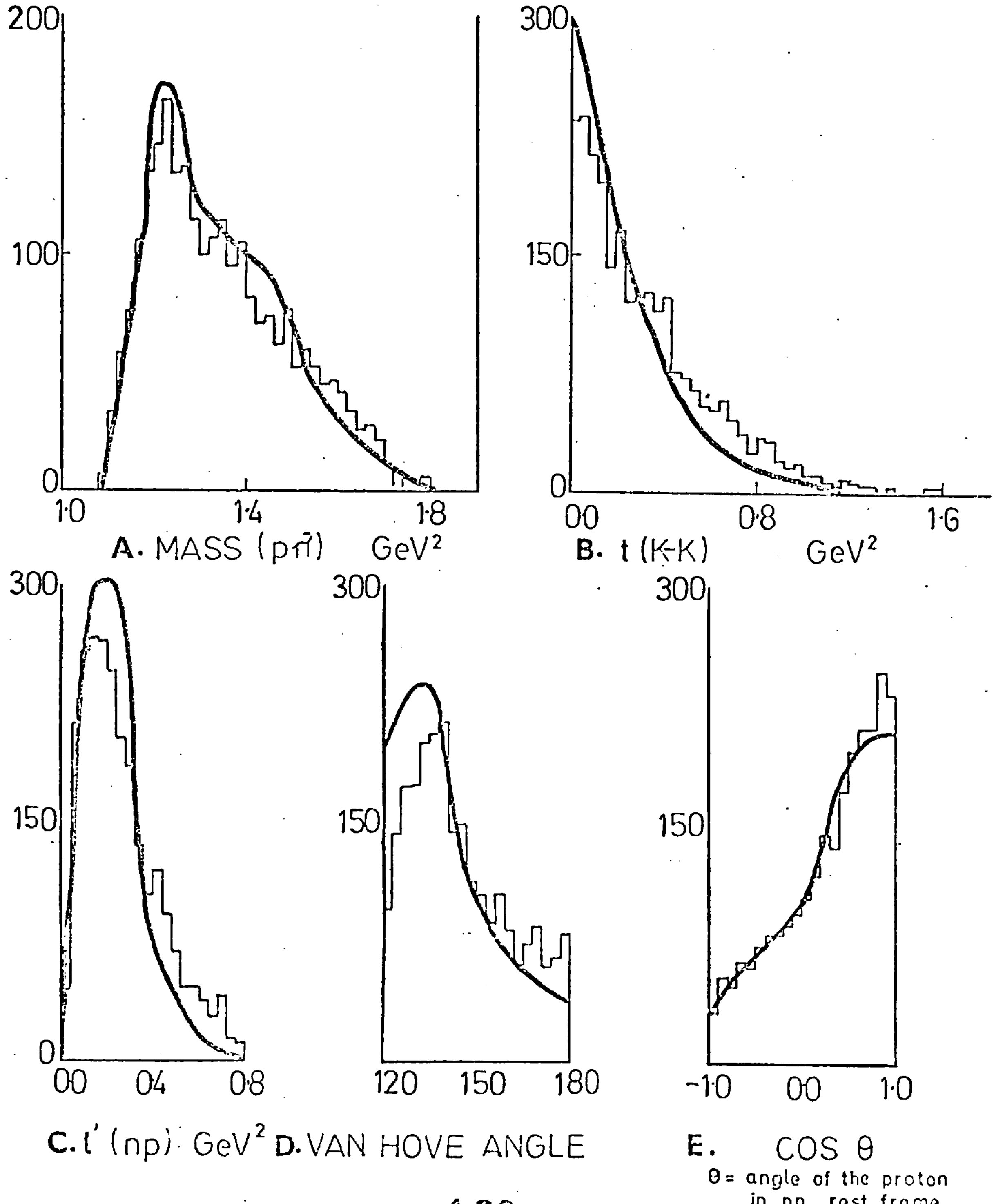

4.29

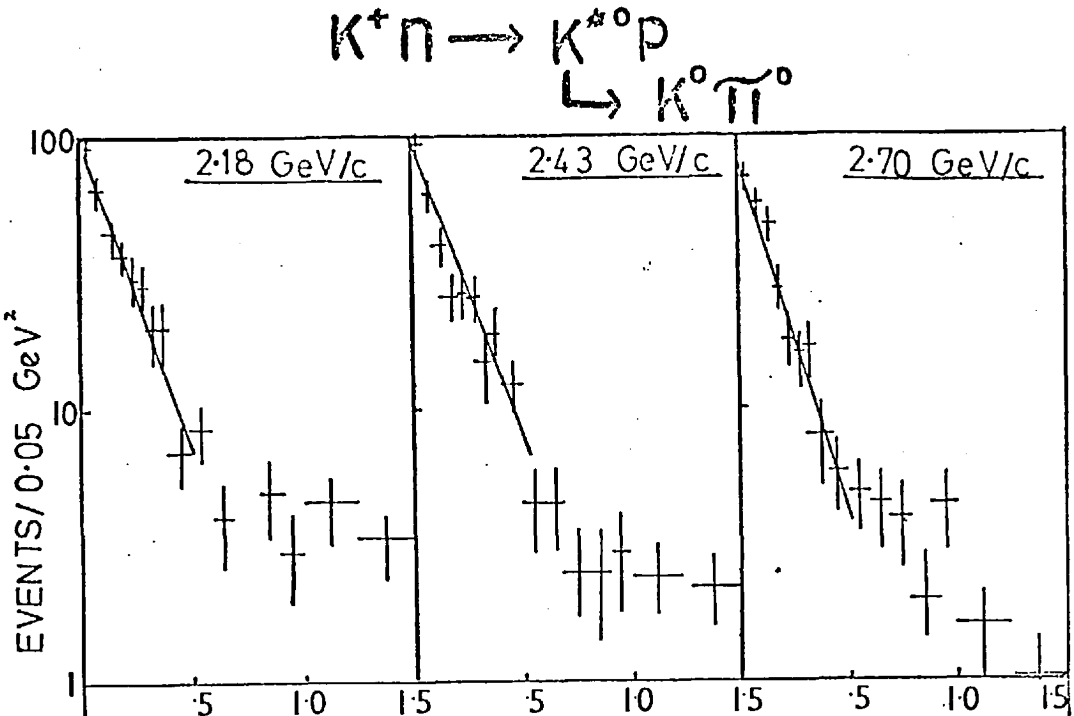

$K^+n \to K^{*0}p$
$\hookrightarrow K^0\pi^0$
2·18 GeV/c
2·43 GeV/c
2·70 GeV/c
EVENTS/ 0·05 GeV²
100
10
1
·5
1·0
1·5

4.30

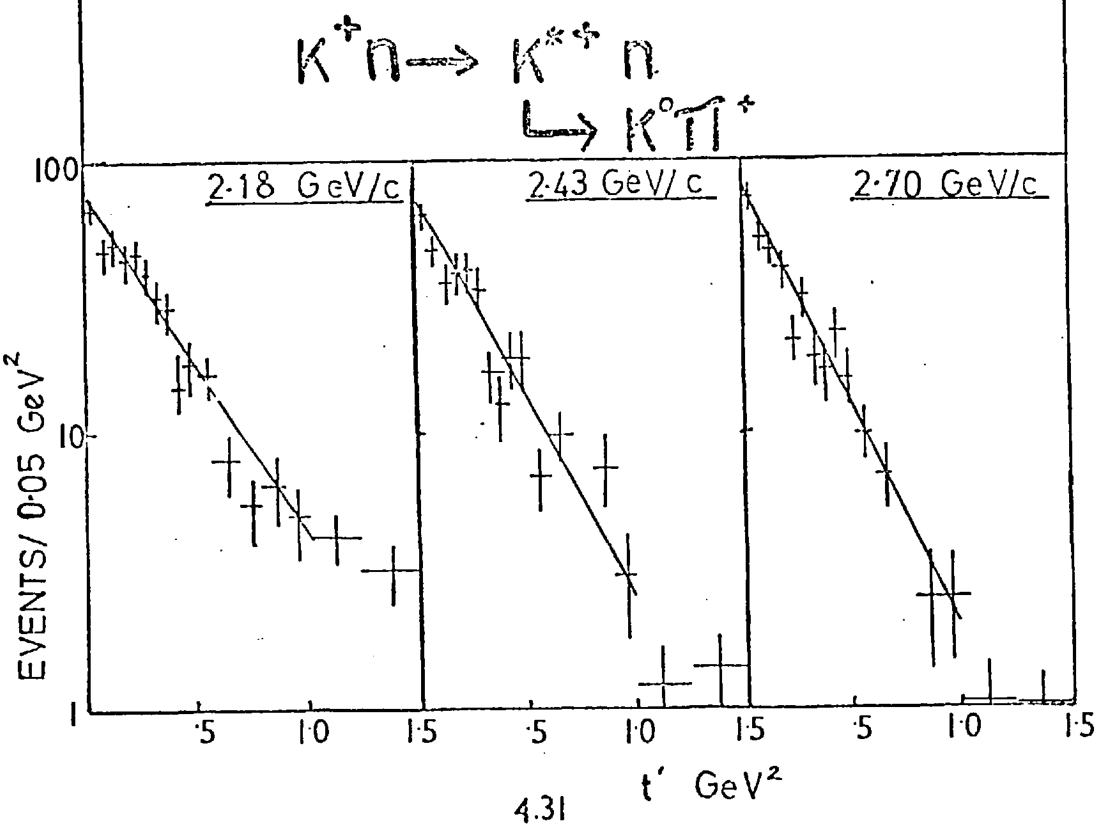

$K^+n \to K^{*+}n$
$\hookrightarrow K^0\pi^+$
2·18 GeV/c
2·43 GeV/c
2·70 GeV/c
EVENTS/ 0·05 GeV²
100
10
1
·5
1·0
1·5
t' GeV²

4.31

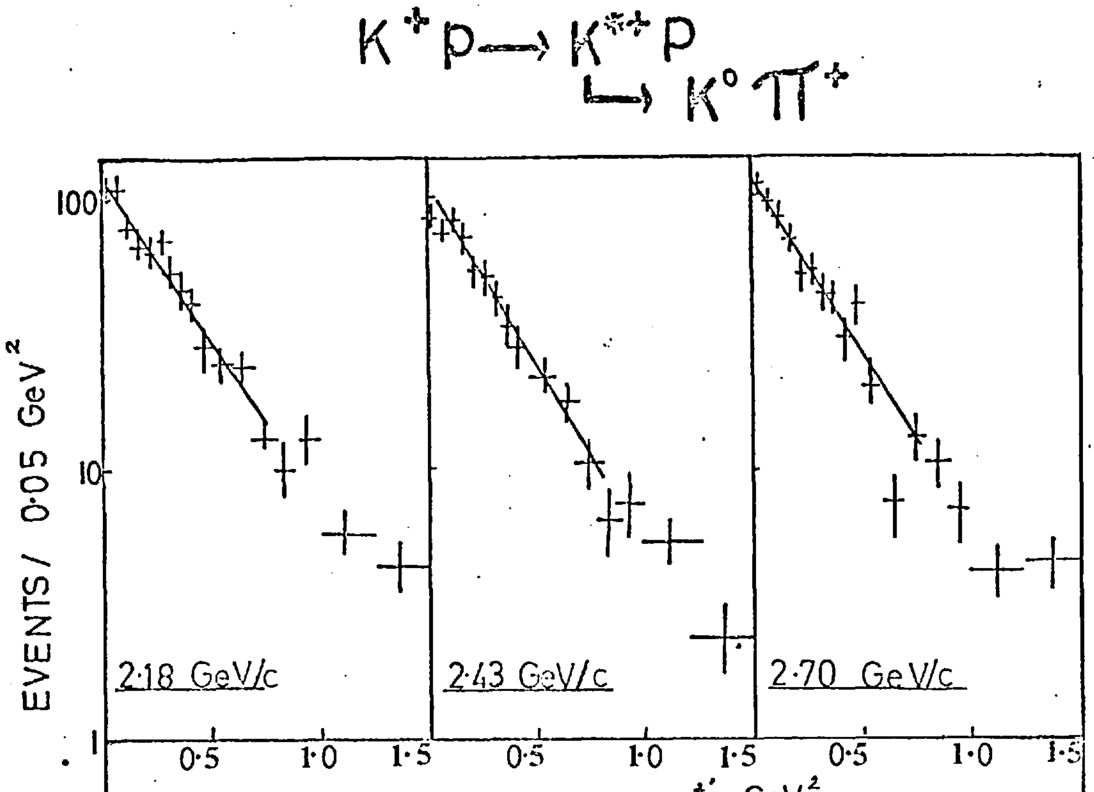
$K^+p \rightarrow K^{*+}p$
$\hookrightarrow K^0\pi^+$
EVENTS / 0·05 GeV²
2·18 GeV/c
2·43 GeV/c
2·70 GeV/c
t' GeV²

4.32

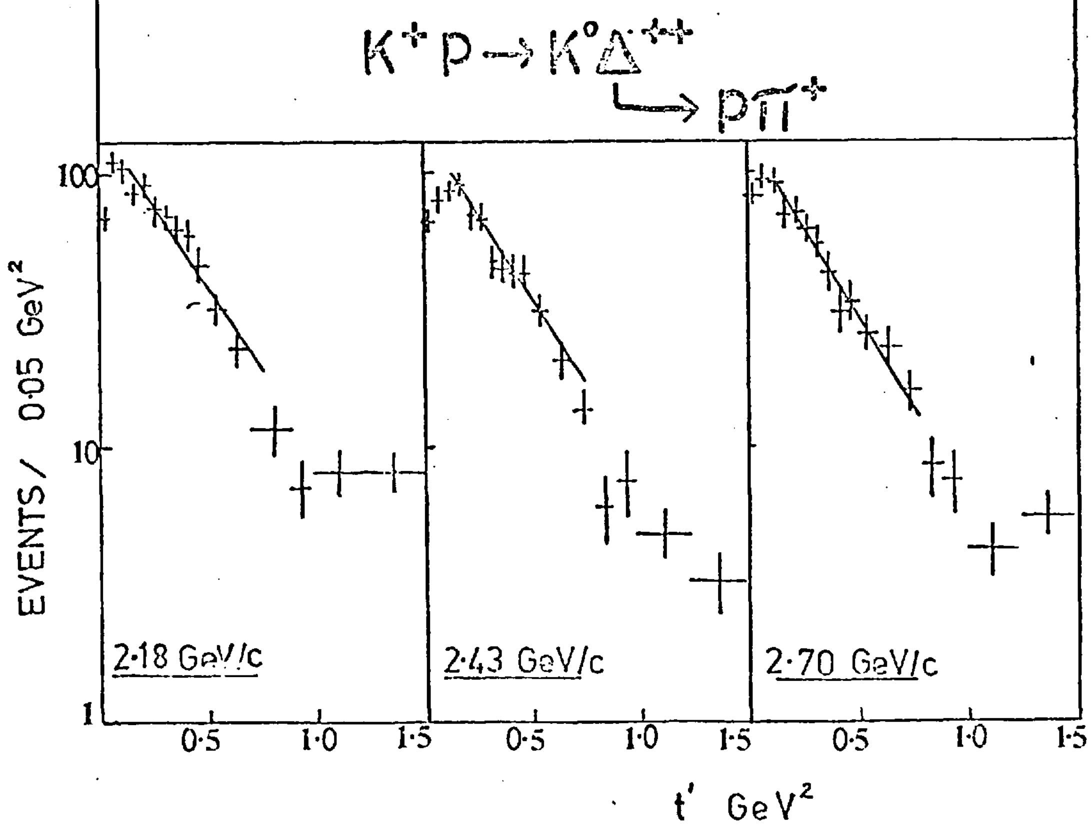
$K^+p \rightarrow K^0\Delta^{++}$
$\hookrightarrow p\pi^+$
EVENTS / 0·05 GeV²
2·18 GeV/c
2·43 GeV/c
2·70 GeV/c
t' GeV²

4.33

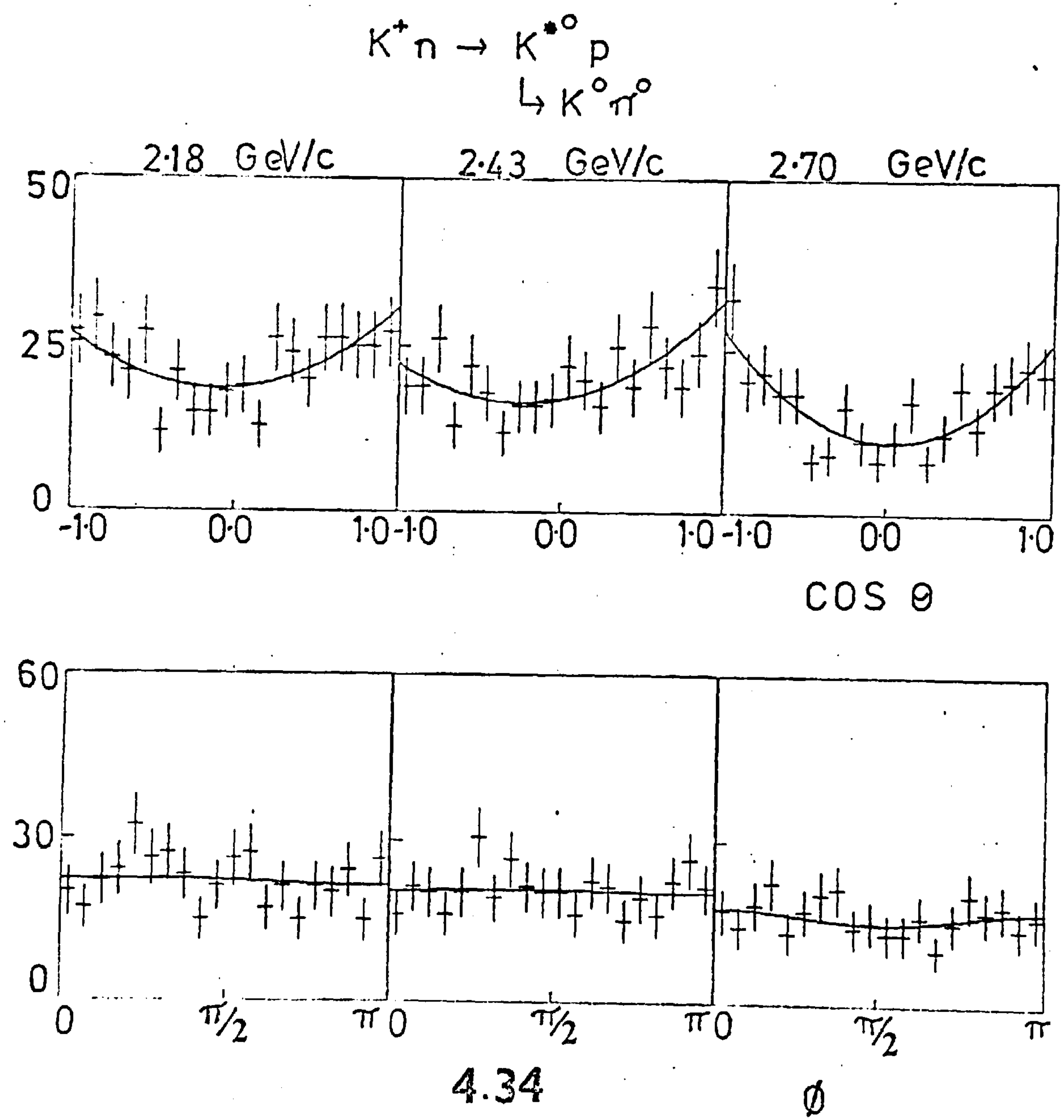

$K^+ n \rightarrow K^{*0} p$
$\hookrightarrow K^0 \pi^0$
2·18 GeV/c
2·43 GeV/c
2·70 GeV/c
50
25
0
-1·0
0·0
1·0
COS θ
60
30
0
π/2
π
ϕ

4.34

$K^{+}n \rightarrow K^{*+}n$
$\hookrightarrow K^{0}\pi^{+}$

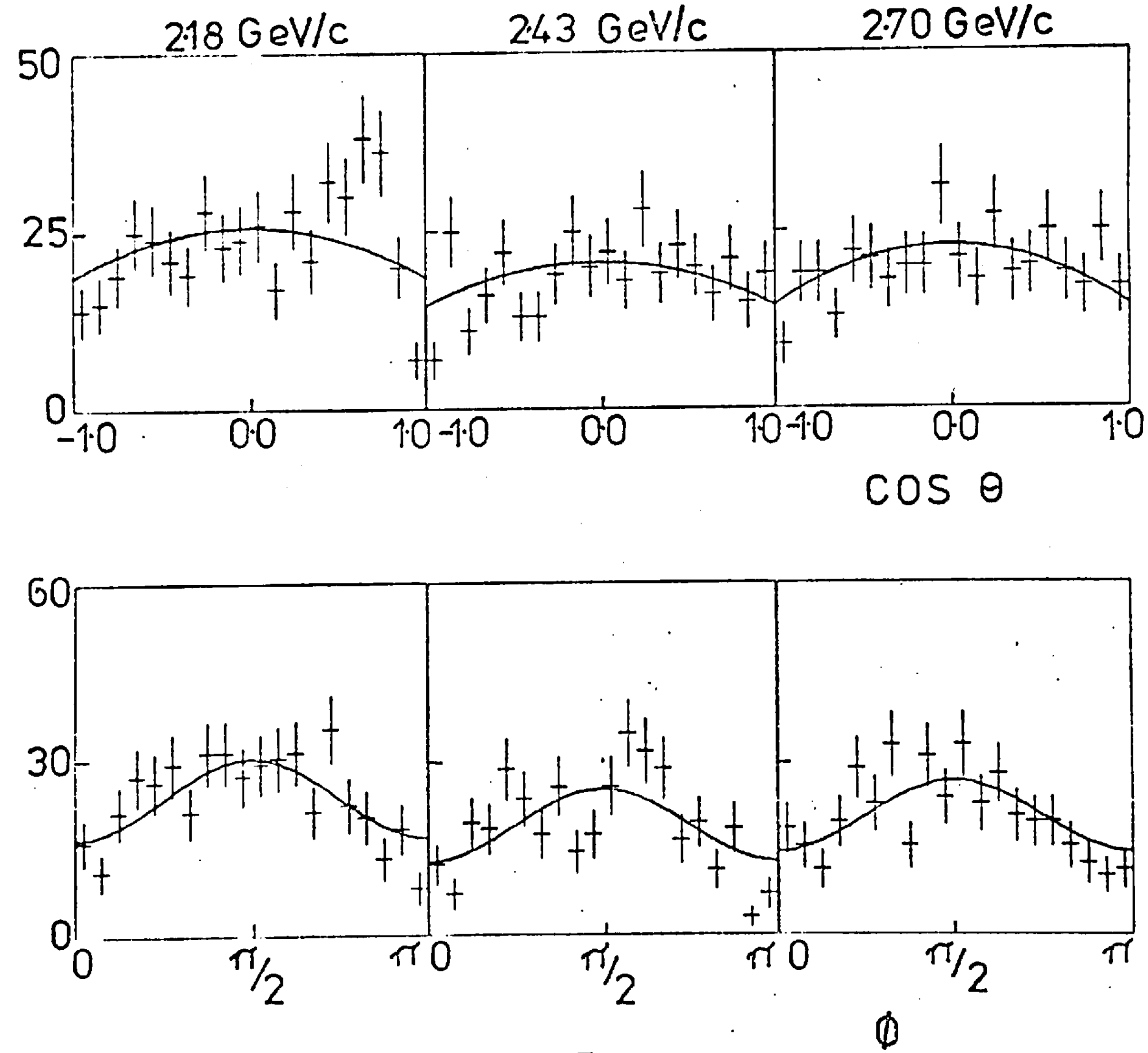

4.35

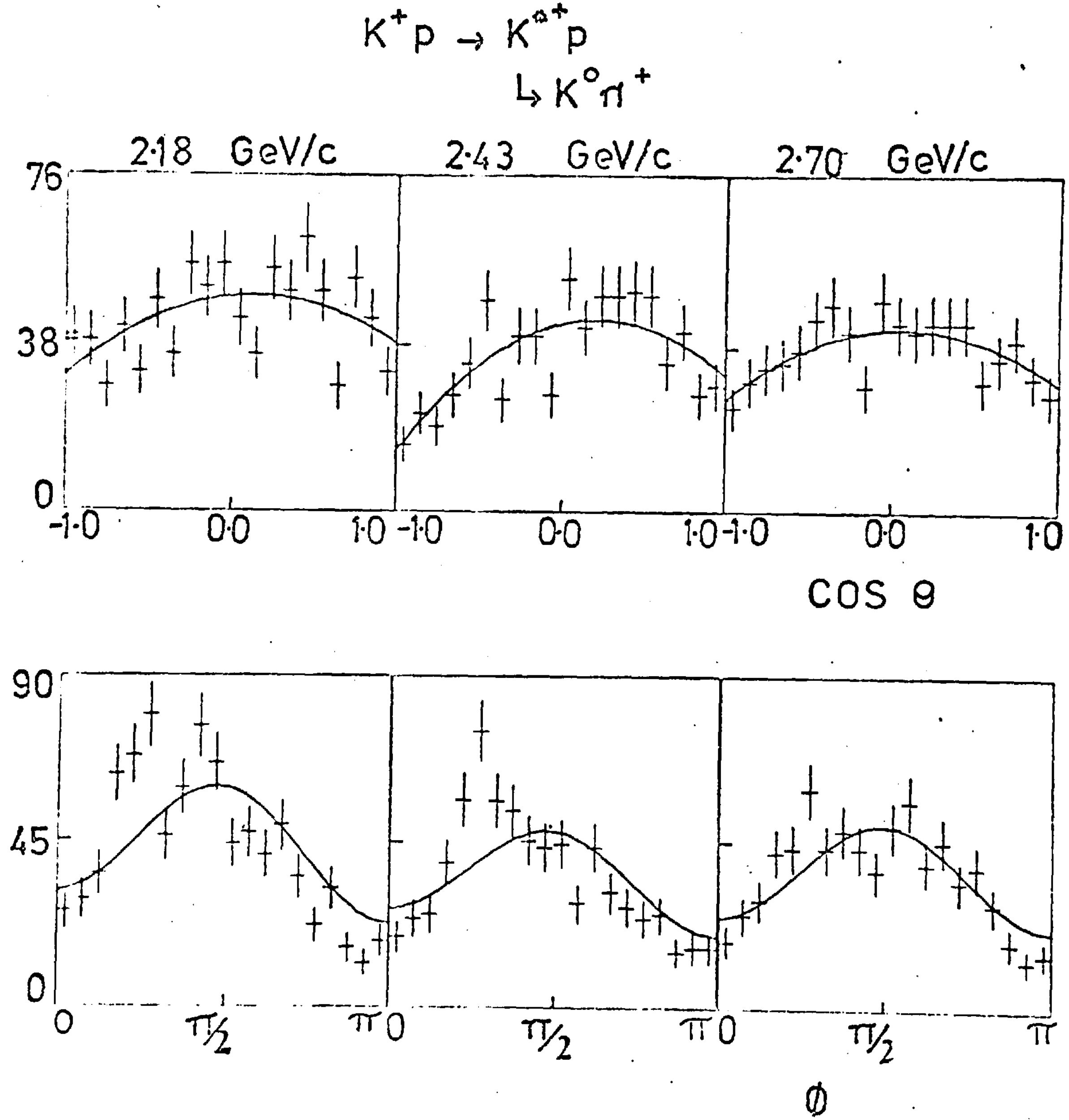
$K^+p \rightarrow K^{*+}p$
$\hookrightarrow K^0\pi^+$
2·18 GeV/c
2·43 GeV/c
2·70 GeV/c
76
38
0
-1·0
0·0
1·0
COS θ
90
45
0
0
π/2
π
φ

4.36

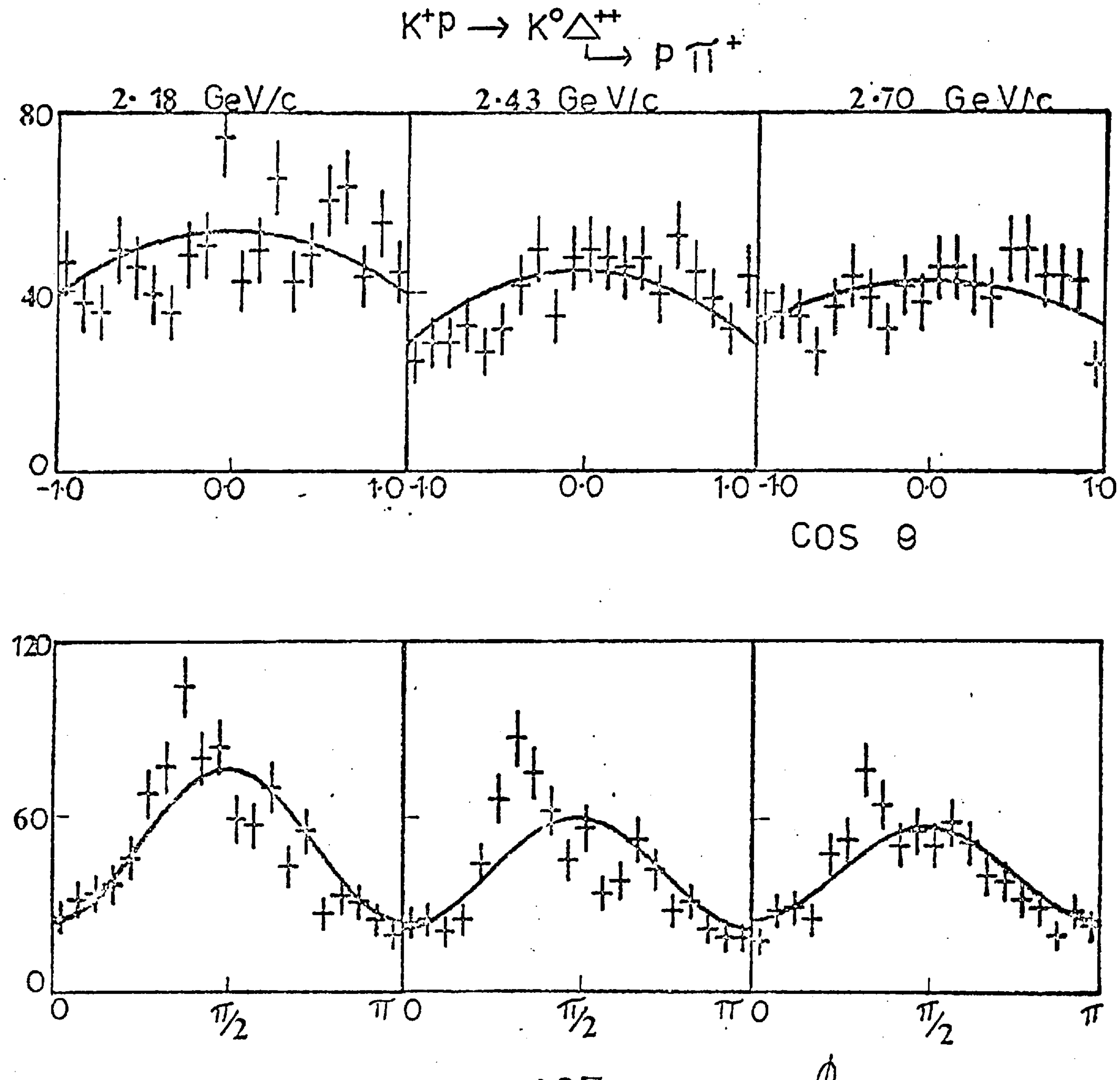
$K^+p \to K^0\Delta^{++}$
$\hookrightarrow p\pi^+$
2·18 GeV/c
2·43 GeV/c
2·70 GeV/c
80
40
0
-1·0
0·0
1·0
COS θ
120
60
0
π/2
π
φ

4.27

CHAPTER 5

As discussed earlier, there is a strong motivation to look for the existence of a $S=1$ baryon resonance. Recently Litchfield (1974) compared the existing K^+N phase shift analysis results with the πN phase shift analysis results and his finding is that the resonance solutions in the K^+N phase shifts look very similar to the background solutions in the πN phase shifts. This leaves a black shadow on the K^+N partial wave analyses. However, Aaron's prescription (1971) gives a dynamical mechanism for producing such Baryon resonances. He considered the rapid opening of some inelastic threshold and solved the relativistic three body equations using a K^* box potential. This led the SS1 and DD3 waves in the I=0 K^+N elastic scattering process to be resonating near the $K^*(890)$ threshold. These waves are in fact coupled to the K^*N S-waves. The present experiment is carried out near the $K^*(1420)$ threshold. So one would expect the partial waves coupled with the $K^*(1420)$-N S-wave would be driven resonant by a similar mechanism. Such waves in KN elastic scattering are PP3 and FF5 whereas in $K^+N \rightarrow K^*(890)N$, there are three waves PP3, FP5 and FF5 all coupled to the $K^*(1420)N$ S wave. Here one uses a LL'2J nomenclature for a partial wave where L, L' are the spectral notations of the orbital angular momenta in the initial and the final states and J is the total angular momentum of the system.

This experiment measures the elastic charge exchange reaction (Chapter 3) in the K^+N system. But that particular process is a mixture of isospin 1 and isospin 0 states. Since one does not measure two (one) prong events here, it does not have any data for the elastic noncharge exchange scattering. So here it is not possible to separate out the contribution of the isospin 1 and the isospin 0 states. Further due to the suppression factor for a K_o decay, the statistics is rather poor to carry out a partial wave analysis of the system. So here such a partial wave analysis has not been attempted.

However the $K^*(890)$ production (Chapter 4) has a large cross-section at this energy and so the statistical accuracy is better. Also here one observes the production of both neutral and charged K^* state and with neutron and proton targets. So it is possible to separate the different isospin states. Further the decay distribution of the $K^*(890)$ can be utilised to give information about the helicity state of the $K^*(890)$ meson. The continuous coverage of centre of mass energy from 2.2 to 2.6 GeV in this experiment is also useful for an energy dependent fit. With these facts in mind, one can proceed with a partial wave analysis of the system. The formalism of such an analysis has been developed in the folowing sections.

5.1. DATA

To have a systematic study of the charge exchange final state or $K^*(890)$ production, the distribution of the centre of mass scattering angle was investigated, the angle being measured from the beam direction. Since the target is unpolarised one can assume an azimuthal symmetry about the beam direction. So the differential cross-section can basically be given by the production angular distribution

$$\frac{d\sigma}{d\Omega} = \frac{\sigma}{2\pi N} \frac{dN}{d\cos\psi} \qquad 5.1.$$

where σ is the total channel cross-section, N is the total number of events in the distribution. The energy dependence of this production angular distribution is better understood when the angular distribution is expanded into a set of orthogonal d^J functions.

$$\frac{dN}{d\cos\psi} = \sum_{l=0}^{n} A_l \, d^l_{00}(\psi) \qquad 5.2.$$

The use of orthogonal functions has the advantage that the value of $(n+1)$, the total number of terms to be considered in the expansion does not affect any particular l^{th} coefficient. The orthogonality condition of the d^J function is given by

$$\int_{-1}^{1} d^J_{00}(\psi)\, d^{J'}_{00}(\psi)\, d\cos\psi = \frac{2}{2J+1}\,\delta_{JJ'} \qquad 5.3$$

Thus $$\int \frac{dN}{d\cos\psi}\, d^J_{00}(\psi)\, d\cos\psi = \int_{-1}^{1}\sum_l A_l\, d^l_{00}(\psi)\, d^J_{00}(\psi)\, d\cos\psi$$

$$\therefore\ A_J = \frac{2J+1}{2}\int d^J_{00}\, dN \qquad 5.4$$

For a large number of events, the integration in 5.4 can be replaced by a summation over the number of events

$$A_J = \frac{2J+1}{2}\sum_N d^J_{00} \qquad 5.5$$

Hence $$A_J/A_0 = (2J+1)\,\overline{d^J_{00}} \qquad 5.6$$

If one of the final state particles decay e.g. $K^*(890)$ decaying into K and π, the decay distribution gives further information about the production mechanism. If the decay distribution is given by $W(\theta,\phi)$, Then

$$W(\theta,\phi) = N'\sum_{\lambda_\alpha \lambda_\beta m m'} |M(\lambda_\alpha,\lambda_\beta)|^2\, D^j_{m\lambda}(\phi,\theta,0)\, D^{j*}_{m'\lambda}(\phi,\theta,0)\, \rho_{mm'} \qquad 5.7$$

where N' = a normalisation factor

$M(\lambda_\alpha,\lambda_\beta)$ = reduced matrix element for final state particles in helicity states λ_α and λ_β respectively

$\lambda = |\lambda_\alpha - \lambda_\beta|$

$\rho_{mm'}$ = density matrix element

Assuming a pure P wave decay of $K^*(890)$ ($J^P = 1^-$ state) into two pseudo-scalar states, $W(\theta,\phi)$ can be expressed as

$$W(\theta,\phi) = \frac{3}{4\pi}\Big[\sqrt{\frac{16\pi}{5}}\,\frac{1}{6}(3\rho_{00}-1)Y_{20} + \frac{\sqrt{4\pi}}{3}\,Y_{00} - \sqrt{\frac{32\pi}{15}}\,\rho_{1-1}\,\mathrm{Re}Y_{22} - \sqrt{\frac{64\pi}{15}}\,\mathrm{Re}\,\rho_{10}\,\mathrm{Re}Y_{21}\Big] \qquad 5.8$$

Thus $$W(\theta,\phi)\frac{dN}{d\cos\psi}=\sqrt{\frac{1}{4\pi}}\,Y_{00}\frac{dN}{d\cos\psi}+\sqrt{\frac{1}{20\pi}}\,Y_{20}(3\rho_{00}-1)\frac{dN}{d\cos\psi}-\sqrt{\frac{12}{5\pi}}\,\mathrm{Re}\rho_{10}\,\mathrm{Re}Y_{21}\frac{dN}{d\cos\psi}-\sqrt{\frac{6}{5\pi}}\,\rho_{1-1}\,\mathrm{Re}Y_{22}\frac{dN}{d\cos\psi} \qquad 5.9$$

One expands the angular distribution $\rho_{mm'}\frac{dN}{d\cos\psi}$ in terms of orthogonal polynomials as

$$\rho_{mm'}\frac{dN}{d\cos\psi}=\sum_l a_l\, d^l_{M0}(\psi) \qquad 5.10$$

where $M = m - m'$

Thus $$W(\theta,\phi)\frac{dN}{d\cos\psi}=\left(\sqrt{\frac{1}{4\pi}}\,Y_{00}-\sqrt{\frac{1}{20\pi}}\,Y_{20}\right)\sum_{l=0}A_l\, d^l_{00}(\psi)+\sqrt{\frac{1}{20\pi}}\,Y_{20}\sum_{l=0}B_l\, d^l_{00}(\psi)-\sqrt{\frac{12}{5\pi}}\,\mathrm{Re}Y_{21}\sum_{l=1}C_l\, d^l_{10}(\psi)-\sqrt{\frac{6}{5\pi}}\,\mathrm{Re}Y_{22}\sum_{l=2}D_l\, d^l_{20}(\psi) \qquad 5.11$$

Using orthogonality conditions of d^J functions and spherical harmonics, one gets

$$\begin{aligned}
A_l &= \sqrt{\frac{1}{4\pi}}\,\frac{2l+1}{2}\int Y_{00}\, d^l_{00}\, dN\\
B_l &= \sqrt{\frac{20}{\pi}}\,\frac{2l+1}{6}\int Y_{20}\, d^l_{00}\, dN + \frac{A_l}{3}\\
C_l &= -\sqrt{\frac{5}{12\pi}}\,\frac{2l+1}{2l(l+1)}\int \mathrm{Re}Y_{21}\, d^l_{10}\, dN\\
D_l &= -\sqrt{\frac{5}{6\pi}}\,\frac{2l+1}{2(l+2)(l+1)l(l-1)}\int \mathrm{Re}Y_{22}\, d^l_{20}\, dN
\end{aligned} \qquad 5.12$$

The number of polynomials contributing to the angular distribution is related to the number of partial waves in the reaction. Because of angular momentum conservation one expects in a reaction which contains partial waves with total spin up to J, the maximum number of coefficients to be less than or equal to 2J. In a semi classical argument, one can have a further restriction on the relative orbital momentum L_{max} in a partial wave

$$p\cdot b \sim \sqrt{l_{max}(l_{max}+1)}\,\hbar \qquad 5.13$$

where p is the incident momentum and b is the impact parameter. Taking b to be the pion compton wavelength, one finds that at this energy L = 3,4 waves begin to become significant. This puts an upper limit of n to be 7 or 9. However this idea is rather crude. Different processes depending on the t-channel exchanged particles have different values of b, e.g. π exchange processes are in general more peripheral than vector exchange reactions and hence have a larger value of b. The method one uses here to calculate n is to calculate the coefficients by the method of moments and then to decide, by looking at the data, the value of l beyond which the coefficients are compatible with zero. The coefficients beyond this particular value of l are truncated and not considered in the subsequent part of the analysès.

In the case of elastic charge exchange reaction, the initial and final states are mixed isospin states. So one can obtain the scattering amplitude of the process, assuming isospin invariance in strong interaction,

$$\begin{aligned} \langle K^+n|T|K^\circ p\rangle &= \langle 1/2, 1/2, 1/2, -1/2|T|1/2, 1/2, -1/2, 1/2\rangle \\ &= (1/\sqrt{2}\langle 1\ 0| + 1/\sqrt{2}\langle 0\ 0|)|T|(1/\sqrt{2}|1\ 0\rangle - 1/\sqrt{2}|0\ 0\rangle) \\ &= \frac{1}{2}(T_1 - T_0) \end{aligned} \qquad 5.14$$

So in the coefficients A_l's of the polynomial expansion of the angular distribution, one sees the joint effect of isospin 1 and isospin 0 states.

However in the case of $K^*(890)$ production one can have three different reactions

I	$K^+p \rightarrow K^{*+}(890)p$	5.15
II	$K^+n \rightarrow K^{*+}(890)n$	5.16
III	$K^+n \rightarrow K^{*\circ}(890)p$	5.17

And the amplitudes for these three processes can be written in terms of pure isospin (0 and 1) amplitudes as

$$T_1 = T_1 \qquad 5.18$$

$$T_{II} = \frac{1}{2}(T_1 + T_0) \qquad 5.19$$

$$T_{III} = \frac{1}{2}(T_1 - T_0) \qquad 5.20$$

Thus $$T_1 T_1^* = T_I T_I^* \qquad 5.21$$

and $$T_0 T_0^* = 2(T_{II}T_{II}^* + T_{III}T_{III}^*) - T_I T_I^* \qquad 5.22$$

Hence one can separate out the two isospin contributions.

Further one can utilise the centre of mass energy spreading due to the Fermi motion of the nucleons inside the deuteron nucleus. This effect when combined with the beam energy spreading and also with the choices of three different beam momenta, gives more or less a uniform population of events between 2.2 GeV and 2.6 GeV in the centre of mass energy.

For the elastic charge exchange reaction, the coefficients have been shown up on figure 3.10. As has been mentioned earlier, this shows coefficients up to A_7 to be significantly different from 0 and there is a dip in the coefficients A_3, A_4, A_5 at about 2.4 GeV. For the I=1 contribution to the $K^*(890)$ production there is a dip in the coefficients A_4, A_5, A_6 near 2.5 GeV and coefficients beyond l =7 are compatible with zero (figures 5.1, 5.2, 5.3, 5.4). The isospin zero components (figures 5.5, 5.6, 5.7, 5.8) has significant structures in A_4, A_5, A_6, A_7, A_8. This uses a larger number of polynomials. This is probably due to the fact that the process 5.17 involves pion exchange whereas the reactions 5.15 and 5.16 are dominated by some vector exchange processes.

5.2 FORMALISM

To express the partial differential cross-section as a series of partial wave products and orthogonal d^J functions, the approach of S.M.Deen (1968) via helicity amplitudes was used. In an inelastic scattering process $A+B \to C+D$, the differential cross-section can be written in terms of the helicity states amplitudes as

$$\frac{d\sigma}{d\Omega} = \left(\frac{2\pi}{k}\right)^2 \sum_{\lambda_A\lambda_B\lambda_C\lambda_D} |\langle \hat{x}_f, \lambda_C\lambda_D|T|\hat{x}, \lambda_A\lambda_B\rangle|^2 \qquad 5.23$$

where $\lambda_A, \lambda_B, \lambda_C, \lambda_D$ are the helicity states of A,B,C,D respectively: T is the scattering matrix: $\hat{x}$, $\hat{x}_f$ are unit vectors along the directions P_A and P_C in the overall centre of mass frame and K is the initial state centre of mass momentum.

Introducing the JM representation in initial and final states, one gets

$$\langle \hat{x}_f, \lambda_C\lambda_D|T|\hat{x}, \lambda_A\lambda_B\rangle = \sum \frac{2J+1}{4\pi} D^{J*}_{M\mu}(\phi_f, \theta_f, \phi_f)$$
$$\cdot \langle \lambda_C\lambda_D|T^J|\lambda_A\lambda_B\rangle D^J_{M\lambda}(\phi, \theta, \phi) \qquad 5.24$$

where $\lambda = \lambda_A - \lambda_B$; $\mu = \lambda_C - \lambda_D$. θ , ϕ , θ_f , ϕ_f are the polar and azimuthal angles defined in the barycentric frame of initial and final states respectively. The assumption of choosing the initial direction $\hat{x}$ to coincide with the z-axis makes the expansion a lot simpler

$$D^J_{M\lambda}(\phi, 0, \phi) = \exp(i(\lambda - M)\phi)\, d^J_{M\lambda}(0) = \delta_{M\lambda} \qquad 5.25$$

Thus

$$\langle x_f, \lambda_C\lambda_D|T|x, \lambda_A\lambda_B\rangle = \sum_J \frac{2J+1}{4\pi} \langle \lambda_C\lambda_D|T^J|\lambda_A\lambda_B\rangle\, d^J_{\lambda\mu}(\theta_f)$$
$$\cdot \exp(i(\lambda-\mu)\phi_f) \qquad 5.26$$

The total cross-section for unpolarised particles can be worked out using the following result for the product of two d^J functions

$$d^J_{\lambda\mu}(\theta)\, d^{J'}_{\lambda'\mu'}(\theta) = \sum_{l=|J-J'|}^{J+J'} \langle l, \lambda-\lambda' | J, J', \lambda, -\lambda'\rangle \langle l, \mu-\mu' | J, J', \mu, -\mu'\rangle$$
$$\cdot (-1)^{\lambda'-\mu'} d^l_{\lambda'-\lambda, \mu'-\mu}(\theta) \qquad 5.27$$

Then
$$\frac{d\sigma}{d\Omega_f} = \frac{\pi^2 k^2}{(2S_A+1)(2S_B+1)} \sum_{\substack{\lambda_A\lambda_B \\ \lambda_C\lambda_D}} \sum_{J\,J'} (2J+1)(2J'+1)\,(-1)^{\lambda-\mu} \langle \lambda_C\lambda_D|T^J|\lambda_A\lambda_B\rangle^*$$

$$\cdot \langle \lambda_C\lambda_D|T^{J'}|\lambda_A\lambda_B\rangle \sum \langle l,0|J,J',\lambda,-\lambda\rangle \langle l,0|J,J',\mu,-\mu\rangle\, d^l_{00}(\theta_f) \qquad 5.28$$

If however the helicity state of C in the final state is determined from a study of its decay density matrix elements the relation 5.28 can be modified to

$$\rho_{\lambda_c \lambda_c'} \frac{d\sigma}{d\Omega_f} = \frac{\pi^2 k^2}{(2S_A+1)(2S_B+1)} \sum_{\lambda_A \lambda_B \lambda_D} \sum_{J J'} (2J+1)(2J'+1)(-1)^{\lambda-\mu} \langle \lambda'_C \lambda_D | T^J | \lambda_A \lambda_B \rangle^*$$

$$\langle \lambda_C \lambda_D | T^J | \lambda_A \lambda_B \rangle \sum_l \langle l,0 | J,J,\lambda,-\lambda \rangle \langle l,m | J,J,\mu,-\mu' \rangle d^l_{m0}(\theta_f) \qquad 5.29$$

where $\mu' = \lambda'_C - \lambda_D$ and $m = |\mu - \mu'|$

To expand the helicity states into orbital angular momentum states, a Clebsch-Gordan transformation was used

$$\langle \lambda_C \lambda_D | T^J | \lambda_A \lambda_B \rangle = \sum_{l s l' s'} \langle \lambda_C \lambda_D | JMls \rangle \langle JMls | T | JMl's' \rangle \langle JMl's' | \lambda_A \lambda_B \rangle$$

$$= \sum_{l s l' s'} \langle l, s, 0, \mu | J, \mu \rangle \langle S_C, S_D, \lambda_C, -\lambda_D | s, \mu \rangle \langle l', s', 0, \lambda | J, \lambda \rangle$$

$$\cdot \langle S_A, S_B, \lambda_A, -\lambda_B | s', \lambda \rangle \langle l, s | T^J | l', s' \rangle \quad \frac{\sqrt{(2l+1)(2l'+1)}}{(2J+1)} \qquad 5.30$$

$$\text{Thus } \rho_{\lambda_c \lambda_c'} \frac{d\sigma}{d\Omega_f} = \frac{\pi^2 k^2}{(2S_A+1)(2S_B+1)} \sum \sqrt{(l_1'+1/2)(l_1+1/2)(l_2'+1/2)(l_2+1/2)} \; (-1)^{\lambda-\mu}$$

$$C^{l_2 S_2 J}_{0 \mu \mu} \; C^{S_C S_D S_2}_{\lambda_C \lambda_D \mu} \; C^{l_1 S_1 J}_{0 \lambda \lambda} \; C^{S_A S_B S_1}_{\lambda_A \lambda_B \lambda} \; C^{S_C S_D S_2'}_{\lambda_C' \lambda_D \mu'} \; C^{l_2' S_2' J'}_{0 \mu' \mu'} \; C^{l_1' S_1' J'}_{0 \lambda \lambda}$$

$$C^{S_A S_B S_1}_{\lambda_A \lambda_B \lambda} \; C^{J J' l}_{\lambda -\lambda 0} \; C^{J J' l}_{\mu -\mu' m} \; \langle l \; S | T^J | l \; S \rangle^*$$

$$\langle l' \; S' | T^{J'} | l' S' \rangle \quad d^l_{m0}(\theta_f) \qquad 5.31$$

where $C^{l_1 l_2 l}_{m_1 m_2 m}$ represents the Clebsch Gordan coefficient $\langle l_1, l_2, m_1 m_2 | l, m \rangle$.

On the other hand from 5.10

$$\rho_{\lambda_c \lambda_c'} \frac{d\sigma}{d\Omega} = \lambda\!\!\!^{-2} \sum a_l \; d^l_{m0}(\theta_f)$$

Thus each of these polynomial coefficients can be expressed in terms of the products of partial waves as

$$a_l = \sum R_l(l_1, l_2, J, l_1', l_2', J') \; \langle l_2 | T^J | l_1 \rangle^* \langle l_2' | T^{J'} | l_1' \rangle \qquad 5.32$$

where R_l's are the Tripp's coefficients.

In this experiment one studies spin $0^- \frac{1}{2}^+ \rightarrow 0^- \frac{1}{2}^+$ scattering in the case of elastic charge exchange process and also $0^- \frac{1}{2}^+ \rightarrow 1^- \frac{1}{2}^+$ scattering for the $K^*(890)$ production reaction. That the strong interaction is invariant under parity transformation makes a constraint on the partial waves. Parity conservation leads to

$$\langle l' S' | T^J | l S \rangle = \eta \langle l' S' | T^J | l S \rangle \qquad 5.33$$

where $\eta = \frac{\eta_C \eta_D}{\eta_A \eta_B} (-1)^{l'-l}$

$\eta_A, \eta_B, \eta_C, \eta_D$ being the intrinsic parities of the particles A,B,C,D. Thus in this case, l and l' can differ by zero or multiples of 2 to have a nonzero partial wave.

5.3 ANALYSIS AND RESULTS

The elastic charge exchange process has all coefficients beyond a_7 to be compatible with zero. So one needs to consider partial waves up to $J = 7/2$. Angular momentum conservation together with parity conservation restrict the number of partial waves to 8. They have been listed in table 5.1 and their contributions to various d^J function coefficients, via Tripp's coefficients have been summarised in table 5.2. The energy dependence of A_1 and A_2 is reasonably smooth. In the coefficient A_3 it starts to show a structure near 2.4 GeV. This structure is dominantly present in A_4 and also A_5. But it again starts to smooth out in A_6 and A_7. The structure in A_3 or A_4 is prominent by at least two standard deviations. So one should look for partial wave combination whose relative contribution to A_3 or A_4 is at least 4 times in magnitude than that to A_1 or A_2.

Only the $J = 7/2$ waves contribute to the coefficients A_6 and A_7. The facts that A_6 and A_7 are small and quite structureless, suggest that the

J=7/2 waves are rather small and structureless at this energy. A look at the table 5.2 suggests that the interference of J=½ and J=7/2 waves has a large contribution to A_3 and A_4 as compared to zero contribution to A_1 and A_2. So this could be a possible candidate for the cause of the structure. Since one assumes J=7/2 waves are structureless, one is left with J=½ waves. However the interference of J=½ waves with J=3/2 or 5/2 waves have significant contribution to A_1 and A_2. So either the J=3/2 and 5/2 waves also have some inherent structures to compensate the effects of J=½ waves or the J=½ waves are rather structureless. If one assumes minimum structure in the partial waves, i.e. there is only one partial wave which is causing all the structures at 2.4 GeV and if also one considers the structure in A_5, one is left with J= 3/2 or J=5/2 partial waves. However, these assumptions are not based on any physics reasoning and so one cannot possibly conclude about the energy dependence of the partial waves.

For $K^*(890)$ production process, the number of partial waves to be considered are quite large in number. The parity constraint reduces the number of partial waves to four for each J value. However for J=1/2 this number is 3. If one compares the number of partial waves to be considered to the total number of observables at each energy, one finds that the number of degrees of freedom in an energy independent fit to be zero. There is no obvious way of truncating the partial waves. One can assume that due to angular momentum suppression factor, higher L value partial waves should be small compared to the smaller L waves. So fits were tried where LL'' 2J wave was omitted if there exists a LL'2J wave with L'< L''. But this procedure could not lead to a minimum in the minimising routine.

A partial wave was parametrised as

$$T^J \equiv f = A^J \exp(i\phi^J) \qquad 5.34$$

where A^J is the amplitude and ϕ^J is the phase. A^J was restricted between 0.0 and 0.5 due to the unitarity bound. An angular momentum barrier factor for the final states was introduced by $(q')^{L'}$, q' being the centre of mass momentum in the final state.

For the isospin 1 component, all the partial waves with $J \leq 7/2$ were included (table 5.1). The energy dependence of the partial wave was introduced by parametrising A^J and ϕ^J as functions of energy. ϕ^J was parametrised to be a linear function of the initial state centre of mass momentum whereas a little more complicated parametrisation of A^J was required to restrict it within the unitarity bound.

$$\phi^J = \phi^\circ + \phi' q \qquad 5.35$$

$$A^J = \frac{0.5}{1+(A^\circ + A'q)^2} \qquad 5.36$$

A x^2 minimisation method was used to fit the moments, using the Tripp's coefficients. As can be seen, the fit is quite sensitive to the parametrisation of the amplitude. But one cannot go for a freer parametrisation since this will increase the number of parameters in the fit significantly and thereby reducing the efficiency of the minimising programme. In the several random starts, one usually gets the same broad features regarding the partial waves. As the whole procedure is rather crude, one cannot expect to get an exact reproduction in all the different random starts, x^2 per degree of freedom at the minimised position is approximately 1.6. In all the fits, the phase of SD1 was always fixed to zero since there is always one undetermined overall phase in the analysis. This makes the direct comparisons of various fits a lot easier. The partial wave amplitudes have been shown on figure 5.9.

The large partial waves in the fits are SD1, PP1, PF3, DD3. All the J=7/2 waves are very small in magnitude. PP3, DD5 and FP5 were also found to be small. The phase variation of DD3 with respect to SD1 is large, all other partial waves have much slower variation in phase with respect to the SD1 wave. The partial waves SS1, and FF5 vary wildly in different runs, thus the fits are quite insensitive to those partial waves. The partial waves DS3 and DG5 were found to be strongly energy dependent. They increase in magnitude but the phase variations are small. All the fits thus agree with the fact that the partial wave DD3 stays large throughout the energy region and has got a relatively strong phase variation.

In the case of isospin zero case, the situation was much more complicated since one has to consider up to 9th order polynomials and thus go over to theJ=9/2 partial waves. This was necessary because the energy independent fits (with zero constraints) cannot find a minimum at the highest energy point without the 9/2 partial waves. Also the crude calculation with the idea of impact parameter suggests G and H waves are opening up near a centre of mass energy of 2.5 GeV in the pion exchange process. In this case, one however gets two distinct solutions. The difference in the solutions mainly arise from the behaviour of the partial wave SS1. SS1 in both the solutions was found to be large, but in one solution, it stays at the same phase with the partial wave SD1 whereas in the other it is changing a lot in the energy region considered (figure 5.10) here. The partial waves DS3, FP5, GD7 and HF9 are all large and relatively in the same phase. They are quite stable in the different solutions. However their variation of phase with respect to SD1 is quite large. Also PF3, DG5, FH7, GI9 have similar phase dependence and large amplitude. PP1 is also large but the fit is insensitive to its phase. The rest of the partial waves are relatively small in size. But the orders of magnitude of the largest and the smallest partial waves are not very different. Also the phase variation of these partial waves with respect to the SD1 is quite small. The fit to the data points is not very good as can be seen in the figures 5.5 - 5.8. The x^2 per degree of freedom is 2.0 which is rather large. This may be attributed to the fact that the large number of parameters involved in the fitting procedure. This makes the minimising routine going very slowly and ending up at some secondary minimum points. Also a freer energy dependent parametrisation seems to be necessary.

In these crude fits one does not find a partial wave which dominates over the others and has the major contribution to the total cross-section. This observation goes against the possibility of a Z^* resonance at this energy. A serious conclusion cannot however be made. One needs more data points and also should consider a real three body analysis to accommodate the reflection of the Δ-production in the $N\pi$ channel.

TABLE 5.1

PARTIAL WAVES TO BE CONSIDERED FOR THE PROCESS $K^+n \to K^op$.	PARTIAL WAVES TO BE CONSIDERED FOR THE PROCESS $K^+N \to K^*(890)N(I=1)$	PARTIAL WAVES TO BE CONSIDERED FOR THE PROCESS $K^+N \to K^*(890)n(I=0)$
SS1	SS1	SS1
PP1	SD1	SD1
PP3	PP1	PP1
DD3	PP3	PP3
DD5	PF3	PF3
FF5	DS3	DS3
FF7	DD3	DD3
DD7	DD5	DD5
	DG5	DG5
	FP5	FP5
	FF5	FF5
	FF7	FF7
	FH7	FH7
	GD7	GD7
	GG7	GG7
		GG9
		GI9
		HF9
		HH9

TABLE 5.2

TRIPP'S COEFFICIENTS FOR $0^{-}\frac{1}{2}^{+} \rightarrow 0^{-}\frac{1}{2}^{+}$ SCATTERING

	A_o	A_1	A_2	A_3	A_4	A_5	A_6	A_7
SS1*SS1+PP1*PP1	1							
SS1*PP1		2						
SS1*PP3+PP1*DD3		4						
SS1*DD3+PP1*PP3	0		4					
SS1*DD5+PP1*FF5	0		6					
SS1*FF5+PP1*DD5		0		6				
SS1*FF7+PP1*GG7		0		8				
SS1*GG7+PP1*FF7	0		0		8			
PP3*PP3+DD3*DD3	2		2					
PP3*DD3		4/5		36/5				
PP3*DD5+DD3*FF5		36/5		24/5				
PP3*FF5+DD3*DD5	0		12/7		72/7			
PP3*FF7+DD3*GG7	0		72/7		40/7			
PP3*GG7+DD3*FF7		0		8/3		40/3		
DD5*DD5+FF5*FF5	3		24/7		18/7			
DD5*FF5		18/35		16/5		100/7		
DD5*FF7+FF5*GG7		72/7		8		40/7		
DD5*GG7+FF5*FF7	0		8/7		360/77		200/11	
FF7*FF7+GG7*GG7	4		100/21		324/77		100/33	
FF7*GG7		8/21		24/11		600/91		9800/429

ISOSPIN 1

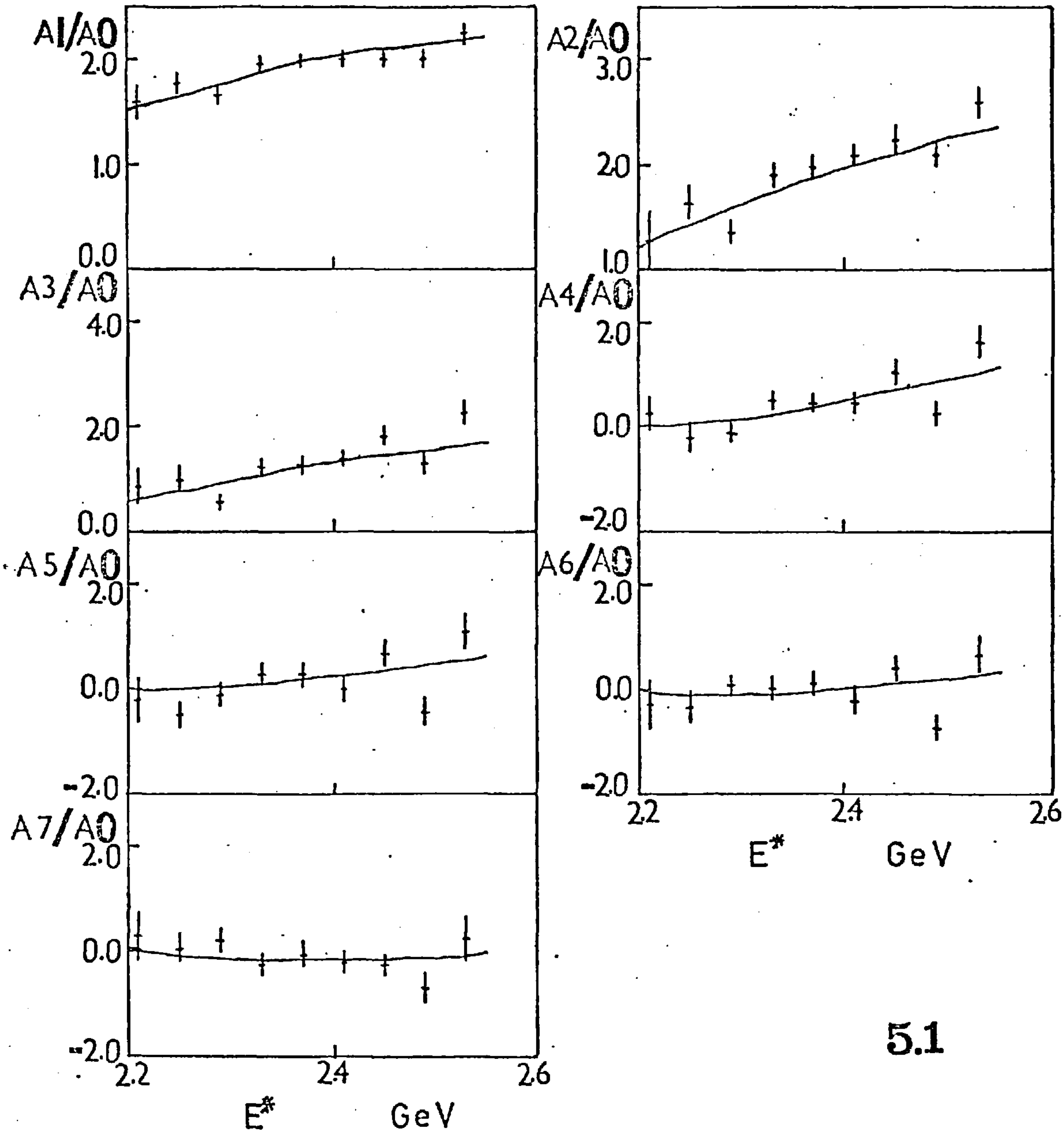
A1/A0
2.0
1.0
0.0
A2/A0
3.0
2.0
1.0
A3/A0
4.0
2.0
0.0
A4/A0
2.0
0.0
-2.0
A5/A0
2.0
0.0
-2.0
A6/A0
2.0
0.0
-2.0
2.2
2.4
2.6
E*
GeV
A7/A0
2.0
0.0
-2.0
2.2
2.4
2.6
E*
GeV

5.1

ISOSPIN 1

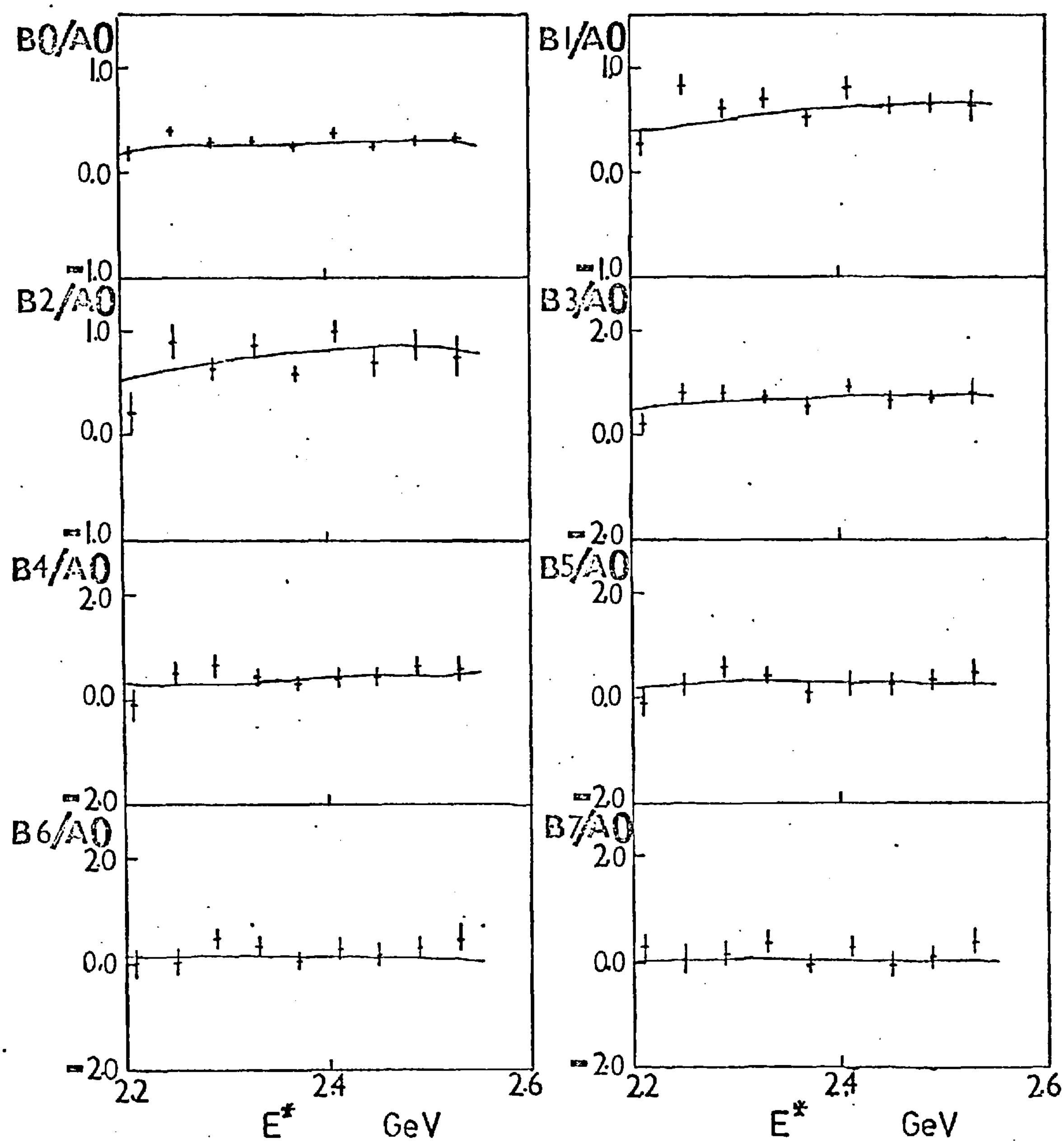
B0/A0
B1/A0
B2/A0
B3/A0
B4/A0
B5/A0
B6/A0
B7/A0
1.0
0.0
-1.0
2.0
-2.0
2.2
2.4
2.6
E* GeV

5.2

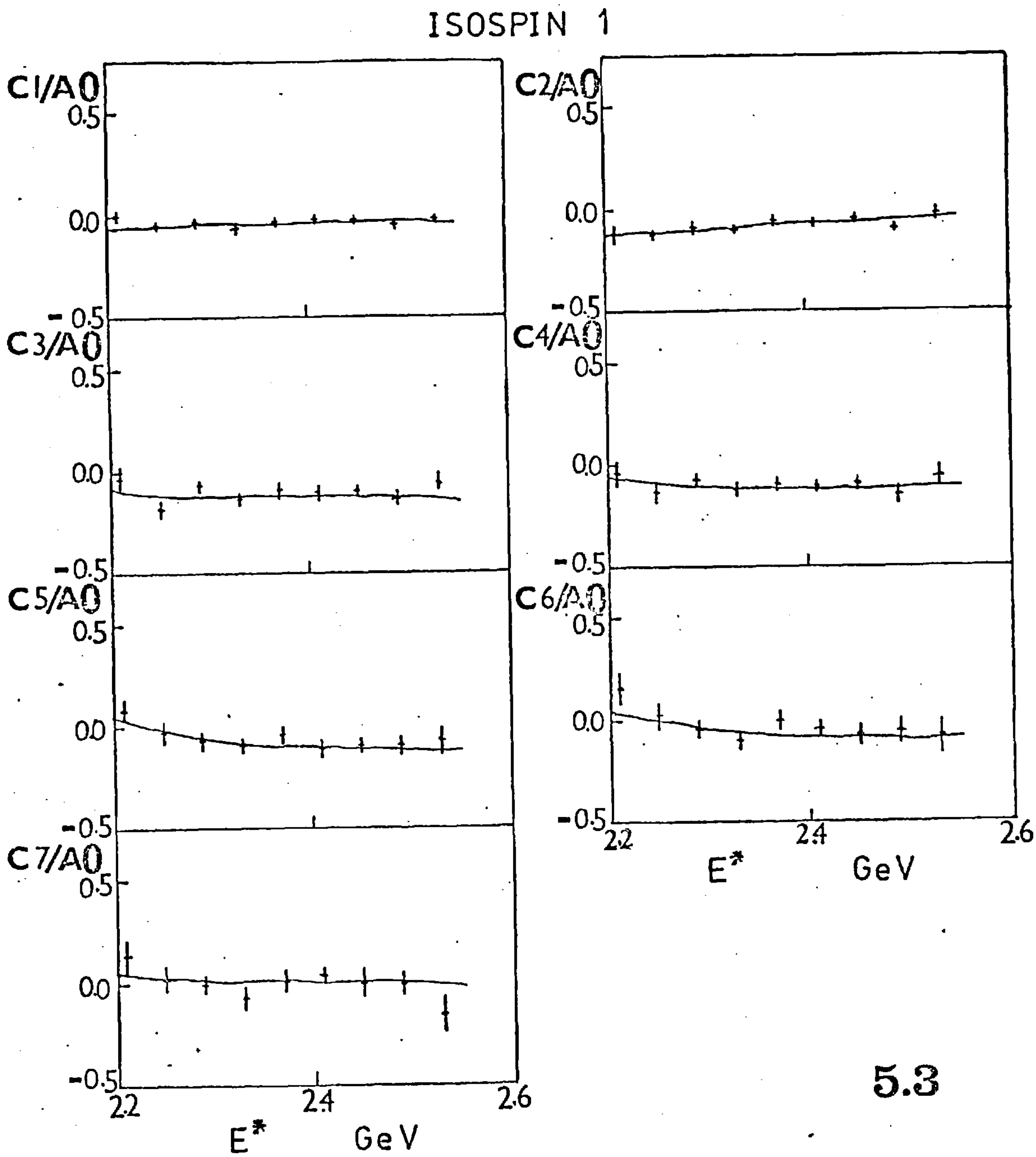
ISOSPIN 1
C1/A0
C2/A0
C3/A0
C4/A0
C5/A0
C6/A0
C7/A0
0.5
0.0
-0.5
2.2
2.4
2.6
E*
GeV

5.3

ISOSPIN 1

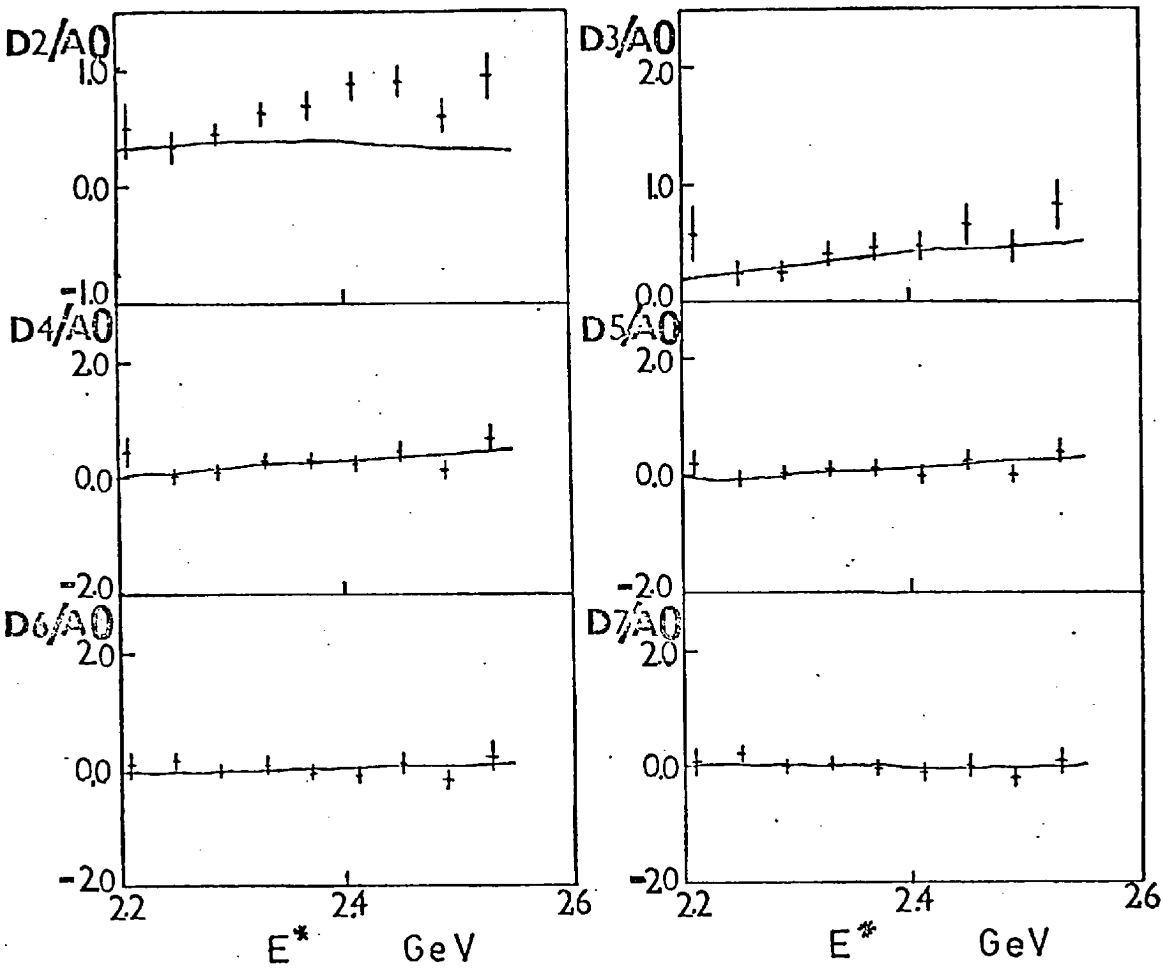

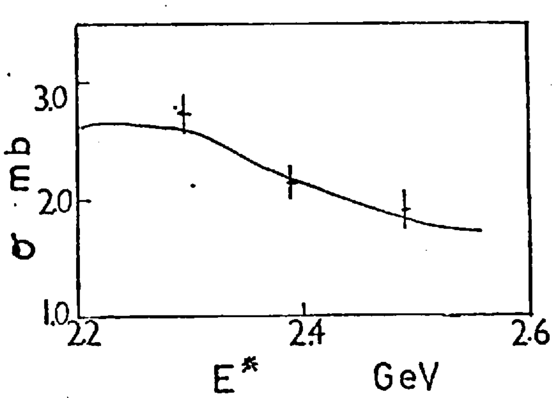

5.4

ISOSPIN 0

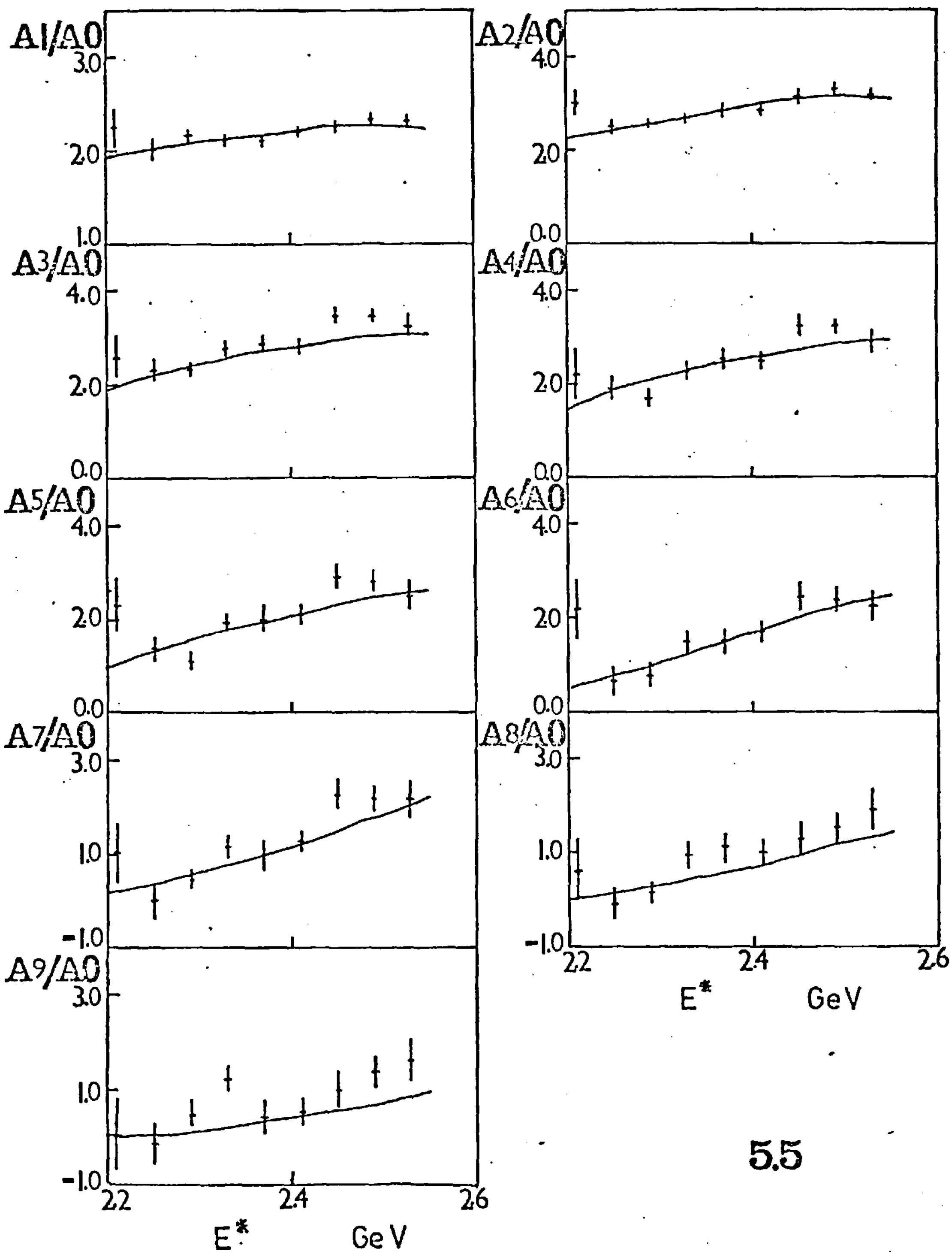

5.5

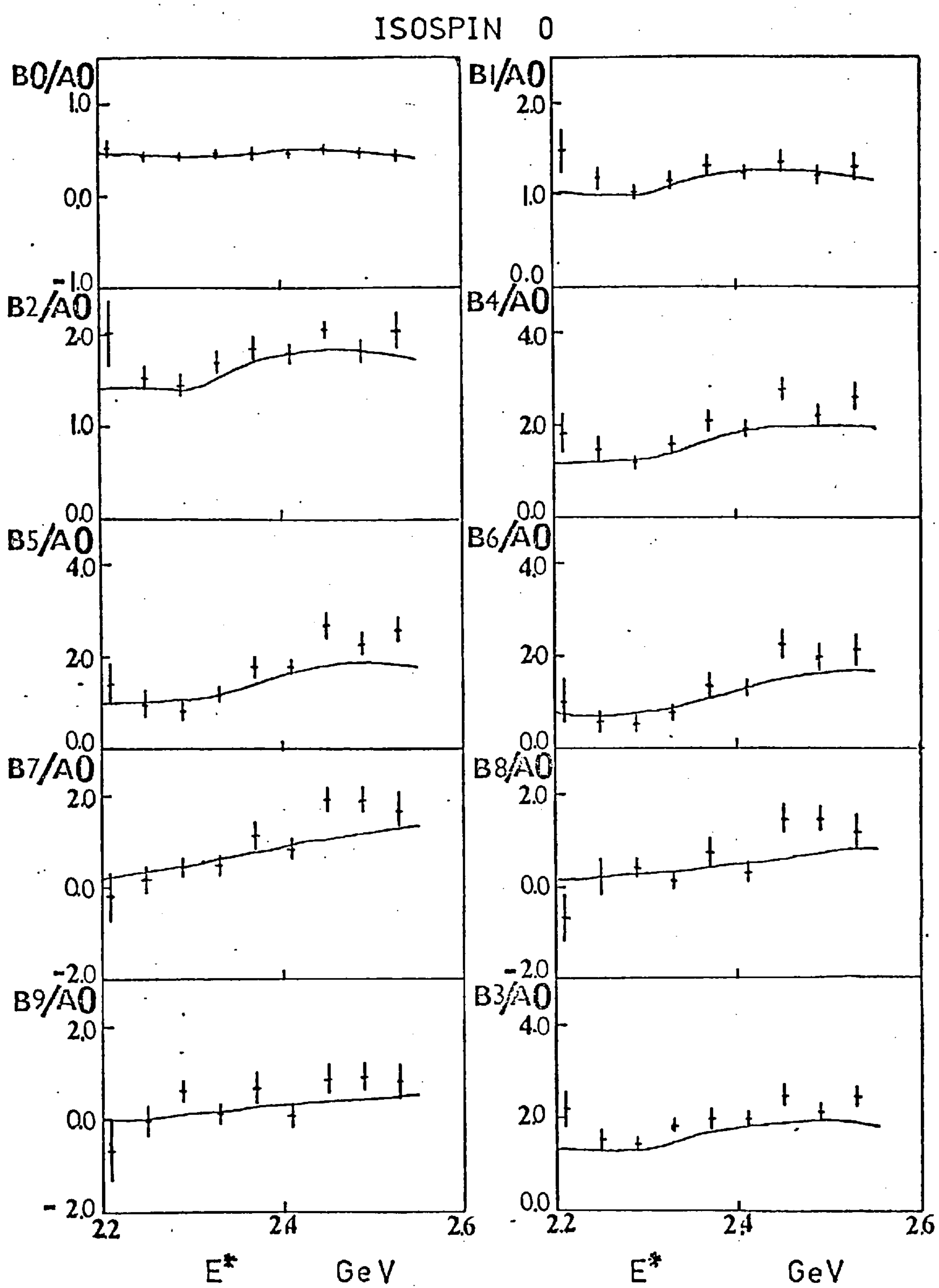
ISOSPIN 0
B0/A0
1.0
0.0
-1.0
B1/A0
2.0
1.0
0.0
B2/A0
2.0
1.0
0.0
B4/A0
4.0
2.0
0.0
B5/A0
4.0
2.0
0.0
B6/A0
4.0
2.0
0.0
B7/A0
2.0
0.0
-2.0
B8/A0
2.0
0.0
-2.0
B9/A0
2.0
0.0
- 2.0
B3/A0
4.0
2.0
0.0
2.2
2.4
2.6
E*
GeV

5.6

ISOSPIN 0

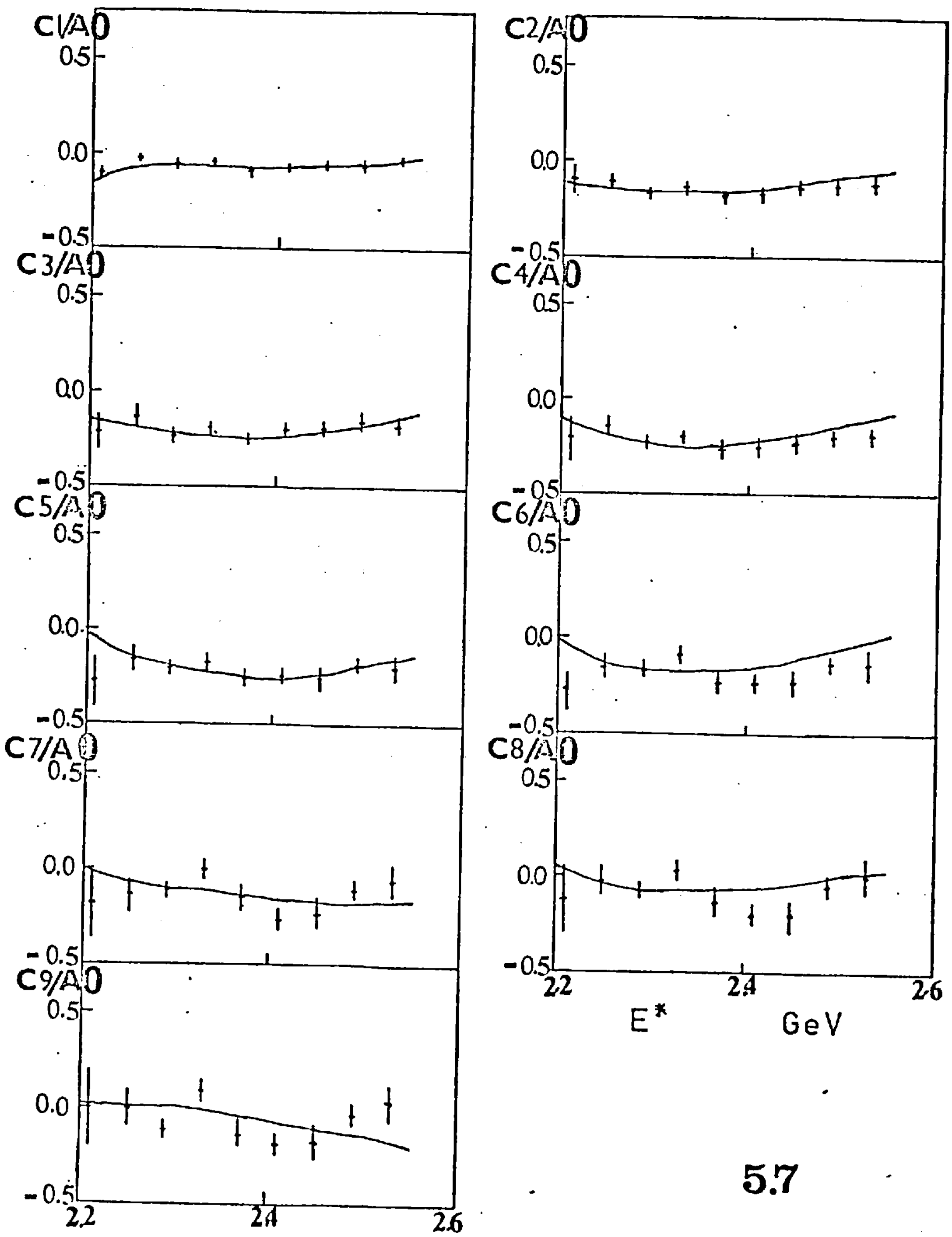

C1/A0
C2/A0
C3/A0
C4/A0
C5/A0
C6/A0
C7/A0
C8/A0
C9/A0
0.5
0.0
-0.5
2.2
2.4
2.6
E* GeV

5.7

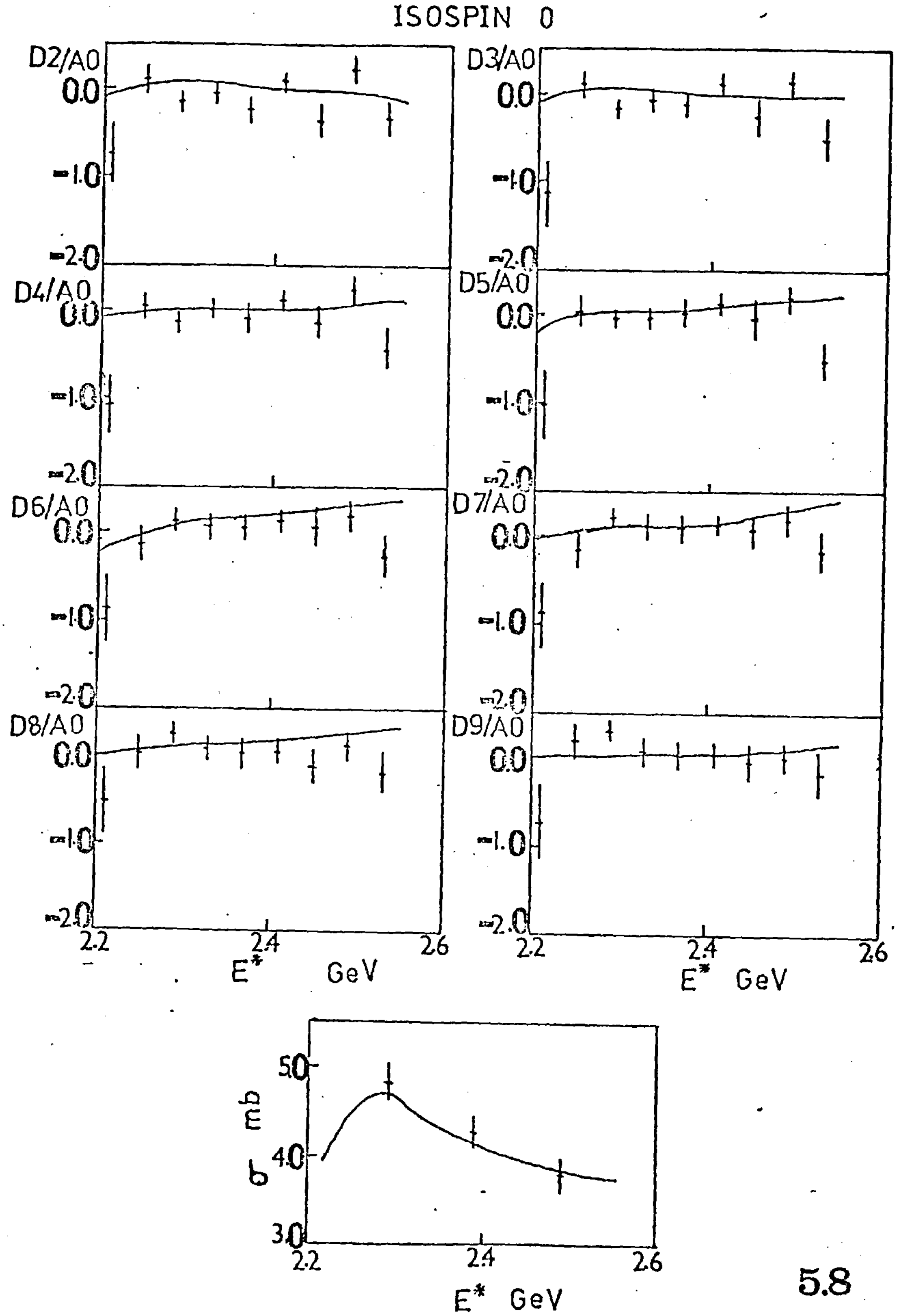
ISOSPIN 0
D2/A0
D3/A0
D4/A0
D5/A0
D6/A0
D7/A0
D8/A0
D9/A0
0.0
-1.0
-2.0
2.2
2.4
2.6
E* GeV
σ mb
50
40
30

5.8

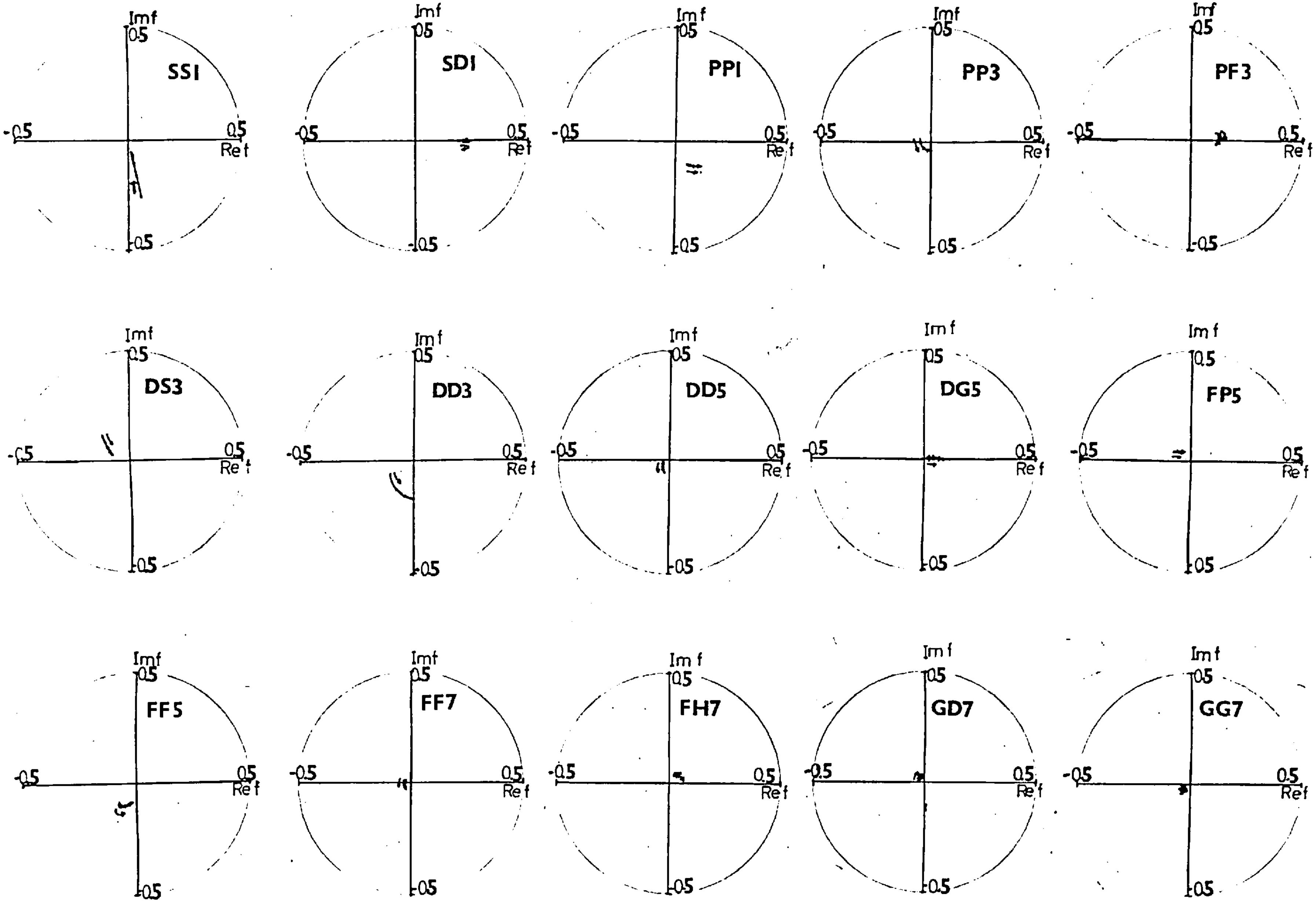

5.9 PARTIAL WAVE AMPLITUDES (I=1)

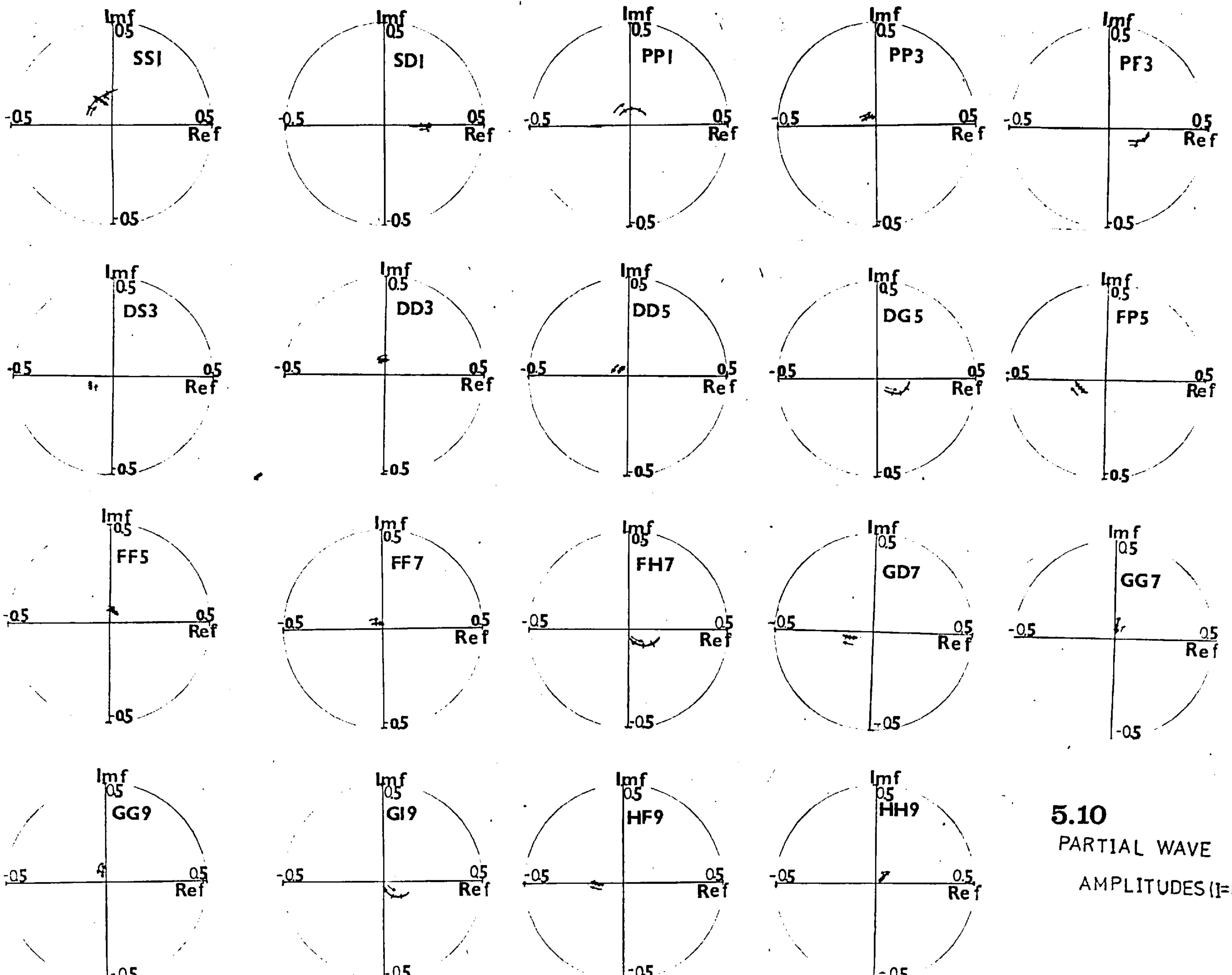

5.10
PARTIAL WAVE
AMPLITUDES (I=0)

CHAPTER 6

Since the deuteron is an isospin zero state, the reactions with a final state deuteron involve only zero isospin exchange in the crossed t-channel (Figure 6.2). This isospin filter is useful to study the exchange mechanisms in these reactions. The reactions studied in this Chapter are one and two pion production with a deuteron in the final state namely

$$K^+d \rightarrow K^0\pi^+d \qquad 6.1$$

$$K^+d \rightarrow K^+\pi^+\pi^-d \qquad 6.2$$

Other possible coherently produced deuteron final states involving single or double pion production are

$$K^+d \rightarrow K^+\pi^0 d \qquad 6.3$$

$$K^+d \rightarrow K^+\pi^0\pi^0 d \qquad 6.4$$

$$K^+d \rightarrow K^0\pi^+\pi^0 d \qquad 6.5$$

Of these hypotheses 6.3 and 6.4 could be fitted to only two prong events without a visible V_o decay. During scanning the rolls such topologies were rejected because statistically good data already exist for the corresponding reactions which can be fitted to such topologies (mostly elastic scattering off neutron and proton) at this energy and it would have been difficult to get a pure unbiased sample of such final states when the final state neutron cannot be identified. However the reaction 6.5 could be observed in two prong events with an associated V_o decay. But the number of constraints in such kinematic fits is one and the contamination and biases in the sample would be quite high. The reactions 6.1 and 6.2 both can be fitted with four constraints and they result from two (or one) prong events with a V_o and four (or three) prong events respectively.

6.1 AMBIGUITY AND SELECTION OF EVENTS

Though the reactions 6.1 and 6.2 give rise to highly constrained fits, the level of contamination in the sample is quite high. This is due to the two following reasons. The kinematic ambiguity between a proton and a deuteron is very acute. Furthermore coherent reactions are very rare at this energy. So one cannot always prefer a coherent event to the corresponding break up events by counting the number of constraints. So it was decided at the GRIND choicing stage, a deuteron fit will always be accepted together with the break up fits

$$K^+d \rightarrow K^0\pi^+pn \qquad 6.6$$

$$K^+d \rightarrow K^+\pi^+\pi^-pn \qquad 6.7$$

The final data sample contains 550 events of reaction 6.1 and 340 events of reaction 6.2. 61.7% of events of the reaction 6.1 and 68.0% of events of the reaction 6.2 were ambiguous with the corresponding break up events. 45.2% of the events fitting to the reaction 6.2 belonged to the topology 300. Most of these 300 topology events give a spurious bump in the $K^+\pi^-$ mass distribution. Changing the K^+ mass to that of a pion, the effective mass squared of the '3π' system has been plotted on figure 1.6. This gives an enormous peak at the 'K^+' mass (Figure 6.1A). They in fact arise from the K^+ meson decay to 3π final state. These events are also associated with a very low kinematic probability. Excepting these two possible contaminations, the sample is pure in a sense that the events are uniquely fitted from ionisation measurement or a good measurement of the deuteron momentum.

To get rid of the contamination from misfitted tau decays, a cut on the '3π' effective mass squared was made at 0.28 GeV^2. However to distinguish a deuteron event from the corresponding break up event is not very simple. The method used here is based on the assumption that a neutron-proton system travelling together with a relative momentum as expected from the deuteron form factor should be identified as a deuteron. Tests were made on the effective mass of the neutron-proton system and also on the angle between the neutron and the proton directions. One expects for a misfitted coherent event the neutron-proton mass should be close to the deuteron mass (Figure 6.1B) and the angle between the neutron and the proton close to zero (Figure 6.1C). Further one gets an extra test from the range momentum relation for the proton and the deuteron. For a stopping track, one expects for a misidentified proton track, the ratio of neutron to proton momentum along the proton direction to be 0.62, i.e. $R = P_n \cos\theta_{np}/P_p = 0.62$. This test and also the test on the angle cannot be applied when the proton has not been observed or when it is badly measured. So these tests were applied for only those events which has got proton lengths greater than 0.5 c.m. and neutron momentum greater than 100 MeV/c. The cuts imposed were at 1.90 GeV for the proton-neutron mass; 1.0 radian for the neutron proton angle in the laboratory frame and R was restricted between 0.5 and 0.8. The number of events for each of the two reactions have been summarised in table 6.1.

In the single pion production, the production of K* should mediate through zero isospin exchange, i.e. w or f meson-exchange should be dominant in the reaction $K^+d \rightarrow K^{*+}d$. This should make the decay density matrix element ρ_{oo} for the K^{*+} close to a zero value. However when one plots ρ_{oo} as a function of t' in figure 6.8 where t' is the momentum transfer squared between the K^{*+} and the incident K^+ meson ($t'=t-t_{min}$), one gets unusually high values of ρ_{oo} for small values of t'. Small t' events correspond to a very short or unobserved deuteron track where the contamination of break up events is maximum. In the break reaction, the isospin restriction is not present, so one can

have pion exchange as well which will give rise to a large ρ_{00} .
So a further cut was made on events of type 6.1. and only those events which have got a value of t' larger than 0.04 GeV^2 were accepted for further analysis.

6.2 SINGLE PION PRODUCTION

6.2A) Cross Section and resonance production:

The cross-section quoted on table 6.2 is calculated on the basis of the cuts mentioned in Section 6.1. These have been compared with the cross sections from other experiments, namely at 2.0 GeV/c (Firestone et al. 1973), 2.3 GeV/c (Butterworth et al. 1965c), and 4.6 GeV/c (Charriere et al., 1974) on figure 6.4A. The values of cross sections for those experiments were recalculated after imposing the t' cut at 0.04 GeV^2. The results of this experiment is in good agreement with the other experiments. The cross-sections follow a A P_{lab}^{-n} behaviour with A = 1.06$\pm$0.10 mb and n = 1.49$\pm$0.15. If one assumes that the process can be written as a pseudo two body process which is mediated by the exchange of Regge trajectories in the crossed channel. One usually gets an energy dependence of the cross-section as $(P_{lab})^{2\alpha(0)-2}$ where $\alpha(0)$ as the intercept of the effective trajectory exchanged. From the calculation of this experiment; $\alpha(0)$ turns out to be 0.26$\pm$0.08. If one assumes that ω-trajectory exchange is the dominant feature for this process , $\alpha(0)$ should have been 0.38 which agrees with the experimental value within errors.

All the events of the three different beam momenta have been combined and shown in the Dalitz plot (figure 6.5). This clearly shows a strong K^*(890) production. In addition to that there is some accumulation of events near small $d\pi^+$ mass ($\sim$ 2.14 GeV). This is not an effect of combining the 3 different beam momenta and this was observed separately at each of the three momenta. This was not observed at 2.3 GeV/c or 3.0 GeV/c, (K. Buchner et al. 1969) where statistics was rather poor. However in the experiment at 4.6 GeV/c, some sign of enhancement at that low mass has been observed. Such a mass enhancement was observed several times in the double pion production reaction with a K or π beam in association with a K^* or a ρ. In such reactions it has been interpreted as a final state effect involving the recombination of the decay nucleon from a pion exchange induced $\Delta(1236)$ and the spectator nucleon to form a final state deuteron. But pion exchange is forbidden here and natural parity isovector exchange is required. In the 4.6 GeV/c experiment, the decay distribution of the $d\pi^+$ system was found to be equatorially peaked. The symmetric decay distribution can be associated with the decay of a single J^P state and so a d^* resonance could be suggested. However in this experiment the decay distribution of the d^* (as shown in figure 6.9) has been found to be highly forward peaked. Here the d^* events were selected using a mass cut $2.1\ GeV < M(d\pi) < 2.2\ GeV$. Further the forward-backward asymmetry and polar-equatorial asymmetry factors have been plotted as a function of the $d\pi^+$ mass in figure 6.11. The asymmetry factors are defined by

$$A_{FB} = \frac{N_F - N_B}{N_F + N_B} \qquad 6.8$$

$$A_{PE} = \frac{N_P - N_E}{N_P + N_E} \qquad 6.9$$

where the indices F, B, P, E refer to different regions in $\cos\theta$ distribution, θ being the angle between the final and the initial state deuterons in the $d\pi^+$ rest frame.

$$F \equiv \cos\theta \geq 0.0 \qquad 6.10$$

$$B \equiv \cos\theta < 0.0 \qquad 6.11$$

$$P \equiv |\cos\theta| \geq 0.5 \qquad 6.12$$

$$E \equiv |\cos\theta| < 0.5 \qquad 6.13$$

Within errors the asymmetry factors show smooth behaviour with the mass of the deuteron-pion system. There is no appreciable change when one antiselects the K^* events using a mass-selection on the $K\pi$ mass for a K^* to be $0.84\ GeV < M(K\pi) < 0.94\ GeV$. All these evidences suggest that no single J^P state is responsible for this mass enhancement. It could be a final interaction effect.

An attempt was made to fit the Dalitz plot with the maximum likelihood program described in Chapter 4. But that could not produce any reasonable fit. One possible explanation to this is that the fitting program assumes that the background is a pure phase space term which is unfortunately not so in the case of coherent production. This reaction is characterised by a sharp t-distribution. So some modification was made of the likelihood program. The normalization integrals N and A in 4.2 defined by

$$N = \int BW_{K^*} PH_{K^*} dR \qquad 6.14$$

and

$$A = \int dR \qquad 6.15$$

where R is the three body phase space element were calculated prior to the actual fitting, by a Monte Carlo method. Since the integrals were calculated simultaneously absolute normalisations were not important. In calculating the integrals, the events were weighted according to their respective t' by a factor $\exp(-Bt')$. This program however does not make use of any angular information of the decay of the resonance. So minor features in the distributions did not show up in the fit. The fit is insensitive to the parametrisation of the resonance masses and widths. In this reaction $K^*(890)$ was only included with the resonance mass and width fixed. The values used are

$$M_{K^*} = 0.892\ GeV \text{ and } \Gamma_{K^*} = 0.050\ GeV \qquad 6.16$$

To incorporate the combining of the beam momenta, a broad beam momentum was assumed. A Gaussian distribution peaked at 2.44 GeV/c and half width 0.26 GeV/c was used. The results of the fit have been summarised in table 6.2 and the solid curves in the diagram 6.6 and 6.7 are prediction from this fit. The low mass enhancement in $d\pi^+$ mass spectrum was not reproduced. A Breit Wigner for d^* with mass $\sim$2.1 GeV and width $\sim$ 0.1 GeV can however explain this enhancement. But there is no physics justification for including such a resonance. One can however qualitatively explain such a bump in the $d\pi$ mass plot by considering diagrams like 6.3 where the Δ^{++} produced by the interaction of the K^+ meson and proton recombines with the neutron to give the final state deuteron.

6.2 B) Production and decay of K^*(890):

As there is strong K^*(890) production in this channel one can select out K^* events using a cut in the $K^o\pi^+$ mass spectrum [0.84 GeV < $M(K\pi)$ < 0.94 GeV]. As has been stated earlier K^*(890) production has a strong t-dependence. This is expected from the presence of the deuteron form factor in the expression for the cross-section of coherent scattering (Gourdin, 1959). Using a pure S-wave deuteron form factor, the expected slope to be $\sim$20.0 GeV^{-2}. The t' distribution has been shown in figure 6.12. It has a sharp exponential fall and using data from t' = 0.04 GeV^2 to t' = 0.20 GeV^2, the slope B of the exponential fit has been found out to be B = 15.0$\pm$3.0 GeV^{-2}. This is comparable to the corresponding values obtained at 2.0 GeV/c and 3.0 GeV/c.

The polar and azimuthal decay distributions of the $K^o\pi^+$ system have been shown in figure 6.10. Assuming the $K^o\pi^+$ system to be entirely P-wave, density matrix elements were calculated in the Gottfried-Jackson frame by the method of moments and have been listed in table 6.4. The solid lines in figure 6.10 are predictions of the decay distribution from the density matrix elements. The smallness of ρ_{00} and also Re ρ_{10} suggest that the K^* production proceeds through vector meson exchange. Natural parity exchange contribution as from the value of $\rho_{11}+\rho_{1-1}$ seems to be the dominant one.

The dominance of isoscalar natural parity exchange in both $K^+d \to K^{*+}d$ and $K^-d \to K^{*-}d$ suggests the exchange of w and f_o trajectories. Furthermore the closeness of the cross sections of the two processes may suggest that either the exchanged trajectories are strongly exchange degenerate or one of the exchanges is suppressed. Combining the existing data of $K^{\pm}d \to K^{*\pm}d$ with the data points of this experiment, an attempt was made to fit the natural parity exchange component with an effective trajectory parametrised by

$$\alpha_{eff}(t) = \alpha_o - \alpha' t' \qquad 6.17$$

Noting that the differential cross-section can be well explained by an exponential t' distribution, one can write at an incident momentum P_{LAB},

$$(\rho_{11}+\rho_{1-1})\frac{d\sigma}{dt'} = \frac{A'}{P_{LAB}^2}\left(\frac{s-u}{s_o}\right)^{2\alpha_{eff}(t)} \qquad 6.18$$

Fixing α' and s_o to 1.0, the fit was made using 36 data points. This leads a value of $\alpha_o = 0.43 \pm 0.03$ with a $x^2/N = 1.8$. The poor fit is perhaps due to the fact that the relative normalization among the data points in different experiments is rather poor. Further the energy region that has been used is not the truly asymtotic region for Regge trajectory exchanges. However, if one draws a linearly rising trajectory passing through the mass-squared of the w and f_o meson, one gets the degenerate trajectory with slope 1.00 ± 0.01 GeV^{-2} and intercept 0.38 ± 0.01 which is in excellent agreement with this rather crude analysis.

6.3 DOUBLE PION PRODUCTION

6.3 a) Cross Section and resonance fractions:

Since there is no restriction of exchange particle in this process, no selection criterion for low t' events can be made. Furthermore most of the 300 topology events were not accepted as they appear to be misfitted tau decays. The cross-sections as quoted in table 6.5 are calculated from a part of the whole sample which comes from these rolls which have gone through at least one measurement on the conventional measuring machine. The figure 6.13A shows a plot of cross-section against laboratory beam momentum along with data from other experiments at 2.3 GeV/c (Butterworth et al. 1965c), 3.0 GeV/c (Buchner et al. 1969), 4.6 GeV/c (Dunwodie et al., 1974), 12.0 GeV/c (Firestone et al. 1972). The cross-section is rising with laboratory momentum at this energy and within errors the results of this experiment are compatible with the measurements at other energies.

The data at the different momenta show the same major features and so they have been combined for further analysis. Figure 6.14 shows the scatter plot of invariant mass squared of the $K^+\pi^-$ system against the mass squared of the $d\pi^+$ system. The reaction seems to ge entirely through $K^{*o}(890)$ production. The $d\pi^+$ mass spectrum (as shown in figure 6.16) also shows a bump at a mass of 2.18 GeV. This has been observed in all the previous experiments and explained as a final state interaction between the spectator and the decay product of a Δ, so that the enhancement occurs closely to the mass of a Δ-nucleon system with zero relative momentum. The $d\pi^-$ mass spectrum shows the same feature as the $d\pi^+$ mass spectrum but on a much reduced scale. The $\pi^+\pi^-$ mass spectrum shows no evidence of ρ-production. The K^+d mass spectrum shows no structure whatsoever. The $K^+\pi^+\pi^-$ spectrum shows a broad bump near 1.1 GeV which becomes clearer for events in the K^{*o} mass band ($0.84\ GeV < M(K\pi) < 0.94\ GeV$). This has also been observed in the K^+n noncharge exchange and charge exchange reactions and has been discussed in detail elsewhere (G. Hall 1974). At those reactions, this enhancement however occurs at a slightly higher $K\pi\pi$ mass and has been referred to as Q meson. The shift to a lower mass could be due to a t_{min} effect in this experiment.

The maximum likelihood method described in Section 6.2 A has been used here for calculating the resonance fraction. R in 6.14 however here refers to the 4 body phase space. This reaction is even more peripheral and hence the weighting factor $\exp(Bt')$ is more important. Only $K^*(890)$ with mass M = 0.892 GeV and width Γ = 0.050 GeV was used in the fit. The results of the fit have been summarised in table 6.5 and also can also be seen from the solid lines in figures.

6.3 B) Production and decay characteristics of the resonances:

The t'(d-d) distribution has been plotted on figure 6.18 and has been found to be consistent with an exponential t' distribution. The slope of the distribution B has been calculated to be B = 25.4 ± 2.2 GeV^{-2}. This highly peripherality was also observed in the $K^{*o}(890)$ production. K^{*o} events were selected using a mass cut $0.84 GeV < M(K\pi) < 0.94 GeV$. The $t'(K-K^*)$ distribution (as shown in figure 6.18) has also been fitted with an exponential with slope B = 15.0 ± 1.6 GeV^{-2}. These values are consistent with the measurement at 3.0GeV/c.

Figures 6.21 show the polar and the azimuthal angular distribution of the $K^+\pi^-$ decay (in the K^* mass band) in the Gottfried-Jackson frame. The azimuthal angular distribution has been found to be essentially flat as would have been expected from a π-exchange. The decay density matrix elements have been calculated by the method of moments assuming a pure P-wave decay of the $K^+\pi^-$ state. They have been calculated in both Gottfried-Jackson and helicity frames and they are listed in table 6.7. Statistics could not allow any S-P interference effect to be detected. The solid lines on figure 6.21 show the expected angular distribution from the density matrix elements. The largeness of ρ_{00} suggests pseudoscalar exchange to be dominant. Further the smallness of $\rho_{11}+\rho_{1-1}$ suggests that the natural parity exchange contribution to be very small. Thus the t-channel exchange should be dominated by the pion trajectory.

If the reaction 6.2 proceeds through the production of Q meson ($J^P = 1^+$) by pomeron exchange (which is only allowed in this reaction) and then the Q decays to a K^*, one should expect the z component of the spin to be zero in the Gottfried-Jackson frame. It therefore follows that the K^* decay product has also z-component of the spin zero in the Gottfried-Jackson frame i.e. $\rho_{10} = 0$ and $\rho_{00} = 1$ which one obtains here in the case of $K^*(890)$ production. So one should look for some Q-production. Due to limited statistics in this channel, only the decay angular distribution of the $K\pi\pi$ system has been studied. The decay distribution can be expanded in terms of spherical harmonics as

$$W(\theta,\phi) = \sum a^l_m Y_{lm}(\theta,\phi) \qquad 6.19$$

The orthonormality property of the spherical harmonics lead to

$$\langle Y^*_{lm}\rangle = \int W(\theta,\phi)\, Y^*_{lm}(\theta,\phi)\, d\cos\theta\, d\phi = a^l_m \qquad 6.20$$

θ,ϕ being defined by the direction of the K^* in the $K\pi\pi$ rest frame. The real parts of the coefficients a^l_m calculated in the helicity frame has been plotted against the ($K\pi\pi$) mass for $l \leqslant 3$ (Figure 6.22). Within errors some systematic variation with mass has been observed in $\mathrm{Re}\,a^1_0, \mathrm{Re}\,a^2_0, \mathrm{Re}\,a^2_1, \mathrm{Re}\,a^2_2$. This implies S and P wave decays of the $K^*\pi$ system which leads to the possibilities $J^P = 1^+$, and $J^P = 0^-, 1^-, 2^-, \ldots$ in the $K\pi\pi$ final state. Further the moments with $l \geqslant 3$ are consistent with zero in this mass region. So $J^P = 0^-$ and $J^P = 1^+, 1^-$ states are only important in the $K\pi\pi$ mass spectrum near Q region.

6.3 C) Reggeised Deck Model:

From the broad bump in the $d\pi^+$ mass spectrum, one is tempted to associate the π^+ meson with the deuteron to form a resonating state. But the polar angular distribution of the decay of the $d\pi^+$ system in the $d\pi^+$ rest frame shows a very sharp forward peak (figure 6.23D) which implies that the $d\pi^+$ system does not form a single resonant state. Also the fact that $K^*\pi^+$ shows a low mass enhancement makes one undecided with which particle the π^+ meson has been associated. There are two other interesting features, the first is that K^* is produced almost entirely by pseudoscalar exchange and the second is that the VanHove angle of almost all the events (95.3%) lie between 120° and 180°. Here the VanHove angle is defined by the angle made by the particle with the deuteron direction in the triangular plot of the longitudinal momenta of d, K^* and π^+ (figure 6.23A). These observations lead to a Deck-type model with the dominant diagrams as one which associates the K^* and the deuteron at the two vertices and they are coupled to the π^+ meson by pion and pomeron exchange respectively. Berger (1969) used a Reggeised pion trajectory and he parametrised the squared matrix element in the following way:

$$|M|^2 \sim \left(\frac{\bar{s}_{K^*\pi}}{s_0}\right)^{2\alpha_\pi} \frac{1}{1-\cos\pi\alpha_\pi} (\bar{s}_{d\pi})^2 \exp(B t_{dd}) \qquad 6.21$$

where

$$\left.\begin{aligned} \bar{s}_{d\pi} &= M^2(d\pi^+) - t_{KK^*} - m_d^2 - 0.5(m_\pi^2 - t_{dd} - t_{KK^*}) \\ \bar{s}_{K^*\pi} &= M^2(K^*\pi^+) - t_{dd} - m_K^2 + 0.5(m_\pi^2 - t_{dd} - t_{KK^*})(m_{K^*}^2 - m_K^2 - t_{KK^*})/t_{KK^*} \\ \text{and} \quad \alpha_\pi &= \alpha'_\pi \quad (t_{KK^*} - m_\pi^2) \end{aligned}\right\} \qquad 6.22$$

Thus the total scattering amplitude has been split up into 3 components one the scattering of the K^+ meson with an off-shell pion at the top vertex, then the scattering of the deuteron with the off-shell pion and finally the coupling of the two trajectories at the centre emitting a pion. The off-shell pion has been replaced by a pion trajectory and whole amplitude has been constructed in a traditional Regge form. The peripherality of the process is built in by the exponential factor. The model prediction was obtained by generating events with Monte Carlo phase space program FOWL, for 3 body final states (K^*, π^+, d) and weighting the events by $|M|^2$. The width of the K^* has been neglected and the combining of the 3-beam momenta was compensated by allowing a Gaussian spread of the beam by 0.26 GeV. The values of the parameters used here are

$$\alpha' = 1.0\ \text{GeV}^{-2},\ \bar{s} = 0.70\ \text{GeV}^2,\ B = 25.4\ \text{GeV}^{-2} \qquad 6.23$$

The fits have been shown by solid curves in diagram 6.23 reproduction of the experimental distributions is reasonable. The term $(\bar{s}_{K\pi})^{2\alpha_\pi}$ is roughly approximate to $(\bar{s}_{K\pi})^{-0.32}$ since t_{KK^*} peaks at $-0.3\ \text{GeV}^2$. Thus it can easily reproduce the low mass enhancement in the $K^*\pi$ mass distribution. Also the exponential t distribution explains the $d\pi^+$ decay distribution in a satisfactory way. However it cannot completely explain the $d\pi^+$ mass enhancement. This double Regge-pole model should have been applicable only for events in the central part of the Dalitz plot so that $S_{K^*\pi}$ and $S_{d\pi}$ are both large. So one cannot expect the model to reproduce sharp resonance-like detail, rather it will explain the gross features in $S_{K^*\pi}$, $S_{d\pi}$ and other distribution. One cannot however exclude an intermediate Δ^{++} formation in the reaction 6.2.

TABLE 6.1

Channel	Number of events before selection			Number of events after selection		
	2.18 GeV/c	2.43 GeV/c	2.70 GeV/c	2.18 GeV/c	2.43 GeV/c	2.70 GeV/c
$K^{+}d \rightarrow K^{0}\pi^{+}d$	161	206	183	86	114	95
$K^{+}d \rightarrow K^{+}\pi^{+}\pi^{-}d$	116	149	72	72	126	49

TABLE 6.2

Beam Momentum GeV/c	Reaction cross-section for $K^{+}d \rightarrow K^{0}\pi^{+}d$ μb	Reaction cross-section for $K^{+}d \rightarrow K^{*+}d$ μb
2.18	137.2±14.5	137.1±23.0
2.43	176.2±18.0	175.9±28.0
2.70	142.8±15.0	142.7±23.4

TABLE 6.3

Range of t' GeV^2	dσ/dt for the process 6.1 mb/GeV^2	dσ/dt for the process $K^{+}d \rightarrow K^{*+}d$ ($\rightarrow K^{0}\pi^{+}$) mb/GeV^2
0.04-0.05	1.50±0.28	0.52±0.16
0.05-0.06	1.24±0.25	0.67±0.19
0.06-0.07	1.08±0.24	0.52±0.16
0.07-0.08	1.08±0.24	0.41±0.15
0.08-0.10	0.31±0.09	0.10±0.05
0.10-0.12	0.44±0.11	0.18±0.07
0.12-0.14	0.62±0.13	0.16±0.06
0.14-0.16	0.39±0.10	0.18±0.07
0.16-0.18	0.36±0.10	0.08±0.04
0.18-0.22	0.12±0.04	0.03±0.02
0.22-0.26	0.19±0.05	0.09±0.03
0.26-0.30	0.13±0.04	0.06±0.03
0.30-0.34	0.12±0.04	0.06±0.03
0.34-0.38	0.12±0.04	0.03±0.02
0.38-0.42	0.09±0.03	–
0.42-0.46	0.09±0.03	0.04±0.02
0.46-0.50	0.04±0.02	–
0.50-0.60	0.05±0.02	0.03±0.011
0.60-0.70	0.02±0.01	0.010±0.007
0.70-0.80	0.02±0.01	0.010±0.007
0.80-0.90	0.03±0.01	0.010±0.007
0.90-1.00	0.04±0.01	0.005±0.005

TABLE 6.4

Density matrix elements for $K^{*+}(890)$ decay in Gottfried Jackson frame

t' in GeV^2	ρ_{00}	ρ_{1-1}	Re ρ_{10}	$\rho_{11}+\rho_{1-1}$
0.01 ± 0.01	0.89 ± 0.09	-0.06 ± 0.05	-0.11 ± 0.05	0.00 ± 0.07
0.03 ± 0.01	0.58 ± 0.12	0.16 ± 0.08	-0.02 ± 0.06	0.37 ± 0.10
0.05 ± 0.01	0.25 ± 0.12	0.09 ± 0.12	-0.04 ± 0.10	0.46 ± 0.16
0.07 ± 0.01	0.16 ± 0.14	0.08 ± 0.13	-0.22 ± 0.08	0.50 ± 0.13
0.115 ± 0.035	0.28 ± 0.12	0.21 ± 0.16	-0.02 ± 0.07	0.58 ± 0.17
0.225 ± 0.075	0.04 ± 0.10	0.26 ± 0.13	0.14 ± 0.06	0.73 ± 0.14
0.85 ± 0.55	-0.04 ± 0.09	0.33 ± 0.12	-0.09 ± 0.06	0.85 ± 0.13
All events with $t'>0.04$ GeV^2.	0.12 ± 0.06	0.21 ± 0.06	-0.06 ± 0.04	0.65 ± 0.07

TABLE 6.5

Beam Momentum GeV/c	Reaction Cross-section for $K^+d\to K^+\pi^+\pi^-d$ μb	Reaction Cross-section for $K^+d\to K^{*0}\pi^+d$ μb
2.18	89.0 ± 12.0	73.0 ± 11.0
2.43	89.0 ± 12.0	73.0 ± 11.0
2.70	94.0 ± 12.0	77.0 ± 11.0

TABLE 6.6

t'(d-d) range GeV^2	$d\sigma/dt$ for the process 6.2 mb/GeV^2	t'(K-K*) range GeV^2	$d\sigma/dt$ for the process $K^+d\to K^{*0}\pi^+d$, $\hookrightarrow K^+\pi^-$ mb/GeV^2
0.00-0.01	6.42 ± 1.07	0.00-0.01	2.18 ± 0.53
0.01-0.02	4.90 ± 0.88	0.01-0.02	2.18 ± 0.53
0.02-0.03	3.37 ± 0.69	0.02-0.03	1.52 ± 0.43
0.03-0.04	2.50 ± 0.58	0.03-0.04	1.74 ± 0.47
0.04-0.05	1.63 ± 0.45	0.04-0.06	1.09 ± 0.27
0.05-0.06	1.63 ± 0.45	0.06-0.08	0.87 ± 0.23
0.06-0.08	0.92 ± 0.24	0.08-0.12	0.41 ± 0.11
0.08-0.10	0.98 ± 0.25	0.12-0.16	0.25 ± 0.09
0.10-0.12	0.44 ± 0.16	0.16-0.20	0.19 ± 0.07
0.12-0.14	0.44 ± 0.16	0.20-0.30	0.07 ± 0.03
0.14-0.18	0.11 ± 0.06	0.30-0.40	0.03 ± 0.02

TABLE 6.7

Decay density matrix elements of K^{*o}

Channel		Gottfried Jackson frame	Helicity frame
$K^+d \rightarrow K^{*o}\pi^+ d$ $\hookrightarrow K^+\pi^-$	ρ_{oo}	0.92 ± 0.06	0.76 ± 0.06
	ρ_{1-1}	-0.02 ± 0.04	-0.04 ± 0.04
	$\mathrm{Re}\rho_{10}$	-0.09 ± 0.04	-0.06 ± 0.06
	$\rho_{11}+\rho_{1-1}$	0.02 ± 0.05	0.08 ± 0.05

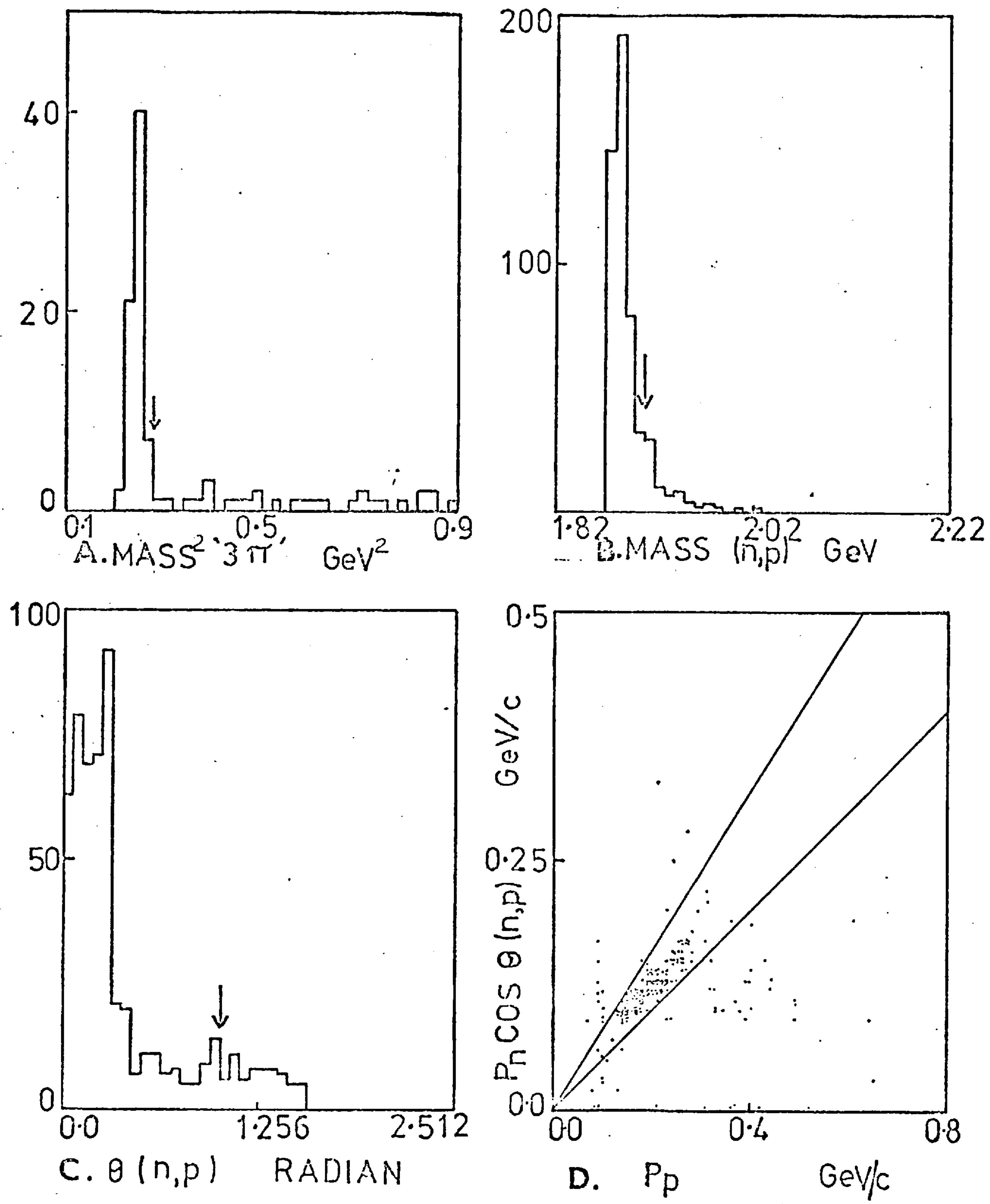

40
20
0
0·1
0·5
0·9
A. MASS² 3π GeV²
200
100
1·82
2·02
2·22
B. MASS (n,p)² GeV
100
50
0
0·0
1·256
2·512
C. θ (n,p) RADIAN
0·5
0·25
0·0
0·0
0·4
0·8
P_n COS θ (n,p) GeV/c
D. P_p GeV/c

6.1

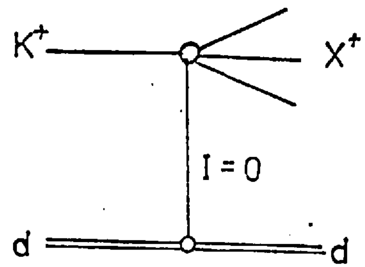

6.2

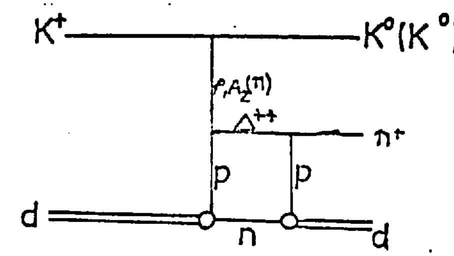

6.3

$K^+ d \longrightarrow K^\circ \pi^+ d$

$K^+ d \longrightarrow K^{*+} d$

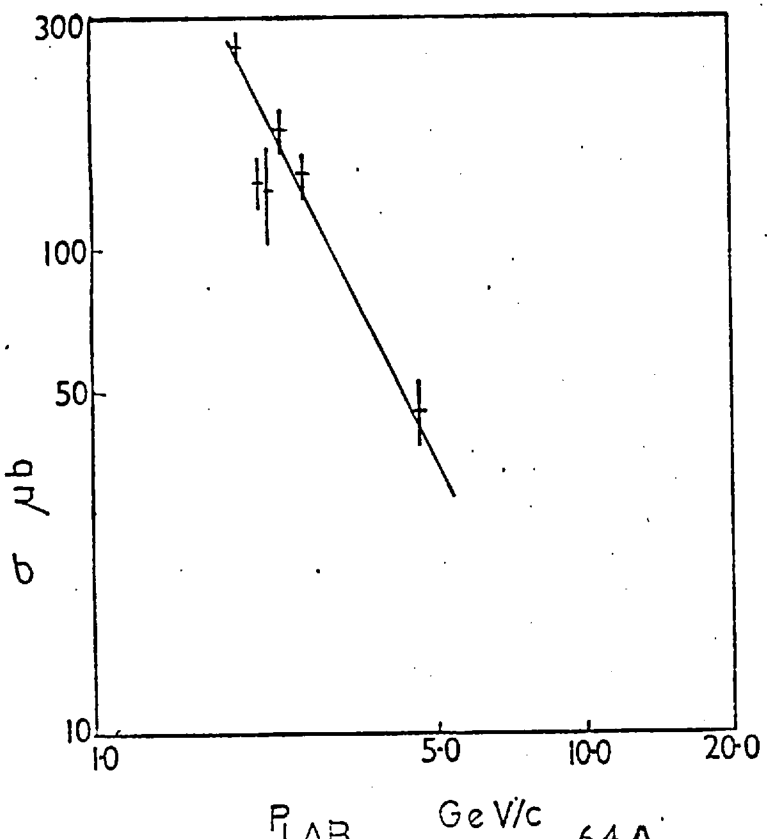

6.4 A

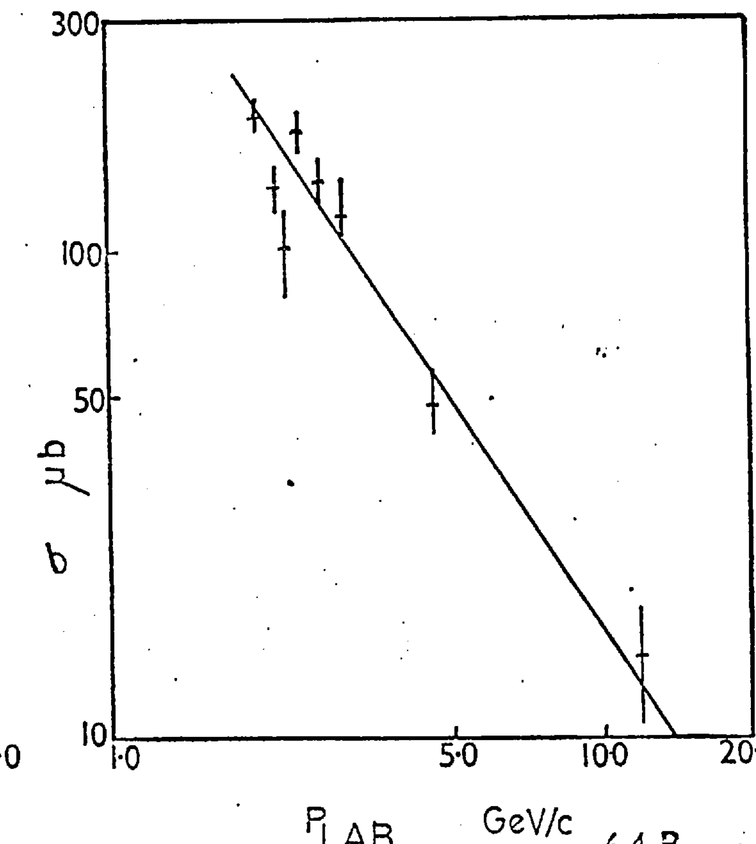

6.4 B

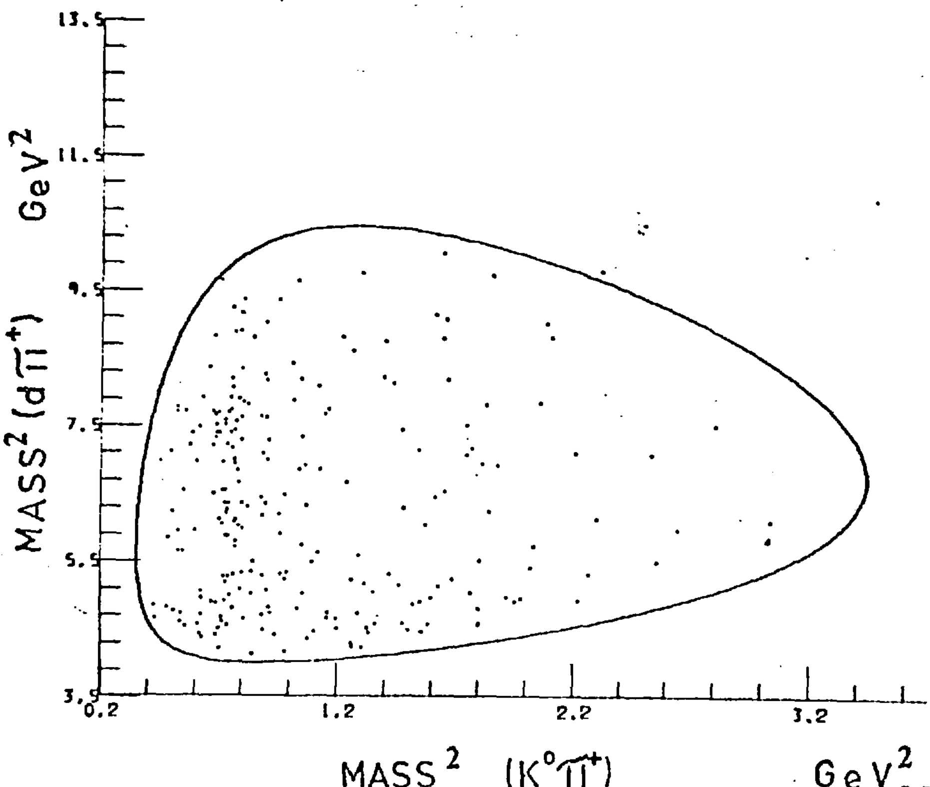

6.5

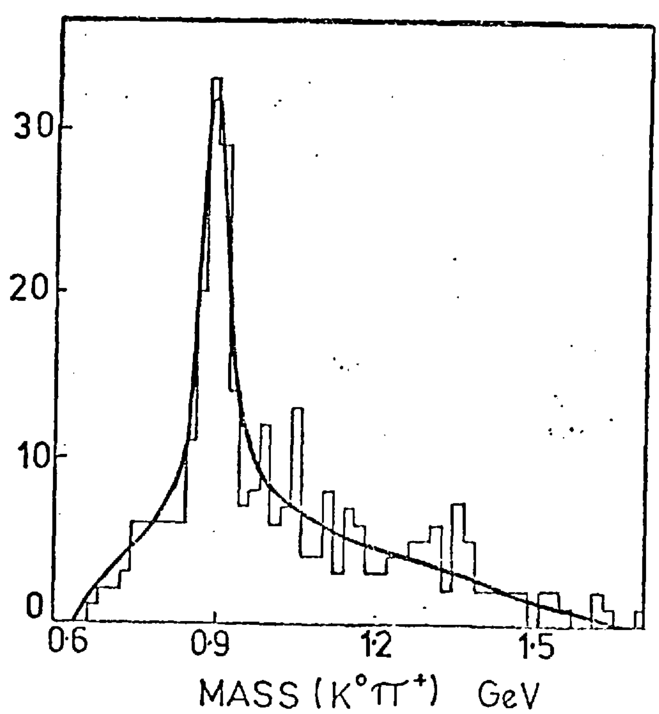

6.6

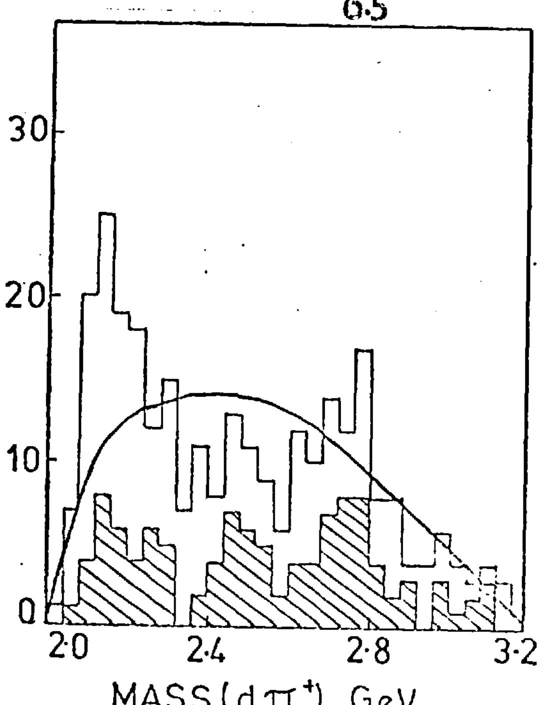

Shaded region corresponds to the events in the K^* band

6.7

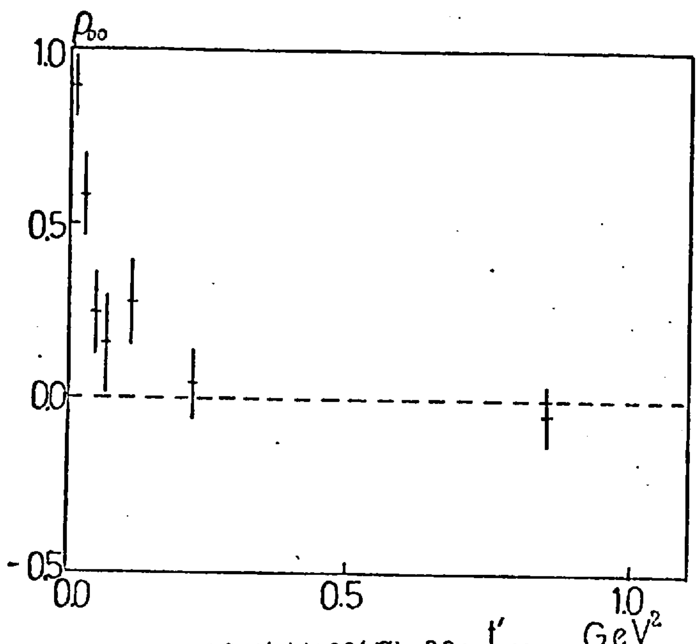

0.84 GeV<MASS($K\pi$)<0.94 GeV

6.8

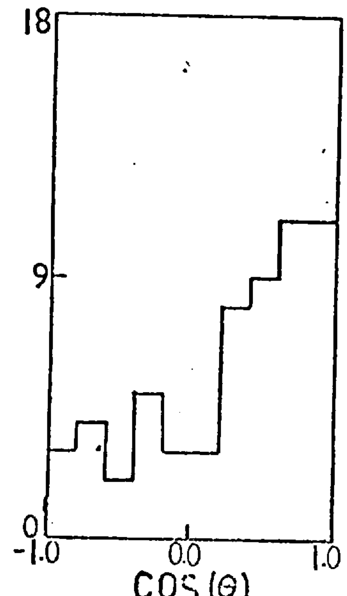

2.1 GeV< MASS($d\pi$)< 2.2 GeV

6.9

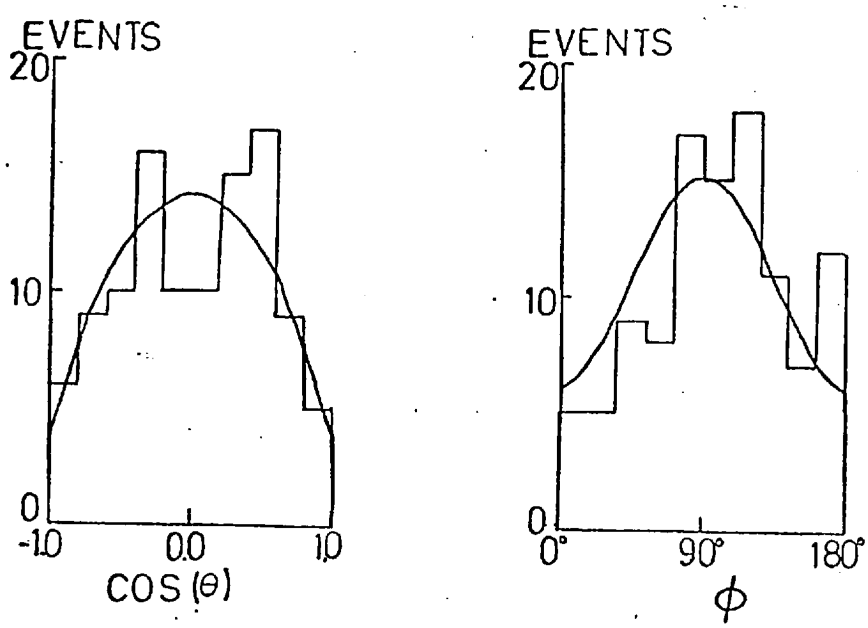

K^* Decay Distribution

6.10

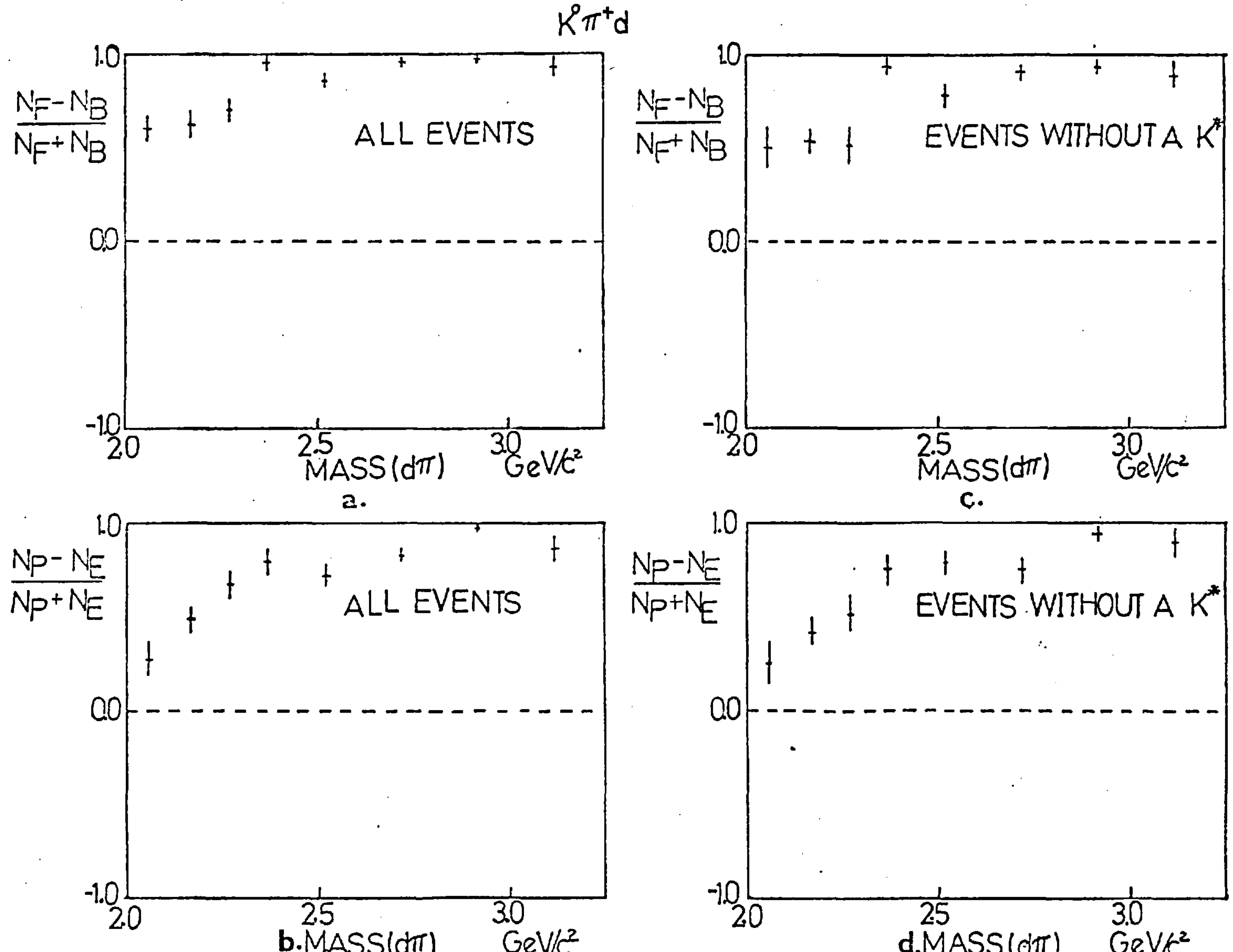
$K^0\pi^+d$
$\frac{N_F - N_B}{N_F + N_B}$
ALL EVENTS
EVENTS WITHOUT A K^*
$\frac{N_P - N_E}{N_P + N_E}$
1.0
0.0
-1.0
2.0
2.5
3.0
MASS(dπ)
GeV/c²
a.
b.
c.
d.

6.11

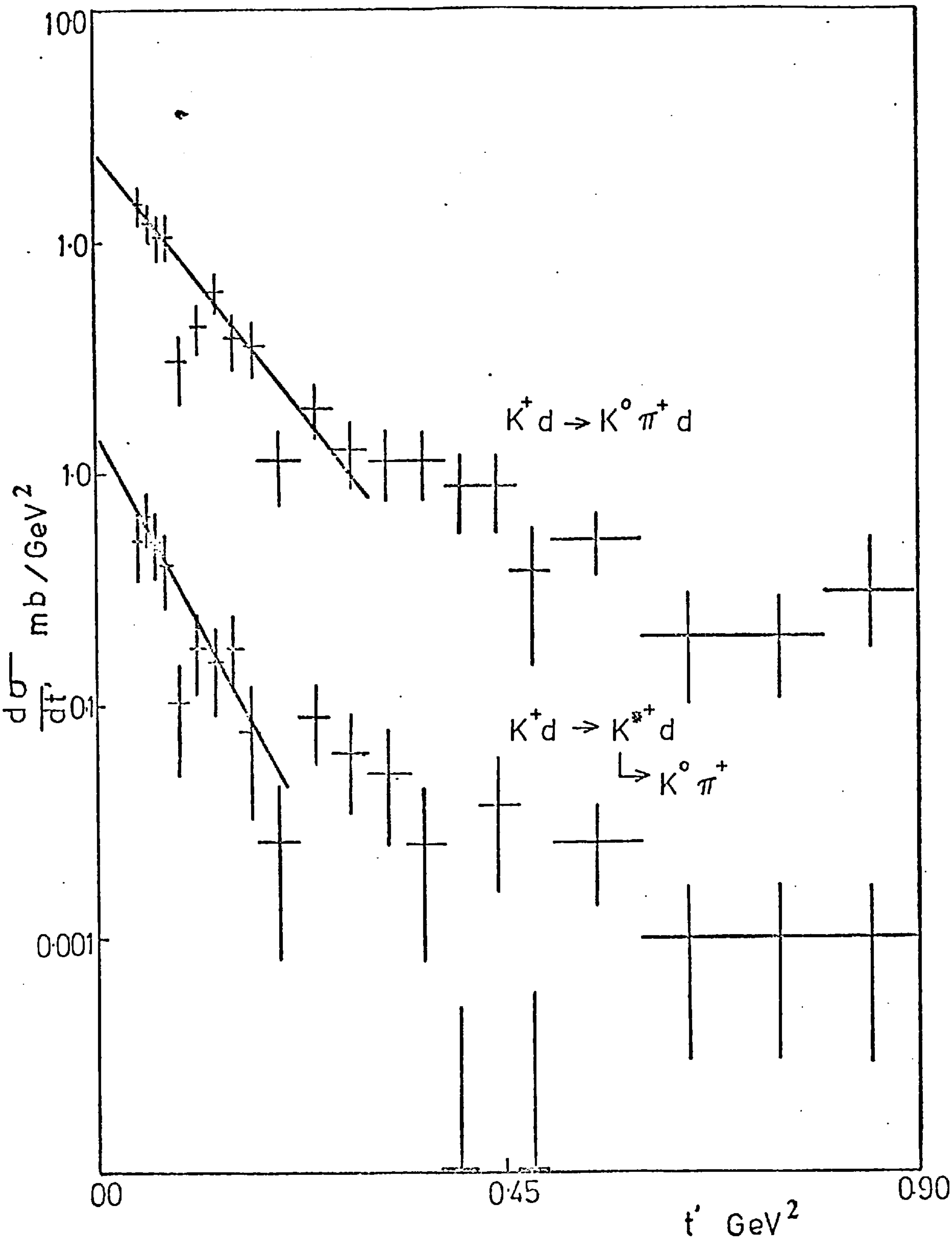
100
1·0
1·0
0·1
0·001
$\frac{d\sigma}{dt'}$ mb / GeV^2
00
0·45
0·90
t' GeV^2
$K^+d \to K^0\pi^+d$
$K^+d \to K^{*+}d$
$\hookrightarrow K^0\pi^+$

6.12

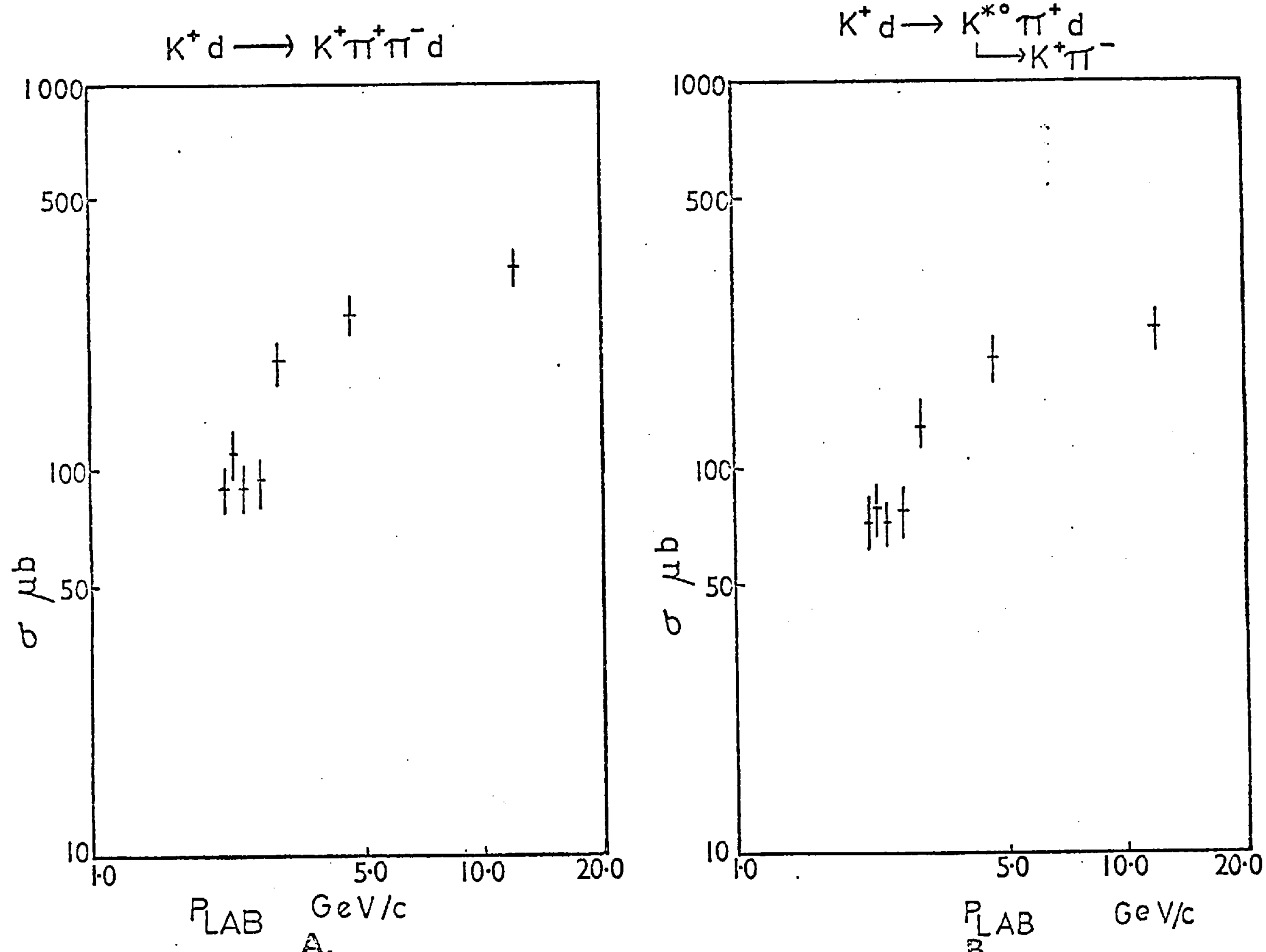
$K^+d \longrightarrow K^+\pi^+\pi^-d$
1000
500
100
50
10
σ μb
1·0
5·0
10·0
20·0
P_{LAB} GeV/c
A.
$K^+d \longrightarrow K^{*o}\pi^+d$
$\hookrightarrow K^+\pi^-$
1000
500
100
50
10
σ μb
1·0
5·0
10·0
20·0
P_{LAB} GeV/c
B.

6.13

$K^+ d \rightarrow K^+ \pi^+ \pi^- d$

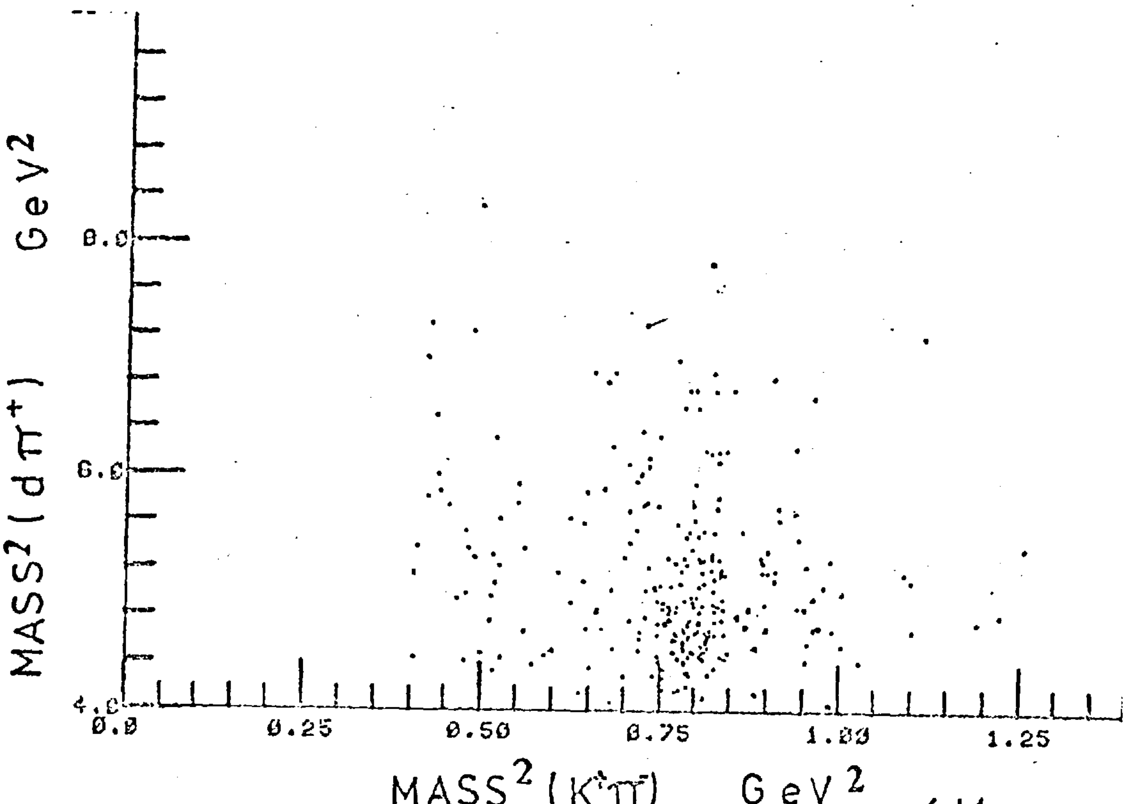

6.14

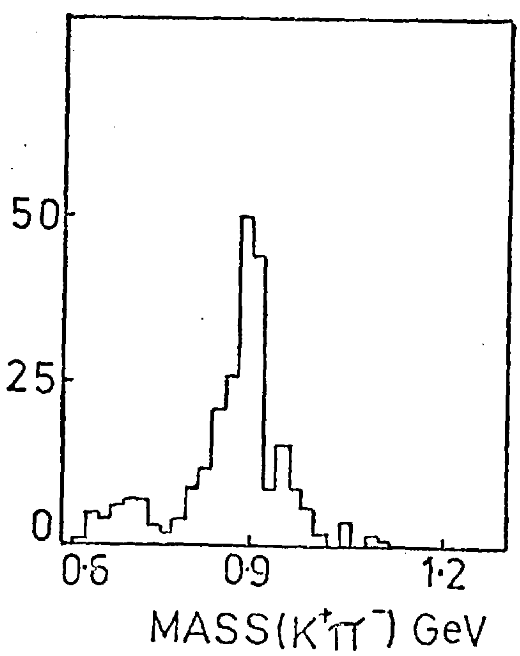

6.15

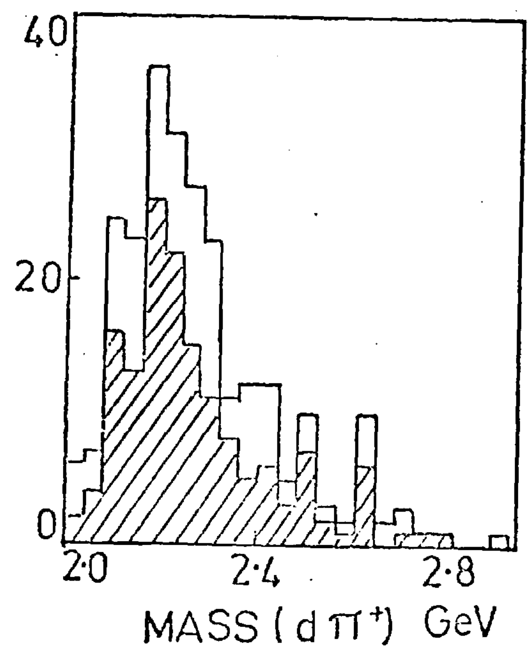

6.16

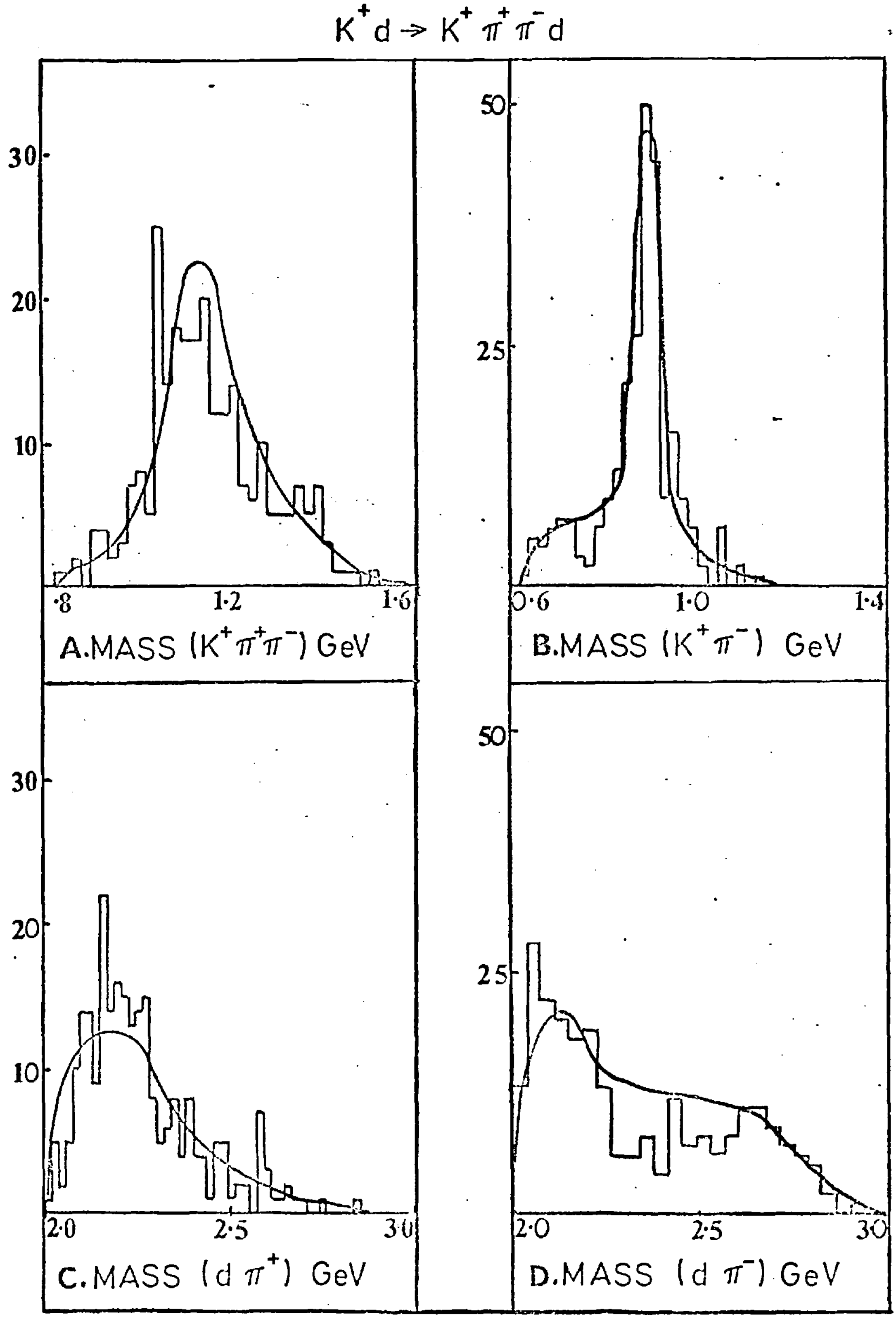

$K^+d \rightarrow K^+\pi^+\pi^-d$
30
20
10
·8
1·2
1·6
A. MASS ($K^+\pi^+\pi^-$) GeV
50
25
0·6
1·0
1·4
B. MASS ($K^+\pi^-$) GeV
30
20
10
2·0
2·5
3·0
C. MASS ($d\pi^+$) GeV
50
25
2·0
2·5
3·0
D. MASS ($d\pi^-$) GeV

6.17

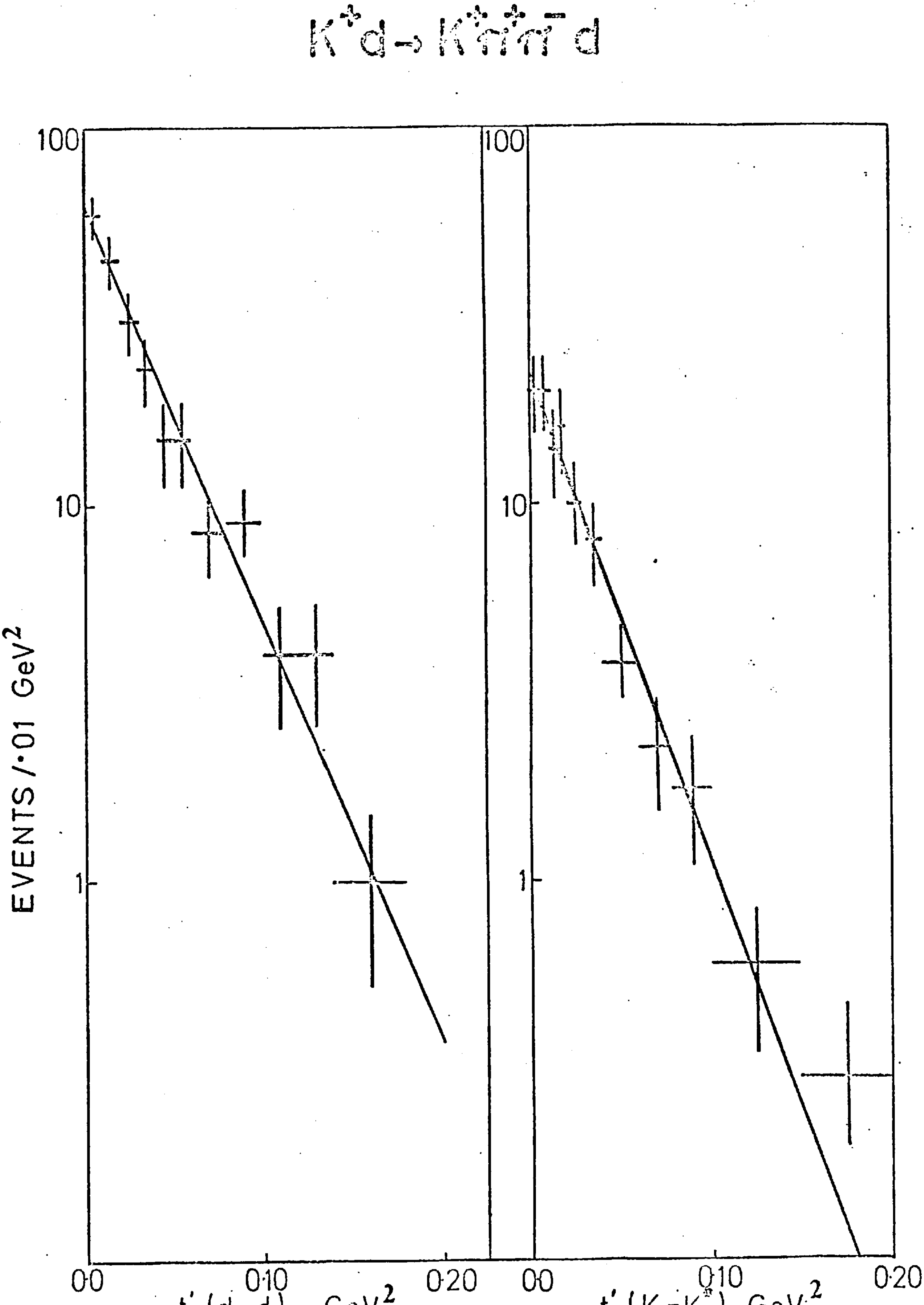

$K^+d \to K^+\pi^+\pi^- d$
100
10
1
EVENTS / ·01 GeV^2
0·0
0·10
0·20
t′ (d-d) GeV^2
100
10
1
0·0
0·10
0·20
t′ (K-K*) GeV^2

6.18

$K^+d \rightarrow K^+\pi^+\pi^-d$

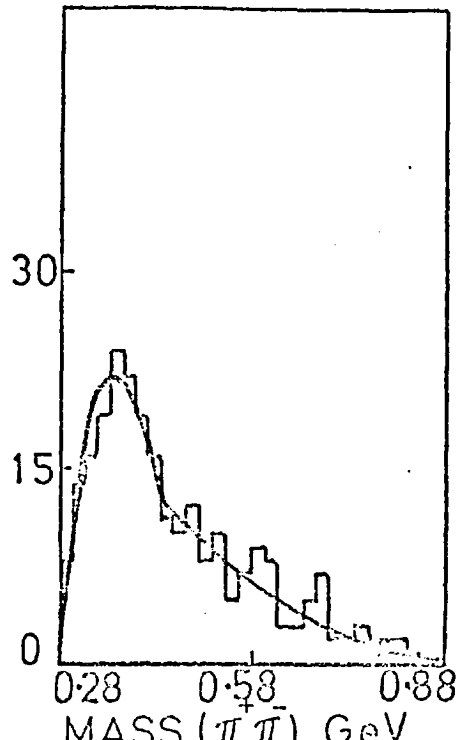

6.19

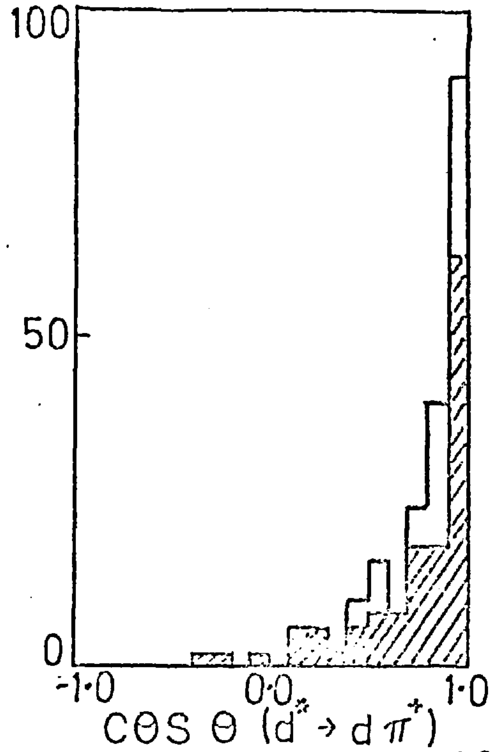

6.20

DECAY DISTRIBUTION OF K^{*0}

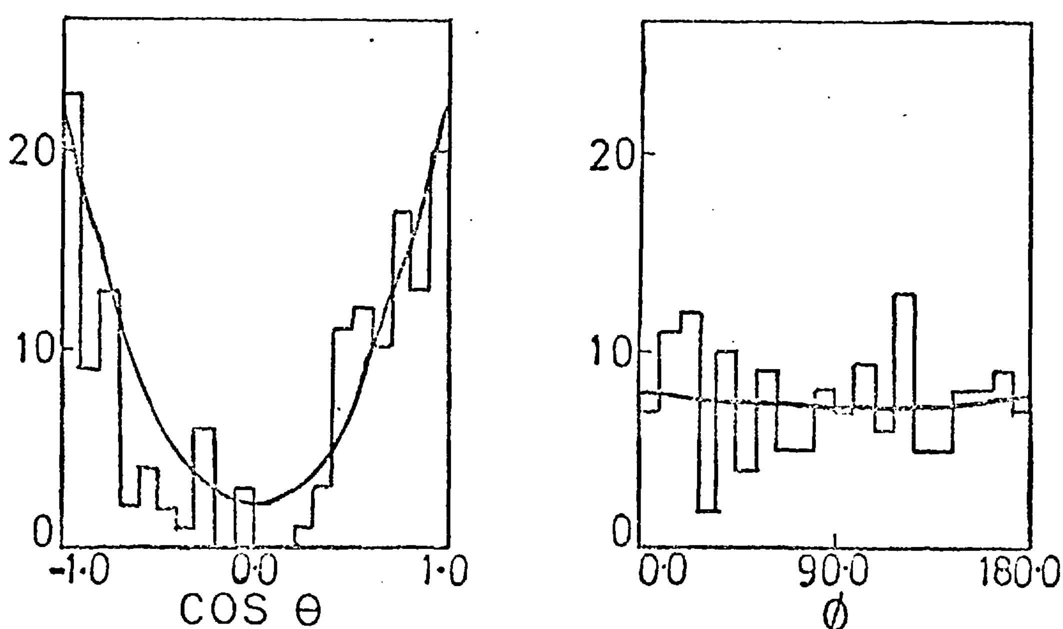

6.21

$K^+d \rightarrow K^{*0}\pi^+d$

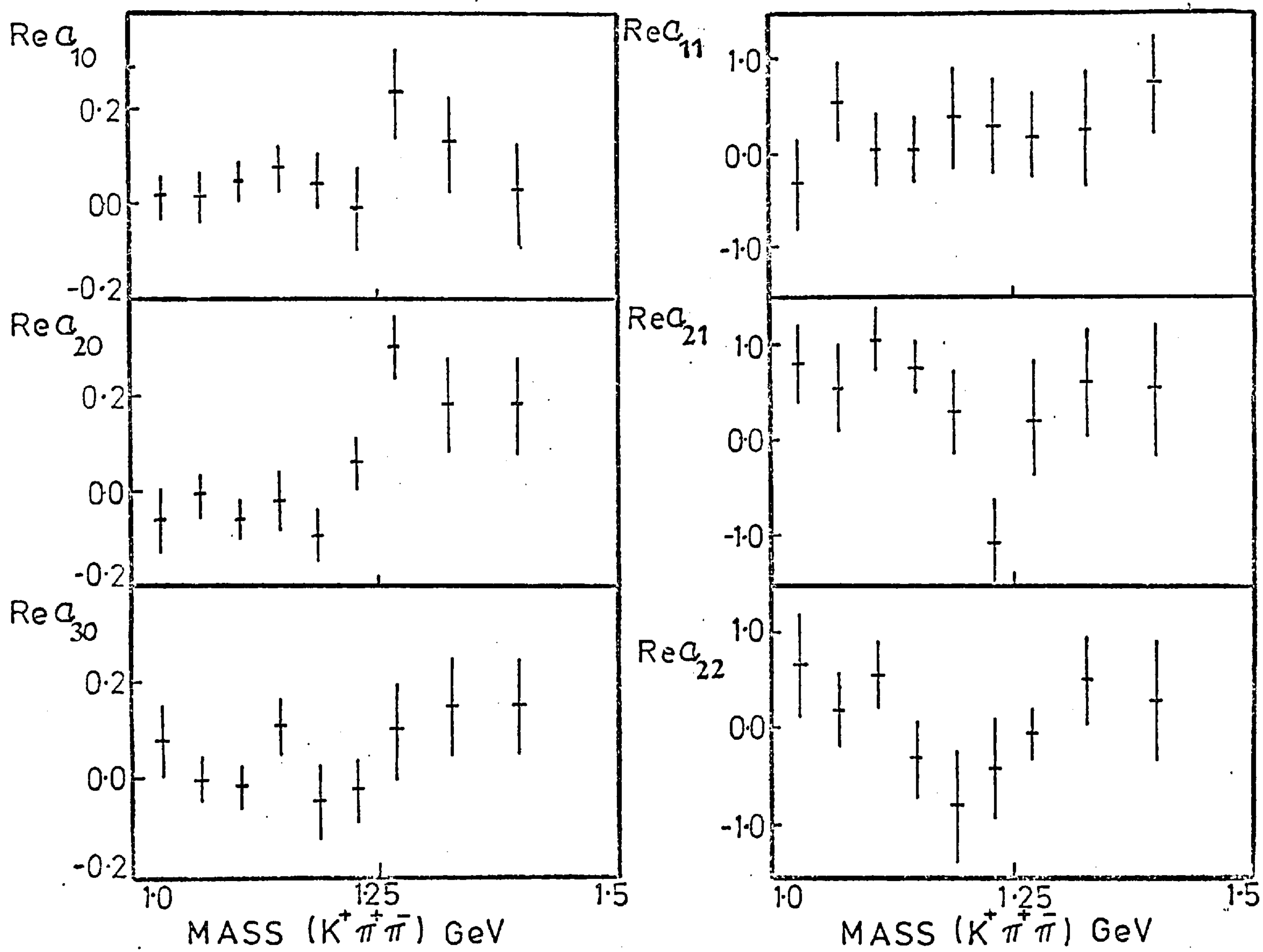

$K^+\pi^+\pi^-d$

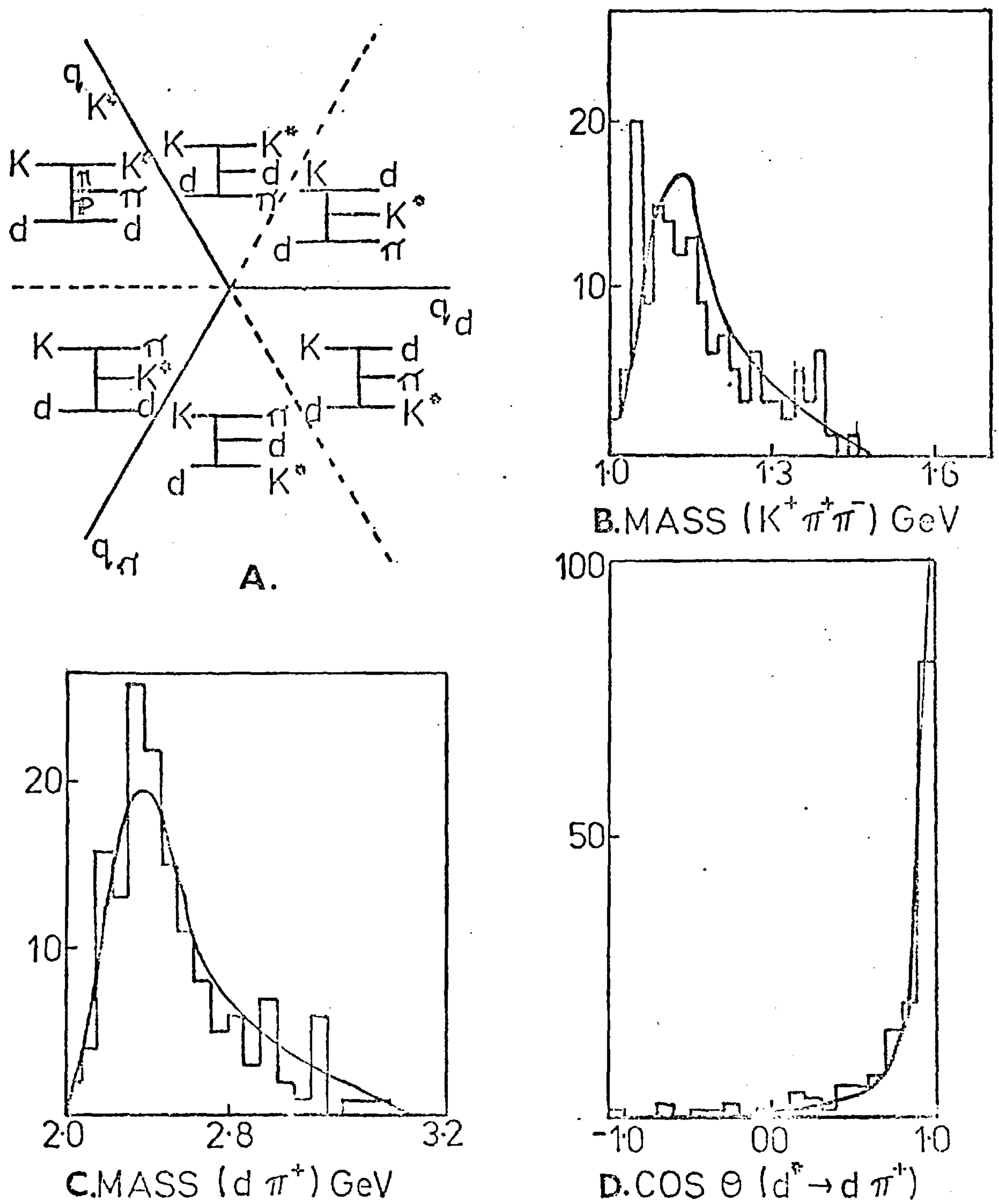

6.23

CHAPTER 7

This chapter describes the final states where 3 pions have been produced. Three or four prong events with an associated V_o decay can give constrained fits to such final states. The fittable hypotheses are

$$K^+d \rightarrow K^0\pi^+\pi^-\pi^0pp \qquad 7.1$$

$$K^+d \rightarrow K^0\pi^+\pi^+\pi^-pn \qquad 7.2$$

If one considers the deuteron to be an effective neutron or proton target, one can study three such triple pion production reactions in these reactions

$$K^+n \rightarrow K^0\pi^+\pi^-\pi^0p \qquad 7.3$$

$$K^+n \rightarrow K^0\pi^+\pi^+\pi^-n \qquad 7.4$$

$$K^+p \rightarrow K^0\pi^+\pi^+\pi^-p \qquad 7.5$$

7.1 AMBIGUITY

The three pion production threshold correspondsto a K^+ beam momentum of 1.2 GeV/c and even at the energy level of this experiment, the final state particles travel rather slowly in the laboratory frame, so that with the help of ionisation information one can identify a track unambiguously. There is in fact practically no contamination in any of these final states. Here however one has not included the deuteron final state as a possible hypotheses in the GRIND fitting stage. But a comparison of double pion processes with deuteron intact and breakup gives an estimate of 6% of total events which could be coherent deuteron final state. This is definitely an over estimate because here the number of final state particles is even higher and this would reduce the probability of having the proton and neutron in a coherent state.

In these reactions, one observes 22% of events having their spectator momenta greater than 300 MeV/c. This fraction is rather large but not very surprising because the probability of multiple scattering increases as one goes up in multiplicity.

7.2 CROSS SECTION AND RESONANCE PRODUCTION

The cross-sections for the processes 7.3, 7.4 and 7.5 have been quoted in table 7.1. These quoted values are based on those events which have their spectator momentum less than 300 MeV/c and normalised on a subsample which has got both first and second measurements. In all the three reactions cross-sections seem to rise with energy. The only available data on similar cross-section measurements from other experiments is for the reaction 7.5. The cross-section measurements for this channel is compatible with other experimental results (figure 7.1) which shows a turn over near 6 GeV/c.

Since the number of events at each beam momentum is small, one combines the data from three beam momenta. This is somewhat justified as there is no significant structure in the channel cross-sections and also within the limited statistics, the various distributions seem to be similar.

The various effective mass plots for the final state 7.3 has been shown on figure 7.6. The major effects are the two bumps in the $\pi^+\pi^-\pi^o$ mass plot. They correspond to the masses of η and ω respectively. The $K^o\pi^+$ or the $K^o\pi^o$ mass distributions seem to be rather structureless. There are some shoulder effects near the $K^*(890)$ mass but statistically they are not significant. It is rather surprising since the $K^*(890)$ threshold corresponds to a beam momentum of 1.75 GeV/c whereas the w threshold is near 1.98 GeV/c. It should also be noted that $K^*(890)$ production is the most dominant feature in the reactions 7.4 and 7.5. Also the $p\pi$ combinations did not show up any significant structure. The phase space fitting programme as has been described in section 6.2 was modified to fit this channel with 5 particles in the final states. Only the most obvious resonances observed in the mass distributions were considered in the fit. The masses of η and w were taken to be 648.8 MeV and 782.7 MeV respectively.

The widths of η and w are nominally (as quoted in particle data book handbook) 2.63 KeV and 10 MeV respectively. But due to the limited resolution of this experiment, the widths were taken to be the resolution limit of the experiment i.e. 15 MeV. The results of the fit have been shown by the solid lines on the diagram 7.6. The fractions of η and w were found to be $7.0 \pm 2.0\%$ and $11.3 \pm 1.4\%$ respectively. Thus the cross-sections at 2.7 GeV/c for η and w production which subsequently decay into the $\pi^+\pi^-\pi^0$ made are 23.4 ± 6.6 μb and 37.8 ± 3.9 μb respectively. Using the branching ratios, the total η and w production cross-sections were found to be 97.9 ± 27.5 μb and 42.1 ± 4.5 μb respectively.

Since η decays mostly into neutral particles, one expects that it should also be observed in the final state

$$K^+d \longrightarrow K^0pp + \text{Missing Mass} \qquad 7.6.$$

The missing mass squared for the process has been plotted on figure 7.2. This plot shows a bump at 0.0 GeV^2 which is clearly due to a misfitted π^0 final state or an elastic charge exchange reaction. There is also a broad bump near the η mass. One expects this bump to be more prominent than what one observes in the $\pi^+\pi^-\pi^0$ final state. But unfortunately the background for 2 or more π^0 is very close to that mass. Also the energy resolution for these 'NOFIT' final states is worse than that in the reaction 7.3 and there is some measurement bias as well in these final states. So no further effort has been made to extract any information about the neutral decay mode of η.

The mass plots of the reactions 7.4 and 7.5 have been shown in figures 7.7 and 7.8. Both the reactions show similar characteristics. These processes are dominated by $K^*(890)$ production. The phase space fitting programme has been used to estimate the fraction for $K^*(890)$ production. The quality of the fits has been shown by the solid lines on the figures. The estimated fractions are $55.8 \pm 8.0\%$ and $68.5 \pm 6.0\%$ for the processes

7.4 and 7.5 respectively. This uses a $K^{*}(890)$ mass and width to be 0.892 GeV and 0.050 GeV respectively.

The momentum transfer distributions (between the initial and final state nucleons) have been shown on figures 7.3, 7.4 and 7.5. In all the reactions, the t-distributions do not show any strong forward peak which further supports that there is no contamination from any coherent deuteron final state in any of these reactions.

TABLE 7.1

Reaction	Cross-section at 2.18 GeV/c μb	Cross-section at 2.43 GeV/c μb	Cross-section at 2.70 GeV/c μb
$K^+n \to K^o \pi^+ \pi^- \pi^o p$	102.0 ± 13.2	171.5 ± 16.3	334.8 ± 22.6
$K^+n \to K^o \pi^+ \pi^+ \pi^- n$	32.8 ± 7.5	44.8 ± 8.3	117.1 ± 13.3
$K^+p \to K^o \pi^+ \pi^+ \pi^- p$	24.2 ± 6.5	52.5 ± 9.0	170.4 ± 16.0

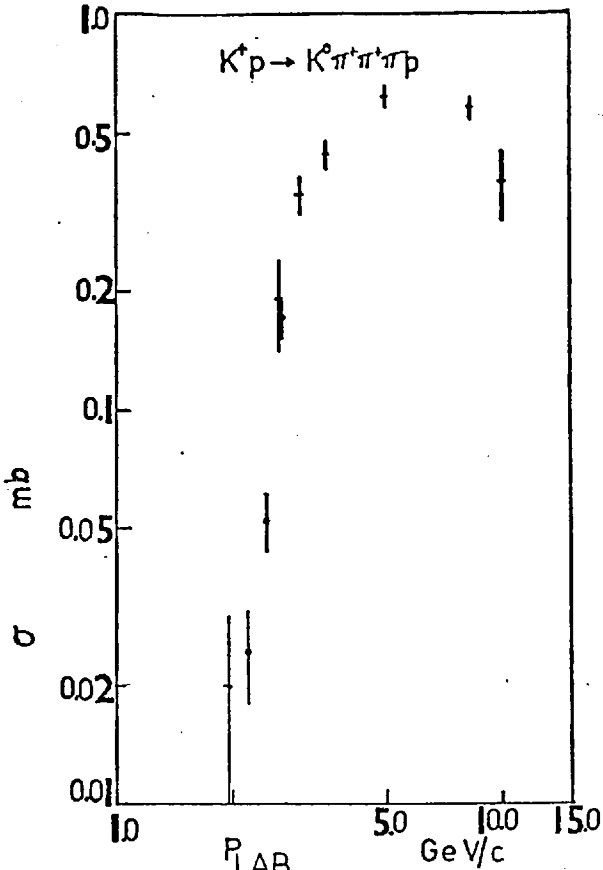

K⁺p → K°π⁺π⁺π⁻p
1.0
0.5
0.2
0.1
0.05
0.02
0.01
σ mb
1.0
5.0
10.0
15.0
P_LAB GeV/c

7.1

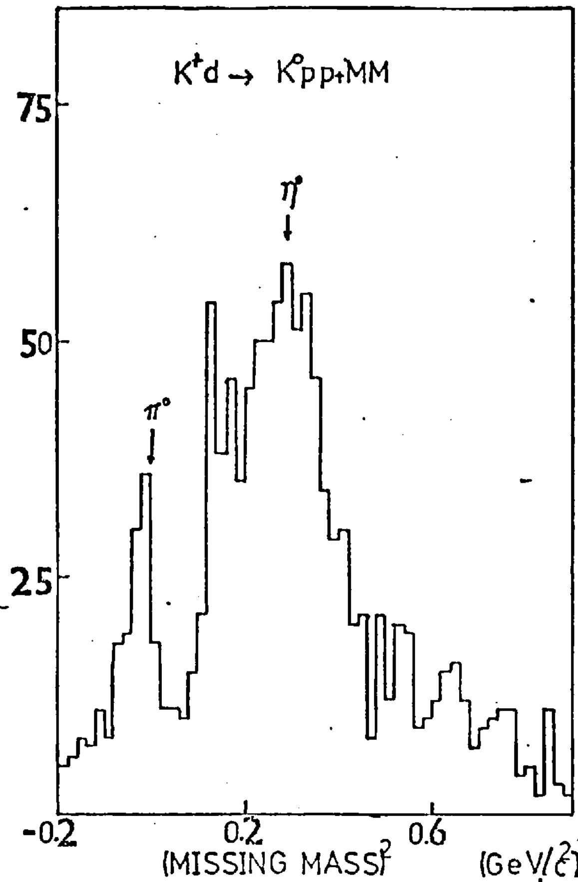

K⁺d → K°pp+MM
π°
η°
75
50
25
-0.2
0.2
0.6
(MISSING MASS)² (GeV/c²)²

7.2

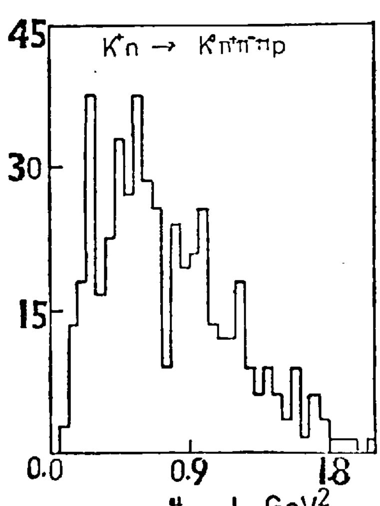

K⁺n → K°π⁺π⁻π⁻p
45
30
15
0.0
0.9
1.8
|t_n-p| GeV²

7.3

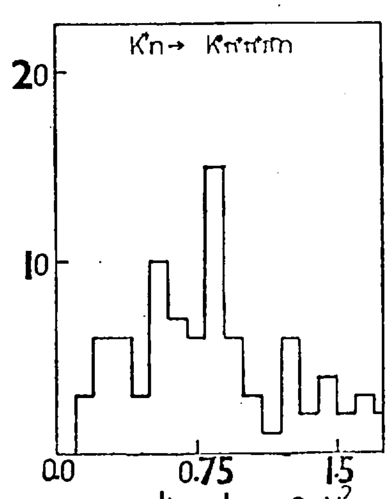

K⁺n → K°π⁺π⁻π⁻n
20
10
0.0
0.75
1.5
|t_n-n| GeV²

7.4

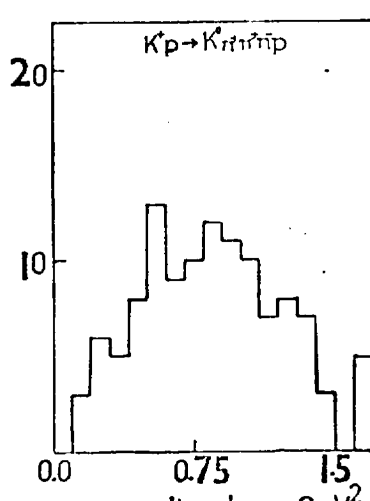

K⁺p → K°π⁺π⁺π⁻p
20
10
0.0
0.75
1.5
|t_p-p| GeV²

7.5

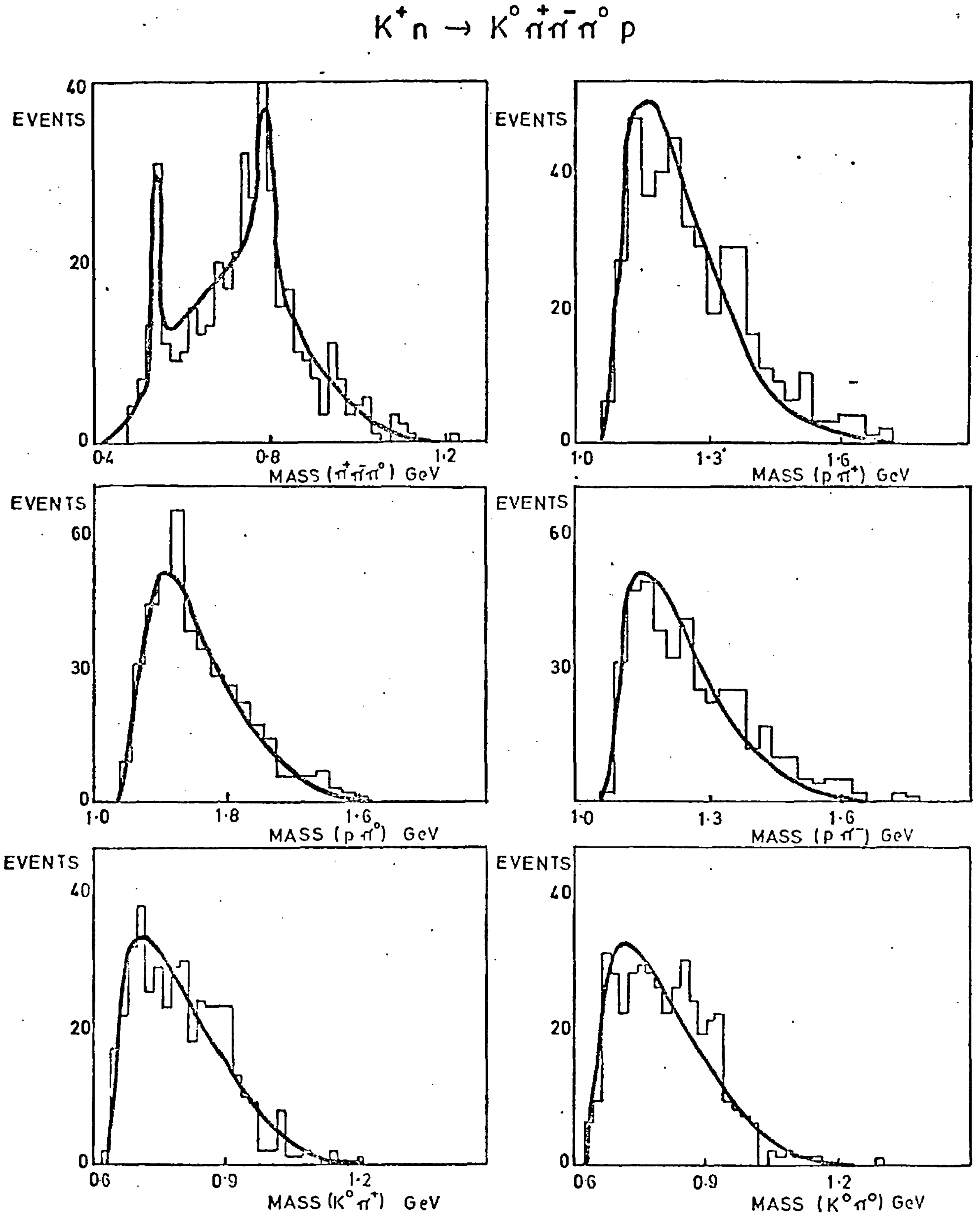
K⁺n → K° π⁺ π⁻ π° p
EVENTS
40
20
0
0·4
0·8
1·2
MASS (π⁺π⁻π°) GeV
EVENTS
40
20
0
1·0
1·3
1·6
MASS (p π⁺) GeV
EVENTS
60
30
0
1·0
1·8
1·6
MASS (p π°) GeV
EVENTS
60
30
1·0
1·3
1·6
MASS (p π⁻) GeV
EVENTS
40
20
0
0·6
0·9
1·2
MASS (K° π⁺) GeV
EVENTS
40
20
0
0·6
0·9
1·2
MASS (K° π°) GeV

7.6

$K^+ n \rightarrow K^0 \pi^+ \pi^+ \pi^- n$

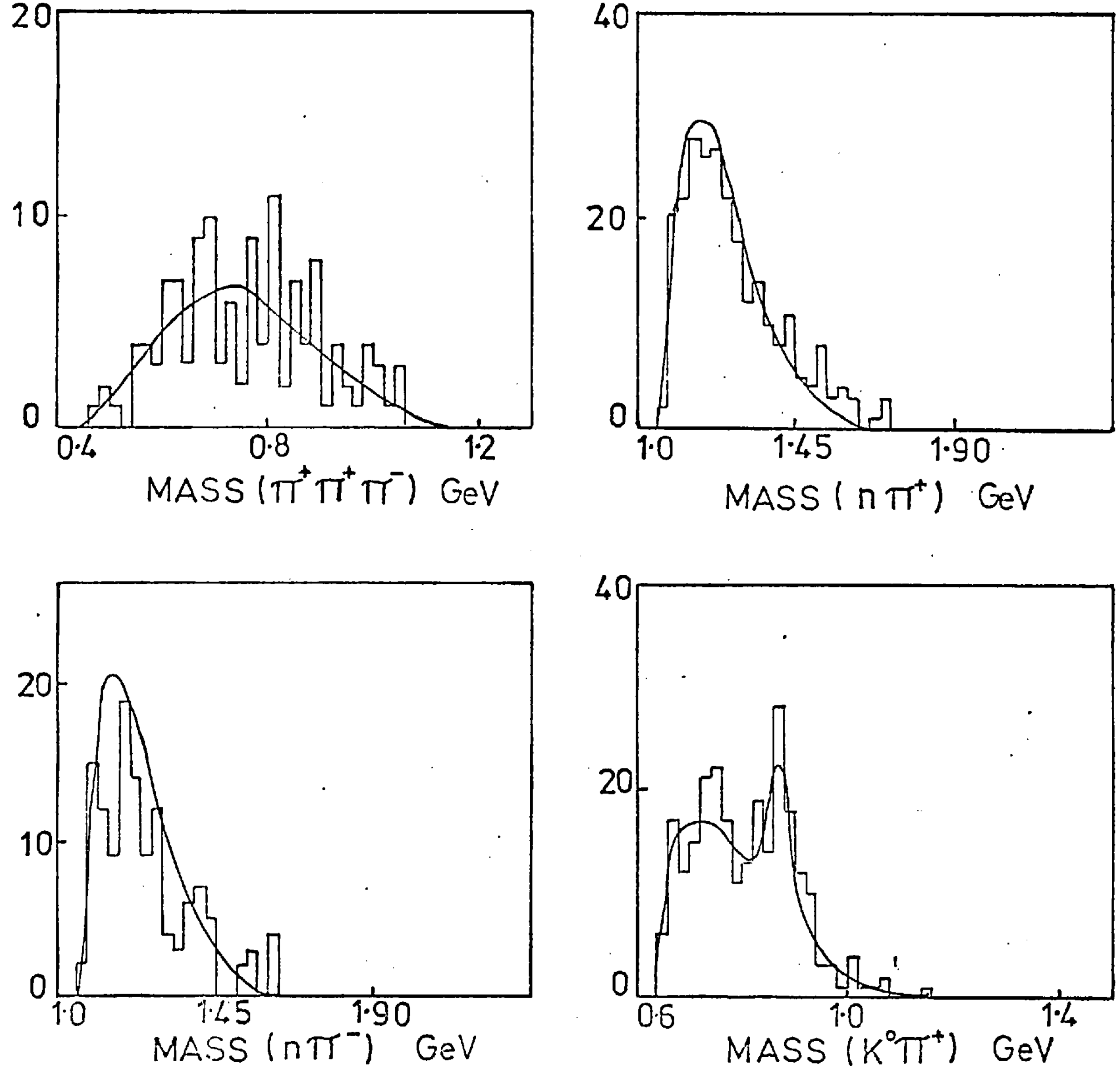

N.B. $n\pi^+$ and $K^0\pi^+$ mass plots have got two entries for each event

7.7

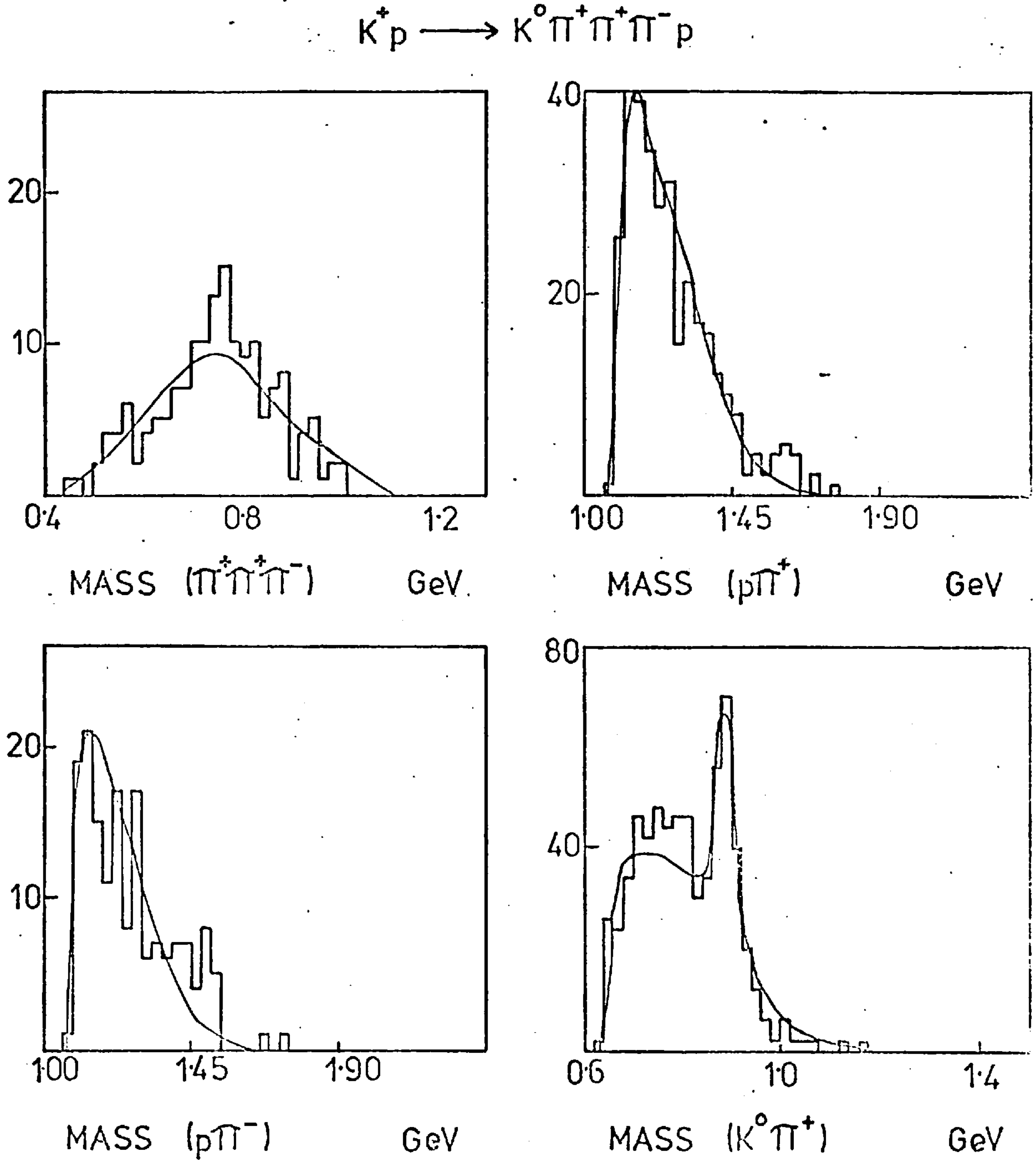

7.8

N.B. $p\pi^+$ and $K^0\pi^+$ mass plots have got two entries for each event

REFERENCES

1. R. Aaron et al., Phys. Rev. Letters 26, (1971), 407.
2. R.J. Abrams et al., Phys. Rev. Letters 19 (1967), 259.
3. R.J. Abrams et al., Phys. Rev. D1 (1970), 1917.
4. J.V. Allaby et al., Phys. Letters 29B (1969), 198.
5. H.L. Anderson et al., Phys. Rev. Letters 26 (1971), 108.
6. T.C. Bacon et al., Phys. Rev. 162 (1967), 1320.
7. W. De Baere et al., Contribution to the International Conference in High Energy Physics, Kiev (1970).
8. S.L. Baker et al., Imperial College Preprint IC/HEP/74/11 (1974).
9. V. Barger and D. Cline, Phys. Rev. 156 (1967), 1522.
10. V. Barger, Plenary Session talk at the XVII International Conference in High Energy Physics, London (1974).
11. K.W.J. Barnham, et al., Nucl. Phys. B28 (1971), 171.
12. G. Bassompierre et al., Phys. Letters 27B (1968), 468.
13. G. Bassompierre et al., Nucl. Phys. B16 (1970), 125.
14. E. Berger et al., Phys. Rev. 179 (1969), 1567.
15. J.C. Berlinghieri, et al., Nucl. Phys. B8 (1968), 333.
16. BGRT Collaboration (G. Giacomelli et al.), Nucl. Phys. B71, (1974), 138.
17. A. Bialas and K. Zalewski, Nucl. Phys. B6 (1968), 449.
18. J.M. Brunet et al., Nucl. Phys. B37, (1972), 114.
19. K. Buchner et al., Nucl. Phys. B9 (1969), 287.
20. K. Buchner et al., Nucl. Phys. B45 (1972), 333.
21. I.Butterworth et al., Phys. Rev. Letters 15 (1965a), 734.
22. I. Butterworth et al., Phys. Rev. Letters 15 (1965b), 737.
23. I. Butterworth et al., Phys. Rev. Letters 15 (1965c), 500.
24. I. Butterworth et al., RHEL Proposal No. 56 (1967).
25. G. Charriere et al., Nucl. Phys. B76 (1974), 333.
26. G.F. Chew and F.E. Low, Phys. Rev. 113 (1959), 1640.

27. D. Cline et al., Nucl. Phys. B22 (1970), 247.

28. R.L. Cool et al., Phys. Rev. Letters 17 (1966), 102.

29. D. Cords et al., Phys. Rev. D4 (1971), 1974.

30. G.V. Dass, C. Michael and R.J.N. Phillips, Nucl. Phys. B9 (1969), 549.

31. D.W. Davies et al., Phys. Rev. D5 (1972),1.

32. S.M. Deen, Rutherford Laboratory preprint RPP/H/68 (1968).

33. G. Dehm et al., Nucl. Phys. B60 (1973), 247.

34. R. Diebold et al., Argonne National Laboratory Preprint ANL/HEL (February, 1974).

35. W. Dunwoodie, et al., CERN preprint CERN/DPhII/74-41 (1974).

36. P. Eberhard and M. Pripstein, Phys. Rev. Letters 10 (1963), 351.

37. A. Firestone et al., Phys. Rev. Letters 25 (1970), 958.

38. A. Firestone et al., Phys. Letters 36B (1971), 513.

39. A. Firestone et al., Phys. Rev. D5 (1972), 505.

40. A. Firestone et al., Nucl. Phys. B52 (1973), 403.

41. G.C. Fox et al., Phys. Rev. D4 (1971), 2647.

42. C. Fu et al., Nucl. Phys. B28 (1971), 571.

43. G. Girardi, R. Lacaze and R. Peschanski, Nucl. Phys. B69 (1974), 107.

44. R.J. Glauber, Phys. Rev. 100 (1955)242.

45. Y. Goldschmidt-Clermont et al., Phys. Letters 27B (1968), 602.

46. M. Gourdin and A. Martin, Nuovo Cimento 11 (1959), 670.

47. G. Hall, Ph.D Thesis, Rutherford Laboratory reprint HEP/T/52 (1974).

48. H. Harari, Ann. Phys. 63 (1971), 432.

49. B.J. Hartley and G.L. Kane, Nucl. Phys. B57 (1973), 157.

50. R.M. Heinz et al., Phys. Rev. 167 (1968), 1232.

51. C.P. Horne et al., Florida State University Preprint 74-6-13 (1974).

52. L. Hülthen and A. Sugawara, Handbuch der Physik, Vol. 34 (1957).

53. J.D. Jackson, Nuovo Cimento 34 (1964), 1644.

54. D. Johnson et al., University of Kansos preprint (1972).

55. L. Kisslinger, Proceedings of the 3rd Internationa Conference on High Energy Physics and Nuclear Structure, New York (1970).

56. V.G. Lind et al., Nucl. Phys. B14 (1969).

57. D. Lissauer et al., Phys. Rev. D6, (1972), 1852.

58. P.J. Litchfield, Baryon Resonances Rapporteurs talk at the XVII International Conference in High Energy Physics, London (1974).

59. J.S. Loos and J.A.J. Mathews, Phys. Rev. D6 (1972), 2463.

60. W. Moninger et al., Phys. Rev. D8 (1973), 38.

61. L. Pape et al., Laboles Hautes Energies Bruxelles preprint 96 (1968).

62. L. Stodolsky and J.J. Sakurai, Phys. Rev. Letters 11 (1963), 90.

63. W. Rarita and B.N. Schwarzschild, Phys. Rev. 162 (1967), 1378.

64. G. Ringland and D.P. Roy, Phys. Letters 36B (1971), 110.

65. G. Thompson, Ph.D Thesis, Rutherford Laboratory publication HEP/T/13 (1971).

66. C. Wilkin, Phys. Rev. Letters 17 (1966), 561.

67. W.L. Yen et al., Phys. Rev. D9 (1974), 1210.

ACKNOWLEDGEMENT

A large number of people have contributed to this experiment and it is impossible to mention all by name. So I would like to thank everybody working in this group at present and also those who participated in this experiment in various ways.

I thank Professor I. Butterworth for the opportunity of carrying out research as a member of this High Energy Physics Group.

I am thankful to Dr. D.B. Miller for acting as my supervisor and to Dr. J.R. Campbell for his advices and many useful discussions.

Thanks are also due to Annette for her excellent typing of this thesis.